Consistent estimates of sea level and vertical land motion based on satellite radar altimetry

Kleinherenbrink, Marcel

DOI
10.4233/uuid:b1be0112-b5ff-4530-a730-4c8c1f176a91

Publication date
2018

Document Version
Final published version

Citation (APA)
Kleinherenbrink, M. (2018). *Consistent estimates of sea level and vertical land motion based on satellite radar altimetry*. [Dissertation (TU Delft), Delft University of Technology].
https://doi.org/10.4233/uuid:b1be0112-b5ff-4530-a730-4c8c1f176a91

Consistent estimates of sea level and vertical land motion based on satellite radar altimetry

Marcel Kleinherenbrink

Cover
Design: Rémi Charton.
Jason-3 satellite, courtesy of NASA/JPL-Caltech.
Earth from space, courtesy of NASA.

Consistent estimates of sea level and vertical land motion based on satellite radar altimetry

PROEFSCHRIFT

ter verkrijging van de graad van doctor
aan de Technische Universiteit Delft,
op gezag van de Rector Magnificus prof. dr. ir. T.H.J.J. van der Hagen,
voorzitter van het College voor Promoties,
in het openbaar te verdedigen op
maandag 12 november 2018 om 12.30 uur

door

Marcel KLEINHERENBRINK

Ingenieur Luchtvaart en Ruimtevaart
geboren te Zwolle.

Dit proefschrift is goedgekeurd door:

Promotor: Prof.Dr. -Ing. habil. R. Klees
Copromotor: Dr. R.E.M. Riva

Samenstelling promotiecommissie:

Rector Magnificus	voorzitter
Prof. dr.-Ing. habil. R. Klees	Technische Universiteit Delft, promotor
Dr. R.E.M. Riva	Technische Universiteit Delft, copromotor

Onafhankelijke leden:

Prof. dr. L.L.A. Vermeersen	Technische Universiteit Delft
Prof. dr. Dipl.-Ing. F.N. Teferle	Université du Luxembourg
Prof. dr. G. Mitchum	Florida State University
Dr. F.M. Calafat	National Oceanography Centre
Dr. ir. R. Scharroo	EUMETSAT
Prof. dr. ir. R.F. Hanssen	Technische Universiteit Delft, reservelid

Dit onderzoek is financieel mogelijk gemaakt door de Nederlandse Organisatie voor Wetenschappelijk Onderzoek (NWO).

Keywords: sea-level change, sea-level budget, satellite radar altimetry, vertical land motion

ISBN 978-94-6186-986-9

Printed by: ProefschriftMaken|| www.proefschriftmaken.nl

Typeset by the author with the LaTeX Documentation System.

Contents

Summary

Satellite radar altimetry is often considered to be the most succesful spaceborne remote sensing technique ever. Satellite radar altimeters were designed for static geodetic and ocean dynamics applications. The goal of the geodetic mission phases, which have a dense ground-track spacing, is primarily to acquire information about the marine gravity field. This enables the estimation of mean dynamic topography (geographical sea surface height patterns due to ocean currents) and deep-ocean bathymetry. The primary goal of the oceanographic mission phases is to gain information about time-varying currents and ocean dynamics. TOPEX/Poseidon is the first altimetry mission to reveal sea surface height variations related to ocean dynamics as the El Niño Southern Oscillation (ENSO). During the mission it became clear that secular changes in sea level could also be monitored. Already in 1995, *Nerem* (1995) computed a Global Mean Sea Level (GMSL) time series from the TOPEX/Poseidon data. Currently, the GMSL record spans 26 years, in which TOPEX/Poseidon time series is extended with the Jason-1&2&3 observations. The estimated secular trend of GMSL over the altimetry era is approximately 3 mm yr^{-1}.

The succes of the TOPEX/Poseidon mission spawned the Argo project with the deployment of the first floats in the year 2000. One argued that Argo would support the future Jason missions in separating changes into the two components (density and mass) of sea level. The Argo project aims to estimate temperature and salinity over a depth of 2000 meter using floats, which enable the estimation of density or steric sea level changes. By subtracting the steric signal from the absolute sea level measured by Jason (steric-corrected altimetry), the second component of sea level changes, mass, is estimated. The launch of the Gravity Recovery And Climate Experiment (GRACE) satellites in 2002 made it possible to independently validate oceanic mass variations. If the sum of the mass and steric components equals total sea level within the uncertainties, the sea level is said to be closed. Besides these two oceanic components, ocean bottom deformation or Vertical Land Motion (VLM) also affects the sea level observed by altimeters. Over the open ocean VLM signals are generally small after a correction for Glacial Isostatic Adjustment (GIA), but near large mass variations they might become significant. Additionally, tide-gauge records are affected by VLM changes, because they are connected to land. Therefore they measure sea level relative to the sea floor, while the satellite altimeters observe the absolute variations. To bring tide gauges in the same reference frame as the altimeters, corrections for VLM have to be applied, which is usually done with nearby Global Navigation Satellite System (GNSS) data.

This thesis investigates the consistency of satellite radar altimetry and other

(geodetic) data from two perspectives on various spatial scales. From a sea level budget perspective, altimetry is used in combination with GRACE and Argo floats to contrain steric, mass and absolute sea level change on unprecedented small scales over the open ocean. The budgets are further investigated over complicated coastal regions, where no Argo floats are present and therefore temperature and salinity estimates from ocean reanalyses are used. From a VLM perspective, altimetry is used in combination with tide gauges and GNSS, to contrain absolute sea level and VLM trends near tide gauges. We focus on consistency in terms of VLM over the whole altimetry era and aim to detect and correct drifts in the altimetry record of one of the missions (TOPEX).

Sub-basin-scale sea level budgets in the North Atlantic Ocean
For the first time an attempt is made to close sea level budgets over the open ocean on a scale of 1/10th of the North Atlantic Ocean using Jason-1&2, GRACE and Argo. For ten regions, the GRACE mass component is summed with the Argo steric component after which the resulting time series are compared to the altimetry-derived mean sea levels. The size of the averaging regions is chosen such that the uncertainty of the trends is smaller than 1 mm yr^{-1}. The consistency of the three observation systems is investigated in terms of a secular trend, the amplitude of the annual cycle and residual signals. State-of-the-art processing methods are used to compute regionally-averaged absolute sea level time series for altimetry. Argo steric sea levels are first objectively interpolated and then averaged over the region. Variance-covariance matrices, using well-known ocean correlation scales, are computed to estimate the uncertainties for the steric and absolute sea level time series. Four (filtered) GRACE gravity solutions are used to estimate the mass time series of sea level: Wiener filtered degree-90 Institute of Theoretical geodesy and Satellite Geodesy (ITSG90-W) gravity fields, Wiener filtered degree-60 and degree-96 Center for Space Research (CSR60-W and CSR96-W) and DDK-filtered degree-96 CSR (CSR96-DDK) solutions. Their uncertainties are propagated from the accompanying variance-covariance matrices. We determine that the best sea level budget closure is obtained using ITSG90-W gravity fields. In terms of trends, the results with ITSG90-W, CSR96-W and CSR96-DDK close nine-out-of-ten budgets if a GIA correction uncertainty of 10-20% is assumed. For the amplitudes of the annual cycle, ITSG-W and CSR96-DDK solutions outperform the other two solutions. Argo summed with ITSG90-W explains the largest part of the residual signal, after removing the annual cycles and the trend. The choice of gravity fields is not important for interannual variability studies in the North Atlantic Ocean, because it is primarily a steric signal.

Separation of mass and steric sea level in the Tropical Asian Seas
In GMSL budgets the Tropical Asian Seas (TAS) are often omitted, because of potential hydrological signal leakage in GRACE mass estimates and the lack of Argo floats in the region. We have separated the mass and steric components of sea level changes in the TAS using a combination of Jason satellite altimetry, GRACE satellite gravimetry and ocean reanalyses. Using observational uncertainties, statistically-weighted

time series for both components have been computed in four regions within the TAS over the period January 2005 - December 2012. Studies have already shown that absolute sea level variations in the TAS correlate strongly with the Pacific equatorial wind stress, which is related to the ENSO and the Pacific Decadal Oscillation (PDO). By regression of the first two principal components (PC1&2) of Pacific equatorial wind stress and the Dipole Mode Index (DMI) through the time series, the drivers of mass and steric sea level in different parts of the TAS are determined. Sea level in the northernmost region, the South China Sea is not affected by any of the atmosphere-ocean dynamics considered. Steric variability in the TAS is largest in the deep Banda and Celebes seas and is affected by both PCs and the DMI, while mass variability is largest on the shallow continental shelves, which is primarily controlled by PC1. We argue that a water flux from the Western Tropical Pacific Ocean is the cause for mass increase during La Niña events. Parts of the TAS experience sea level trends in excess of 10 mm yr^{-1}. The largest contribution comes from the steric trend, which is about 2 mm yr^{-1} larger than the mass trend in the TAS. A significant part of the mass trend can be explained by the aforementioned indices and the nodal cycle. Trends obtained from modelled mass redistribution are statistically equal to the residual mass trends (approximately 2 mm yr^{-1}) when the nodal cycle and the indices are taken into account. The large trends in the TAS have also a substantial effect on the global sea level budget. The effect of omitting the TAS in global sea level budgets is estimated to be 0.3 mm yr^{-1}, which is primarily of steric origin.

Improving altimetry-tide gauge and GNSS vertical land motion trend estimates
Estimates of VLM trends are required to convert tide-gauge-derived sea level trends into an geocentric reference frame. The goal is to improve the quality and increase the number of VLM estimates at tide gauges. Since only a few tide gauges are equiped with a GNSS antenna, (multiple) neighbouring antennas are used to estimate VLM at the tide-gauge location. Eight approaches, that combine the GNSS trends to estimate VLM at tide gauges, have been compared against differenced altimetry-tide gauge (ALT-TG) trends. The range between the eight approaches is similar in size as the formal uncertainties of the GNSS trends. The best agreement with ALT-TG trends is obtained by taking the median of the GNSS trends within the considered radius of 50 km. An attempt is also made to improve VLM trends from differenced ALT-TG time series. By only using highly correlated along-track altimetry and tide-gauge time series, we aim to eliminate residual ocean signals in ALT-TG time series or time series containing discontinuities due to for example earthquakes. This technique reduces the standard deviation of ALT-TG time series up to 10% and as a consequence there are spatially coherent changes in the trends. The reduction in the RMS of differences between ALT-TG and GNSS trends is insignificant, but correlation thresholds also acts like a filter to remove problematic tide-gauge time series. Compared to other studies, we reduce the RMS of differences between the GNSS and ALT-TG trends (from 1.47 to 1.22 mm yr^{-1}), while we increase the number of locations (from 109 to 155). Depending on the methods, the mean of differences between ALT-TG and GNSS trends varies between 0.1-0.2 mm yr^{-1}. The mean is further reduced by modelling and correcting for non-linear effects of elastic deformation due to present-day mass re-

distribution.

Calibration of the TOPEX global mean sea level record

Several recent studies claim that issues in the processing and internal calibration of the TOPEX measurements are the cause for the absence of an acceleration in the GMSL record. The issues are related to the degradating performance of the TOPEX-A side altimeter near the end of its lifetime and its effect on the internal calibration, referred to as 'cal-1'. Other studies have corrected the TOPEX GMSL time series by a calibration with tide gauges or by not applying the cal-1. After the cal-1 removal, a significant acceleration becomes detectable in GMSL time series derived from the TOPEX and Jason satellites. For the calibration with tide gauges, separate drifts for the redundant TOPEX-A (1992-1999) and TOPEX-B (1999-2002) sides and an TOPEX-A/B intramission bias are estimated. We argue that this calibration is likely biased, because the time span is short enough for residual interannual ocean signals in ALT-TG time series to affect the result. Additionally, the intramission bias appears to be geographically varying, which makes the heterogenous tide-gauge network inadequate to determine an accurate intramission bias. Therefore we performed an additional crossover analysis with European Remote sensing Satellite (ERS)1&2 sea surface heights. The comparison confirms that not applying cal-1 is justified, so it is removed. It also reveals that the magnitude of the intramission bias depends on the applied Sea State Bias (SSB) correction and whether cal-1 is removed from TOPEX-A or from the whole TOPEX time series. By estimating a single drift over the whole TOPEX time series and a TOPEX-A/B intramission bias, consistent negative drifts for TOPEX GMSL are found of approximately 1.1 ± 0.3 mm jr^{-1} with respect to ERS, independent of the applied SSB correction. By using the 'old' SSB correction of *Gaspar et al.* (1994) and removing only cal-1 over TOPEX-A, no intramission bias estimate is required and a statistically equivalent drift is obtained. The latter is confirmed by a validation using tide-gauge data records. Therefore we suggest to calibrate TOPEX, after unapplying cal-1, based on the crossovers. This eventually yields a statistically insignificant acceleration in the TOPEX/Jason-1/Jason-2 GMSL time series, contrasting other recent studies.

Samenvatting

Satellietradaraltimetrie wordt vaak gezien als de meest succesvolle aardobservatietechniek vanuit de ruimte ooit. Altimetersatellieten zijn ontworpen voor geodetische en oceaandynamische applicaties. Het belangrijkste doel van geodetische missiefases, die een dichte bemonsteringsdichtheid hebben loodrecht op de vliegrichting, is het vergaren van informatie over het gravitatieveld op zee. Hiermee is het mogelijk om de gemiddelde dynamische topografie (zeespiegelvariaties veroorzaakt door oceaanstromingen) en de bathymetrie in de diepe oceaan te schatten. Het belangrijkste doel van de oceanografische missiefases is het vergaren van informatie over veranderende oceaanstromingen en oceaandynamica. TOPEX/Poseidon is de eerste radaraltimetriesatelliet die zeespiegelveranderingen veroorzaakt door oceaandynamica, zoals de El Niño Southern Oscillation (ENSO), meette. Tijdens de operationele fase van deze missie werd duidelijk dat het ook mogelijk was om trends in de zeespiegel te meten. In 1995 was *Nerem* (1995) al in staat om een Globale Gemiddelde Zeespiegel (GGZ) tijdreeks te maken. Tegenwoordig spant de GGZ tijdreeks 26 jaar en zijn Jason-1&2&3 metingen gebruikt om de tijdreeks te verlengen. De geschatte trend van de GGZ over de altimetrieperiode bedraagt ongeveer 3 mm jr^{-1}.

Het succes van de TOPEX/Poseidonmissie leidde tot het Argo project, waarbij de eerste boeien te water werden gelaten in het jaar 2000. Argo zou de toekomstige Jasonmissies kunnen ondersteunen in het scheiden van de twee belangrijkste componenten (dichtheid en massa) van zeespiegelstijging. Het Argo project heeft als doelstelling de temperatuur en het zoutgehalte over een diepte van 2000 meter te meten, wat het mogelijk maakt om de dichtheidveranderingen of sterische zeespiegelveranderingen te kunnen schatten. Door het sterische signaal van de absolute zeespiegelstijging af te trekken, kan er een schatting gemaakt worden van de massacomponent. De lancering van de Gravity Recovery And Climate Experiment (GRACE) satellieten in 2002, maakte het mogelijk om de geschatte massavariaties onafhankelijk te kunnen valideren. Het zeespiegelbudget is gesloten op het moment dat de som van de massacomponent en de sterische component de absolute zeespiegel benadert tot binnen de onzekerheidsniveaus. Naast de twee oceanische componenten, heeft oceaanbodemdeformatie of Vertical LandBeweging (VLB) ook nog een effect op absolute zeespiegel gemeten door altimeters. Over de open oceaan zijn deze bewegingen over het algemeen klein nadat er gecorrigeerd is voor Postglaciale Opheffing (PO), maar ze kunnen significant worden in de buurt van grote massavariaties. Daarnaast worden metingen van peilmeetstations beïnvloed door VLB, omdat ze vastzitten aan het land. Ze meten dus de zeespiegel ten opzichte van de zeebodem, terwijl satellietaltimeters absolute zeespiegelveranderingen meten. Om peilmeetstations in het-

zelfde referentiesysteem te brengen als de altimeters moeten er correcties voor de VLB worden toegepast, die meestal geschat worden uit Global Navigation Satellite System (GNSS) data.

Dit proefschrift onderzoekt de consistentie van satellietradaraltimetrie en andere (geodetische) datasets vanuit twee perspectieven op verschillende schalen. Vanuit een zeespiegelbudgetperspectief zal altimetrie gebruikt worden in combinatie met GRACE en Argo om massaveranderingen, sterische veranderingen en absolute zeespiegelveranderingen te bepalen op ongeëvenaard kleine schalen over de open oceaan. De budgetten worden verder onderzocht in gecompliceerde kustgebieden waar geen Argoboeien aanwezig zijn en waarvoor temperatuur- en zoutgehalteschattingen uit oceaanheranalyses gebruikt moeten worden. Vanuit een landbewegingsperspectief zal altimetrie gebruikt worden in combinatie met peilmeetstations en GNSS om de absolute zeespiegel- en VLB-trends in de buurt van peilmeetstations te bepalen. We richten ons hierbij op de consistentie van VLB over de gehele altimetrieperiode en we proberen drifts in een van de altimeters (TOPEX) te detecteren en te corrigeren.

Zeespiegelbudgetten op deelgebieden van de Noord-Atlantische Oceaan

Voor het eerst is er een poging gedaan om zeespiegelbudgetten te sluiten op de open oceaan op een schaal van 1/10e van de Noord-Atlantische Oceaan met behulp van Jason-1&2, GRACE en Argo. Voor tien regio's zijn de massacomponent van GRACE en de sterische component van Argo berekend en opgeteld, om vervolgens vergeleken te worden met de gemiddelde zeespiegels berekend uit altimetriedata. De grootte van de regio's is zo gekozen, dat de onzekerheid van de trends niet groter is dan 1 mm jr^{-1}. De consistentie van de drie observatiesystemen is onderzocht op basis van trends, amplitudes van het seizoenssignaal en de overgebleven residuën. Om de gemiddelde zeespiegelstijging in de gebieden te bepalen zijn de modernste verwerkingstechnieken voor altimetrie data gebruikt. De sterische zeespiegelschattingen van Argo zijn eerst objectief geïnterpoleerd en vervolgens gemiddeld over de gebieden. Variantie-covariantiematrices, gebaseerd op alom bekende oceaancorrelatieschalen, zijn gebruikt om de onzekerheden in de sterische en absolute zeespiegelgemiddelde te schatten. Vier GRACE gravitatieveldoplossingen zijn gebruikt om de masscomponent te berekenen: de Wiener filters zijn toegepast op de graad-90 Institute of Theoretical geodesy and Satellite Geodesy (ITSG90-W) en de graad-60 en graad-90 Center for Space Research (CSR60-W and CSR96-W) gravitatievelden en het Dichte DeKorrelation-5 filter is toegepast op het graad-96 CSR gravitatieveld (CSR96-DDK). De onzekerheden van de gemiddelde massavariaties zijn berekend met behulp van de meegeleverde variantie-covariantiematrices. We bepalen dat de beste budgetsluiting wordt verkregen als de ITSG90-W-oplossingen worden gebruikt. Met betrekking tot de trend worden de budget gesloten in negen van de tien regio's met de ITSG90-W-, de CSR96-W- of de CSR96-DDK-oplossingen onder de aanname dat de correctie voor PO een onderzekerheid van 10-20% heeft. ITSG90-W en CSR96-DDK zorgen voor de beste budgetsluiting met betrekking tot de amplitude van de seizoenscyclus. Na het verwijderen van de trend en de seizoenscycli wordt het grootste deel van het residu in de altimetrietijdreeksen verklaard met behulp van Argo in combinatie

met de ITSG90-W-oplossing. De keuze voor de gravitatievelden is minder belangrijk wanneer er wordt gekeken naar interjaarlijkse veranderingen van de zeespiegel in de Noord-Atlantisch Oceaan, omdat dit voornamelijk een sterisch signaal is.

Scheiden van de massa- en sterische zeespiegelveranderingen in de Tropische Aziatische Zeëen

In GGZ-budgetten worden de Tropische Aziatische Zeëen (TAZ) vaak buiten beschouwing gelaten, vanwege mogelijke lekkage van hydrologische signalen in de GRACE massacomponent en de afwezigheid van Argoboeien. Wij hebben de massacomponent van de sterische component gescheiden met behulp van Jason-1&2 satellietaltimetrie, GRACE satellietgravimetrie en oceaanheranalyses. Door gebruik te maken van de observatieonzekerheden zijn statistisch gewogen tijdreeksen berekend voor beide componenten in vier regio's in de TAZ over de period januari 2005 - december 2012. Andere studies hebben al laten zien dat zeespiegelvariaties sterk correleren met de Pacifische equatoriale windbelasting, die gerelateerd is aan de ENSO en de Pacifische Decadale Oscillatie (PDO). Door de regressie van de eerste twee HoofdComponenten (HC1&2) van de Pacifische equatoriale windbelasting en Dipole Mode Index (DMI) met de tijdreeksen, laten we zien waardoor massavariaties en sterische variaties worden gedreven. In de noordelijkste regio, de Zuid-Chinese Zee, kan geen correlatie worden gevonden tussen de bovengenoemde indices en de componenten. De sterische variabiliteit is het grootst in de diepere Banda-Celebesregio en die wordt gedreven door beide HCs en de DMI, terwijl de massavariaties het grootste zijn in de twee minder diepe regio's, waar de massavariaties voornamelijk correleren met PC1. Wij redeneren dat een waterverplaatsing vanuit de westerlijke tropische Pacifische Oceaan tijdens La Niña's de oorzaak is voor de massa veranderingen. Delen van de de TAZ hebben zeespiegeltrends van meer dan 10 mm jr^{-1}. Het grootste deel hiervan wordt veroorzaakt door sterische expansie, die ongeveer 2 mm jr^{-1} groter is dan de massatrend. Een groot deel van de massatoename kan worden verklaard met de voorgenoemde indices en de knopencyclus. Trends berekend uit modellen gebaseerd op globale massaverplaatsingen zijn statistisch gelijk aan de massatrends (ongeveer 2 mm jr^{-1}) als de indices en knopencyclus worden meegenomen in de regressie. De grote trends in de TAZ hebben ook een substantieel effect op het globale zeespiegelbudget. Het weglaten van de TAZ in globale zeespiegelbudgetten heeft een effect van 0.3 mm yr^{-1} op de globale trend. Deze trend heeft hoofdzakelijk een sterische oorzaak.

Het verbeteren van verticale landbewegingschattingen uit altimetrie, peilmeetstations en GNSS

Schattingen van VLB zijn nodig om zeespiegeltrends geschat uit data van peilmeetstations om te zetten naar geocentrisch referentiesysteem. Het doel is om de kwaliteit en het aantal VLB-schattingen bij peilmeetstations te verhogen. Omdat slechts enkele peilmeetstations beschikken over een GNSS-antenne, worden (meerdere) antennes in de buurt gebruikt om de VLB te schatten. Voor het combineren van meerdere GNSS-trends zijn acht verschillende methodes gebruikt, die vergeleken worden met

gedifferentiëerde ALTimeter-PeilMeetStation (ATL-PMS)-trends. De verschillen tussen de acht methodes zijn van vergelijkbare grootte als de formele onzekerheden van de GNSS trends. Door de mediaan te nemen van de GNSS-trends binnen een radius van 50 km van het peilmeetstation, wordt de beste overeenkomst gevonden met de ALT-PMS-trends. Er is ook een poging ondernomen om VLB-trends geschat uit gedifferentiëerde ALT-PMS-tijdreeksen te verbeteren. Door alleen sterkgecorreleerde altimetrie- en peilmeetstationtijdreeksen te gebruiken, pogen we het residuë oceaansignaal in ALT-PMS-tijdreeksen te verwijderen en daarbij ook tijdreeksen te verwijderen die discontinuïteiten bevatten door bijvoorbeeld aardbevingen. Deze techniek reduceert de standaarddeviatie van ALT-PMS-tijdreeksen met ongeveer 10% en veroorzaakt daarbij een geografisch coherente verandering in de VLB trends. Hiermee wordt het kwadratisch gemiddelde van de verschillen tussen de ALT-PMS- en GNSS-trends niet significant gereduceerd, maar de correlatiedrempels filteren wel problematische peilmeetstationtijdreeksen. Vergeleken met andere onderzoeken verlagen we het kwadratisch gemiddelde tussen ALT-PMS- en GNSS-trends (van 1.47 mm jr^{-1} naar 1.22 mm jr^{-1}), terwijl we het aantal locaties waarbij de trends zijn vergeleken verhogen (van 109 naar 155). Afhankelijk van de methodes, wordt er een gemiddeld verschil tussen ALT-PSM- en GNSS-trends gevonden van 0.1-0.2 mm jr^{-1}. Dit gemiddelde wordt verder gereduceerd door het modelleren en corrigeren van nonlineaire effecten van elastisch deformatie door de huidige geografische massaverplaatsingen.

De kalibratie van de global zeespiegeltijdreeks van TOPEX

Verscheidene recente onderzoeken claimen dat problemen met de verwerking en de interne kalibratie van TOPEX-metingen de oorzaak zijn voor de afwezigheid van een acceleratie in de GGZ-tijdreeks. De problemen zijn gerelateerd aan de verminderde prestaties van de TOPEX-A-altimeter aan het einde van zijn operationele periode en de effecten daarvan op de interne calibratie genaamd 'cal-1'. Andere onderzoeken hebben de GGZ-tijdreeks van TOPEX gecorrigeerd door middel van een kalibratie met peilmeetstations of door het niet toepassen van cal-1. Na het verwijderen van cal-1 is er een significante acceleratie meetbaar in de GGZ-tijdreeksen gebaseerd op TOPEX- en Jasonsatellieten. Voor de kalibratie met peilmeetstations worden er twee verschillende drifts bepaald voor TOPEX-A (1992-1999) en TOPEX-B (1999-2002) en daarnaast wordt er een TOPEX-A/B intramissieverschil geschat. We beargumenteren dat deze manier van kalibreren fouten oplevert, omdat de tijdreeksen kort genoeg zijn om de resultaten te laten beïnvloeden door overgebleven oceaansignalen in ALT-PMS-tijdreeksen. Daarnaast blijkt het intramissieverschil tussen TOPEX-A&B geografisch te variëren, wat het heterogene peilmeetstationnetwerk ongeschikt maakt voor het schatten van een nauwkeurig intramissieverschil. Daarom voeren wij een extra crossoveranalyse met zeespiegelmetingen van de European Remote Sensing (ERS)1&2-satellieten uit. De verlijking laat zien dat het verwijderen van cal-1 verdedigbaar is, dus passen we deze niet toe. Met de crossovers wordt het ook duidelijk dat de grootte van het intramissieverschil afhangt van de toegepaste Sea State Bias (SSB) correctie en het hangt ook af of cal-1 verwijderd wordt van de hele TOPEX tijdreeks of slecht van TOPEX-A. Door het tegelijktijdig schatten van een enkele drift

door TOPEX-A/B en een intramissieverschil wordt er een consistente negatieve drift gevonden van 1.1±0.3 mm jr^{-1}, die onafhankelijk is van de toegepaste SSB-correctie. Als cal-1 alleen van TOPEX-A wordt verwijderd en de oude SSB-correctie van *Gaspar et al.* (1994) wordt gebruikt, hoeft er geen intramissieverschil te worden geschat en wordt er weer een statistisch equivalente drift gevonden. Deze laatste bewering wordt ondersteund door een validatie met peilmeetstationdata. Daarom stellen we voor om TOPEX te kalibreren, na het verwijderen van cal-1, gebaseerd op de crossovers. Door deze kalibratie wordt de acceleratie in de GGZ-tijdreeks van TOPEX, Jason-1 en Jason-2 insignificant, in tegenstelling tot recente onderzoeken.

List of Abbreviations

ALES	Adaptive Leading Edge Waveform
ALT-TG	ALTimetry - Tide Gauge
AMOC	Atlantic Meridional Overturning Circulation
ANS	Anisotropic Non-Symmetric
AOD	Atmosphere and Ocean Dealiasing
AVISO	Archiving, Validation and Interpretation of Satellite Oceanographic data
B17	Beckley et al. (2017)
CATS	Create and Analyze Time Series
COD	Coefficients Of Determination
CP	Control Point
CLS	Collecte Localisation Satellites
CSR	Center for Space Research
DAC	Dynamic Atmosphere Correction
DDK	Dichte DeKorrelation (dense decorrelation)
DMI	Dipole Mode Index
DORIS	Doppler Orbitography and Radiopositioning Integrated by Satellite
ECCO	Estimating the Circulation & Climate of the Ocean
ECMWF	European Centre for Medium-range Weather Forecasts
ENSO	El Niño Southern Oscillation
ERS	European Remote Sensing satellite
EWH	Equivalent Water Height
GIA	Glacial Isostatic Adjustment
GMSL	Global Mean Sea Level
GNSS	Global Navigation Satellite System
GPS	Global Positioning System
GRACE	Gravity Recovery And Climate Experiment
GSFC	Goddard Space Flight Center
ITSG	Institute of Theoretical geodesy and Space Geodesy
JPL	Jet Propulsion Laboratory
J1	Jason-1
J2	Jason-2
OBP	Ocean Bottom Pressure
OMCT	Ocean Model for Circulation and Tides
PC	Principal Component
PCR-GLOBWB	PCRaster GLOBal Water Balance

PDO	Pacific Decadal Oscillation
PSMSL	Permanent Service for Mean Sea Level
PTR	Point Target Response
MC	Mass Component
MIDAS	Median Interannual Difference Adjusted for Skewness
MSL	Mean Sea Level
MSLA	Mean Sea Level Anomaly
NGL	Nevade Geodetic Laboratory
NOAA	National Oceanic and Atmospheric Administration
RADS	Radar Altimetry Database System
RMS	Root-Mean-Square
SAR	Synthetic Aperture Radar
SSB	Sea-State Bias
SLA	Sea Level Anomaly
SWH	Significant Wave Height
TAS	Tropical Asian Seas
TEOS-10	Thermodynamic Equation Of Seawater 2010
TG	Tide Gauge
TOPEX	ocean TOPography EXperiment
TP	TOPEX/Poseidon
TWS	Terrestrial Water Storage
T/S	Tempature/Salinity
UHSLC	University of Hawaii Sea Level Center
UK	United Kingdom
ULR	University of La Rochelle
VLM	Vertical Land Motion
W15	Watson et al. (2015)
WTPO	Western Tropical Pacific Ocean

Author Contributions

This thesis consists of a set of three published articles and an article in preparation. The research and writing of the articles have been performed by several authors. The contributions of the authors to each article are therefore listed below.

Chapter 2
Sub-basin-scale sea level budgets from satellite altimetry, Argo floats and satellite gravimetry: a case study in the North Atlantic Ocean.
Authors: Kleinherenbrink, M., Riva, R., & Sun, Y. (2016).

M.K. and R.R. conceived the idea. M.K. performed the altimetry and Argo computations. M.K. and Y.S. performed the gravimetry computations. R.R. supervised the project. M.K. wrote the manuscript. R.R. and Y.S. provided critical comments on the manuscript.

Chapter 3
Trends and interannual variability of mass and steric sea level in the Tropical Asian Seas.
Authors: Kleinherenbrink, M., Riva, R., Frederikse, T., Merrifield, M., Wada Y. (2017).

M.K. and R.R. conceived the idea. M.K. performed the majority of the computations. Y.W. computed the land hydrology loads. T.F. performed the sea level equation computations. M.M. provided insight into the ocean dynamics. R.R. supervised the work. M.K. wrote the manuscript. All authors provided critical comments on the manuscript.

Chapter 4
A comparison of data weighting methods to derive vertical land motion trends from GNSS and altimetry at tide gauge stations.
Authors: Kleinherenbrink, M., Riva, R., & Frederikse, T. (2018).

M.K. and R.R. conceived the idea. M.K. performed the computations. T.F. modelled the non-linear vertical land motion. R.R. supervised the research. M.K. performed the writing. All authors provided critical comments on the manuscript.

Chapter 5
Calibration of the TOPEX global mean sea level record using ERS1&2.
Authors: Kleinherenbrink, M., Riva, R., & Scharroo, R. (2018).

M.K. and R.S. conceivd the idea. M.K. performed the computations. R.R. supervised the work. All authors provided critical comments on the manuscript.

Chapter 1

Introduction

1.1 Multi-timescale sea-level variations

Although sea-level rise is commonly associated with the ongoing discussion about climate change, large variations in sea level have occurred before the industrial revolution. Since the peak of the last glacial period (22,000 years before present) Global Mean Sea Level (GMSL) has risen approximately 120 meters, due to meltwater from massive ice sheets entering the ocean. Before the glacial period, in the last interglacial maximum (125,000 years before present), when temperatures were about 1° above pre-industrial levels, GMSL reached a peak value of 6-9 meter above the current level (*Dutton et al.*, 2015). In the late Holocene (the last 3000 years) before the industrial revolution (1850), however, GMSL was relatively stable and fluctuated up to a decimeter (*Kopp et al.*, 2016). The fluctuations in sea level over the past 3000 years are primarily driven by global temperature changes. After 1850 global temperatures started increasing and currently reach the level of the last interglacial maximum. Around 1900 GMSL started to increase unabatedly, with rates unprecented in the late Holocene (Fig. 1.1) (*Kopp et al.*, 2016). The increase is often attributed to the change in global temperature and believed to be of human origin. As GMSL is closely linked to global temperature, but the response of oceans and ice sheets to temperature changes is very slow, it is argued that the Earth is already committed to a sea-level rise of 1.0-10.8 (*Levermann et al*, 2013). In addition, sudden rapid increases (*Mercer*, 1978) are expected due to the instability of the West Antarctic ice sheet (*Hulbe*, 2017). Recent studies demonstrate an increase in the rate of sea-level rise in the 22^{th} century up to 5 cm yr^{-1} in a high-emission scenario (*DeConto and Pollard*, 2016).

From around 1900 enough tide-gauge records with sufficient length became available to estimate the 20^{th} century GMSL. Due to the sparsity and the poor geographical distribution of the tide gauges in the first half of the century and differences in reconstruction techniques, the estimates of the 20^{th} century sea-level trend vary between 1-2 mm yr^{-1} (*Church and White*, 2011; *Dangendorf et al.*, 2017). The reconstructed GMSL sea-level curves are characterised by decadal variability (Fig. 1.1), i.e. fluctuations in the 20-year trends between 0-3 mm yr^{-1} (*Dangendorf et al.*, 2017). Despite the decadal variations, a significant acceleration is detectable in

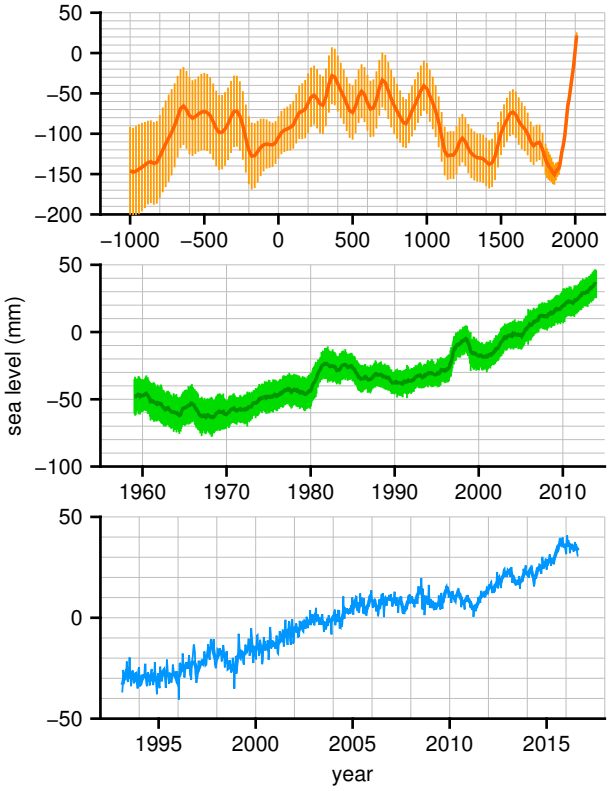

Figure 1.1: Time series of estimation GMSL variations over three periods. The top figure shows the reconstruction from *Kopp et al.* (2016), in the middle the reconstruction from *Frederikse et al.* (2018) and in the bottom the altimetry-derived GMSL curve based on Radar Altimetry Database Data (RADS) data (*Scharroo et al.*, 2012).

reconstructed GMSL (*Jevrejeva et al.*, 2014). Both trends and acceleration estimates are required to give insight into current and future changes in sea level. Interpreting trends from individual tide-gauge records is non-trivial and requires knowledge about interannual and decadal variability as well as estimates of Vertical Land Motion (VLM) at the tide-gauge location (*Santamaría-Gómez et al.*, 2014; *Frederikse et al.*, 2016; *Santamaría-Gómez et al.*, 2017). In addition, the estimated accelerations from stand-alone records are not evident due to large interannual and decadal variability (*Haigh et al.*, 2014).

During the satellite era (1992-2018), which is the focus of this thesis, an even larger trend is estimated using satellite radar altimetry, ranging between 3.1-3.4 mm yr^{-1}. The uncertainty of this trend is believed to be at the 0.4 mm/yr level based on a validation with tide-gauge records (*Mitchum*, 1998, 2000). The short altimetry-derived GMSL time series exhibit significant interannual variability of which the most prominent signals are associated with the El Niño Southern Oscillation (ENSO) (*Boening et al.*, 2012; *Piecuch and Quinn*, 2016). Interannual signals make it difficult to detect a climate-related acceleration in the altimetry-derived GMSL time series.

Nevertheless, recent studies claim to have found an acceleration in the 25-year long time series by reprocessing the altimetry data and/or correcting for interannual signals (*Beckley et al.*, 2017; *Nerem et al.*, 2018).

1.2 Regional variations and causes of sea-level change

Besides temporal variability in sea level there are strong geographic variations. The trends computed over the period 1993-2015 show clear evidence of ocean dynamics (Fig. 1.2). Trend maps highlight decadal variability in the ocean, while more subtile contributions, barely visible in the maps, are of more importance in the long term. Therefore care should always be taken when interpreting regional sea-level trends and especially accelerations.

Under the assumption that vertical ocean floor motion is negligible, sea-level changes are often separated into two contributions: mass and steric signals. The steric signal represents density changes and comprises a halosteric component, due to salinity changes, and a thermosteric component, due to temperature changes. If the temperature of the ocean increases, the water column expands causing the sea level to rise. The opposite happens when the ocean gets more saline; the density increases and sea level will drop. On the long term and on large scales, temperature changes are the main driver of steric sea level (*Ishii et al.*, 2006). The contribution of salinity changes to global mean steric sea level is close to zero, but regionally the effects can be significant (*Llovel and Lee*, 2015; *Wang et al.*, 2017). Over the Argo era (2005-2015) the contribution of the steric component to GMSL is estimated to be approximately 1 mm yr^{-1} (*Wei and Zhong*, 2015; *Chambers et al.*, 2017). Therefore steric changes contribute to about 1/3th of GMSL. The strong geographical variations in the altimetry plot are mostly of steric origin, except on the continental shelves. On an interannual scale, ocean-atmosphere dynamics like ENSO change sea level by several decimeters, primarily around the equator (*Philander*, 1983). On a decadal scale, similar dynamics exist, like the Pacific Decadal Oscillation (PDO) (*Mantua and Hare*, 2002), which is the primary cause for the large sea-level trends in the Western Tropical Pacific Ocean (Fig. 1.2). Estimated steric trends therefore require careful interpretation and should not be extrapolated.

The mass component is currently the largest contributor to the GMSL trend, with approximately 2 mm yr^{-1} (*Leuliette and Willis*, 2011; *Chambers et al.*, 2017). Long-term secular rates in sea level, regional and global, are primarily caused by water exchange between ocean and land. The main contribution comes from the ice sheets (Greenland and Antarctica), glaciers, land hydrology and dam retention. Greenland's melting ice sheet contributes most to the rising sea levels, while dam retention has a small negative effect (*Frederikse et al.*, 2016). Interannual changes in global ocean mass are often associated with ENSO phases, during which precipitation change could influence groundwater storage (*Boening et al.*, 2012; *Piecuch and Quinn*, 2016). The contribution of mass to GMSL is referred to as barystatic sea level (*Gregory et al.*, 2013). Regionally, deviations from barystatic sea level occur due to ocean dynamics or gravitational effects (*Farrell and Clark*, 1976). For example, large

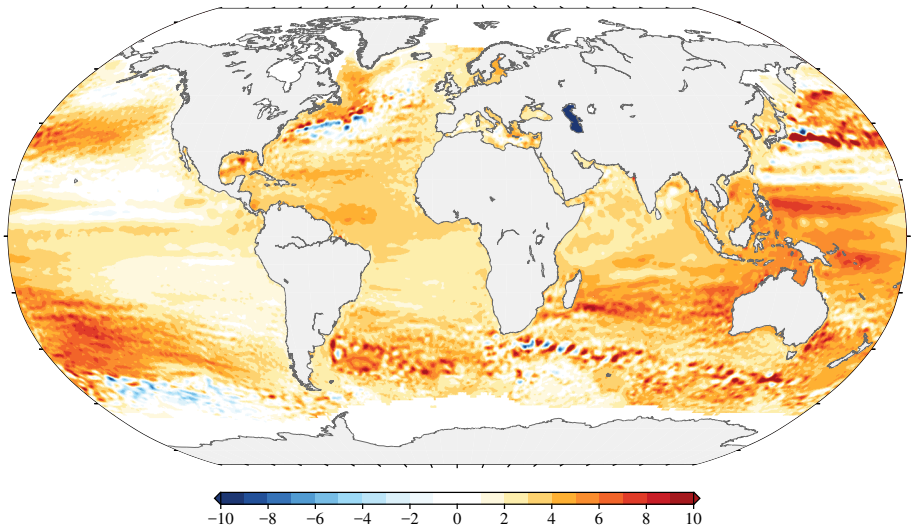

Figure 1.2: Sea surface height trends (mm yr^{-1}) over the period 1993-2015 based on Ssalto/Duacs gridded satellite altimetry data downloaded from AVISO (*Pujol et al.*, 2016).

mass changes can occur on continental shelves as the ocean dynamically responds to steric changes in the nearby deep ocean (*Hughes and Meridith*, 2006; *Landerer et al.*, 2007). The largest gravitational effects occur near the Greenland and West-Antarctic ice sheets (*Bamber and Riva*, 2010). Near the point of mass loss the sea level drops, because the shrinking mass reduces the gravitational pull on the water. This drop extends over several thousands of kilometer, so that the melt of Greenland will not lead to large sea-level rise at the Dutch coast. On the other side of the world, sea level increases slightly more than barystatic.

Two indirect effects occur due to mass redistribution. First, it causes a change in the spatial loading pattern. The load changes deform the ocean floor and so the sea level observed with an altimeter will differ from the sum of the steric and mass components. Changes with respect to the ocean floor are referred to as relative sea level, while the altimeter measures geocentric, or absolute sea level. In most regions this effect is small and can be ignored, but in the vicinity of ice sheets and on continental shelves the ocean floor deformation is significant. Second, mass redistribution causes a change in the Earth's rotation (*Milne and Mitrovica*, 1998). As a consequence, the centrifugal force will change, which affects sea level.

1.3 Sea-level observations in the satellite era

Chapters 2 and 3 focus on the consistent estimation of total sea level and its steric and mass components. Since 1992 satellite radar altimeters have continuously measured geocentric sea level, i.e. the sea level with respect to the center-of-mass of the Earth. GMSL time series are commonly constructed using the data collected during the repeat-mission periods of the Jason series of dedicated altimetry satellites, which

consist of TOPEX/Poseidon (TP) (1992-2002), Jason-1 (J1) (2002-2008), Jason-2 (J2) (2008-2017) and Jason-3 (2016-present). These satellites orbit the Earth in a 10-day repeat orbit at a 66° inclination, which leaves a large gap a the poles and a 315 km track spacing at the equator. Based on comparisons with tide gauges, the uncertainty of the trend in altimetry-derived GMSL is estimated to be 0.4 mm yr^{-1} (*Mitchum*, 2000). Due to the length of the GMSL time series, some studies suggest that it is possible to estimate a statistically significant acceleration (*Beckley et al.*, 2017; *Nerem et al.*, 2018). It depends strongly on the processing techniques or calibrations of the TOPEX altimeter, which monitored sea level over the TOPEX-A (1992-1999) and TOPEX-B (1999-2002) periods. Especially TOPEX-A is a concern, because the intstrument deteriorated at the end of the period, which increased the uncertainty of the altimeter calibration parameters.

Statistically interpolated grids of altimetry data, which are used as input for Fig. 1.2, also involve data from the ERS-1&2, Envisat and SARAL missions (Envisat series), which orbit the Earth in a 35-day repeat orbit (*Pujol et al.*, 2016). Besides denser ground-tracks at the equator, these missions ensure a better coverage at the poles, because their orbits have an inclination of 98°. However, the mean sea-level time series from the Envisat series is not continuous and is therefore often omitted in long-term sea-level studies. In regional sea-level studies where spatially denser coverage is required, these missions are often incorporated next to the standard Jason series. Standard altimetry products are often not accurate in the coastal zone (within several 10s of kilometers from the shore), due to land signals that contaminate the observations and due to uncertain geophysical corrections in coastal areas. With the use of new processing techniques, e.g., Delay/Doppler which gives a better along-track resolution, satellite altimeters like Cryosat-2 and Sentinel-3 make it possible to measure coastal areas. Unfortunately, these type of altimeters have only been flown for the last eight years and are not used so far in sea-level trend estimation. Some improvements have been obtained by the use of dedicated coastal altimetry algorithms, like the Adaptive Leading Edge Subwaveform (ALES) retracker (*Passaro et al.*, 2014).

In 2002 the Gravity Recovery And Climate Experiment (GRACE) satellites were launched into a polar low Earth orbit. The satellites utilized low-low satellite-to-satellite tracking to measure differential accelerations. From the acceleration differences the gravity field is estimated. Under the assumption that gravity changes are driven by mass redistribution at the Earth's surface, they can be expressed in terms of surface mass anomalies, which (after correcting for the GIA signal) are primarily linked to the redistribution of water. For ocean applications the surface mass anomalies are expressed in Equivalent Water Height (EWH). The resolution of mass variations obtained from GRACE is typically 250-300 km (*Siemes et al.*, 2013) and to minimize signal leakage from land the coastal zones are therefore often omitted in sea-level studies. The conversion to surface mass anomalies takes the deformation of the solid Earth due to loading into account. Therefore it is also possible to estimate the deformation of the sea floor from GRACE (*Fenoglio-Marc et al.*, 2012), however this is often neglected because the signal is small in most oceanic regions.

The Argo program became operational in 2000 with the deployment of the first floats. Currently, more than 3000 floats measure temperature and salinity up to a depth of 2000 meters every ten days. The Argo floats complement the Jason altimetry satellites in observing sea-level variability in the ocean, because they enable to estimate steric sea level. Steric sea level is usually computed with the Thermodynamic Equation Of Seawater 10 (TEOS-10) software package (*Pawlowicz et al.*, 2012). In 2007 the target of 3000 floats was reached (*Canabes et al.*, 2013), i.e. one float per 3°× 3° box, but it is often assumed that the coverage since 2004 or 2005 is enough to accurately estimate global mean steric sea level (*Leuliette and Miller*, 2009). Due to their ability to freely drift, the distribution of Argo floats is non-homogeneous. The temperature and salinity measurements are therefore often statistically interpolated to a equiangular grid (*Ishii et al.*, 2006; *Roemmich and Gilson*, 2009). This, however, still leads to problematic regions around the poles and on continental shelves where no Argo floats are present (*Roemmich and Gilson*, 2009; *Von Schuckmann et al.*, 2014). For the estimation of steric sea level in these regions it is better to use ocean reanalysis products (*Dieng et al.*, 2015), which assimilate Argo data, and physically propagate signals over the continental shelves.

The simultaneous presence of the three observing systems: satellite altimetry, satellite gravimetry and Argo, makes it possible to construct sea-level budgets. *Leuliette and Miller* (2009) were the first to close the sea-level budget on a global scale. With these type of budgets, it is shown that the mass trend in GMSL became larger than the the steric trend after 2005. Several other studies used the three systems on the scale of large basins to either close the budget or to constrain the mass or steric component (*Chambers and Willis*, 2010; *Marcos et al.*, 2011; *Von Schuckmann et al.*, 2014). Similar studies have been performed in marginal seas, like the Red Sea (*Feng et al.*, 2014; *Wahr et al.*, 2014) or the Mediterranean (*García et al.*, 2006; *Fenoglio-Marc et al.*, 2006; *Calafat et al.*, 2010), where mass variations are large. However, sub-basin-scale budget closures over the open ocean have never been attempted, nor at continental shelves such as the Tropical Asian Seas.

1.4 Vertical land motion in the satellite era

As mentioned before, absolute sea level, or geocentric sea level, is affected by VLM. On large scales (>1000 km), the largest VLM signals are caused by Glacial Isostatic Adjustment (GIA), which is the visco-elastic response of the Earth due to loading and unloading during glacial cycles. A GIA correction of 0.3 mm yr^{-1} is often applied to altimetry-derived GMSL to compensate for the expansion of ocean basins, but locally this can reach 15 mm yr^{-1} (*Gutenberg et al.*, 1941; *Peltier et al.*, 2015). The largest positive GIA VLM signals are found at the locations of former ice sheets, like Canada and Scandinavia, while the largest negative signals are found at the collapsing forebulges, for example at the coasts of North America (*Peltier et al.*, 2015). Present-day mass redistribution also causes the sea floor to move vertically (*Riva et al.*, 2017). Greenland and Antarctica, for example, loose mass, which causes the solid Earth in the vicinity of the ice sheets to respond elasticly and move upwards. The melting of

ice, however, increases the ocean mass and as a consequence the sea floor will drop slightly far away from the ice sheets. While the melting of ice sheets and glaciers is the primary source for a secular trend or even an acceleration (*Riva et al.*, 2017), interannual variability in surface loading is mostly caused by atmosphere and ocean dynamics and land hydrology storage changes (*Boening et al.*, 2012; *Pfeffer et al.*, 2017). These large-scale processes can be modelled using (visco-)elastic models that require estimated loads as inputs. Over the open ocean, altimetry-derived sea level is often only corrected for secular GIA trends, but not for VLM due to present-day loading, because the signals are small in most regions.

Superimposed on the large-scale effects are the regional processes, which are primarily affecting regional tide-gauge records. Since tide gauges are connected to land, they measure local relative sea level, so when the land moves upward, a falling sea level is measured. Earthquakes induce sudden discontinuities in tide-gauge time series and sometimes a substantial post-seismic signal(*Broerse et al.*, 2015). Corrections are non-trivial and often the only solution is to discard the tide gauge from the analysis (*Watson et al.*, 2015). Changes in local groundwater storage exhibit interannual and decadal signals, which move the soil. Groundwater related signals are highly spatially variable and to eliminate them from the tide-gauge records, VLM estimates in the close vicinity of the tide gauge are required. In large cities, like Jakarta, Bangkok and Manila, the VLM signal reaches the decimeter-per-year level, due to groundwater extraction (*Rodolfo and Siringan*, 2006). Several other local effects occur, which are primarily anthropogenic, like mining and construction. At present, no accurate modelling exist for regional VLM.

For sea-level studies, VLM estimates at tide gauges are required to convert between geocentric and relative sea level in order to compare those records with altimetry records. Using the Global positioning System (GPS) is one of the techniques to measure local VLM (*Wöppelmann et al.*, 2007). When referring to GPS, we will use the more general term Global Navigation Satellite Systems (GNSS), which also includes other satellite positioning systems available nowadays. Typical formal uncertainties on the GNSS trends are 0.5 mm yr^{-1} for a time series of 12 years (*Wöppelmann et al.*, 2009; *Wöppelmann and Marcos*, 2016) based on a power-law noise model. A more realistic uncertainty is for most GNSS trends closer to 1 mm yr^{-1}, because the results strongly depend on the applied discontinuity detection methods (*Gazeaux et al.*, 2013). Unbiased VLM corrections for tide gauges also require knowledge of the relative motion between the tide gauge and the GNSS antenna. This is either achieved by co-locating the GNSS antenna with the tide gauge or by regular levelling campaigns. Unfortunately, for only a few tide gauges this is done. Therefore the nearest GNSS station is often assumed to be exposed to similar VLM as the tide gauge. In practice the VLM trends vary several millimeters per year over several tens of kilometers (*Santamaría-Gómez et al.*, 2017) and therefore the VLM estimates are biased. Another issue is the geographical distribution of tide gauges for which accurate GNSS trends are available (Fig. 1.3). Most of them are located in Australia, Europe or North-America. As a consequence, calibration and validation of altimeters and sea-level reconstructions based on tide gauges might be biased.

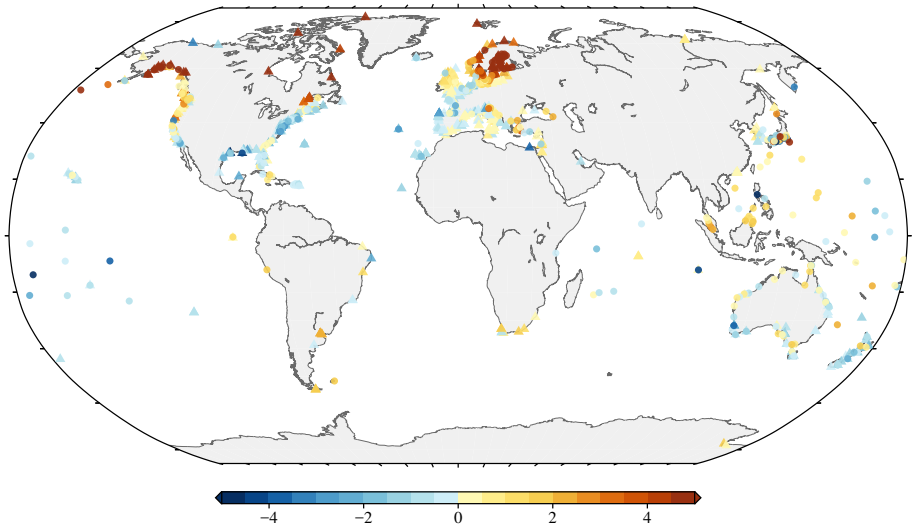

Figure 1.3: VLM (mm yr^{-1}) at tide gauges derived from NGL GNSS (triangles) and ALT-TG (circles) time series. Clear uplift signals are visible in the regions of former ice sheets (Canada, Alaska and Scandinavia).

To reduce the issue of non-homogeneously spaced VLM trends, a second indirect method is used to estimate VLM near tide gauges (*Nerem and Mitchum*, 2002; *Ostanciaux et al.*, 2012; *Wöppelmann and Marcos*, 2016; *Pfeffer and Allemand*, 2016). VLM is then estimated by subtracting relative sea level, as measured by tide gauges, from geocentric sea level, as measured by altimetry satellites. Preferably, the altimetry measurements are made at the same location as the tide gauge, but this is practically not possible. Therefore residual oceanic signals in the differenced altimetry - tide-gauge (ALT-TG) time series might bias trends estimated with this method. If those biases are characterised by regional patterns that cannot be easily removed, they could lead to biases in altimetry validations and calibrations. Since residual oceanic signals are most prominent on interannual scales, validations and calibrations over short time spans (<10 years) are most likely to be biased. When the whole altimetry record is used the uncertainties of ALT-TG trends are of the same order as those obtained with GNSS, due to the relatively long time span compared to most GNSS stations. A comparison between the GNSS and ALT-TG trends at more than 100 stations yields an RMS of differences of 1.47 mm yr^{-1} (*Wöppelmann and Marcos*, 2016). This is not yet at the required level of 1 mm yr^{-1} for regional sea-level studies.

1.5 Research objectives

This thesis focusses on two main topics in sea-level research: sea-level budgets and VLM. Both are entangled and can therefore never be considered completely separately. The sea-level budget related chapters focus on consistent estimates of absolute sea level from satellite altimetry, the mass component from GRACE and steric sea

level using either Argo floats or ocean reanalyses on regional scales. With consistent estimates, we imply that the sea-level budget should be closed to within a certain confidence interval. Chapters 4 and 5 of this thesis focus on improving the consistency between GNSS, tide gauge and altimetry observations. Firstly, to constrain VLM trends at tide gauges and secondly to use tide-gauge time series and VLM trends to detect drifts in altimeters. The following research questions will be answered:

Can the sea-level budget be closed on a regional scale in the North Atlantic Ocean using satellite altimetry, satellite gravimetry and Argo float observations?
The density of Argo floats in the North Atlantic provides the possibility to constrain sub-basin-scale steric sea-level variability. Summed with monthly ocean mass time series estimated from monthly GRACE gravity fields they should be approximately equal to the total sea-level observations from Jason-1&2 altimeters. We use established ocean dynamics correlation scales to estimate uncertainties for the altimetry and Argo total and steric sea-level time series. Several GRACE solutions are used and their uncertainties are propagated from the associated variance-covariance matrices. The budget is closed in terms of trend and annual cycle, if the sum of the components matches the total sea level to within a 95% confidence interval. After removal of the trend and annual cycles, it is investigated whether the residuals explain remaining interannual variability.

How can we consistently separate the mass and the steric component of sea level on continental shelves and in coastal regions?
Due to the lack of Argo floats above continental shelves and the limited resolution of GRACE, which causes land hydrology signal leakage into the ocean mass estimates in coastal zones, these areas are often omitted in sea-level budgets. We use the Tropical Asian Seas to demonstrate how mass and steric sea level can be separated using Jason-1&2, GRACE and ocean reanalysis by statistically weighting their observations and estimates. No statistical information is provided with the ocean reanalyses, so the mean of the steric sea levels derived from eight reanalyses is taken and the spread between them is used in the weighting process. After separating the components, the interannual variability and trends are linked to atmosphere-ocean dynamics and present-day mass redistribution processes. Eventually, the effect of omitting the Tropical Asian Seas in GMSL budgets is quantified.

Can we improve the ALT-TG-derived and GNSS-derived VLM estimates at tide gauges?
Since altimeter validations and tide-gauge reconstructions require accurate VLM estimates at tide gauges, we aim to show an improvement with a cross-validation between the ALT-TG and GNSS techniques. First, it is determined whether the GNSS station closest to a tide gauge should be used or if another combination/weighting method provides more reliable results. The dependence on a single GNSS per tide gauge makes the method prone to outliers and therefore we compare this commonly-used approach to seven other approaches involving multiple tide gauges. Second,

correlations between the tide gauge and the altimetry sea levels are exploited to reduce the oceanic signals in the ALT-TG time series. In addition, we introduce a correlation threshold that should act as a filter to remove eratic and unreliable ALT-TG time series e.g., contaminated by earthquakes or by (unregistered) equipment changes. Finally, discrepancies between the two methods are further reduced by correcting for non-linear VLM caused by present-day mass redistribution.

How to process and calibrate GMSL derived from the TOPEX altimeter using crossovers, tide gauges and VLM estimates?
This question focusses on the processing and calibration of the problematic TOPEX GMSL time series. *Watson et al.* (2015) and *Beckley et al.* (2017) showed that TOPEX-A is drifting with respect to tide gauges. Additionally, an intramission bias between TOPEX-A&B has to be removed to obtain a continuous GMSL time series. Both methods to cope with these drifts rely on tide-gauge comparisons. By comparing sea surface heights of TOPEX, to those of two other altimeters on board of ERS1&2 at crossovers, we aim to estimate a more accurate intramission bias and TOPEX-A&B drifts. The robustness and the geographical effects of the tide-gauge comparison are validated with respect to drift and intramission bias estimations, by applying various averaging strategies. Then, we suggest a calibration procedure for the TOPEX altimeter based on crossovers and validated with tide gauges. Eventually, the effect of the calibration on the GMSL record is quantified.

1.6 Outline

In chapter 2 we aim to close the sea-level budget on sub-basin scales in the North Atlantic Ocean. Research objective 1 is answered by summing the steric sea level and mass time series from Argo and GRACE and comparing it to the sea level observed by Jason. The focus is on the processing of the three datasets, but primarily on the GRACE solution used. Budget closure is investigated based on the secular trend, the annual cycle and the interannual signals. Potential reasons for non-closure in several regions are discussed. Furthermore, the effects of the GIA corrections for GRACE and Jason are addressed.

Research question 2 is addressed in chapter 3. This region requires however several adaptations to the processing procedures and ocean reanalyses, due to the absence of Argo floats. A statistical weighting procedure between the observations is applied to consistently separate steric and mass signals. Effects of earthquakes, ocean signals and mass redistribution are investigated to either correct or to explain the trends and interannual signals observed. We also apply a correction for ocean bottom deformation due to loading, because the mass signals over the continental shelves are large compared to the open ocean.

Chapter 4 focusses on the estimation of vertical land motion trends at tide gauges and therefore deals with research question 3. We try to increase the number of GNSS trends, while at the same time the accuracy is improved. To achieve this, the larger Nevada Geodetic Laboratory (NGL) dataset (*Blewitt et al.*, 2016) instead of the Uni-

versity of La Rochelle (ULR) dataset (*Wöppelmann and Marcos*, 2016) is used for GNSS trends. We compare several approaches to combine nearby GNSS trends into a single VLM trend estimate at the tide gauges. Additionally, the VLM trends obtained from ALT-TG differenced time series are investigated. Correlation thresholds and weights are applied to mitigate the influence of uncorrelated ocean signals between the altimeter and the tide gauge on the VLM trends. Cross validation between the GNSS and ALT-TG trends is applied to determine the best configuration for both techniques.

In chapter 5 the last research question is answered. We correct the tide-gauge time series for the GNSS trends and compare the resulting absolute sea levels to those of the TOPEX, to detect drifts an biases in the altimeter. The results are compared to a crossover analysis between TOPEX and ERS1&2. By different weighting schemes the stability of the VLM corrected tide-gauge results are investigated. Additionally, we investigated whether the tide-gauge network is suitable for detecting an intramission bias between TOPEX-A&B and separate drifts for both periods. A consistent processing and calibration approach for TOPEX is eventually suggested and the consequences for the GMSL acceleration are discussed.

Chapter 6 lists the conclusions and summarizes the answers to the research questions. Several recommendations on how to improve or continue this work are also provided.

Chapter 2

Sub-basin-scale sea level budgets from satellite altimetry, Argo floats and satellite gravimetry: a case study in the North Atlantic Ocean

2.1 Introduction

If the sum of individual components is statistically consistent to the total sea level variations the budget is closed. Total sea level variations and its components are observed by in-situ and satellite measurements, but can also be modelled. Several studies have attempted to close the sea level budget by using satellite altimetry, satellite gravimetry and observations or reanalyses of ocean temperature and salinity on a global scale. Closure of the budgets is required to get a consistent division between the Mass Component (MC) and steric-related sea level changes. This helps us to identify the contributors to present day sea level changes. Contributors that affect the MC are glacier and ice sheet melt and land water storage, while heat fluxes between ocean and atmosphere contribute to steric changes. Note that heat fluxes also drive ocean dynamics, which have an effect on both the regional MC and the steric change in sea level.

One of the first attempts to close the sea level budget compared time series of total sea level from satellite altimetry with the sum of the MC from satellite gravimetry and the steric component from Argo floats (*Willis et al.*, 2008). That study showed that between the middle of the years 2003 and 2007 the sum and the total sea level have comparable seasonal and interannual sea level variability, however, the 4-year trends did not agree. *Cazenave et al.* (2008) found comparable estimates of steric sea level estimated from Argo and from the difference between altimetry and the Gravity Recovery And Climate Experiment (GRACE) observations over 2003-2008. Using the same methods as *Willis et al.* (2008) the global sea level budget was closed within error bars by *Leuliette and Miller* (2009) over the period 2004-2008 and by

Parts of this chapter have been published as: Kleinherenbrink, M., Riva, R., & Sun, Y. (2016). Sub-basin-scale sea level budgets from satellite altimetry, Argo floats and satellite gravimetry: a case study in the North Atlantic Ocean, Ocean Science, doi:10.5194/os-12-1179-2016.

Leuliette and Willis (2011) over the period 2005-2010.5. All of the aforementioned studies used a form of reduced space objective interpolation (*Bretherton et al.*, 1976) to create grids of Argo data. *Li et al.* (2013) attempted to close the global budget using temperature and salinity grids from *Ishii et al.* (2006).

While time series of satellite gravimetry and Argo observations became longer and the processing of satellite gravity data improved, it became possible to look at basin-scale budgets and patterns. Several studies focussed on Ocean Bottom Pressure (OBP), which can be seen as the integrated mass of the ocean and the atmosphere pushing on the ocean floor. *Chambers and Willis* (2010) compared global gravimetry-derived maps of OBP to those obtained with steric-corrected altimetry, whereas *Marcos et al.* (2011) investigated the distribution of steric and OBP contributions to sea level changes and looked at differences in the Atlantic, Indian and Pacific Oceans. *Purkey et al.* (2014) analysed differences between basin-scale OBP from satellite gravimetry and steric-corrected altimetry using Conductivity-Temperature-Depth (CTD) profiles over the period 1992-2013. They showed that both methods captured the large-scale OBP change patterns, but that differences occur when deep-steric contributions below 1000 m are not considered. Over the North Atlantic Ocean the OBP trends from satellite gravimetry and steric-corrected altimetry were found to be statistically equal, but with large error bars for the steric-corrected altimetry trends. *Von Schuckmann et al.* (2014) found global and large-scale regional (a third of the total ocean) consistency in sea level trends of the three systems (e.g., satellite altimetry, satellite gravimetry and Argo) in the Tropics as long as areas like the Tropical Asian Archipelago are not considered, but they did not manage to close the budget between 30-60 N. They argued that the unability of Argo to resolve eddies in the western intensifications caused the difference in trends.

Some other studies focussed on sea level budgets in small basins. *García et al.* (2006); *Calafat et al.* (2010); *Fenoglio-Marc et al.* (2006) compared sea level trends in the Mediterranean from satellite altimetry, satellite gravimetry and the ECCO (Estimating the Circulation and Climate of the Ocean) model (*Menemenlis et al.*, 2005). ECCO is also used by *Feng et al.* (2012) to determine trends in the South China Sea. Time series of sea level budgets have been investigated in the Red Sea using Ishii grids (*Feng et al.*, 2014).

Compared to previous studies, we improve the treatment of each dataset, in particular with respect to an accurate description of the uncertainties. We avoid using precomputed grids for Argo and altimetry, because no covariances between nodal values are provided, and we use full variance-covariance matrices of the GRACE gravity field solutions. Secondly, we address the effect of several processing steps particularly on gravimetry data in terms of trend, annual amplitude and (residual) time series. For altimetry, we briefly discuss the effect of different averaging methods and analyse the effect on the trends of having a latitude dependent intermission bias (*Ablain et al.*, 2015). For GRACE, DDK5-filtered solutions (*Kusche*, 2007; *Kusche et al.*, 2009) are compared with the anisotropic Wiener-filtered (*Klees et al.*, 2008) solutions. Finally, basin and sub-basin scale budgets are created, problematic areas are identified and potential causes for non-closure are discussed.

We apply our method to the North Atlantic basin, because the coverage of Argo is sufficient to computed mean steric sea levels on sub-basin scales during the 2004-2014 period, which allows the construction of budgets over a 10-year time span. Secondly, for both steric sea level and the MC different regimes are present in terms of trend, annual cycle and interannual variability, which allows us to investigate the performance of the method under various conditions. Additionally, we are able to address the effect of the Glacial Isostatic Adjustment (GIA) on the trends, which is a large contributor in the northwest of the North Atlantic basin and therefore also a potentially large source of error.

The dataset used in this study is briefly described in Chapter 2.2. Secondly, the processing of the three datasets is discussed in the methodology section. In Chapter 2.4 the processed datasets are compared to existing products. The resulting basin and sub-basin scale budgets are described in Chapter 2.5. In the final section conclusions are drawn based on the results.

2.2 Data description

This section shortly discusses the data from the three observing systems that are used to determine the sea level budgets.

For the determination of the sum of the steric and the mass components of sea level satellite altimetry data are used. The altimetry data are obtained from the Radar Altimetry Database System (RADS) (*Scharroo et al.*, 2012). RADS contains 1 Hz along-track data, which corresponds to an along-track separation of sea level measurements of approximately 6 km. The files contain ranges, orbits and geophysical corrections for all altimeters that have been flown. In this study, only the data of the Jason-1 and Jason-2 satellites are considered to have homogeneous sampling in space and time over the period 2004-2014. The data of Jason-1 during its geodetic mission phase (2008-2013) are not used for the altimetry time series. Both satellites have a repeat-track of approximately ten days and the same orbital plane, which results in a ground-track separation of approximately 315 km, or 2.8 degrees, at the equator.

The steric component of sea level rise is determined using measurement profiles of temperature and salinity from the Argo float network. Since the first deployments of Argo floats in the year 1999, the number of Argo floats rapidly increased until approximately 3900 floats currently. Argo reached maturity around the year 2007, when at least 3000 floats were in the water (*Leuliette and Willis*, 2011; *Canabes et al.*, 2013), which means that there is on average approximately one float per 3° × 3° box. For the North Atlantic Ocean, steric sea levels can be analysed from 2004, because most areas in the North Atlantic are sampled already by Argo floats as shown in Fig. 2.1. In the North Atlantic Ocean the areas around the Antilles and north of Ireland are poorly sampled. Most floats descend to a depth around 1000-2000 m and measure temperature and salinity while travelling upward. The resurfacing time of an Argo float is approximately 10-12 days. The steric sea level is computed using the Thermodynamic Equation Of Seawater (TEOS-10) software (*IAPSO*, 2010), which

requires the distribution of temperature and salinity over depth as input.

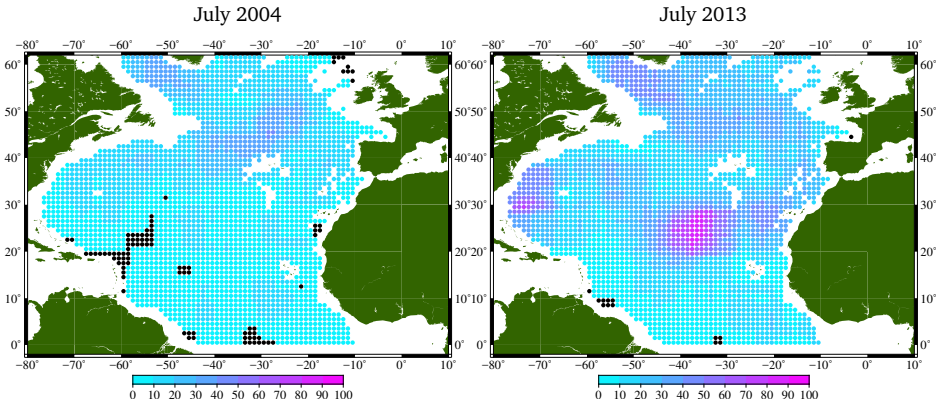

Figure 2.1: Number of Argo floats within a 10° × 10° box for grid cells where the depth is larger than 1000 m. Only floats considered in this study are used for the statistics (Sect. 2.3.2). The black dots indicate no floats in the 10° × 10° box.

The Earth's time-variable gravity field is measured since 2002 by the Gravity Recovery And Climate Experiment (GRACE). This mission measures changes in the Earth's gravity field by low-low satellite-to-satellite tracking. Traditionally the Earth's gravity field is expressed in spherical harmonics. In this study the release 5 monthly spherical harmonic solutions computed at the Center for Space Research (CSR) (*Tapley et al.*, 2004), together with the ITSG-GRACE2016 solutions (*Klinger et al.*, 2016) computed at the Institute for Theoretical geodesy and Satellite Geodesy (ITSG) are used. The CSR solutions are computed up to degree and order 60 and 96, while the ITSG solutions are computed up to degree and order 90. All three products are provided with full variance-covariance or normal matrices, which allows for statistical filtering. In case of a proper error description, we expect that the results of the CSR 60- and 96-degree solutions give comparable results, except in areas with large gradients in gravity. However, since the differences in variance-covariance matrices are small during the periods July 2003-December 2010 and February 2011-July 2013, but the orbit geometry substantially varies within these periods, the provided variance-covariance matrices are not expected to be suitable for statistical filtering. *Klinger et al.* (2016) showed that the gravity field variability over the oceans indeed increases substantially during periods when GRACE enters repeat-orbits. As a consequence, the months July-October 2004 are excluded from the analysis, when GRACE entered a near 4-day repeat-orbit. The addition of the ITSG solutions, enables us to compare an independent solution computed with a different approach to the standard CSR products. The non-dimensional gravity field coefficients are converted to units of Equivalent Water Height (EWH) before filtering, to make them compatible with the other two observing systems. For comparison, we also used the publicly available Directional Decorrelation Kernel (DDK)-filtered solutions of CSR, however no variance-covariance matrices for those solutions are publicly available. From here

Table 2.1: Designations of filtered gravity field solutions.

Processing group	Degree	Filter	Designation
CSR	60	Wiener	CSR60-W
CSR	96	Wiener	CSR96-W
ITSG	90	Wiener	ITSG90-W
CSR	60	DDK5	CSR60-DDK
CSR	96	DDK5	CSR96-DDK

on the designations listed in Table 2.1 are used to refer to the GRACE gravity field solutions. In the processing phase, the Atmosperic and Ocean De-aliasing Level-1B (AOD1B) product is incorporated (*Dobslaw et al.*, 2013), which is based on the Ocean Model for Circulation and Tides (OMCT) and the European Centre for Medium-range Weather Forcecast (ECMWF) model. Monthly averages of the OMCT and the ECMWF are restored after processing to the time-varying gravity field in the form of spherical harmonics (*Chambers and Willis*, 2010). Details on the processing are described in Sect. 2.3.3.

2.3 Methodology

The data described in the previous section are processed such that they are suited for establishing monthly regional sea level budgets. It implies that the equation

$$\bar{h}_{sla,GIA} = \bar{h}_{ssla} + \bar{h}_{mca,GIA} \tag{2.1}$$

is satisfied within uncertainties, where $\bar{h}_{sla,GIA}$ is the Glacial Isostatic Adjustment (GIA)-corrected Mean Sea Level (MSL) anomaly derived from the Jason satellites, $\bar{h}_{ssla}$ the mean steric sea level anomaly derived from Argo and $\bar{h}_{mca,GIA}$ the mean GIA-corrected MC anomaly in terms of EWH derived from GRACE. Note that MSL is inverse barometer corrected and we consistently apply this to the Mass Component (MC) anomalies from GRACE. This section describes therefore the processing strategies for the three observation types from individual measurements to an average over a specified region in the ocean including the propagation of the formal errors.

As far as altimetry is concerned, after computing individual along-track sea level anomalies, two important processing steps are described in this section: a suitable averaging method to come to a time series of MSL for a given area and a way to deal with geographical dependencies of the intermission bias between the two Jason missions (*Ablain et al.*, 2015).

To compute steric sea levels from Argo temperature and salinity measurements the TEOS-10 software is used (*Pawlowicz et al.*, 2012). Since the Argo measurements are heterogeneously distributed over the ocean, the steric sea levels are first interpolated using an objective mapping procedure to a grid of $1° \times 1°$, before being averaged.

Monthly GRACE solutions of CSR and ITSG are provided with full variance-covariance matrices, which allows the use of an anisotropic Wiener filter (*Klees et*

al., 2008). Compared to other existing filters, it strongly reduces the stripes that are still present in the DDK-filtered solutions (cf. Sect. 2.4, while not reducing the spatial resolution as much as a Gaussian filter of suitable width would do. A fan filter (*Zhang et al.*, 2009) is applied after the optimal filter to reduce ringing artefacts that occur close to Greenland due to the limited number of spherical harmonic coefficients (degree and order 60-96).

2.3.1 Jason sea level

Individual sea level anomalies h_{sla} measured from the Jason-1 and Jason-2 satellites are computed with respect to the mean sea surface (*mss*) DTU13 as:

$$h_{sla} = a - R - \Delta R_{corr} - mss, \tag{2.2}$$

where a is the ellipsoidal height of the satellite, R the Ku-band range and ΔR_{corr} the applied geophysical corrections. The satellite altitude is taken from the GDR-D orbits and the latest versions of the geophysical corrections are applied, as listed in Table 2.2. The 35-second smoothed dual-frequency delay is used to reduce the relatively large noise in the individual ionospheric corrections. For the wet tropospheric correction, we use the latest delay estimate from the radiometer, while the dry tropospheric delay is computed from the European Centre for Medium-range Weather Forecasts (ECMWF) pressure fields. Tidal corrections from the GOT4.10 model are applied, which are based on Jason data instead of TOPEX data as in the GOT4.8 model (*Ray*, 2013). The Cartwright-Taylor-Edden solid earth tide model is applied (*Cartwright and Taylor*, 1971; *Cartwright and Edden*, 1973) and an equilibrium model for the pole tide (*Wahr*, 1985). For the sea state bias correction the non-parametric model of *Tran et al.* (2012) is used. To correct for high frequency (periods < 20 days) wind and pressure effects on the sea surface a dynamic atmospheric correction is applied based on the MOG2D model (*Carrère and Lyard*, 2003). The dynamic atmospheric correction in RADS also includes an inverse barometer correction as described on the AVISO website, which corrects for the low-frequency (> 20 days) sea level anomalies caused by regional sea level pressure variations with respect to the time-varying global mean over the oceans. Sea level anomalies larger than 1 m are likely in error and are therefore removed from further processing, as in the National Oceanic and Atmospheric Administration (NOAA) GMSL time series (*Masters et al.*, 2012).

In GMSL time series an intermission bias correction is applied, which is determined from the average GMSL difference between Jason-1 and Jason-2 during their tandem phase, in which the satellites orbit the same plane only a minute apart (*Nerem et al.*, 2010). However, the differences reveal a geographical dependence as shown in Fig. 2.2. Regional sea level budgets established in this study are more prone to these geographical differences than when estimating global sea level budgets. This problem is partly corrected for by estimating a polynomial through the intermission differences, which only depends on latitude (*Ablain et al.*, 2015) and is given by:

$$\Delta h_{sla,ib}(\lambda) = c_0 + c_1 \cdot \lambda + c_2 \cdot \lambda^2 + c_3 \cdot \lambda^3 + c_4 \cdot \lambda^4, \tag{2.3}$$

Table 2.2: List of geophysical corrections applied in this study and for the MSLs of NOAA.

	This study	NOAA
Ionosphere	Smoothed dual-frequency	Smoothed dual-frequency
Wet troposphere	Radiometer	Radiometer
Dry troposphere	ECMWF	ECMWF
Ocean tide	GOT4.10	GOT4.8
Loading tide	GOT4.10	GOT4.8
Pole tide	Wahr	Wahr
Solid Earth tide	Cartwright-Taylor-Edden	Cartwright-Taylor-Edden
Sea state bias	Tran2012	CLS11
Dynamic atmosphere	MOG2D	MOG2D

where λ is the latitude and $\Delta h_{sla,ib}(\lambda)$ is the intermission correction. The sea level anomaly $h_{sla,c}$ corrected for intermission differences is then computed as:

$$h_{sla,c} = h_{sla} - \Delta h_{sla,ib}. \tag{2.4}$$

This correction is only applied to Jason-2 sea level anomalies i.e., Jason-1 is the reference. The parameters c_n, with $n = 0, 1.., 4$, depend on the applied geophysical corrections. For the corrections given in Table 2.2 the values for the parameters are given in Table 2.3. In the middle of the North Atlantic Ocean (approximately 40° N), the intermission difference is several millimeters less than when only including the constant c_0 parameter (which is slightly different if the other parameters are not estimated). This results in an approximate trend difference of several tenths of a millimeter over a period of 10 years.

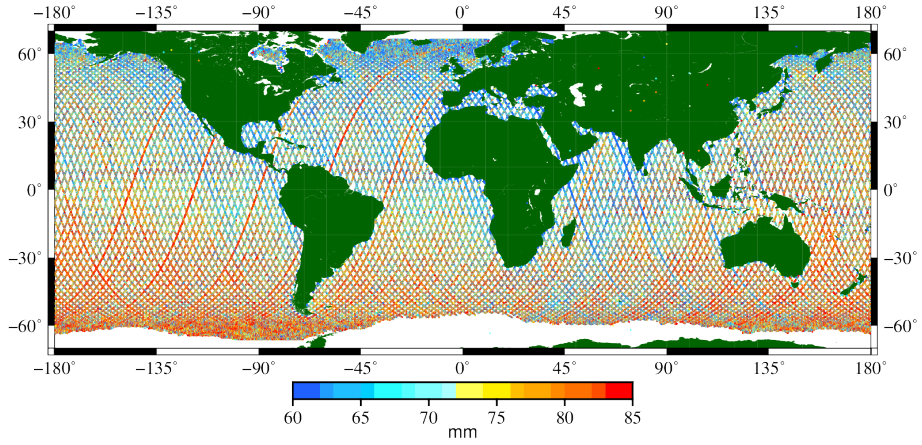

Figure 2.2: Geographical differences between Jason-1 and Jason-2 sea level estimates averaged over the tandem period.

Due to the limited sampling of the Argo network and the relatively large errors in the gravity field solutions it is necessary to integrate sea level anomalies over extended areas. Previous GMSL studies have used two different techniques (*Masters et al.*, 2012): gridding or latitude-dependent weighting based on the inclination of

Table 2.3: Values for the parameters of the intermission difference correction.

Parameter	Value	Unit
c_0	71.9	mm
c_1	-74.7·10^{-3}	mm deg^{-1}
c_2	51.1·10^{-5}	mm deg^{-2}
c_3	-43.3·10^{-7}	mm deg^{-3}
c_4	-15.1·10^{-8}	mm deg^{-4}

the orbit (*Wang and Rapp*, 1994; *Nerem*, 1995), which was simplified for a spherical Earth approximation by *Tai and Wagner* (2011). From here on the latter is referred to as the 'Wang and Rapp method'. The gridding method is problematic when using the Jason satellites, because of their large track spacing at the equator, causing the number of invidual observations per grid cell to decrease at low latitudes (*Henry et al.*, 2014). A solution to this problem is to increase the grid cell size, but this has a disadvantage if sea level budgets are constructed over an irregular and/or a small polygon. The Wang and Rapp method has the disadvantage that it underweights measurements at high latitudes ($> 50°$) (*Scharroo*, 2006), because it assumes the number of measurements to go to infinity at latitudes equal to the inclination of the satellites.

Therefore it is suggested to average the sea level anomalies based on the number of available measurements within a latitudinal band. The method connects the weights assigned to the measurements to the number of measurements N_l in a latitude band l of one degree and the area of the sea surface A_l as:

$$\omega_i(l) = \frac{A_l}{N_l}. \tag{2.5}$$

These weights are normalized:

$$w_i = \frac{\omega_i}{\sum_{i=1}^{I} \omega_i}, \tag{2.6}$$

where I is the total number of observations. A MSL anomaly $\bar{h}_{sla}$ for an area is computed as:

$$\bar{h}_{sla} = \hat{w}^T \hat{h}_{sla,c}, \tag{2.7}$$

where $\hat{w}$ is the vector of normalized weights and $\hat{h}_{sla,c}$ is the vector of sea level anomalies corrected for intermission differences.

For the error estimation, variance-covariance matrices are computed as described in *Le Traon et al.* (1998). This method separates the long-wavelength errors from representativity errors. The representativity errors captures sea level variability caused by the undersampling of high-frequency ocean dynamics. White measurement noise is not considered here, because it becomes very small when averaged over large areas. Among the long-wavelength errors, we consider the orbit, ocean tide and inverse barometer errors. These errors are assumed to be fully correlated between measurements within the track and uncorrelated between inter-track measurements. It is

noted that those correlations do not hold over large basins (> 2000 km in the East-West direction) (*Le Traon et al.*, 1998) and therefore the error is overestimated. The decorrelation time is taken from *Le Traon et al.* (2001) and the zero crossing of the correlation distance function d_{corr} is given by (*Le Traon et al.*, 2001):

$$d_{corr} = 50 + 250\frac{900}{\lambda_{avg}^2 + 900}, \tag{2.8}$$

where λ_{avg} is the average latitude of two measurements in degrees. Ultimately, this results in equations for the covariance of respectively measurements in different tracks and on the same track:

$$\begin{aligned} \langle \epsilon_i, \epsilon_j \rangle &= \rho_{ij}\sigma_{ov}^2 \\ \langle \epsilon_i, \epsilon_j \rangle &= \rho_{ij}\sigma_{ov}^2 + \sigma_{lw}^2 \ , \end{aligned} \tag{2.9}$$

where ρ_{ij} is correlation computed with the decorrelation time and distance provided above, σ_{ov}^2 is the ocean variability variance, which is linked to eddy amplitudes, and σ_{lw}^2 is the long-wavelength variance. The values for σ_{ov} and σ_{lw} are assumed 100 mm and 15 mm, where the first number comes from typical mesoscale variability (*Chelton et al.*, 2007). By putting these equations in the variance-covariance matrix C_{sla}, the standard error $\bar{\sigma}_{sla}$ for the mean sea level anomaly is computed using:

$$\bar{\sigma}_{sla} = \sqrt{\hat{w}^T C_{sla} \hat{w}}. \tag{2.10}$$

Both the satellite altimetry mean sea level anomalies as well as the MC from GRACE are affected by Glacial Isostatic Adjustment (GIA). For the corrections to GRACE and altimetry we use the solution of *Peltier et al.* (2015) based on an Earth model with VM5a viscosity profile and ICE-6G deglaciation history. The altimetric measurements are corrected by subtracting the GIA geoid trend averaged over the region of interest. Errors in the GIA trends are typically assumed to be in the order of 30% of the signal (*Von Schuckmann et al.*, 2014), which is due to the lack of any realistic GIA error estimates.

Because the CSR gravity fields are created on a monthly basis and the altimetry measurements are averaged over a cycle of approximately ten days, the altimetry measurements are low-pass filtered. A low-pass filter f_{lp} is computed by taking an Inverse Discrete Time Fourier Transform, which results in:

$$f_{lp} = \frac{\sin(2\pi f_c(t - t_m))}{\pi(t - t_m)}, \tag{2.11}$$

with f_c the cut-off frequency, which is taken as 12 cyc/year, t is the time in years of the altimetry time series and t_m the time at the middle of a month. This filter is infinitely long, so therefore we cut it at two months. To obtain a better frequency response the filter is windowed using a Hamming window w_H:

$$w_H = 0.54 - 0.46\cos(\frac{2\pi(t - t_m - L/2)}{L}), \tag{2.12}$$

where L is the length of the window in years. We take a window length of two months. The applied filter h_{lp} is then written in the time domain as:

$$h_{lp} = f_{lp} \circ w_H, \tag{2.13}$$

where $\circ$ is the element-by-element multiplication. The mean of the GIA-corrected, low-pass filtered time series is subtracted, which provides the MSL anomaly $\bar{h}_{sla,GIA}$ of Eq. (2.1).

2.3.2 Argo steric sea level

Using the Argo profile instead of a precomputed temperature/salinity (T/S) grid has the primary advantage that error covariances can be computed between steric sea level grid cells.

First, steric sea levels are computed from the individual Argo T/S-profiles using the TEOS-10 package. This package requires the conversion of the PSS-78 practical salinity values measured by Argo to the absolute salinity S_A (*Grosso et al.*, 2010) as well as the ITS-90 temperatures to conservative temperature Θ as defined in the TEOS-10 user manual (*IAPSO*, 2010). The TEOS-10 program numerically integrates the equation for the geostrophic steric sea level (*IAPSO*, 2010):

$$h_{ssl} = -\frac{1}{g_0} \int_{P_0}^{P} \hat{\delta}(S_A(P'), \Theta(P'), P') dP', \tag{2.14}$$

where $\hat{\delta}$ is the specific volume, P_0 is the surface pressure, P is the reference pressure, which is set to 1000 dbar (approximately 1000 m depth) and g_0 is a constant gravitational acceleration of 9.7963 m s^{-2}, which is the average gravitational acceleration over the ocean surface (*Griffies et al.*, 2004).

In the analysis only profiles that reach at least 1000 m depth are included and at least have a measurement above 30 m depth, which is the typical depth of the mixed layer over the open ocean, but it can be substantially deeper in regions like the subpolar gyre. A 'virtual measurement' is created at 1 m depth, assuming the same salinity and potential temperature values as the highest real measurement, so that the top steric signal is not missed. Only measurements that have error flag '1' (good) or '2' (probably good) are used and the measurements are cleaned by moving a 5° × 5° block to remove steric sea level estimates more than 3σ from the mean.

To be able to average measurements monthly over a basin or a polygon, a grid is constructed by statistical interpolation of the steric sea levels at the profile locations based on the method described in *Bretherton et al.* (1976) and *Gaillard et al.* (2009). First, a background field is constructed by estimating a model through the 1000 closest measurements of a profile or grid cell location. This model contains a constant, a second-order 2-D longitude-latitude polynomial and six intra-annual to annual cycles (*Roemmich and Gilson*, 2009). The background sea surface height is taken as the model evaluated at the grid cell (or profile) location.

Then, the background field vector $\hat{h}_{ssl,b}$ is subtracted from the sea level estimates, which results in:

$$\delta\hat{h}_{ssl} = \hat{h}_{ssl} - \hat{h}_{ssl,b}, \tag{2.15}$$

where $\delta\hat{h}_{ssl}$ are the residuals. The ocean variance σ_t^2 is assumed to be 100 cm^2 (typical mesoscale variability (*Chelton et al.*, 2007)), which is close to the average squared RMS-of-fit of the differences of the measurements and the model. These variances are subdivided into three components to represent different correlation scales as follows (*Roemmich and Gilson*, 2009):

$$\begin{aligned} \sigma_1^2 &= 0.77\sigma_t^2 \\ \sigma_2^2 &= 0.23\sigma_t^2 \\ \sigma_3^2 &= 0.15\sigma_t^2 \,, \end{aligned} \tag{2.16}$$

which are then used to construct covariance matrices $C(d)$ based on those used for the Scripps fields (*Roemmich and Gilson*, 2009), such that:

$$C(d) = \sigma_1^2 e^{-\left(\frac{d}{140}\right)^2} + \sigma_2^2 e^{-\frac{d}{1111}}, \tag{2.17}$$

and the measurement and representativity error matrix R:

$$R = diag(\sigma_3^2), \tag{2.18}$$

where d is a measure for the distance in kilometers between the profiles p and the grid points g, such that:

$$d = \sqrt{a^2 d_x^2 + d_y^2}. \tag{2.19}$$

The parameter a is 1 above 20 degrees latitude and below that it decays linearly to 0.25 at the Equator, in order to represent the zonal elongation of the correlation scale here (*Roemmich and Gilson*, 2009).

Using the covariances C_{pg} (between profiles and grid points) and C_p (between profiles), the weight matrix K is computed as:

$$K = C_{pg}(C_p + R)^{-1}. \tag{2.20}$$

The weight matrix is then used to compute a vector of steric sea levels $\hat{h}_{ssl,g}$ for every grid point within the area:

$$\hat{h}_{ssl,g} = K\delta\hat{h}_{ssl} + \hat{h}_{ssl,b}, \tag{2.21}$$

for which also the variance-covariance matrix $C_{ssl,g}$ is computed, as:

$$C_{ssl,g} = C_g - KC_{pg}^T, \tag{2.22}$$

where C_g are the covariances of the background grid.

To average the steric sea level anomalies, the values are weighted by the cosine

of the latitude, which results in:

$$\omega_i = \cos(\lambda_i). \tag{2.23}$$

Like for altimetry, the weights are normalized:

$$w_i = \frac{\omega_i}{\sum_{i=0}^{I} \omega_i}. \tag{2.24}$$

Finally, these are used to compute the mean steric sea level $\bar{h}_{ssl}$ and its associated error $\bar{\sigma}_{ssl}$, with

$$\bar{h}_{ssl} = \hat{w}^T \hat{h}_{ssl,g}, \tag{2.25}$$

and

$$\bar{\sigma}_{ssl} = \sqrt{\hat{w}^T C_{ssl,g} \hat{w}}. \tag{2.26}$$

Subtraction of the mean from the mean steric sea level time series yields the steric sea level anomalies $\bar{h}_{ssla}$ used in Eq. (2.1).

2.3.3 GRACE mass

We use the full variance-covariance matrices to filter the spherical harmonic coefficients with an Anisotropic Non-Symmetric (ANS) filter (*Klees et al.*, 2008). This Wiener filter exploits the ratio between the variance of the error and of the signal to filter the coefficients. With the variance-covariance matrices C_x and D_x, for the errors and the signals respectively, the spherical harmonic coefficients $\hat{x}$ are filtered as:

$$\hat{x}_{of} = (C_x^{-1} + D_x^{-1})^{-1} C_x^{-1} \hat{x}. \tag{2.27}$$

For the filtered coefficients $\hat{x}_{of}$ a corresponding variance-covariance matrix $C_{x,of}$ is computed. This is a joint inversion of a static background field, which is set to zero, and the time-varying coefficients, resulting in:

$$C_{x,of} = (C_x^{-1} + D_x^{-1})^{-1}. \tag{2.28}$$

The derivation is elaborated in Appendix A.

The filtered grids contain ringing effects around strong signals over Greenland and the Amazon region, which can have substantial effects on the estimated trends in the ocean (cf. Sect. 2.4). If averaged over large areas this will have hardly any effect, but on regional scales the ringing should be reduced. To obtain smoother fields, we use a fan filter (*Zhang et al.*, 2009; *Siemes et al.*, 2013), which is given as:

$$\hat{x}_{ff} = sinc(\frac{l}{l_{max}}) \circ sinc(\frac{m}{l_{max}}) \circ \hat{x}_{of}, \tag{2.29}$$

which is a function of the degree l, the order m and the maximum degree l_{max}. For a maximum degree of 60 and 96, this is comparable to a Gaussian filter of 280 km and

110 km, respectively (*Siemes et al.*, 2013). Suppose $F_f = diag(sinc(\frac{l}{l_{max}})sinc(\frac{m}{l_{max}}))$, then the resulting covariance matrix $C_{x,ff}$ is written as:

$$C_{x,ff} = F_f C_{x,of} F_f. \tag{2.30}$$

Note that there is a fundamental difference between filtering the CSR and ITSG solutions. The CSR solutions are computed with respect to a static gravity field, while the ITSG solutions are computed with the respect to a time-varying field comprising of a static part, a secular trend and an annual cycle. As a consequence, the CSR spherical harmonic coefficients and signal variance-covariance matrices include the annual and the secular trend at the moment the Wiener and fan filters are applied. The ITSG gravity fields are Wiener-filtered first, then the annual cycle and the secular trend are added back and after that the fan filter is applied.

Since the degree-1 coefficients are not measured by GRACE, we add those of *Swenson et al.* (2008) to the CSR solutions. Based on the same approach degree-1 coefficients are computed for the ITSG solutions. Furthermore, we replace the C_{20} coefficient with satellite laser ranging estimates (*Cheng et al.*, 2013).

The intersatellite accelerations of GRACE are dealiased for high frequency ocean and atmosphere dynamics with the Atmospheric and Ocean De-aliasing Level-1B (AOD1B) product. Monthly averages of the AOD1B are provided as the GAD product for both CSR and ITSG, where the mass changes over land are set to zero. To be able to combine the GRACE MC with inverse barometer corrected altimetry, the GAD products containing the modelled oceanic and atmosphere mass are added back in the form of spherical harmonics. Because the ocean model in the AOD1B product is made mass conserving by adding/removing a thin uniform layer of water to or from the ocean, the degree zero is removed before subtraction from the GAD product to compensate for the mean atmospheric mass change over the ocean, which is not measured by inverse barometer corrected altimetry (*Chambers and Willis*, 2010).

To compute the MC on a grid, the 4π-normalized associated Legendre functions Y^T are evaluated at the latitude-longitude locations of the grid. The vector of MCs $\hat{h}_{mc}$ is then computed as:

$$\hat{h}_{mc} = Y^T \hat{x}_{ff}. \tag{2.31}$$

It is possible to compute the grid's variance-covariance matrix C_{mc} as (*Swenson and Wahr*, 2002):

$$C_{mc} = Y^T C_{x,ff} Y. \tag{2.32}$$

The averaging over an area is equal to that of the Argo grids. Suppose that $\hat{w}$ are the normalized latitude weights for the gridded MC. Then,

$$\bar{h}_{mc} = \hat{w}^T \hat{h}_{mc} \tag{2.33}$$

is the mean MC and

$$\bar{\sigma}_{mc} = \sqrt{\hat{w}^T C_{mc} \hat{w}} \tag{2.34}$$

is its error.

To correct the GRACE MC for the GIA trend, we first convert the GIA spherical harmonic coefficients into EWH. Note that GRACE only measures degrees 2 and higher and therefore the coefficients of degree 0 and 1 are not taken into account. Eventually, the GIA spherical harmonic coefficients are converted to spatial grids, which are then averaged over the considered area, and consecutively the mean GRACE MC is corrected for the mean GIA trend.

The mean MC anomaly $\bar{h}_{mca,GIA}$ used in Eq. (2.1) is obtained by applying the GIA correction to the mean MC $\bar{h}_{mc}$ and subtracting the mean of the time series.

2.4 Comparison with existing products

In this section a comparison is made between existing products and the sea levels from altimetry, gravimetry and Argo floats. First, we compare the MSL time series over the North Atlantic Ocean with the existing time series provided by the NOAA Laboratory for Satellite Altimetry (*Leuliette and Scharroo*, 2010) and we show the effect of a latitude dependent intermission bias. Second, amplitude and trend grids of steric sea level are compared to those computed from Scripps salinity and temperature grids (*Roemmich and Gilson*, 2009) and the Glorys reanalyses grids (*Ferry et al.*, 2010). Third, the optimally and fan filtered gravimetry grids are compared to the DDK5-filtered gravity fields (*Kusche*, 2007; *Kusche et al.*, 2009).

2.4.1 Total sea level

Fig. 2.3 shows a comparison of the NOAA time series with the ones computed in this study, for the North Atlantic Ocean north of 30° N. The NOAA time series were computed by averaging over 3° × 1° grid cells and then weighting them according to their latitude. Three of the time series in Fig. 2.3 are computed using the same geophysical corrections as given in the second column of Table 2.2, while for the light blue line the geophysical corrections in the first column are applied.

As visible from the figure, hardly any differences are observed between all four time series. The RMS differences between all time series computed in this study and NOAA are on the order of 3-4 mm, which is slightly larger than differences found between the GMSL time series (*Masters et al.*, 2012). The fact that the time series in this study (blue) and the one computed with the Wang and Rapp method resemble each other indicates that the underweighting of high-latitude measurements in the Wang and Rapp method hardly has any effect. This also holds for averaging over smaller areas in the North Atlantic Ocean, where the only noticeable difference occurs when a substantial number of satellite tracks are missing, due to some maintainance or orbit manoeuvres.

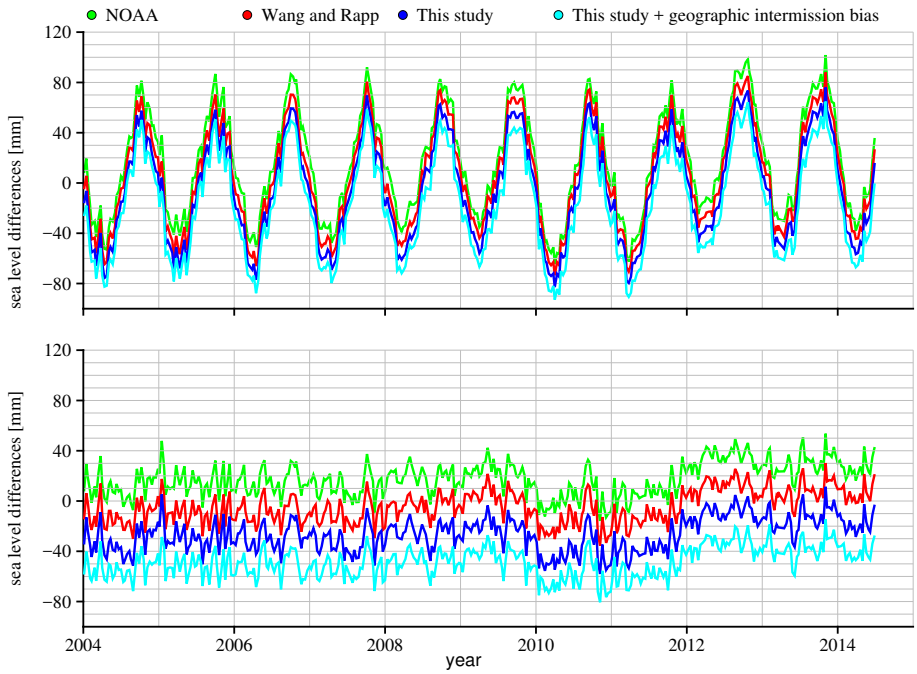

Figure 2.3: Top: Comparison between North Atlantic mean sea level time series of NOAA (green), the Wang and Rapp method (red), our method (blue) and our method using a geographically dependent intermission bias correction and the latest geophysical corrections (light blue). Bottom: Same as the top plot, but with the seasonal signals removed.

The application of a latitude-dependent intermission bias has a substantial effect on the trend. From the NOAA time series a trend of 1.5 mm yr^{-1} is found, while the time series from the Wang and Rapp method and our method provide a trend of 1.8 mm yr^{-1}. The difference is explained by the use of a different averaging technique in the presence of a geographically varying sea level trend. However, if the difference in MSL is computed between Jason-1 and Jason-2 over the North Atlantic Ocean during the tandem phase and the result is used as the intermission bias correction, trends of respectively 1.3 and 1.4 mm/year for the theoretical and the empirical weighting method are found. This is comparable to the trend computed by applying the geographical dependence of the intermission bias (the light blue line of Fig. 2.3), which is 1.4 mm yr^{-1}. To further illustrate this, Fig. 2.4 shows the differences in trend if a constant intermission bias is used or a latitude dependent one. The mean difference of 0.4 mm yr^{-1} is already significant, but locally the differences may attain values of up to 0.8 mm yr^{-1}.

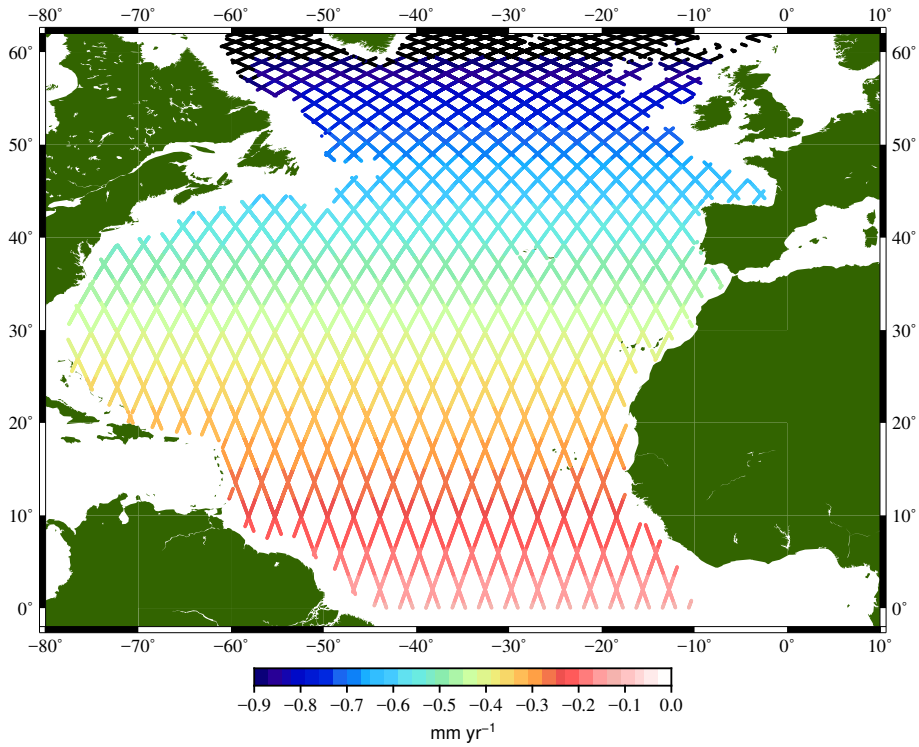

Figure 2.4: Differences in sea level trends computed with and without a latitude-dependent intermission bias.

2.4.2 Steric sea level

Fig. 2.5 shows grids for the amplitudes and trends of the steric signal are shown. The Scripps grids (*Roemmich and Gilson*, 2009) and our solution are solely based on Argo data, while the Mercator reanalyses product Glorys 2V3 assimilates various types of data including altimetry (*Ferry et al.*, 2010), sea surface temperature and Argo. Note that besides the different input data, the Glorys relies on a volume conserving ocean model, while the other two methods are based on data only. Since we use the same correlation structures as Scripps, the resulting grids should resemble each other quite closely. However, to be able to create a variance-covariance matrix between grid cells, it was required to do a 2D-interpolation of the steric sea levels instead of a 3D-interpolation of temperature and salinity profiles. The 2D-interpolation requires different criteria for removing profiles, as described in Sect. 2.3.2, then for the 3D-interpolation. As a consequence of the 2D-interpolation and the differences in the removal criteria the results differ.

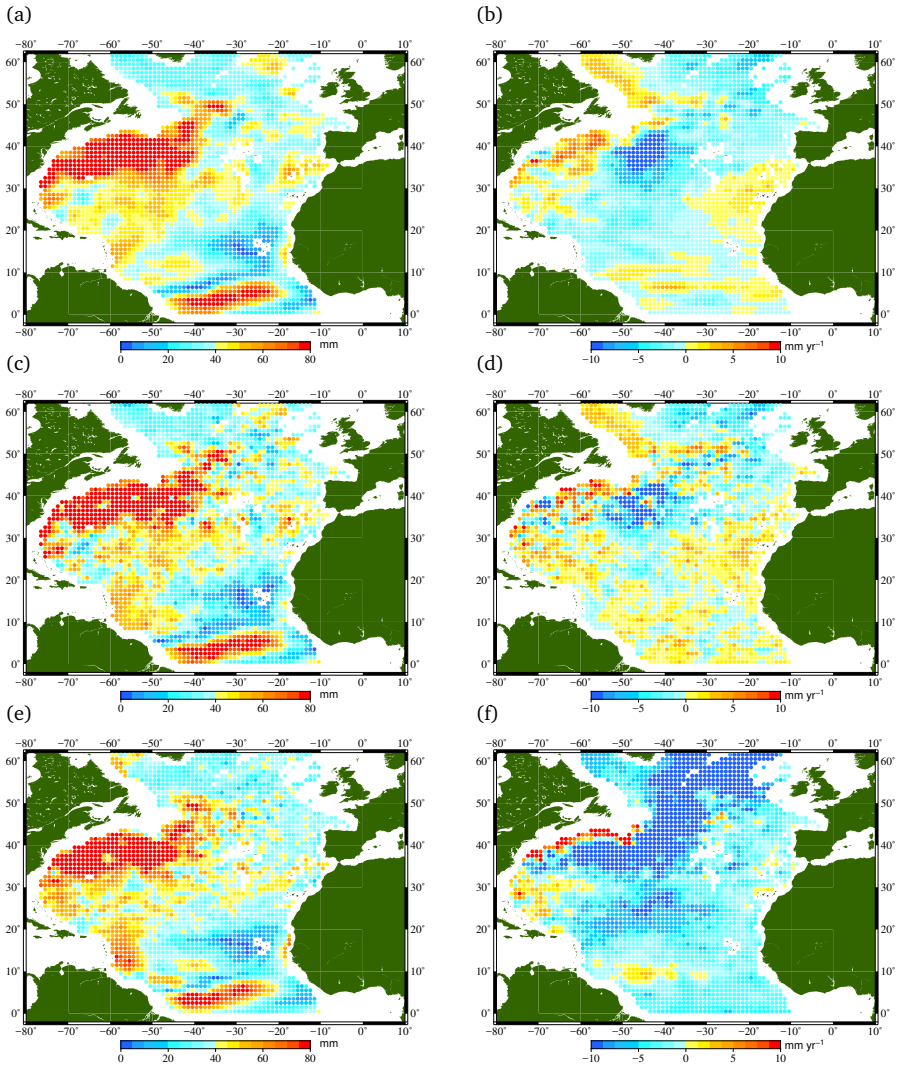

Figure 2.5: Amplitudes of the annual signal (left) and trends (right) computed with the Scripps grids (a,b), the method in this study (c,d) and from the Glorys reanalysis product (e,f).

In terms of the amplitudes of the annual signal, all three methods provide similar results in terms of the large scale features. Typically, amplitudes of 80 mm or more are found in the Gulf Stream region and close to the Amazon basin, while the areas around Greenland and West of Africa have relatively small amplitudes in order of 10-30 mm. The Glorys grid differs from the others primarily in the Labrador sea and Northwest of Ireland. Secondly, the grid computed in this study and the Glorys grid exhibit more short-wavelength spatial variability than the Scripps grid. As long as the regions over which budgets are made are large enough, the methods will not

differ substantially in terms of annual amplitude.

The plots in the right column of Fig. 2.5 reveal a significant difference in trend between the methods and the reanalysis. It is not completely clear what the cause for this difference is, but they are possibly related to interactions between the deep ocean and the continental shelf in the model. Since the Scripps grid and our grid resemble in terms of large scale features and are purely based on T/S-data, we trust the interpolation of Argo. The difference between those two methods are again primarily the noise in the grids and the area around the Antilles, where Argo samples poorly as discussed in Sect. 2.2.

2.4.3 Mass component

Fig. 2.6 shows a comparison of the trends and amplitudes of the CSR96-DDK solution are compared with those obtained from CSR60-, CSR96- and ITSG90-W. Note that the Wiener-filtered solutions are also fan-filtered, as discussed in Sect. 2.3.3, but will be referred to as Wiener-filtered from here on. Both in the annual amplitude and the trend grids some residual striping effects are present for the CSR96-DDK solutions, yielding non-physical trend patterns in the MC. The Wiener filter strongly reduces the striping and as a result especially the trend grids are smoother. However, the ITSG grids also exhibit striping (as it appears at shorter wavelengths), which is the results of adding back the trend and annual cycle from the static field, as discussed in Sect. 2.3.3. A second observation is that the CSR96-DDK and ITSG90-W amplitudes are about 3 mm larger, which indicates that a part of the annual signal is lost in the CSR60- and CSR96-W solutions. Thirdly, *Tamisiea et al.* (2010) estimated a slight increase in MC amplitudes using fingerprint methods based on forward models of water mass redistribution around the Sahel and Amazon of 10-15 mm. In the Wiener-filtered CSR grids, also larger amplitudes are visible in these regions, however their amplitude of 30-60 mm is far too large and are probably the result of hydrological leakage. This leakage is slightly reduced in CSR96-W compared to those of the CSR60-W.

To determine how this affects sub-basin scale MC time series, it is first required to determine the minimum area over which the measurements have to be integrated. GRACE gravity fields have a resolution of typically 250-300 km half-wavelength (*Siemes et al.*, 2013). For small ocean signals after applying filtering procedures, we expect the resolution to be closer to 400-500 km. Argo has approximately one to two floats per 3° × 3° box, so its resolution is in the same range as that of GRACE. Jason-1&2 have an inter-track spacing of 315 km at the Equator, which decreases substantially towards 60° N. Considering all systems, this theoretically makes it possible to create budgets over grid cells of approximately 500x500 km. However, due to the limited length of the time series, the error bars on the trends become much larger than the signals. The size of the polygons is therefore chosen based on the criterion that trend error standard deviation does not exceed 1 mm yr^{-1}.

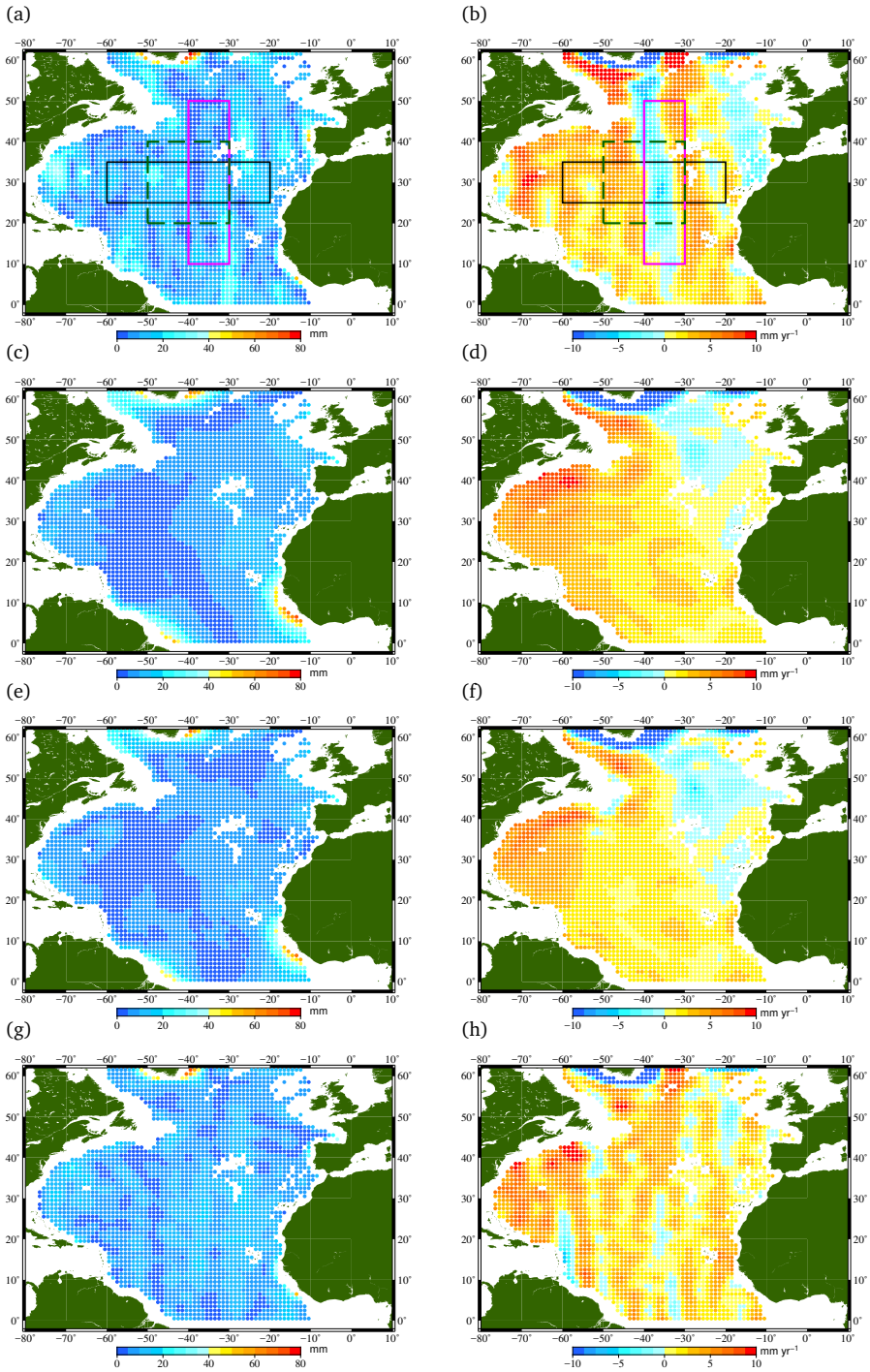

To illustrate the effects of different filters and residual striping on sub-basin scale budgets, Fig. 2.7 shows time series of mass averaged over the polygons shown in Fig. 2.6. All three polygons have approximately the same size, but have different orien-

Figure 2.6: (Caption previous page.) Amplitudes of the annual signal (left) and trends (right) of the mass signal. The first to the third row show the CSR96-DDK solutions (a,b), the CSR60- (c,d) and CSR-96-W (e,f) solutions respectively. The fourth row shows the ITSG90-W (g,h) solution. In the top graphs three polygons are plotted: a meridionally oriented rectangle (purple line), a zonally oriented rectangle (black line) and a square (green dashed line) from which mean MC time series are computed below.

tations. The location is chosen in the middle of the Atlantic to avoid effects of hydrological leakage. Except for the months surrounding the near 4-day repeat-period in 2004, where the variance-covariance matrices of CSR probably do not properly described the noise of the gravity fields, the three of the CSR solutions exhibit less noise than in the other two polygons. In the zonal polygon the noise in CSR96-W is substantially larger than for the other solutions. Futhermore, it becomes clear that the CSR96-DDK solutions do not contain substantial signal above degree 60, because the red and yellow lines are on top of each other, while CSR60- and CSR96-W are substantially different.

The month-to-month noise of CSR60- and CSR96-W time series is comparable for all three polygons. The CSR60- and CSR96-DDK time series become much noisier for the meridionally oriented polygon, where month-to-month jumps of 10-20 mm occur. In addition, the DDK time series exhibit a substantially different trend in the meridional polygon than the other time series. While the mass anomaly in the DDK time series is comparable ot the other time series before 2011, it is significantly lower after 2011. This is probably the result of the orientation of the polygon, which is aligned with the residual stripes (Fig. 2.6). The trend and noise of the DDK time series strongly depend on the orientation of the polygon. Even though the ITSG90-W trend and amplitude grids suffer from striping, they do not become significantly noisier for the meridionally oriented polygon.

2.5 Results and discussion

The first objective of this section is to reveal patterns of sea-level amplitudes and trends in the North Atlantic Ocean and how these resemble for the two different methods: altimetry and Argo+GRACE. Secondly, this section discusses the closure of sea-level budgets over polygons of approximately one-tenth of the North Atlantic Ocean in terms of trend, annual amplitude and residual variability. It is shown for which regions the budget is closed and possible causes for non-closure are discussed. Thirdly, we focus on the best choice of GRACE filter solutions for the MC.

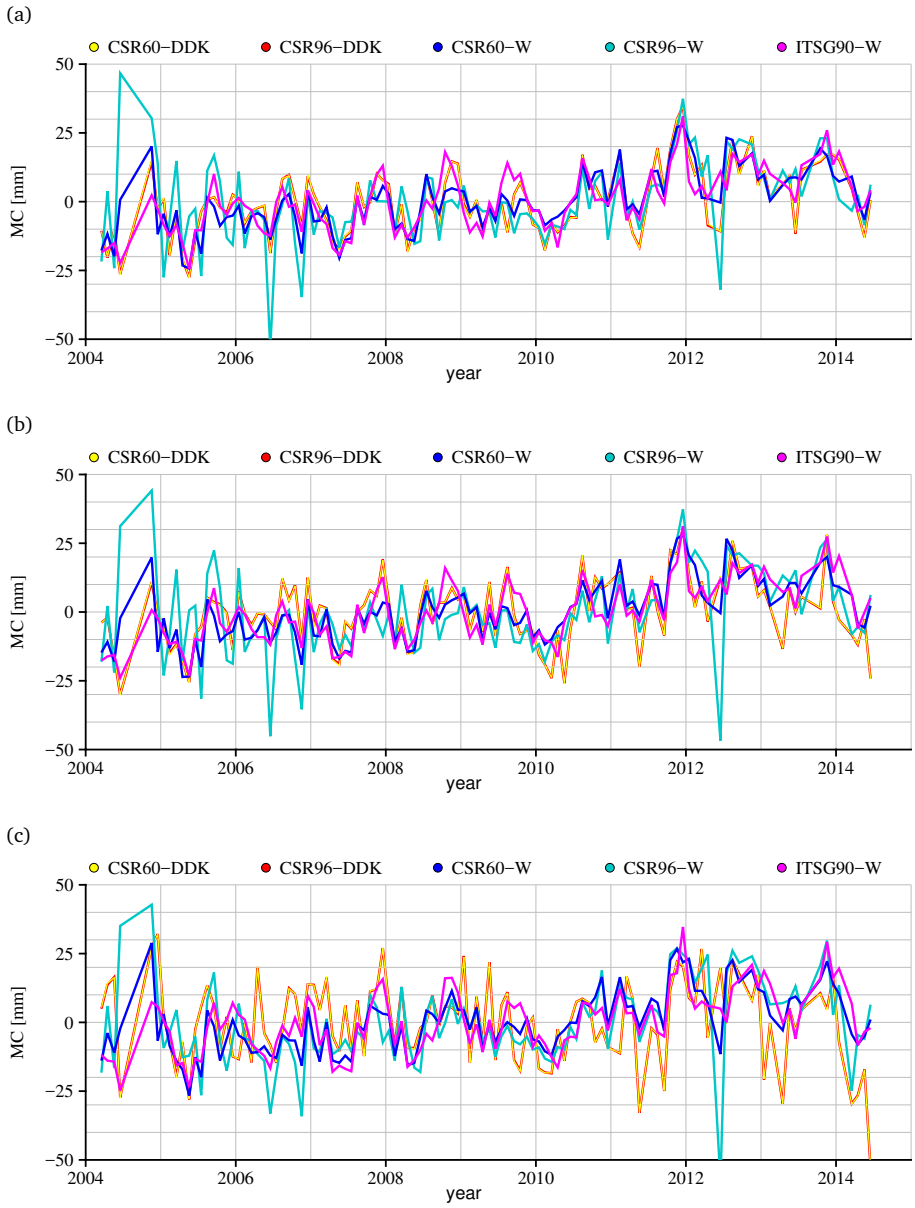

Figure 2.7: Sub-basin scale time series of the MC using various filters for three polygons with different orientation: zonal (a), square (b) and meridional (c). Red and yellow represent the CSR60- and the CSR96-DDK solutions. The blue and light-blue time series represent respectively the CSR60- and the CSR96-W solutions. In purple are the time series of the ITSG90-W solution.

2.5.1 North Atlantic sea-level patterns

In Fig. 2.8 grids of trends and amplitudes computed from Argo+GRACE are overlaid with Jason derived trends and amplitudes at the ground-tracks. In areas where the ground-tracks of altimetry are barely visible, there is a good resemblance between Argo+GRACE and altimetry.

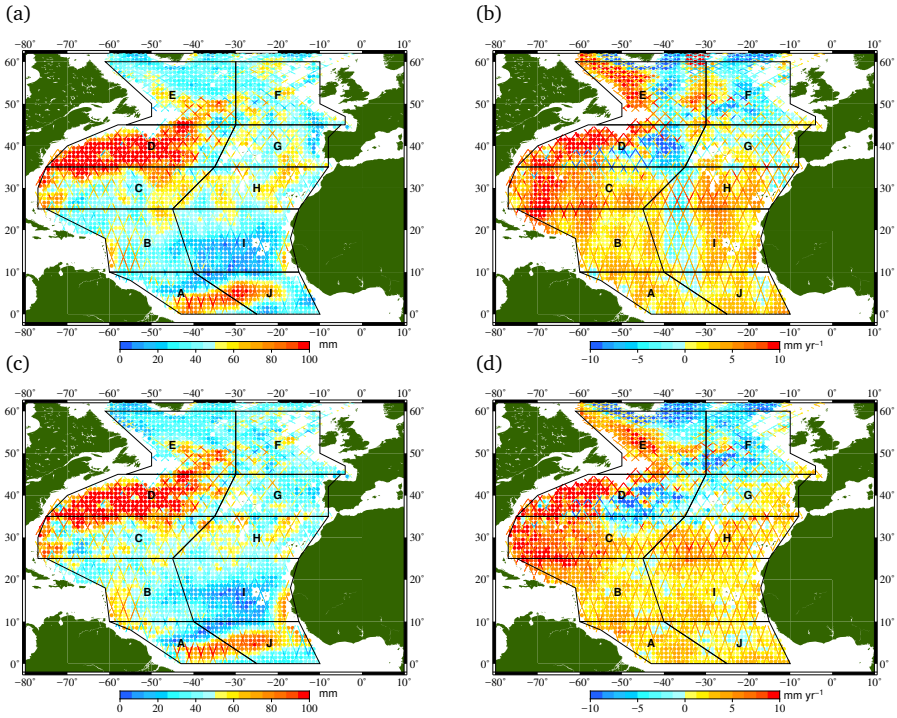

Figure 2.8: Amplitudes of the annual signal (left) and trends (right) computed of the sum of the components (Argo+GRACE) overlayed with those computed from the total sea level measured with altimetry. For the two top figures the CSR96-DDK (a,b) solutions are used and for the bottom two the CSR96-W (c,d) solution.

The grids and ground-tracks shown in the left column indicate that annual signals with an amplitude of 100 mm are present in the Gulf Stream region and in a tongue stretching from the Amazon to the Sahel. A region without any substantial annual signal is located just west of Africa, which is clearly visible in both the Argo+GRACE grid and altimetry. Both methods reveal these large-scale oceanographic features in amplitude, but there are also quite some differences. East of the Antilles, altimetric measurement show an annual amplitude of more than 60 mm, whereas Argo+GRACE estimates are in the range of 40-50 mm, depending on the choice of GRACE filter. Note that in this area, there are barely any Argo floats (Fig. 2.1), which might lead to interpolation problems. A second difference is observed in the Wiener-filtered grid (bottom-left) at the Amazon and Sahel regions. This is

exactly at the areas where the Wiener-filtered MC grids of Fig. 2.6 likely suffer from hydrological signal leakage.

The trends from altimetry in the right column of Fig. 2.8 show a distinct pattern, where positive trends are found south of 35° N and negative trends north of it, with the exception of the North American coastline. Trends of >10 mm yr^{-1} along the North American coast are also found by tide gauge studies (*Sallenger at al.*, 2012), usually attributed to a weakening Atlantic Meridional Overturning Circulation (AMOC). The Argo+CSR96-W solution resemble the trend patterns derived from altimetry measurement better, while the residual stripes in the CSR96-DDK solution are clearly visible. Note that a significantly larger altimetric trend is visible west of the Mediterranean. Possible causes will be discussed below.

2.5.2 Sub-basin scale budgets

The North Atlantic Ocean is split into ten regions, divided in the middle by the Mid-Atlantic ridge, while in the latitude direction trying not to cut through the major oceanographic features, like the salt water tongue in front of the Mediterranean and the Gulf Stream, as shown in Fig. 2.8. Just as in Sect. 2.4.3, the size of the regions is chosen such that the error on the trends does not exceed 1 mm yr^{-1}. First, we will discuss three representative examples of time series. Then budget closure in terms of trend and annual amplitude is addressed and the corresponding best gravity filter is determined. Ultimately, the trends, semi-annual and annual signals are removed from the time series and the best filter choice in terms of residual variability is determined.

Timeseries

Figure 2.9 shows budgets for three representative regions, using the Wiener-filtered MC solutions. The time series for the rest of the regions can be found in Appendix B. The left plots confirm that the main driver for annual fluctuations in sea level is the steric sea level, but that the trend is strongly influenced by a mass component. On the right side we see that the sum of the components and the total sea level agree to within the error bars, but some problems arise in the Gulf Stream area (region D). These are possibly caused by sharp gradients in sea level, mesoscale sub-sampling issues or deep-ocean steric contributions. The sea levels in Polygons D and I also contain some interannual signals, which are especially pronounced between 2010-2012. The left column shows that the interannual variability is primarily a steric signal. Note that the larger size of the error bars in regions B and I is due to the decrease in altimetry track density closer to the equator and the elongation of the correlation radius for the interpolation of Argo floats.

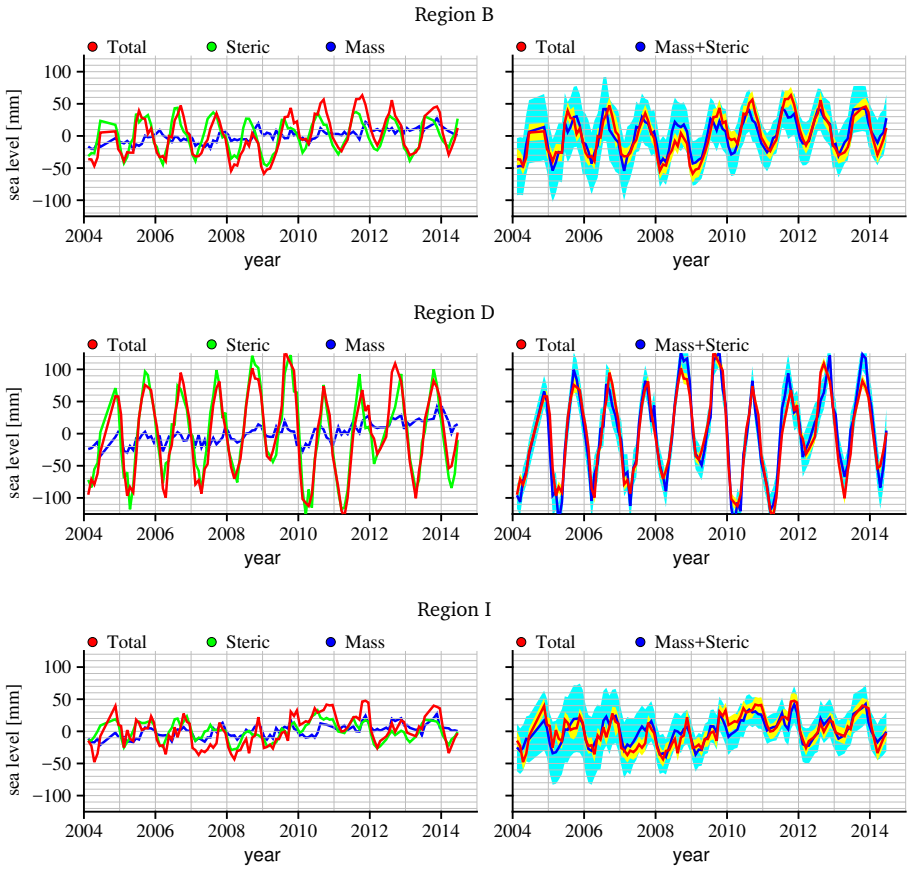

Figure 2.9: Time series of sea-level components for regions B, D and I. Left: total sea level from altimetry in red, steric sea level in green and the ITSG90-W mass in blue. Right: total sea level from altimetry in red and the sum of steric sea level and mass in blue. In yellow and ligth blue their 95% confidence interval. Time series for the other regions and without the annual cycles are found in Appendix B.

Trends

Trends computed from the time series of Fig. 2.9 are given in Table 2.4. Note that the budget is closed when the sum of the components matches total sea level within two standard deviations. In this case, the standard deviation includes the uncertainties of the mass, steric and total sea-level estimates. Close to the equator (A, B, I and J) and over the whole North Atlantic Ocean the trend budget is closed within two standard deviations no matter which of the MC solutions is used. This confirms the results of Fig. 2.8. In the four southernmost regions the GIA correction is relatively small and no sharp gradients or strong features are present in the trend grids, which contribute to proper budget closure. Budget closure is also achieved by all filters in the northeast of the Atlantic (F, G). Again, these regions do not contain significant gradients in trends and only a small GIA correction is applied. The results of the Argo+GRACE however show are larger spread for the different MC solutions. It is

important to note that especially region F suffers from some ringing artefacts before the fan filter is applied and that the far northeast is not very well covered by Argo floats. The trends of CSR96-DDK in region G are a bit further off than the other solutions, probably resulting from striping issues (Fig. 2.6).

In the northwest of the Atlantic the choice of gravity field filter either substantially influences the estimated trends (D and E), or the impact is just outside of two standard deviations (C) for one ore more solutions. Using the CSR96-W solution, the budget is closed within two standard deviations for all three polygons, whereas the other solutions do not close the budget. For region C, the trends obtained with any of the filters are either just within or just outside two standard deviations from altimetry. For region D, the budgets are not closed with the CSR60-W solution, but for the other solutions the sum of the components and total sea level are statistically consistent. In this region, sharp gradients occur not only in the MC with the presence of a neighbouring continental shelf, but also in the steric component. This might lead to leakage of the continental shelf mass signal or problematic interpolation of the Argo steric sea levels. In addition for both of the beforementioned regions, the GIA correction on the MC is relatively large. We did not add an uncertainty to the mass component and total sea level for GIA. If a GIA correction error of 10-20% is assumed, which is smaller than discussed in Sect. 2.3.3, it would close the budgets in regions D and E, except for the CSR60-W solution. In region E, a clear split is visible between the Wiener-filtered CSR solutions, which close the budget, and the other two solutions, which do not close the budget. The difference in results could be caused by the filter not being able to handle the large gradients (*Klees et al.*, 2008) in the MC within this region (Fig. 2.8). However, if we would again add only a 10-20% GIA correction error, it would suffice to close the budget for all filters.

Ultimately, only the budget in region H cannot be closed with any of the solutions. There is no strong GIA signal present, which could be responsible for a large bias. In addition, the sea level in this polygon does not exhibit any strong gradients and the number of Argo floats is substantial. This excludes interpolation or filtering problems. A possible reason for the non-closure is a deep-steric effect, that could be related to variations in the export of saline water from the Mediterranean (*Ivanovic et al.*, 2014), which is not captured by Argo.

In conclusion, it is possible to close the sea-level budget within two standard deviations for nine-out-of-ten regions using CSR96-W. If a 10-20 % GIA correction error is taken into account, the budget for nine-out-of-ten polygons is also closed for CSR96-DDK and ITSG90-W. This also suggests that the commonly assumed GIA correction error of 20-30% (*Von Schuckmann et al.*, 2014) is probably overestimated in the North Atlantic Ocean.

Annual signal

In Sect. 2.4.2, we showed that the seasonal cycles are primarily caused by steric variations in sea level (Fig. 2.9). By comparing the first column with the last column in Table 2.5, it becomes clear that in most cases an additional mass signal is required to close the budget in terms of annual amplitude. The discrepancy between Argo and

Table 2.4: Trends of total sea level (mm yr^{-1}) and their standard deviations from altimetry (Jason) and the sum of steric and mass from Argo (A) and GRACE (CSR, ITSG) for different filter solutions. NA is the trend for the complete North Atlantic Ocean between 0-65° N. The 1σ error bars are computed by propagating the uncertainties using the least-squares normal matrices. A 0.4 mm y^{-1} drift error is taken into account for altimetry based on the comparisons with tide gauges (*Mitchum*, 1998, 2000). GIA Absolute Sea Level (ASL*) correction subtracted from altimetry MSL and GIA Equivalent Water Height (EWH**) correction subtracted from the GRACE MC. In bold the solutions for which the budget closes.

	Jason	CSR96+A	CSR96+A	CSR60+A	ITSG90+A	GIA	GIA
		DDK5	Wiener	Wiener	Wiener	ASL*	EWH**
A	2.6±0.5	**1.8**	**2.4±0.9**	**2.7±0.9**	**2.3±0.9**	-0.3	-2.2
B	2.8±0.5	**3.1**	**3.0±0.7**	**3.7±0.7**	**3.1±0.7**	-0.5	-3.4
C	3.2±0.4	**4.2**	**4.4±0.5**	4.8±0.5	**4.5±0.5**	-0.6	-5.1
D	1.0±0.4	**1.5**	**1.9±0.5**	3.1±0.5	2.3±0.4	-0.6	-6.0
E	0.5±0.4	2.2	**0.3±0.5**	**0.0±0.5**	2.2±0.4	-0.5	-7.1
F	-2.4±0.4	**-2.0**	**-3.4±0.5**	**-3.0±0.5**	**-1.8±0.4**	-0.5	-4.6
G	0.7±0.5	-0.8	**-0.2±0.6**	**0.0±0.6**	**0.4±0.6**	-0.5	-3.6
H	4.7±0.4	1.4	2.5±0.6	2.7±0.6	3.3±0.6	-0.5	-3.5
I	2.3±0.4	**1.4**	**2.1±0.6**	**2.5±0.6**	**2.5±0.6**	-0.5	-2.8
J	2.4±0.4	**1.7**	**1.3±0.7**	**1.3±0.7**	**1.6±0.6**	-0.3	-2.0
NA	1.8±0.4	**1.8**	**1.5±0.3**	**1.8±0.3**	**2.2±0.2**	-0.5	-4.1

altimetry for the whole North Atlantic Ocean reveals that on average in-phase mass signals with an amplitude of approximately 7 mm are required to close the budgets, which is in line with the modelled results of *Tamisiea et al.* (2010). They modelled, using fingerprints, amplitudes of the MC ranging from 3-12 mm, and phases (not shown here) between day 210-330, which is in-phase with the steric signal.

Table 2.5 shows that for virtually every region the choice of filter matters. On top of this, there is a clear difference between the Wiener-filtered CSR solutions and the other two solutions. Adding the CSR60- and CSR96-W solutions increases in a few cases even the discrepancy with altimetry, which is caused by an out-of-phase mass signal. Especially in regions A and J, where the amplitude is underestimated and overestimated, respectively. Only in four regions (B, D, H and I) the amplitude budget closes within two standard deviations using these solutions.

Even though no error bars are computed for the CSR96-DDK, because no variance-covariance matrices are provided with this product, it is clear that the results are far better in terms of budgets closure. The results are comparable to ITSG90-W, which closes seven-out-of-ten budgets within two standard deviations. CSR DDK5+Argo underestimates the amplitude in region B, while ITSG90-W+Argo overestimates the amplitude with respect to altimetry in region D. In region B the estimate of ITSG90-W+Argo is relatively small and in region D the CSR96-DDK+Argo also relatively large. Note that the number of Argo floats in region B is often small (Fig. 2.1) and that large gradients in the steric sea level in region D could cause interpolation problems for steric sea level. Secondly, in both northern polygons E and F both combinations of Argo+GRACE underestimate the amplitude compared to altimetry. Why this underestimation occurs is not completely clear. A likely culprit is the gravity field filtering, but yearly deep convection events in these regions (*Våge et al.* , 2009),

Table 2.5: Amplitudes (mm) of the annual signal from total sea level from altimetry and the sum of steric and mass from Argo and GRACE for different filter solutions. The 1σ error bars are computed by propagating the uncertainties using the least-squares normal matrices. In bold the solutions for which the budget closes.

	Jason	CSR96+A.	CSR96+A.	CSR60+A.	ITSG90+A.	A. only
		DDK5	Wiener	Wiener	Wiener	
A	42.3±1.3	**36.0**	26.8±3.4	28.2±3.4	**36.3±3.1**	32.2±3.1
B	34.2±0.9	27.5	27.8±2.7	**29.6±2.7**	**30.5±2.5**	30.2±2.4
C	54.0±0.7	**52.6**	49.3±2.1	48.5±2.1	**52.9±1.9**	47.1±1.9
D	82.1±0.6	**85.0**	**84.3±2.0**	**82.8±1.9**	88.3±1.7	82.6±1.7
E	48.0±0.5	43.2	40.2±1.9	38.5±1.8	42.8±1.5	39.3±1.4
F	45.8±0.6	40.4	37.6±2.0	39.6±1.9	41.2±1.6	35.1±1.6
G	45.1±0.9	**44.5**	37.7±2.2	39.9±2.1	**43.2±2.0**	38.4±1.9
H	49.9±0.8	**48.8**	**45.1±2.3**	**46.5±2.3**	**48.1±2.1**	39.6±2.1
I	18.7±0.8	**19.0**	**16.0±2.3**	**17.8±2.2**	**19.1±2.0**	11.9±2.0
J	40.3±1.2	**40.8**	46.1±2.5	49.0±2.4	**42.9±2.2**	33.9±2.1
NA	44.6±0.3	**42.6**	39.5±1.1	40.0±1.0	**43.3±0.8**	37.7±0.8

which transport surface water to depth below 1000 m, and the limited number of Argo floats, could also be contributing factors.

Using ITSG90-W, it is also possible to close the budget on the scale of the whole North Atlantic Ocean (last row of Table 2.5). The Argo+ITSG90-W performs best in terms of amplitude budget closure in most regions, even though often characterized by sligthly smaller amplitudes than those derived from altimetry. This suggests that there is either a long-wavelength underestimation of the amplitude in GRACE, an overestimation in altimetry, or a missing steric effect in Argo. This is in line with *Storto et al.* (2017), where on a global scale, steric sea levels computed from reanalyses and gridded T/S fields are found to be smaller than those indirectly derived from altimetry minus GRACE. Additionally, *Marcos et al.* (2011) found differences in phase and amplitude of steric-corrected altimetry and the MC from destriped 500 km Gaussian-filtered GRACE solutions in the North Atlantic.

Residual variability

Time series for the same regions as in Fig. 2.9 are shown in Fig. 2.10, but their trend, semi-annual and annual signals have been removed to show the residual variability. For the rest of the regions plots of the residuals are given in the Appendix B. In contrast to the time series for the whole North Atlantic Ocean (not shown), the sub-basin scale time series show significant interannual variability. Region D, located at the east coast of the United States, shows a drop of 60-70 mm within three months at the end of 2009. This drop is possibly related to a shift in the Gulf Stream described by *Pérez-Hernández and Joyce* (2014) as the largest in the decade, which they relate to the North Atlantic Oscillation. As illustrated in the left column, the shift in the Gulf Stream is primarily of steric nature, however small deviations in the mass signal are also present. It is remarkable that at the same time on the other side of the Atlantic (region I, bottom panels of Fig. 2.10), an increase in sea level is observed by both altimetry and Argo. In region B, we also observe a small interannual effect by altimetry and Argo. However, the amplitude of the signal is larger for altimetry than is captured by Argo, which suggests either some interpolation issues in an area

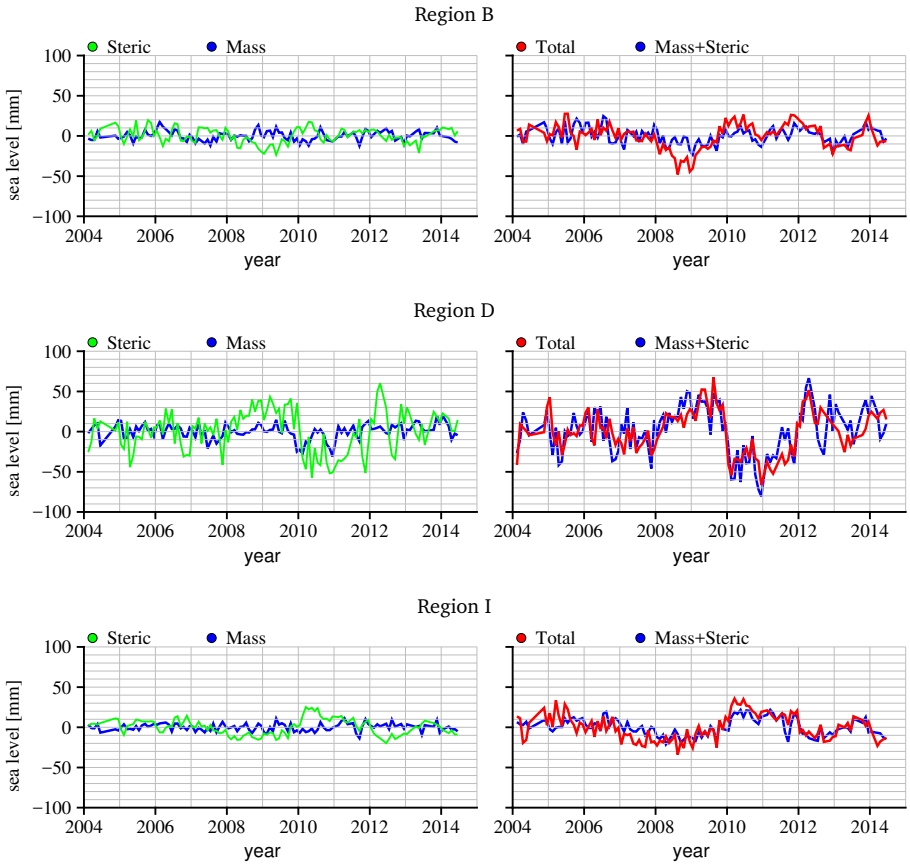

Figure 2.10: Time series of sea-level components for polygons B, D and I after removing the trends and the annual and semi-annual signals. Left: ITSG90-W mass in blue and steric sea level in green. Right: total sea level from altimetry in red and the sum of steric sea level and mass in blue.

without many Argo floats or a deep-steric effect.

Using any of the filtered CSR or ITSG solutions, it is possible to detect the interannual variability described, probably because most of the signal is of steric origin. However, for the interannual signals that are less pronounced, or for high frequency behaviour of sea level there are some differences between the MC solutions. Table 2.6 shows the fraction of variance of the residual signal of altimetry (trend, semi-annual and annual cycles removed) explained by Argo+GRACE.

The third column indicates that Argo in combination with CSR96-W does not explain much of the residual variance, but mostly introduces additional noise, which causes the negative values. Using the DDK5-filtered MC the explained variance increases, but the best performance is obtained with the CSR60-W and especially the ITSG90-W gravity fields. The last column shows that after reducing the trend, and the semi-annual and annual signals, between 24-53% of the residual signal can be explained by the combination of Argo and ITSG90-W. It is remarkable that for the

Table 2.6: Fraction of explained variance, R^2, of altimetry total sea level by Argo+GRACE steric+mass for different gravity field filter solutions after removing the semi-annual and annual signals and the trend. The corresponding time series can be found in Appendix B.

	CSR96+A.	CSR96+A.	CSR60+A.	ITSG90+A.
	DDK5	Wiener	Wiener	Wiener
A	0.32	0.07	0.33	0.38
B	0.02	-0.46	0.09	0.24
C	0.37	0.14	0.38	0.40
D	0.31	0.16	0.36	0.34
E	0.14	-0.19	0.29	0.44
F	0.09	-0.17	0.45	0.52
G	0.13	-0.05	0.29	0.34
H	-0.12	-0.49	0.21	0.27
I	0.34	0.14	0.50	0.49
J	0.39	0.17	0.45	0.53
NA	-0.05	-1.21	-0.06	-0.01

whole North Atlantic Ocean (last row in Table 2.6), no variance is explained by the Argo+GRACE, primarily due to the absence of a clear interannual signal. Note that the value -1.21 for the CSR96-W gravity fields indicates that variance increases after its subtraction from altimetry, which indicates that the Argo+GRACE time series is substantially noisier than the altimetry time series.

2.6 Conclusions

For the first time it is shown that sea-level budgets can be closed on a sub-basin scale. With the current length of the time series it is possible to establish budgets over areas of approximately one-tenth of the North Atlantic Ocean. To obtain error bars on the annual amplitudes, trends and time series, errors for altimetry and Argo profiles are propagated from existing correlation functions, while for GRACE full variance-covariance matrices are used. For altimetry, a latitude dependent intermission bias is applied and it is shown that this leads to trend differences ranging up to 0.8 mm yr^{-1} if the period from 2004-2014 is considered.

To obtain proper averaged mass for sub-basin scale polygons, the gravity fields have to be filtered. The application of an anisotropic Wiener filter on the CSR96 solutions leads to the best closure of the trend budget in nine-out-of-ten regions. In the considered regions also the CSR96-DDK and the ITSG90-W solutions appear to close just as many budgets when a 10-20% GIA correction error is added. The results of the CSR96-DDK filter however, strongly depend on the orientation of the averaging area due to residual meridional striping. The resemblence between trends also suggests that the errors on the GIA model are probably smaller than the commonly assumed 20-30%. Furthermore, a large difference in trend between altimetry and Argo+GRACE is observed in front of the Mediterranean Sea. Since the GIA correction is small, we suggest that this originates from steric effects below the considered 1000 m, where saline water enters the Atlantic Ocean from the Strait of Gibraltar and dives to large depths. Further research is needed to confirm this hypothesis.

The CSR60- and CSR96-W solutions appear to underestimate the amplitude of the annual signal substantially. They also suffer from what appears to be leakage around the Amazon and Sahel, regions with a substantial annual hydrological cycle. Using the CSR96-DDK gravity fields and the ITSG90-W solutions, the sum of the steric and mass components becomes significantly closer to that of altimetry, with closure in seven-out-of-ten regions. However, it must be noted that the altimetry signals tend to be slightly larger. The smaller amplitudes of GRACE+Argo are partly caused by the destruction of the signal by filtering of the gravity fields or limited Argo coverage, or in some regions deep-steric signals.

By removing the semi-annual and annual signals and trends interannual variability can be detected. Since most of the interannual variability in the North Atlantic Ocean is contained in the steric component, the type of filter applied to GRACE monthly gravity models is not really important. However, if we look at differences on a month-to-month basis, high-frequency variations or small interannual fluctuations in mass, the use of CSR60-W the ITSG90-W solutions explains a larger fraction of the altimetric sea level. Using the ITSG90-W solution, 24-53% of the variability in the altimetry-derived sea-level time series is explained. The CSR96-W solution only introduces noise and explains virtually no residual variability of the altimetry time series. Especially in the months around the 4-day repeat-orbits in 2004, the CSR96-W solutions do not give proper estimates of the MC, which partly contributes to a lower explained variance.

To summarize, using the ITSG Wiener-filtered solution the trend budgets close when an error of 10-20% on the GIA correction is assumed. They perform, together with the standard DDK5-filtered CSR solution, best in terms of annual amplitude budget closure. Additionally, the combination of ITSG mass and Argo steric sea levels explains the largest fraction of variance in altimetry time series. Based on this, the best option to establish budgets, at scales considered in this paper, is the ITSG90-W solution. However, due to residual striping in the trend grids from the 'static' background field that are added back after Wiener-filtering, one must take care when averaging the MC over even smaller regions, or meridionally-oriented polygons, which is a even a bigger problem for the standard CSR96-DDK solutions.

Chapter 3

Trends and interannual variability of mass and steric sea level in the Tropical Asian Seas

3.1 Introduction

Sea level trends in the Tropical Asian Seas (TAS) over the altimetry era (1993-present) are among the highest in the world (*Cazenave and Le Cozannet*, 2013). The region is especially vulnerable to sea-level rise due to the many low-lying densily populated areas (*Strassburg et al.*, 2015). Additionally, groundwater depletion in large cities as Manilla, Bangkok and Jakarta (*Phien-Wej et al.*, 2006; *Rodolfo and Siringan*, 2006; *Chaussard et al.*, 2013; *Raucoules et al.*, 2013) causes subsidence and enhances societal and economic risks. Furthermore, the TAS form an interesting area in both sea-level and oceanographic studies, because they serve as a passage for dynamical interactions between the Pacific and Indian oceans (*Wijffels and Meyers*, 2004).

Many studies considered sea-level variability in areas surrounding the TAS, mostly focussing on the Western Tropical Pacific Ocean (WTPO). The large sea-level trends during the altimetry area in the WTPO are attributed to strengthening of the trade winds since the 1990s (*Merrifield*, 2011; *Merrifield and Maltrud*, 2011; *Zhang and Church*, 2012; *England et al.*, 2014). Interannual and decadal variability in trade winds are related to the El Niño Southern Oscillation (ENSO) and the Pacific Decadal Oscillation (PDO), who cause steric fluctuations in the WTPO region. Furthermore, several studies indicated that the ENSO and PDO are also driving the sea level in the Leeuwin Current at Fremantle (*Feng et al.*, 2004; *Lee and McPhaden*, 2008; *Merrifield et al.*, 2012), which requires waves to propagate through the southern parts of the TAS. The trade winds associated with the PDO are expected to weaken over the coming years (*Zhang and Church*, 2012; *England et al.*, 2014), which will lead to lower sea-level trends in the WTPO and the Leeuwin current, but also in the TAS (*Strassburg et al.*, 2015).

Parts of this chapter have been published as: Kleinherenbrink, M., Riva, R., Frederikse, T., Merrifield, M., Wada Y. (2017). Trends and interannual variability of mass and steric sea level in the Tropical Asian Seas, Journal of Geophysical Research: Oceans, doi:10.1002/2017JC012792.

Even though many studies described the relation between sea level, heat content, ENSO and PDO in the TAS area and surroundings, the contributions of other sources are often neglected. *McGregor et al.* (2012a) suggests that an additional mass component is required to be able to capture the full sea-level rise signal. For the South China Sea and east of the Philippines this is confirmed by *Rietbroek et al.* (2016), who performed an inversion of altimetry and Gravity Recovery And Climate Experiment (GRACE) data to obtain trends in sea level driven by global mass redistribution and steric changes. They estimated that at least 25% of the total sea-level rise between 2002-2014 in the SCS and east of the Philippines, respectively 7.6 mm yr^{-1} and 14.7 mm yr^{-1}, is due to mass changes.

Only in the South China Sea separate mass and steric changes have been estimated using GRACE and ocean reanalyses or in-situ measurements of temperature and salinity (*Feng et al.*, 2012). The limited number of studies is mainly due to the absence of Argo temperature and salinity measurements and a commonly applied cut-off of GRACE data in the first 300 km from the coast to avoid hydrological signal leakage. Not considering the individual mass and steric components in the TAS not only limits the understanding of sea-level variability in the region itself, but it also affects studies on larger scales. *Von Schuckmann et al.* (2014) showed that the TAS region is responsible for the non-closure of the sea-level budget in the tropics, caused by the significantly larger sea-level trends in the TAS, and that the omission of the TAS leads to a trend discrepancy of 0.5±0.2 mm yr^{-1} in global sea-level budgets over the January 2005 - December 2010 period.

In this study, we use for the first time altimetry, optimally filtered GRACE solutions and temperature and salinity fields from ocean reanalysis products to separate steric from mass contributions to sea level between January 2005 - December 2012. We derive dedicated variance-covariance matrices for altimetry, use full variance-covariance matrices stemming from GRACE data processing and use the spread of steric sea levels from six ocean reanalyses to obtain a consistent separation between mass and steric sea level. This allows for a correction of global and large-scale regional sea-level budgets to the steric and mass components in the TAS, which have been omitted in previous studies (*Willis et al.*, 2008; *Leuliette and Willis*, 2011; *Von Schuckmann et al.*, 2014). Additionally, we investigate the dynamic mass response in shallow regions to the larger steric response in the deeper ocean and couple both the steric and mass components to the ENSO and the Dipole Mode Index (DMI). The ENSO contribution is investigated in further detail by considering the first two Principal Components (PC) of the Equatorial wind stress as in *McGregor et al.* (2012b) and *Widlansky et al.* (2014). Finally, we quantify how much the mass trend is affected by the tidal nodal cycle and by global mass redistribution, respectively.

3.2 Study Area

To study the TAS in more detail, we separate it into four regions as shown in Fig. 3.1. Region A, the South China Sea is characterised by deep bathymetry in the center and relatively large shallow areas near the Chinese and Vietnamese coasts. There

are several Argo floats present in region A, but not enough to allow for an accurate interpolation.

Region B, referred to as Thailand-Java, is characterised by a very shallow bathymetry, typically less than 100 meters. The steric sea level is poorly constrained due to the absence of any Argo floats and the presence of only a few shipboard measurements of temperature and salinity. GRACE observations are largely affected by the 2004 Andaman-Sumatra Earthquake in this region and therefore, we exclude all observations before 2005. However, as will be discussed in Sect. 3.3.2, the post-seismic relaxation of the solid Earth still affects the observations. Furthermore, as in region A, the neighbouring Mekong basin might introduce a substantial hydrological leakage, which is further discussed in Sect. 3.3.2.

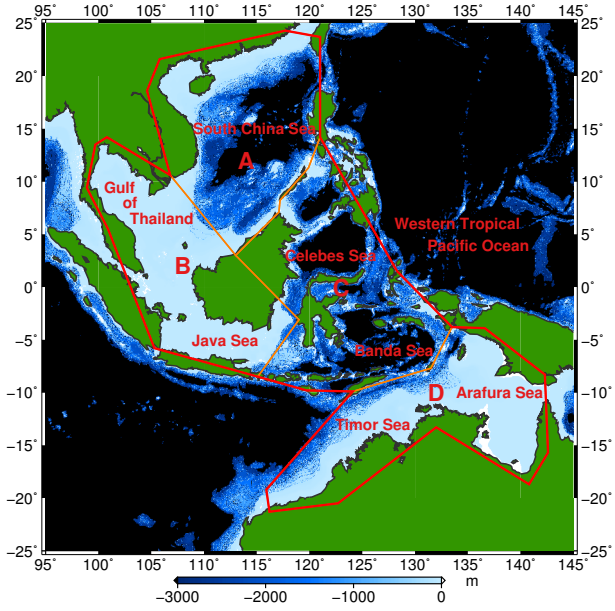

Figure 3.1: Bathymetry and topography in and around the TAS. Visible are four averaging regions. In tables we refer to the regions as A, B, C and D for brevity.

Region C, denoted as Banda-Celebes, is very deep, but the area is divided by many islands into several small basins, with their own regime. As a result, the correlation scales of sea-level variability in this area are shorter than in an open basin, like region A.

Region D is slightly deeper than region B, with maximum depths of 200-300 m. Together with region C it is subject to the throughflow from the Pacific to the Indian Ocean. In the southwest, region D is connected to the Leeuwin Current, where sea level strongly depends on Pacific Ocean indices, like the PDO and the ENSO as mentioned in the introduction. This region will be referred to as Timor-Arafura.

3.3 Data and methods

To obtain a consistent separation of the mean mass $\bar{h}_{mass}$ and steric sea level $\bar{h}_{steric}$ it is required that the sea-level budget equation (*Leuliette and Miller*, 2009)

$$\bar{h}_{total} = \bar{h}_{mass} + \bar{h}_{steric} \tag{3.1}$$

is closed within error bars. While the observation of mean total sea level $\bar{h}_{total}$ in the TAS can be done with altimetry using standard techniques, estimating the mass and steric components is less trivial. The mass component is obtained from GRACE gravity fields, which need to be corrected for contamination by leakage of hydrological signals and gravitational effects of the Sumatra-Andaman earthquake. The absence of Argo floats in the TAS causes difficulties in estimating the steric component and therefore we rely on ocean reanalyses. This introduces additional problems, since most of the reanalysis products have a resolution that cannot capture the detailed structure of the TAS. This section will explain how the different observations and models are used in order to obtain a statistically optimal separation between the mass and steric components.

To explain the behavior of the steric sea level and mass components, we regress indices and principal components (PC) and use mass redistribution fingerprints. This section also describes how the PC of the equatorial wind stress are obtained and briefly introduces the sea-level equation, which is used to obtain the fingerprints.

3.3.1 Altimetry mean sea level

The Mean Sea Level Anomaly (MSLA) is estimated from along-track Jason-1&2 altimetric sea-level measurements, obtained from the Radar Altimeter Database System (RADS) (*Scharroo et al.*, 2012), averaged over the regions indicated in Fig. 3.1. Applied range corrections are the same as in *Kleinherenbrink et al.* (2016), cf. Table 3.1. Additionally, we apply a latitude dependent intermission bias (*Ablain et al.*, 2015). The Sea Level Anomaly (SLA) is then obtained by subtracting the DTU13 mean sea surface (*Andersen et al.*, 2015) from the corrected sea-level measurements. Surface area weighting of the SLAs is done by dividing the ocean area A_l in a latitude band l of 1° by the number of measurements N_l, such that

$$\omega_i = \frac{A_l}{N_l} \tag{3.2}$$

are the nonnormalized weights for measurement i inside a particular latitude band l. The weights are normalized, which results in:

$$w_i = \frac{\omega_i}{\sum \omega_i}. \tag{3.3}$$

The latitude dependent covariance functions of *Le Traon et al.* (2001) are not suitable to obtain error bars for the MSLAs in the TAS due to islands, currents and depth

Table 3.1: List of geophysical correction applied in this study. Details on the geophysical corrections are given in Chapter 2.3.1.

Ionosphere	Smoothed dual-frequency
Wet troposphere	Radiometer
Dry troposphere	ECMWF
Ocean tide	GOT4.10
Loading tide	GOT4.10
Pole tide	Wahr
Solid Earth tide	Cartwright
Sea-state bias	Tran2012
Dynamic atmosphere	MOG2D

variations. For every averaging region a dedicated covariance function is therefore estimated. First, we compute the dissimilarity $\gamma_{i,j}$ between all the measurements over a 10-day repeat period:

$$\gamma_{i,j} = \frac{(h_i - h_j)^2}{2}, \tag{3.4}$$

where h_i and h_j are two SLAs within the considered region in a 10-day repeat orbit relative to a background field. The background field is a second-order polynomial fit through all the measurements in the region during the Jason-1 period. A variogram $\hat{\gamma}_n$ is created by binning and averaging dissimilarities into 20 km range bins n, to have enough measurements per bin to reduce the noise, which are then averaged over all 10-day repeat periods of Jason-1. Using the variance $\hat{\sigma}_h^2$ of the background removed SLAs, the experimental covariance between measurements is computed as:

$$\hat{c}_n = \sqrt{\hat{\sigma}_h^2 - \hat{\gamma}_n}. \tag{3.5}$$

We considered Gaussian, spherical and exponential covariance functions, and found that the exponential one fits the experimental covariances best (not shown). Using the weight vector $\hat{w}$, the distance between the measurements and the fitted covariance functions, the standard error $\sigma_{\bar{h}}$ for mean sea-level time series is computed, such that:

$$\sigma_{\bar{h}} = \hat{w}^T C_{total} \hat{w}, \tag{3.6}$$

where C_{total} is the variance-covariance matrix of the measurements computed from the exponential covariance function. In addition we add an time-dependent error, related to the uncertainty of the drift in the altimeter system, which is validated with tide gauges(*Mitchum*, 1998, 2000). The uncertainty is given as:

$$\epsilon_{drift} = \alpha(t - t_0), \tag{3.7}$$

with t the time in years, t_0 the time of the middle epoch of the time series and $\alpha = 0.4$ mm yr^{-1}.

3.3.2 GRACE ocean mass

To minimize leakage and reduce striping effects, an anisotropic Wiener filter (*Klees et al.*, 2008) is applied to the GRACE gravity fields. The ITSG-Grace2016 spherical harmonic solutions are selected, because they give the best overall performance in combination with the Wiener filter in previous work about the North Atlantic (*Kleinherenbrink et al.*, 2016). Let x be a vector of monthly spherical harmonic ITSG coefficients, then the resulting filtered coefficients are given as:

$$x_f = (D_x^{-1} + N_x)^{-1} N_x x, \tag{3.8}$$

which rely on the signal variance-covariance matrix D_x and the normal matrix N_x of the solution. The corresponding noise variance-covariance matrix $C_{x,f}$ is computed as:

$$C_{x,f} = (D_x^{-1} + N_x)^{-1}. \tag{3.9}$$

The derivation of the Wiener filter is provided in *Klees et al.* (2008) and the derivation of the variance-covariance matrix is found in *Kleinherenbrink et al.* (2016). Note that the monthly mean of background dealiasing products (GAD) has to be added to get the full signal. The mean of GAD product over the ocean is removed, to make GRACE compatible with altimetry corrected for the inverse-barometer. Averaging over a region is performed by weighting with the cosine of the latitude as described in *Kleinherenbrink et al.* (2016).

The mass variability on the continental shelves of the TAS is large with amplitudes reaching 10 cm. The load causes the ocean floor to move several millimeters, which cannot be neglected. Altimetry measures absolute sea level and GRACE the mass component relative to the ocean floor, therefore we will add the ocean floor motion to the GRACE-derived mass time series. To compute the ocean floor motion the GAC instead of the GAD product is added to the GRACE products, which includes atmospheric pressure over land (*Fenoglio-Marc et al.*, 2012). Consecutively, we compute ocean floor motion from monthly GRACE gravity fields in spherical harmonics as (*Wahr et al.*, 1998; *Fenoglio-Marc et al.*, 2012):

$$Y_{vlm}(l,m) = Y_{ewl}(l,m) \frac{3\rho_w}{\rho_e} \frac{h_l}{2l+1}, \tag{3.10}$$

where the $Y_{ewl}(l,m)$ and $Y_{vlm}(l,m)$ are the spherical harmonic coefficients of degree/order (l,m) in equivalent water height and vertical land motion, respectively. The constants ρ_w and ρ_e denote the densities of water and the Earth, while h_l is the Love number that relates the body tide to the static equilibrium tide. The resulting vertical land motion affects the trends up to 0.4 mm yr^{-1} and has an annual cycle with an amplitude of up to 3 mm.

Hydrological signal leakage

From the PCRaster GLOBal Water Balance (PCR-GLOBWB) we obtain monthly averaged Terrestrial Water Storage (TWS), including surface water (*Wada et al.*, 2011).

Groundwater depletion is not considered. Although cities, like Jakarta, extract large quantities of groundwater, the limited resolution TWS model does not include this effect. We do not expect ground water depletion to have a significant influence on the trends, because of the difference in scale between the averaging regions and the groundwater depletion zones. Using the TWS, one can obtain an estimate for the hydrological signal leakage of GRACE gravity fields into the surrounding ocean in terms of equivalent water level. We do this by reducing the resolution of TWS grids to that of the ITSG-Grace2016 and by applying the corresponding filter parameters. Based on the PCRGLOBWB data the TAS area typically has a TWS variability ranging from several centimeters up to decimeters, which is confirmed by a comparison with GRACE in the Mekong basin by *Tangdamrongsub et al.* (2016).

The ITSG-Grace2016 monthly gravity fields are provided as departure from the GOCO05s model, which contains a static field, a trend and an annual cycle (*Klinger et al.*, 2016). To be consistent with the (post-)processing of ITSG-Grace2016 as done in *Kleinherenbrink et al.* (2016), we first isolate the mean, the trend and the annual signal independently for each grid point, which we refer to as the background signal. Then the background signal, excluding the mean, and the residual signal are both converted to spherical harmonics and truncated at degree 90. The degree 0 and 1 terms for the background and residual signal are set to zero and the background signal is converted back to a grid. The same filtering is applied to the spherical harmonics of the residual signal as in Eq. 3.8 and the signal is converted back to a spatial grid. The resulting hydrological leakage has a negligible effect on the time series, the trend and the annual cycle in case of the ITSG-Grace2016 gravity fields. However, this might be different for other GRACE products, such as CSR, which do not compute the gravity field solutions with respect to a background trend and annual cycle.

Sumatra-Andaman earthquake

The gravity field in the Thailand-Java region is strongly affected by the 2004 Sumatra-Andaman earthquake. Even though our time series starts in 2005, post-seismic deformation affects the obtained mass and geoid trends (*Broerse et al.*, 2015). We will also remove the effect of the earthquake before the statistical separation discussed in Sect. 3.3.4. A regression is made of a logarithmic relaxation function (representing post-seismic effects), a trend, annual and semi-annual cycles, PC1&2 of the wind stress and Dipole Mode Index (DMI) to reduce as much variability as possible in the time series of region B. Long-term ocean dynamics, as represented by the mentioned indices, might correlate with the relaxation function and therefore excluding them might lead to significantly different regression parameters (*Einarsson et al.*, 2010). The computation of PC1&2 is explained in Sect. 3.3.5. We will also remove the effect of the nodal cycle before the regression with the mass time series, of which the computation is given in Sect. 3.3.7. The logaritmic relaxation function is given as

(*Hetland and Hager*, 2006):

$$u_{ln,t} = A \cdot \ln(1 + \frac{t - t_{eq}}{\tau_{ln}}), \tag{3.11}$$

where the magnitude A is the parameter to be estimated in the regression and t_{eq} the time of the Sumatra-Andaman earthquake. The relaxation time is $\tau_{ln} = 5$ yrs, which corresponds to the mean relaxation time found by *Broerse et al.* (2015). The regression is repeated for the 95 % confidence intervals of $\tau_{ln} = 1.5$ and $\tau_{ln} = 20.8$ yrs (provided by *Broerse et al.* (2015)) to get an estimate of the spread. A time-dependent standard error is then estimated by subtracting both relaxation functions and dividing them by four. The error is referenced such that it is largest directly after the earthquake and decays to zero at the end of the time series. Eventually, the geoid and mass relaxation functions are subtracted from respectively the total sea level derived from altimetry and the mass component derived from GRACE.

3.3.3 Steric sea level

The steric sea level is inferred from reanalysis temperature and salinity fields using the TEOS-10 package (*Pawlowicz et al.*, 2012), which requires profiles of absolute salinity S_A, conservative temperature Θ and pressure P'. Using the gravitational constant g_0 and the atmospheric pressure P_0, the steric sea level is computed as (*IAPSO*, 2010; *Kleinherenbrink et al.*, 2016):

$$h_{rean} = -\frac{1}{g_0} \int_{P_0}^{P} \hat{\delta}(S_A(P'), \Theta(P'), P') dP', \tag{3.12}$$

with respect to a reference pressure P. The reanalysis products considered in this study are given in Table 3.2. The reference pressure is in all cases set to either the local maximum depth in the models or limited to 2000 dBar, since the limited resolution of some of the models reduces the number of grid cells to a few tens below the reference depth. Not all reanalyses provide conservative temperature, so a conversion from potential to conservative temperature is applied using the TEOS-10 software package. In addition, we add a virtual temperature and salinity observation at 0.5 dBar depth, because the steric sea level is computed at the top pressure level, which varies between 0-10 dBar, so that the whole steric signal is captured (*Kleinherenbrink et al.*, 2016). The virtual temperature and salinity observations have the same values as observations in the top layer of the reanalysis product.

As provided in the table, the resolution and the type of grid varies for the reanalyses. For the tripolar grids, steric sea levels are averaged onto a 0.5° × 0.5° (Glorys and ORAP5) or a 1° × 1° (GFDL) grid. Then, the steric sea levels are weighted with the cosine of their latitude to get a mean steric sea level for a region. Finally, the zero reference of the time series is set to the middle of the time series (approximately 2009) and then the RMS of the suite of reanalyses for each epoch (monthly) is used as an approximation of the error and the mean as the steric sea level for further analysis.

Table 3.2: Reanalyses used in this study. *Tripolar grids.

reanalysis	Resolution[°]	reference
GODAS	1 × 0.33	(*Behringer and Xue*, 2004)
GFDL CM2.1*	1 × 1	(*Zhang et al.*, 2007)
ECCO-JPL	1 × 1	(*Forget et al.*, 2015)
GECCO2 R1	1 × 0.33	(*Köhl*, 2015)
ORAS4	1 × 1	(*Balmaseda et al.*, 2013)
ORAP5.0*	0.25 × 0.25	(*Zuo et al.*, 2015)
Glorys2V3*	0.25 × 0.25	(*Ferry et al.*, 2010)
SODA v3.3.1	0.5 × 0.5	(*Carton and Giese*, 2008)

The ocean reanalyses all make specific choices on, amongst other factors, model specifications, horizontal and vertical resolution, and assimilated techniques. Therefore, over parts of the oceans that are not well-constrained by direct observations, the model spread provides is used as an estimate of the uncertainty of the ocean state. Since some co-varying bias may exist between similar models, such as the models from the ECMWF ocean reanalysis project (ORAS4 and ORAP5), and to enhance the estimate of the underlying uncertainty of the ocean state, we use a large set of ocean reanalysis products from different modelling groups, which include the new generation of eddy-permitting ocean reanalyses, but also reanalyses on coarser grids. Table 3.2 lists the reanalysis that are used.

To check the stability of the mean time series from the eight products a test is performed by each time omitting one reanalysis product. In case of outliers, one of the time series averaged over seven products should deviated significantly from the one averaged over eight reanalysis products. Based on this test, we find that the results do not change significantly if one reanalyis is left out (Appendix C). All reanalyses are contrained by sea surface temperature, satellite altimetry sea surface height, a few CTD and XBT observations and in the surrounding areas and the South China Sea by Argo float observations. Since their physics are also quite similar, it is not expected that the computed steric sea levels deviate significantly.

To examine the relative contributions of temperature and salinity to steric sea level, we compared time series of the full steric sea level against the thermosteric sea level (Appendix C). For the time series of thermosteric sea level, the salinity is kept constant at 35 PSU. Salinity changes only have an affect on the trends in regions A and B. In terms of interannual variability and annual cycles, the steric sea-level variability is primarily driven by thermosteric changes in all regions.

For a comparison between the interannual variability of steric sea level of the WTPO with the mass component in the TAS in Sect. 3.4.2, the independent gridded temperature and salinity product of *Roemmich and Gilson* (2009) is used, so that a correlation will not be an artefact of one of the models. Besides being independent, we expect that the interpolated grid of *Roemmich and Gilson* (2009) performs better in the WTPO than the reanalyses, particularly in terms of steric sea-level trends as shown in *Kleinherenbrink et al.* (2016) over the North Atlantic Ocean. The interpolated grid cannot properly be used inside the TAS, due to a lack of observations at depth, so there we have to rely on the physics of the reanalysis products. This

product is created by statistical interpolation of Argo float temperature and salinity measurements onto monthly 3D grids with a horizontal resolution of 1° × 1°.

3.3.4 Statistical separation

As shown in Fig. 3.2 the time series of summed steric and mass and total sea level for the whole TAS do not always resemble each other within error bars. After subtracting the seasonal cycle (shown in Appendix C), it becomes clear that both methods capture the interannual variability, however they still depart on occassion and their trends are not statistically consistent. Due to the lack of in-situ data, it is difficult to determine where the discrepancies originate from. We assume that our errors properly represent the uncertainties in the datasets. Statistically weighting will then give a more consistent division between the mass and steric components, such that they better match the three observations of mass, steric and total sea level.

The vector y_t for time step t contains three observations: the monthly low-pass filtered altimetric mean sea level $\bar{h}_{alt,t}$, the mean steric sea level $\bar{h}_{rean,t}$ computed from the reanalyses and the mean mass $\bar{h}_{grace,t}$ from GRACE, such that:

$$y_t = \begin{pmatrix} \bar{h}_{alt,t} \\ \bar{h}_{rean,t} \\ \bar{h}_{grace,t} \end{pmatrix}, \quad Q_{yy,t} = \begin{pmatrix} \bar{\sigma}^2_{alt,t} & 0 & 0 \\ 0 & \bar{\sigma}^2_{rean,t} & 0 \\ 0 & 0 & \bar{\sigma}^2_{grace,t} \end{pmatrix}. \tag{3.13}$$

The variance-covariance matrix $Q_{yy,t}$ contains the variances of the observations: $\bar{\sigma}^2_{alt,t}$, $\bar{\sigma}^2_{rean,t}$ and $\bar{\sigma}^2_{grace,t}$, which are obtained as described in the first Sect. 3.3.1, 3.3.2 and 3.3.3. Using the design matrix

$$A = \begin{pmatrix} 1 & 1 \\ 1 & 0 \\ 0 & 1 \end{pmatrix} \tag{3.14}$$

the statistically optimal mean steric sea level $\bar{h}_{steric,t}$ and mean mass $\bar{h}_{mass,t}$ are computed using least-squares:

$$\begin{pmatrix} \bar{h}_{steric,t} \\ \bar{h}_{mass,t} \end{pmatrix} = (A^T Q^{-1}_{yy,t} A)^{-1} A^T Q^{-1}_{yy,t} y_t. \tag{3.15}$$

The corresponding variance-covariance matrix $Q_{\hat{x}\hat{x},t}$ is given by:

$$Q_{\hat{x}\hat{x},t} = (A^T Q^{-1}_{yy,t} A)^{-1}. \tag{3.16}$$

The resulting optimally weighted time series for the whole TAS region are given in Fig. 3.3.

3.3.5 Wind stress and the Dipole Mode Index

Widlansky et al. (2014) showed that sea level in the neighbouring WTPO correlates with the first two principal components of the equatorial wind stress. The first PC

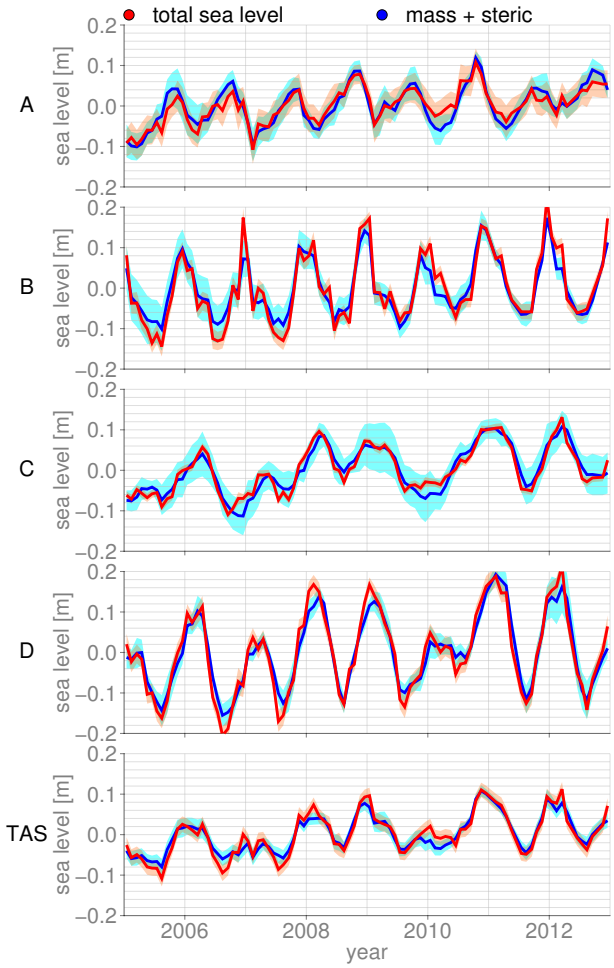

Figure 3.2: Sea level time series for the subregions and the total TAS. The South China Sea, Thailand-Java, Banda-Celebes and Timor-Arafura regions are respectively indicated with A, B, C and D. In blue GRACE mass + steric sea level from the reanalyses. In red altimetry-derived total sea level.

represents eastward equatorial wind stress anomalies, which strongly correlates with the Niño 3.4 sea surface temperature anomalies (*McGregor et al.*, 2012b), while the second PC indicates the seasonal weakening and southward shift of anomalous winds during ENSO events.

To obtain the PCs the monthly ERA-Interim (version 2.0) 10 m wind speed is used between 10°S - 10°N and 100°E - 60°W as in *McGregor et al.* (2012b). The wind stress (τ_x, τ_y) is estimated from the wind speed (u, v) using the relations (*Pugh and*

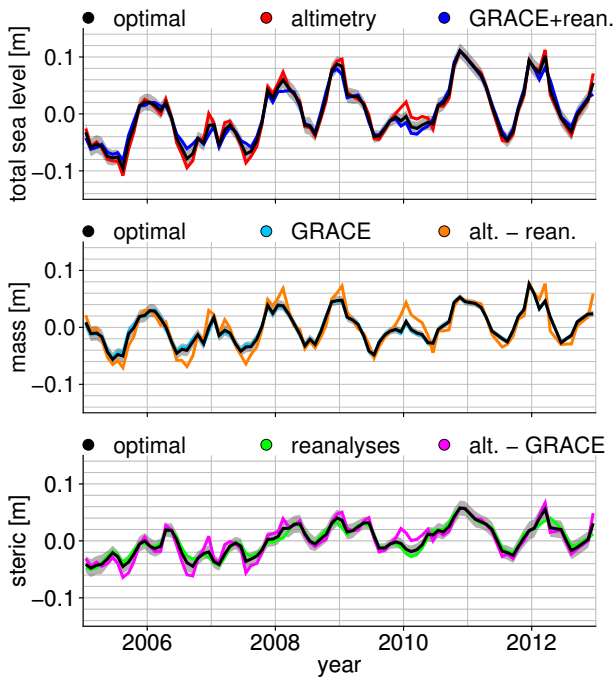

Figure 3.3: Time series of total and steric sea level and mass for the whole TAS region. Top: total sea level from altimetry in red, from GRACE+reanalyses in blue and the optimal solution in black. Middle: mass from GRACE in lightblue, from steric-corrected altimetry in orange and the optimal solution in black. Bottom: steric sea level from the reanalyses in green, from altimetry-GRACE in purple and the optimal solution in black.

Woodworth, 2014):

$$\begin{aligned} \tau_x &= \rho_{air} \frac{(0.8 + 0.065\sqrt{u^2+v^2})}{1000} u\sqrt{u^2+v^2} \\ \tau_y &= \rho_{air} \frac{(0.8 + 0.065\sqrt{u^2+v^2})}{1000} v\sqrt{u^2+v^2}\,, \end{aligned} \tag{3.17}$$

where ρ_{air} is the density of air. We create a 2D-matrix with the wind stress time series in both directions for all 2° × 2° grid cells over the whole dataset (January 1979 - December 2015), so that we capture multiple La Nina and El Nino events. Before computing the covariances, the mean, the annual and semi-annual signals are removed. The Empirical Orthogonal Functions (EOFs) are consecutively computed as the eigenvectors of the variance-covariance matrix of the remaining wind stress anomalies. PC1 and PC2 are the time series for the first two EOFs of the wind stress anomalies, accounting for 25 % and 14 % of the total anomaly variance, respectively (Fig. 3.4).

PC1 peaks in El Niño periods and is negative during La Niña (Fig. 3.4), while PC2 is slightly delayed with respect to PC1. The associated mode 1 spatial pattern

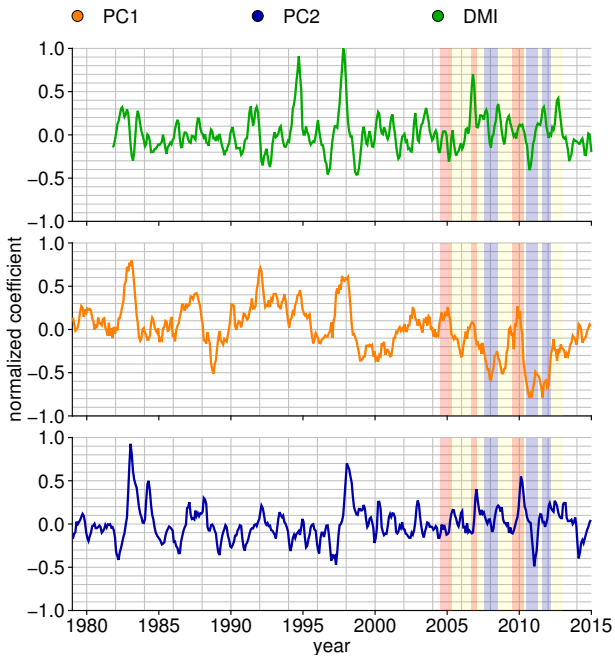

Figure 3.4: The first two PCs of the wind stress anomaly and the DMI. All low-pass filtered with a three month moving average filter to reduce high-frequency noise. The yellow shaded area indicates the period January 2005 - December 2012 over which we have steric and mass time series. The red and blue shades indicate respectively El Niño and La Niña states as given by Climate Prediction Center of NOAA (`http://www.cpc.ncep.noaa.gov/products/analysis_monitoring/ensostuff/ensoyears.shtml`).

(Fig. 3.5), which shows the typical strong easterly wind stress anomaly associated the El Niño. This causes a positive temperature anomaly in the eastern equatorial Pacific and a weak negative temperature anomaly in the WTPO. *Meyers et al.* (2007) showed that during El Niño the sea surface temperature in regions B, C and D (as given in Fig. 3.1) of the TAS drops as well. During La Niña this pattern reverses, causing the thermocline to deepen in the WTPO, which leads to a positive sea-level anomaly in the same area. In regions B, C and D of the TAS we find a positive sea surface temperature anomaly during La Niña events. In the following, significant correlations with PC1 represent variability that is in phase with ENSO and with PC2 variability associated with the seasonal weakening and southward shift of anomalous winds during ENSO events.

Additionally, we investigate the effects of interannual ocean dynamics from the Indian Ocean using the Dipole Mode Index (DMI). The DMI features peaks that at times align with ENSO events (e.g., 2006-07, 2010-11); however; overall the correlations between the DMI and PC1 and PC2 are low. When DMI is negative, a positive sea surface temperature anomaly occurs in the eastern Indian Ocean and in the TAS, with the opposite temperature anomaly for a positive DMI (*Meyers et al.*, 2007). In case of a positive DMI and an El Niño state, the temperature anomalies, especially in

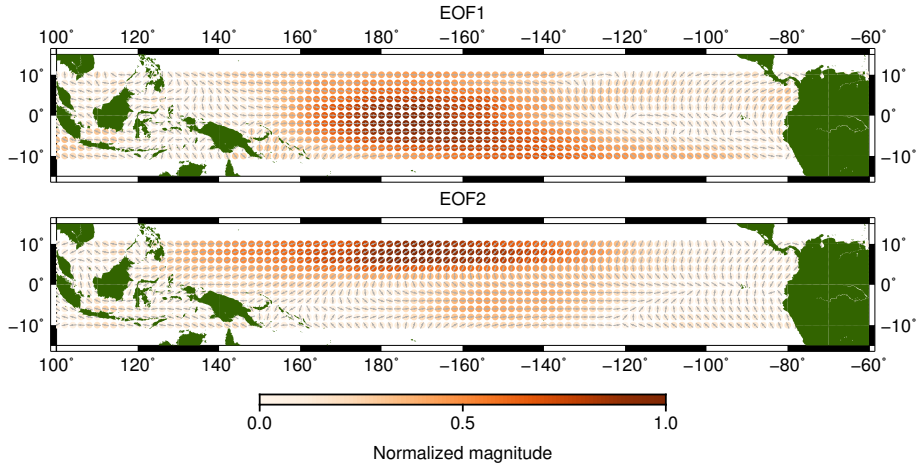

Figure 3.5: The first two EOFs corresponding to the PCs of the wind stress. The colors indicate the intensity of the wind stress and the vectors the direction.

the Banda-Celebes region (C) is strongly enhanced *Meyers et al.* (2007).

3.3.6 Present-day mass redistribution

We compute the contribution to relative sea level associated with mass changes $\Delta L(\theta, \phi, t)$ due to Greenland, Antarctica and glacier ice loss, land hydrology and dam retention. These changes result into geoid height changes $\Delta G(\theta, \phi, t)$ and solid Earth height changes $\Delta R(\theta, \phi, t)$ and a global mass conservation term Λ, which are all related to each other, so that (*Tamisiea et al.*, 2010)

$$\Delta S(\theta, \phi, t) = \Delta G(\theta, \phi, t) - \Delta R(\theta, \phi, t) + \Lambda, \tag{3.18}$$

where $\Delta S(\theta, \phi, t)$ is relative sea-level change at longitude θ, latitude ϕ at time t. For the change in absolute sea level, we only require the change in geoid and the mass conservation term, which is estimated by solving the sea-level equation including rotational feedback (*Farrell and Clark*, 1976; *Milne and Mitrovica*, 1996). Details on the individual contributions are described in the supplement of *Frederikse et al.* (2016).

The resulting contributions to absolute sea-level trends are computed for 2005.5-2012.5 (Fig. 3.6). Note that the input loads are only given on yearly intervals. Only dam retention has a negative contribution to the sea-level trend. Greenland is by far the largest contributor due to its substantial ice loss during the considered period and its remote location. The largest change in sea level is found far away from the source. The average sum of sea-level trends explained by the mass transport obtained with the fingerprint procedure in the TAS is approximately 2.4 mm yr^{-1}. This is only a small fraction of the total sea-level trend in the TAS. A comparison between the trends of fingerprints and the total sea-level trends is shown in Appendix C.

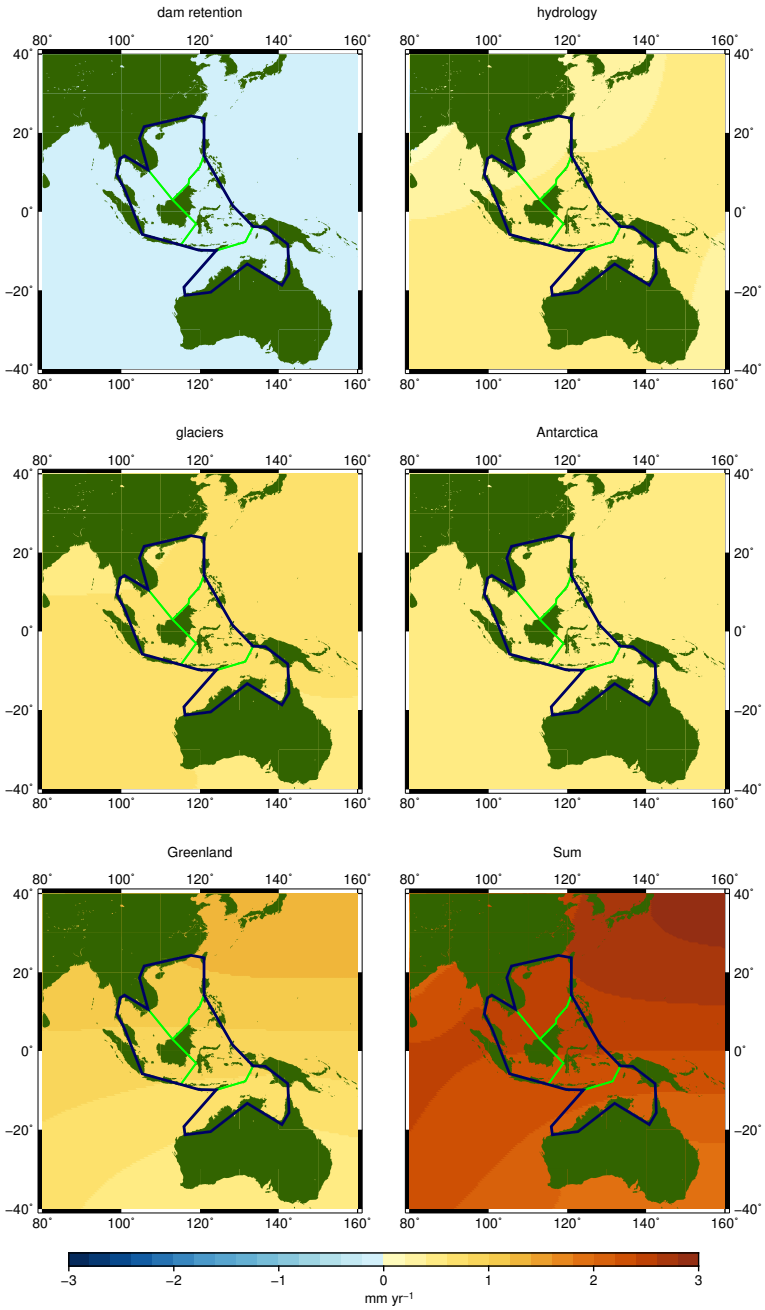

Figure 3.6: Absolute sea-level trends between January 2005 - December 2012 computed from five present-day mass change contributions. In the last figure the sum of all contributions.

3.3.7 Nodal cycle

The effect of the lunar nodal cycles on absolute sea-level trend estimates has not been considered previously for the TAS and surrounding regions. The amplitude of

the nodal cycle at the Equator is approximately 7 millimeters. Since the length of our time series is 8 years and the period of the nodal cycle is 18.61 years, we only capture a part of the cycle, which can introduce mass trends at the millimeter-per-year level.

We evaluate the nodal cycle at the epochs of GRACE. According to *Proudman* (1960), the nodal cycle has a minimum at the equator at the reference time $t_0 = 2006.45$. The mean sea level $\bar{h}_{NC,t}$ caused by the nodal cycle at time t is then given as:

$$\bar{h}_{NC,t} = \bar{\Omega}\cos(2\pi(t - t_0)), \tag{3.19}$$

where $\bar{\Omega}$ is the average amplitude over the considered region. We follow the equilibrium equations of *Proudman* (1960) to compute the amplitude Ω

$$\Omega = \alpha(1 + k_2 - h_2)(3\sin^2(\theta) - 1), \tag{3.20}$$

in which θ is the latitude, α is the tidal magnitude, set to 8.8 mm following Woodworth (2012), and the tidal Love numbers are $k_2 = 0.36$ and $h_2 = 0.60$ as in (*Frederikse et al.*, 2016). Using the approach described in *Woodworth* (2012) and *Frederikse et al.* (2016), geoid changes resulting from the applied load are computed using the sea-level equation from Sect. 3.3.6. Adding the geoid changes to the mass change signal induced by the tide gives the amplitude of the geocentric sea-level response to the nodal cycle, as is given in Fig. 3.7, which should be used to correct altimetry. The geoid response to the nodal cycle is less than 10 % of the nodal cycle load.

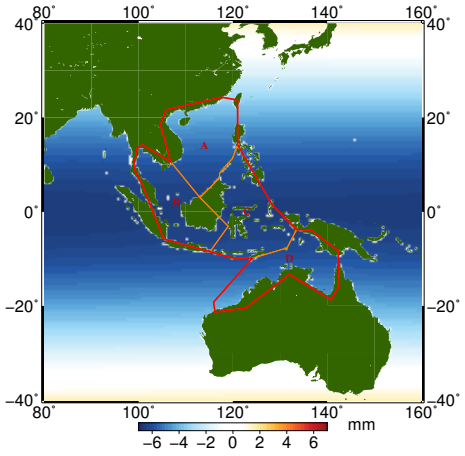

Figure 3.7: Amplitude of the Nodal cycle in the TAS region. Positive values correspond to a peak in the nodal cycle in 2006. Negative amplitudes indicated a minimum in 2006.

3.4 Results

First, we compare the statistically weighted time series from Sect. 3.3.4 with the unweighted time series from GRACE, altimetry and the reanalyses. Then we discuss the behavior of mass and steric sea level in the four TAS regions. In Sect. 3.4.2 we remove the semi-annual and annual cycles and we relate steric sea level and mass to the two PCs of wind stress and Dipole Mode Indices (DMI). In Sect. 3.4.3, we regress the steric and mass components to PC1, PC2, and DMI to examine possible oceanic influences on the estimated trends. In addition for the mass component, we will relate the trends to the nodal cycle and absolute sea-level trends obtained from mass redistribution fingerprints. Lastly, the TAS contribution to GMSL rise is estimated.

3.4.1 Time series

In this section we compare the unweighted and statistically-weighted (Eq. 3.15) mass and steric time series and describe their variability in each TAS region.

Statistically-weighted time series

In Fig. 3.8 time series of mass, steric and total sea level for the four regions are given. The seasonal cycle of the total sea level are captured by both methods (altimetry and GRACE+reanalyses) in the South China Sea region. When the two methods differ, the statistical optimal time series tends to lie between the two time series. This suggests that the error bars of altimetry and GRACE+reanalyses are on the same order of magnitude. The GRACE mass time series shows a more pronounced annual cycle than altimetry-reanalyses, which appears to be noisier. In the South China Sea region, the reanalysis sea-level estimates do not correlate well with the altimetry measurements (*Balmaseda et al.*, 2013; *Zuo et al.*, 2015) and the noise of the altimetry-reanalysis time series is relatively large. The statistical-weighted time series therefore follows more closely the GRACE time series. Both steric sea-level time series (reanalysis and altimetry-GRACE) already matched well, so the statistically weighted one overlaps with both. Note that there are some Argo floats present in this region that helped to constrain the reanalysis products.

In the Thailand-Java region total sea level estimated from GRACE+reanalyses departs from altimetry in the first three years of the time series. This is caused by the effect of post-seismic deformation of the Earth due to the Sumatra-Andaman earthquake, hence, the error model of GRACE was not correct. The statistically-weighted mass time series for the region closely follows GRACE at the end of the time series, but the opposite is true in the first three years, as a consequence of the increased error in GRACE mass estimates as decribed in Sect. 3.3.2. The statistically-weighted steric signal in the bottom plot for Thailand-Java follows the reanalyses, because the altimetry-GRACE steric time series is relatively noisy. We must note that large fresh water fluxes from the Mekong might also reduce the quality of reanalyses steric sea-level estimates, because they are poorly constrained due to a lack of in-situ

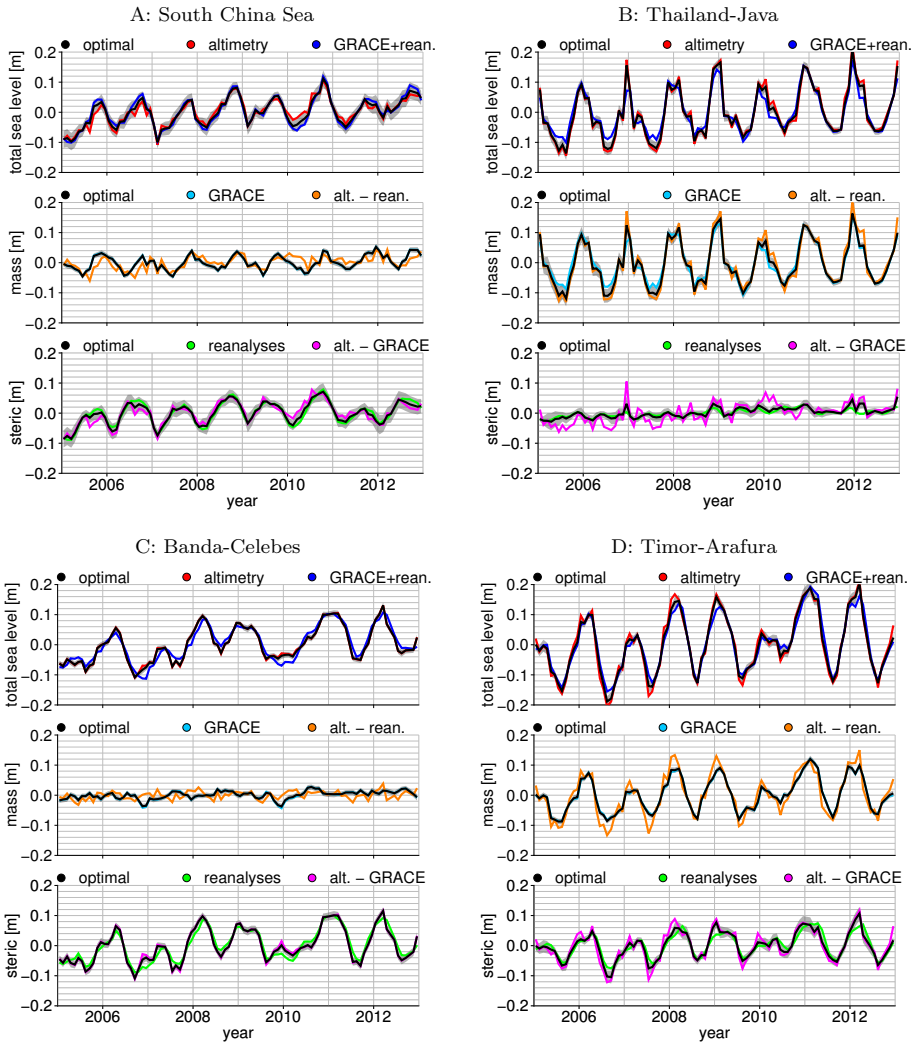

Figure 3.8: Time series of total and steric sea level and mass for the four regions with the annual cycle retained. In this figure the term 'reanalyses' indicates the steric sea level obtained from reanalyses, in order to avoid confusion with the term 'steric' used to indicate statistically-weighted steric sea level. Top: total sea level from altimetry in red, from GRACE+reanalyses in blue and the optimal solution in black. Middle: mass from GRACE in lightblue, from steric-corrected altimetry in orange and the optimal solution in black. Bottom: steric sea level from the reanalyses in green, from altimetry-GRACE in purple and the optimal solution in black.

salinity measurements (*Balmaseda et al.*, 2013).

In the seas of Banda-Celebes, both altimetry and GRACE+reanalyses capture the interannual and annual signals. The statistically weighted time series closely resembles the altimetry time series, because it has relatively small error bars due to short correlation scales. Mass is fully explained by GRACE, so altimetry-reanalyses has barely any influence on the statistically weighted time series. The statistically

weighted steric signal is primarily constrained by altimetry-GRACE, due to larger discrepancies between reanalyses compared to the previous two regions, which inflates the error.

In the Timor and Arafura seas the interannual variability appears to be captured by all time series, but there are discrepancies in the annual cycle. There are substantial observable differences in the annual cycle of mass. The weighted time series for the mass signal closely resembles the GRACE time series, because the errors on the altimetry-reanalyses time series are larger. With the exception of a few peaks,we observe only minor differences between the steric sea-level time series. The statistically weighted steric sea-level time series is closer to altimetry-GRACE than the reanalyses.

Mass and steric variability

Sea level variability in the South China Sea is dominated by the steric component (Fig. 3.8) and as demonstrated in Sect. 3.3.3 this primarily reflects changes in temperature. There is also an annual signal in mass, but this is approximately a factor of two smaller than that of the steric signal, which is several centimeters in amplitude.

Much larger annual cycles in sea level are found in the Thailand-Java region of approximately a decimeter. In contrast with the South China Sea, the largest fraction of the variability is the mass component, indicating a seasonal mass flux component into this basin. The mass signal might have a steric origin, originating from the nearby deep ocean. The seasonal steric component is weak because the region is shallow, which limits thermal expansion, and temperature changes are small over the year, which is evident in the sea surface temperature (*Knudsen et al.*, 1996).

The sea-level time series of the deeper Banda-Celebes region exhibit a small annual cycle compared to Thailand-Java. The annual cycle in steric sea level is however larger than that of Thailand-Java, but the annual cycle in sea surface temperature is comparable as shown by *Knudsen et al.* (1996). Since the water column is deeper, it is able to expand more in response to comparable heating than the Thailand-Java region. The interannual variability is primarily caused by the steric signal.

The largest sea-level variability in the TAS occurs in the Timor and Arafura seas, which are deeper than Thalland-Java and shallower than the other two regions. The variability is a combination of mass fluctuations and temperature changes. The annual cycle in sea level in this region is among the highest in the world (*Vinogradov et al.*, 2008). The annual cycle in the steric time series is several centimeters in amplitude and the mass signal is slightly larger. Note that the interannual variations (for example smaller peaks in 2007 and 2010, coinciding with El Niño events) in the steric and mass signals is comparable. Additionally, the steric time series in Banda-Celebes strongly resembles the mass time series of Timor-Arafura. This suggests that there is a dynamic coupling between the two regions, perhaps as a consequence of the large steric sea-level fluctuations in Banda-Celebes (*Landerer et al.*, 2007; *Bingham and Hughes*, 2012), or the signals have the same driver. In the following section this will be discussed further.

3.4.2 Interannual variability

We next consider possible drivers of interannual sea-level variability in the TWS by regressing steric and mass components to equatorial wind stress (PC1 and PC2) and processes associated with the DMI.In Fig. 3.9, we show the PC1, PC2 of the equatorial wind stress, and the DMI regressed through the steric and the mass components. Before regression, the nodal cycle is removed from the mass time series, which is also plotted as a black dotted line. The trend, the annual and the semi-annual signals are regressed together with the indices and removed from the steric and mass time series. In Table 3.3 we have computed the Coefficients Of Determination (COD) for each of the indices and the sum of them. These CODs represent the ratio of the variances of the regressed index and the mass or steric time series after removing the trend, the nodal, the annual and the semi-annual cycles. The last three columns of Table 3.3 show the p-values of the regressed indices. We also investigate the source of the mass fluctuations in the TAS by looking at correlations with steric sea level in the surrounding oceans.

Regional effects

For the South China Sea, the region farthest from the equator, only a small fraction of mass and steric sea level is explained by the indices. PC1 and the DMI explain a small fraction of the mass variability and have a significant p-value, while PC2 explains a small fraction of the steric variability. Combining the regressed indices shows that only 20% of the variability of the steric signal is explained by PC1, PC2 and the DMI, and that this is even lower for the mass signal. As visible in Fig. 3.9, there is still substantial interannual variability in steric sea level.

In the shallow Thailand-Java region, the steric variability is small compared to the South China Sea. Nevertheless, a substantial fraction (COD of 0.42) of the steric signal is explained by the DMI. The regressed PC1&2 indices are insignificant as indicated by their p-values. A negative (at the end of 2006) and a positive peak (at the end of 2010) are visible in the regressed DMI time series in Fig. 3.9, which correspond respectively to positive and negative peaks in the DMI of Fig. 3.4. This is in line with *Meyers et al.* (2007), who showed that a positive temperature anomaly, causing a steric response, is present during negative DMI. The mass signal in this area is much larger than the steric signal and it is driven primarily by PC1 for which the COD is 0.55. ENSO, which is in-phase with PC1, appears locally as a steric phenomenon which manifestates itself in the WTPO as a deepening of the thermocline during the La Niña phase and with temperature anomalies above as well as below the thermocline (*Zheng et al.*, 2015). We argue that during the La Niña phase water flows into the shallow areas down a pressure gradient established by a large steric response in surrounding deeper area. We will return to this point in Sect. 3.4.2. The opposite occurs during El Niño. An additional fraction of the interannual variability in the Thailand-Java region is explained by PC2, which suggests that during the recovery phase of La Nina, the mass anomaly is positive. The effects of DMI on the mass in Thailand-Java are small, but still a significant regression coefficient is found.

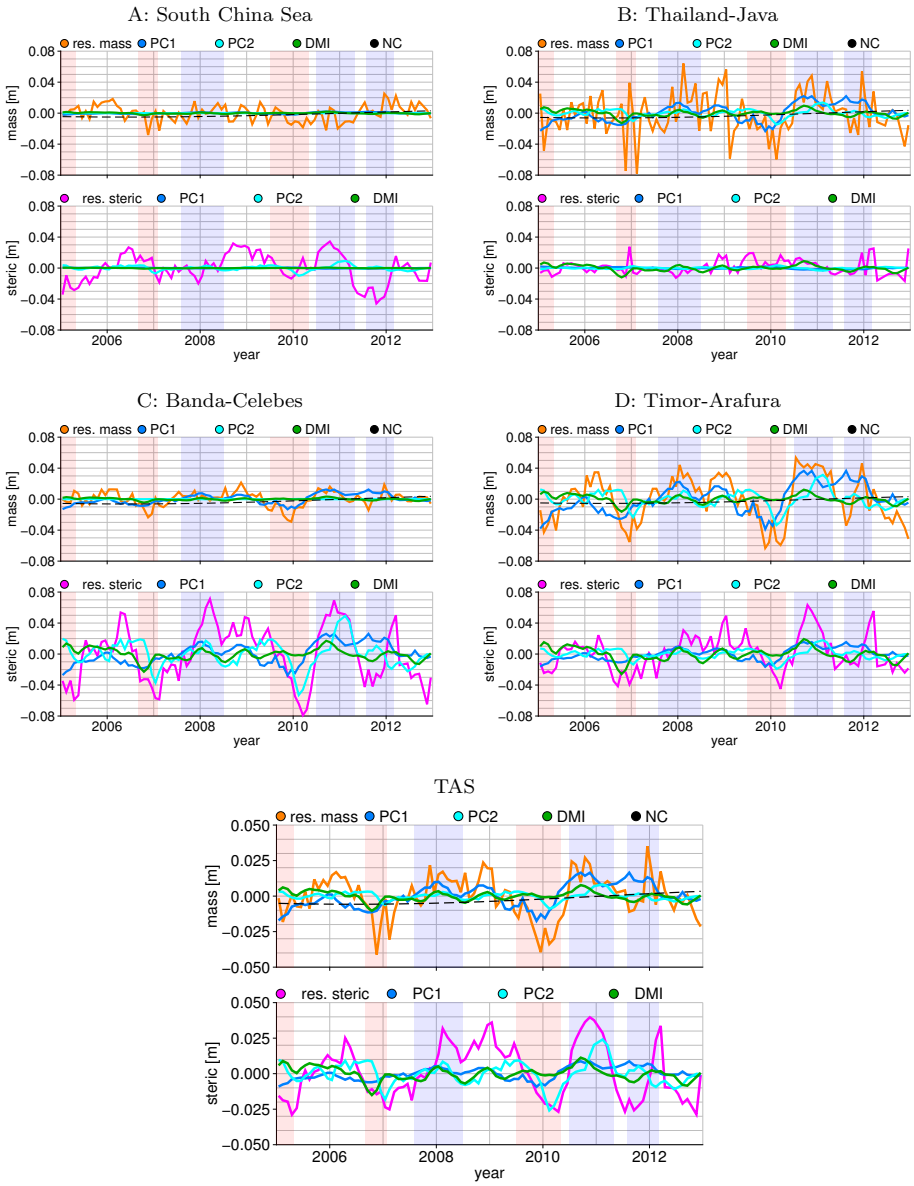

Figure 3.9: Time series of mass (top) and steric sea level (bottom) between January 2005 - December 2012 with annual and semi-annual signals removed. The time series for the TAS are computed as area-weighted averages of the individual regions. In blue the regression of PC1, in lightblue PC2, and in green the DMI. The subtracted nodal cycle is shown as a black dotted line. The red and blue shades indicate respectively El Niño and La Niña states.

The Banda-Celebes seas exhibit only small mass variations at interannual time scales, which are most related to PC1. Note that the mass variations are almost in-phase with those of Thailand-Java, but that the regression with PC2 is insignificant. The interannual steric variability is largest in the region, which is expected as the

Table 3.3: Coefficients of determination for the indices (individually and combined) regressed through the mass and steric time series between January 2005 - December 2012 for the four regions. The regions South China Sea, Thailand-Java, Banda-Celebes and Timor-Arafura are respectively indicated with A, B, C and D. The last three columns indicate the p-value. In italic are the coefficients that are not significantly different from zero based on a 5 % significance level. *The column 'Total' is the COD of the multilinear regression time series of the three indices, which is not equal to the sum of the individual CODs.

		COD				p-val		
		PC1	PC2	DMI	Total*	PC1	PC2	DMI
Steric	A	0.03	0.19	0.01	0.20	*0.37*	0.00	*0.42*
	B	0.16	0.14	0.42	0.44	*0.12*	*0.06*	0.00
	C	0.53	0.50	0.21	0.70	0.00	0.00	0.00
	D	0.49	0.29	0.37	0.64	0.00	0.00	0.00
	TAS	0.35	0.48	0.27	0.63	0.00	0.00	0.00
Mass	A	0.14	0.01	0.08	0.16	0.03	*0.42*	0.05
	B	0.55	0.18	0.14	0.56	0.00	0.00	0.00
	C	0.77	0.01	0.12	0.77	0.00	*0.44*	0.00
	D	0.82	0.35	0.16	0.84	0.00	0.00	0.00
	TAS	0.73	0.18	0.20	0.73	0.00	0.00	0.00

region is deep, which allows the water column to expand more at equal temperature increases. We find significant regression coefficients for all indices for the steric time series, but most of the signal is explained by PC1 and PC2. Because we find negative regression coefficients (not shown) for both PCs and PC1 is in-phase with the Niño 3.4 index, while PC2 responds just out-of-phase, we argue that the steric signal in Banda-Celebes is sligthly delayed with respect to ENSO. The DMI also has an influence (COD of 0.20), which agrees with the temperature patterns found by *Meyers et al.* (2007).

The southernmost Timor-Arafura region exhibits the largest interannual variability, of which mass represents the largest fraction as is visible in Fig. 3.9. All of the regressed indices are significant in this region, as shown by their p-values. The individual COD for the regressed PC1 is 0.82, with a negative regression coefficient this means that the mass anomaly is positive when PC1 is negative. Since this is a relatively shallow area, water is expected to move into the Timor-Arafura region at the moment of La Niña from a region with a large steric response, a comparable effect as for the mass signal in Thailand-Java. Note that at the Fremantle tide gauge, located farther south along Australia's west coast, correlations between sea level and ENSO are observed as well (*Feng et al.*, 2004). Also PC2 has a large COD, which means that the water inflow is slightly delayed with respect to ENSO, which is in-phase with PC1. The steric signal in the Timor-Arafura region is in-phase with the mass signal. Table 3.3 shows that PC1&2 represent a smaller fraction of the steric signal compared to that of the mass and that the DMI is responsible for a large fraction of the variability, although it is still smaller than PC1. Again, this is in line with the sea surface temperature patterns in *Meyers et al.* (2007) as discussed in Sect. 3.3.3.

Remote steric effect

Interannual steric variations summed over the entire TAS correspond primarily to the steric signals in the Banda-Celebes region and the South China Sea. Based on the CODs, PC2 is responsible for the largest part of the steric signal, which indicates the highest and lowest temperatures are found just after La Niña and El Niño events, respectively. Table 3.3 indicates that we can explain about 63 percent of the steric signal for the whole TAS. The interannual variability of the mass signal, which is primarily linked to the Timor-Arafura and Thailand-Java regions, is slightly smaller, but about 73% is explained by the regressed indices of which PC1 respresents by far the largest fraction. While the steric signal can be explained by temperature changes of the water within the TAS, a flux of water is required from outside the TAS to account for the area-weighted mass signal.

In Fig. 3.10, we investigate the origin of the interannual mass fluctuations further. The steric sea-level fluctuations outside the TAS are higher than within. In the deep ocean this would indicate a geostrophic circulations, which causes a balance between the Coriolis force and the pressure gradient. However, we hypothesize that the TAS continental shelf acts like a barrier, which affects balance. This can cause a mass flux on to the continental shelf, which we will refer to as the remote steric effect. Therefore, steric sea level in the surrounding regions of the TAS is computed from interpolated Argo grids (*Roemmich and Gilson*, 2009) (so that they are independent from the reanalyses used in this study) as is done in Sect. 3.3.3, from a reference depth of 1500 dBar. We then compute the difference of steric sea levels in the surrounding regions at each grid point with the mean steric sea level in the TAS. The correlation of these steric sea-level differences with the mass time series in the TAS is depicted in the top-left panel of Fig. 3.10. We find a significant correlation across a large section of the WTPO, indicating that the steric sea level in this region drives a mass flux into the TAS. A small region of high correlation appears near the equator in the Indian Ocean, which may be associated with DMI-related fluctuations. We repeat the calculation using mass from the Timor-Arafura region, where the mass component is strongest, instead of the entire TAS. We find a similar correlation pattern as for the entire TAS (bottom-left panel, Fig. 3.10), but with weaker correlations with the Indian Ocean steric variations, as expected from the lower COD. Comparable, but slightly weaker correlation patterns are found for the Banda-Celebes and Thailand-Java regions (not shown). For the South China Sea, we find correlations of maximally 0.4 in the WTPO, but the patterns looks significantly different (not shown).

To confirm that ENSO is the principal driver of steric sea-level variations in the region, we repeat the analysis but regress and remove PC1 (middle panels, Fig. 3.10), and PC1 and PC2 from the steric height differences (right panels, Fig. 3.10). For the whole TAS, correlations with PC1 removed are reduced from 0.6-0.7 to 0.4 to 0.5 in the WTPO. For the Timor-Arafura region, the correlation is even further reduced to typically around 0.3-0.4 in the WTPO. Reductions in correlation by removing PC1 are also present when considering the mass signals in Thailand-Java and Banda-Celebes regions, but barely for the South China Sea (not shown).

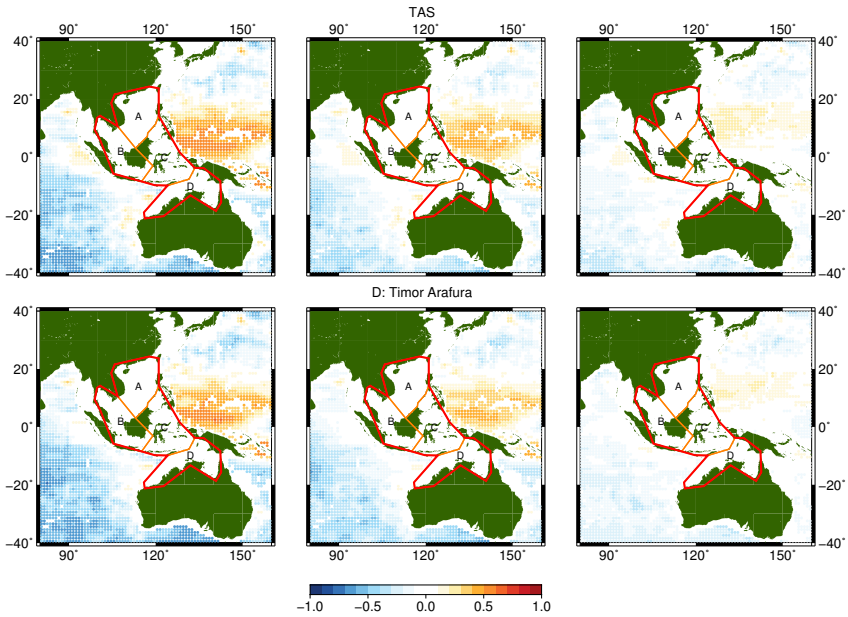

Figure 3.10: Correlation of relative steric sea level (i.e. the steric sea level minus the mean steric sea level in the TAS), surrounding the TAS with the mass in the TAS. Left: Full signal. Middle: PC1 removed. Right: PC1&2 removed.

The correlations drop considerably lower (<0.2) with the inclusion of PC2 (right panels, Fig. 3.10). For the Timor-Arafura seas comparison, correlations are near zero across the WTPO. Similar results are found for the mass in Thailand-Java, while for the Banda-Celebes region a substantial amount of correlation is still present. After removing PC1&2 from the relative steric sea level, the correlation between mass in the South China Sea is virtually unchanged.

In conclusion, mass changes in the TAS are linked to steric sea-level changes in the WTPO. The steric changes in the WTPO are driven by ENSO. Both PCs of the equatorial wind stress are required to remove the largest part of the correlation between mass in the TAS and WTPO. Since PC2 is required, it appears that the dynamic response of the mass is slightly delayed with respect to El Niño and La Niña. Only the mass signal in the South China Sea appears to be decoupled from the first two PCs of the equatorial wind stress.

3.4.3 Trends

Interannual ocean dynamics strongly affect trends computed from short time series and the estimated trends therefore do not provide a proper indication for what happens to sea level on time-scales longer than the considered eight years. We therefore investigate the effects of including indices of ocean dynamics in the regression on the estimated trend from the statistically-weighted steric and mass time series. The trends and their errors are computed using weighted least squares, by propagating

the errors obtained from Eq.3.16 in Sect. 3.3.4. For the mass time series specificially, we also take into account the nodal cycle. Eventually for the mass time series, we compare the trends after removing the nodal cycle and with the regression of the indices to those obtained from mass redistribution fingerprints. In Table 3.4 the estimated steric sea level trends are given, which are computed over the period January 2005 - December 2012. The same is performed for the mass trends and those are given in Table 3.5. In the last three columns the 'negative' regression trends for the three indices are provided, to give an indication how indices affect the trends. A positive value for the regression trends therefore indicates a positive effect on the estimated trend. The regression trends are computed with ordinary least-squares through the PC1, PC2 and DMI regression time series, as given in Fig. 3.9. Summing them gives a different value than the difference between the trends regressed with and without indices, because correlations are not taken into account.

Regional trends

The total steric trend in the South China Sea of 5.3 mm yr^{-1} is about twice as large as the the mass trend of 2.8 mm yr^{-1}. By removing the contribution of the nodal cycle the mass trend reduces by 1.2 mm yr^{-1}. Both tables indicate that the effect of regressing indices has a minimal effect on the estimated mass and steric sea-level trends in the South China Sea region. This is expected, because the CODs of the time series of the indices, given in Table 3.3, are only 0.20 and 0.16, respectively.

In the shallow Thailand-Java region comparable trends are found for mass and steric sea level between 4-5 mm yr^{-1}. The nodal cycle reduces the mass trend to 3.4 mm yr^{-1}. While the steric sea-level trend increases by regression with the indices, primarily as a result of the DMI, the mass trend decreases further due to PC1. The negative effect of PC1 on the trend is the compensation for the high amplitude La Niña event relatively late in the time series (*Boening et al.*, 2012), which affects the mass in Thailand-Java area as discussed in the previous section. PC2 and the DMI have a small positive effect on the mass trends.

The Banda-Celebes seas exhibits by far the largest steric sea-level trend in the TAS, even after the regression with the indices. It is again the negative trend of PC1 that causes this reduction, while part of the trend is recovered by the other two indices. In contrast to steric sea level, the mass component exhibits the smallest trend of the four regions. After removing the nodal cycle and regressing with the indices there is no significant mass trend left.

In the Timor-Arafura region, a larger mass than steric trend is present. After the removal of the nodal cycle, the mass trend still remains significantly (two standard deviations) larger than the steric trend. The ocean dynamics have no influence on the steric trend, because PC2 and the DMI compensate loss of trend caused by the regression of PC1. The mass trend is reduced to 3.6 mm yr^{-1} by regressing indices, which remains the largest mass trend in the TAS.

The steric trend averaged over the whole TAS is about 2 mm yr^{-1} larger than the mass trend. There is a insignificant reduction of the steric trend to 6.1 mm yr^{-1} when

Table 3.4: Steric sea-level trends in mm yr^{-1}. The four regions South China Sea, Thailand-Java, Banda-Celebes and Timor-Arafura are respectively indicated with A, B, C and D. The second column 'Total' shows the trend without regressing the indices. The third column 'Ind rem.' show the trend with regressing the indices. In the last three columns we indicate the regression trends of the indices.

	Total	Ind rem.	PC1	PC2	DMI
A	5.3±0.5	5.4±0.6	0.1	0.1	0.0
B	4.3±0.3	4.8±0.4	0.2	-0.0	0.3
C	9.6±0.3	8.2±0.4	-2.9	0.7	0.5
D	4.5±0.4	4.5±0.4	-1.7	0.3	0.6
TAS	6.4±0.3	6.1±0.4	-1.0	0.3	0.3

Table 3.5: Mass trends in mm yr^{-1}. The four regions South China Sea, Thailand-Java, Banda-Celebes and Timor-Arafura are respectively indicated with A, B, C and D. The second column 'Total' shows the trend without regressing the indices. The third column 'NC rem.' provides the trend after removing the nodal cycle. The fourth column 'Ind rem.' shows trends after removal of the nodal cycle and with regression of the indices. In the fifth column 'FP' the estimated trends from mass redistribution fingerprints is given. In the last three columns we indicate the regression trends of the indices.

	Total	NC rem.	Ind rem.	FP	PC1	PC2	DMI
A	2.8±0.2	1.8±0.2	1.6±0.2	2.5	-0.2	0.0	0.1
B	4.9±0.4	3.4±0.4	2.3±0.5	2.4	-2.5	0.2	0.3
C	2.5±0.2	1.2±0.2	-0.1±0.2	2.4	-1.4	-0.0	0.1
D	7.7±0.2	6.6±0.2	3.6±0.3	2.2	-4.1	0.5	0.4
TAS	4.5±0.2	3.1±0.2	2.0±0.2	2.4	-1.8	0.1	0.2

the indices are regressed. Removal of the nodal cycle and regression of the indices lowers the mass trend to 2.0 mm yr^{-1}, about one-third of the remaining steric trend.

Comparison to mass redistribution fingerprints

Once the major ocean dynamic signals (PC1&2 and DMI) are removed, the residual mass trends are compared to the sum of the mass fingerprints. The mass redistribution fingerprint trends for the individual regions are given in the fifth column 'FP' of Table 3.5. For the whole TAS the yearly sea-level time series of the mass redistribution fingerprints are shown in Fig. 3.11. As visible in the figure, the trend of the fingerprints is close (within the 95% confidence interval) to the observed changes. Based on this correspondence, we infer that the net flux of water mass, after removing the ocean dynamics and mass redistribution effects, through the boundaries of the TAS is statistically insignificant. Table 3.5 shows that there is a positive discrepancy with respect to the fingerprints in the shallow Timor-Arafura region and negative discrepancies in the deep regions. Since the water influx into the TAS is statistically insignificant, this suggests mass exchange between the deep and shallow regions within the TAS, especially between Banda-Celebes and Timor-Arafura.

Time series of the individual fingerprints (Fig. 3.11, bottom panel) show that over the considered time period, Greenland ice loss is the largest contributor to mass trends in the region, followed by continental glacier melt. Not only does the Green-

land ice sheet have the largest mass loss, but its location far away from the TAS increases the contribution with respect to the glaciers and Antarctic melt. Furthermore, while the glaciers contribute spatially quite homogeneously to the trends in the TAS (Fig. 3.6), the contributions of Antarctica and Greenland vary primarily from north to south. The meridional gradient of the Greenland fingerprint is particularly evident, with approximately a 0.3 mm yr^{-1} trend difference between the South China Sea and the Timor-Arafura regions.

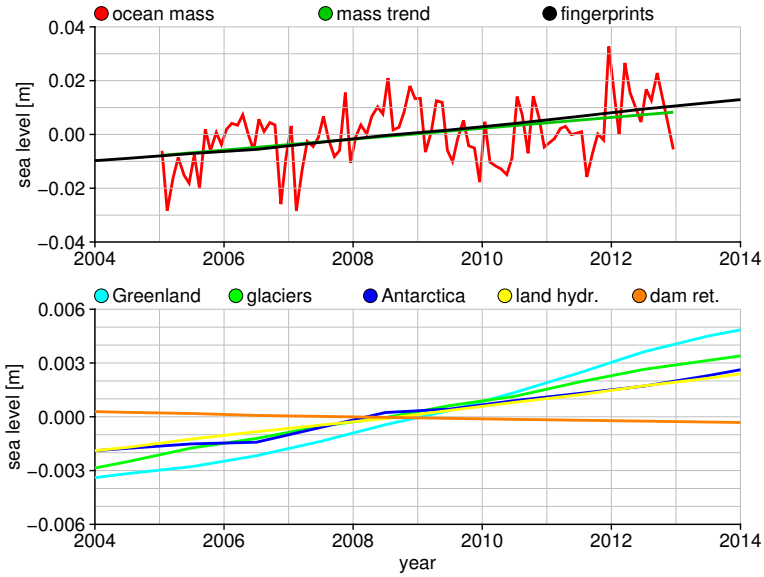

Figure 3.11: Top: In red the sea-level time series (m) for the whole TAS region, after removing the contributions of the regressed PC1&2 and DMI indices, the nodal cycle and the annual and semi-annual cycles. In black the sum of the mass fingerprints. Bottom: The fingerprint time series of Greenland, glaciers, Antarctica, dam retention and land hydrology respectively in lightblue, green, blue, yellow and orange.

3.4.4 Contribution to global mean sea-level rise

To determine the contribution of the TAS to global sea level, we first estimate the global mean mass and steric sea-level trends. Then the differences between the TAS trends and the global trends are computed. An estimate of the contribution of the differenced trends $\Delta t_{relative}$ is then computed using the ratio between the surface area A_{TAS} of the TAS and the rest of the oceans $A_{global} - A_{TAS}$, such that

$$\Delta t_{global} = \frac{A_{TAS}}{A_{global} - A_{TAS}} \Delta t_{relative}, \tag{3.21}$$

is the effect of including the TAS into global ocean budgets. This approach is applied for both the mass and the steric components.

The global mean steric sea level and global mean mass time series are obtained

from the NASA website (*Llovel et al.*, 2014; *Watkins et al.*, 2015). The global mean steric sea level is computed from Scripps temperature and salinity grids (*Roemmich and Gilson*, 2009), in which the TAS region is completely excluded. A 3° × 3° mascon solution is used to construct the global mean mass time series, which includes several cells within the TAS region. Since the effect of the mass in the TAS on the global mean mass trend is only a fraction of the mass trend in the TAS itself, this will not significantly affect the outcome of the computation. The time series trends are computed between January 2005 - December 2010 for comparison with other studies, which results in 0.1 mm yr^{-1} for the steric trend and 1.6 mm yr^{-1} for the mass trend. The trends over the period January 2005 - December 2012 are statistically similar to the trends over the shorter period.

The TAS trends derived from the statisticaly-weighted time series are 8.2 mm yr^{-1} for the steric component, and 4.2 mm yr^{-1} for the mass component (Table 3.6, Col. 1). Taking the difference between the TAS and global trends estimated above (Table 3.6, Col. 2), we compute that the TAS contribution is 0.2 mm yr^{-1} for global steric and 0.1 mm yr^{-1} for global mass. Because the ratio of the surface area of the TAS and the global ocean is small, the error bars on the contribution to the global estimates are small and therefore they are not provided in the table.

Based on the ORAS4 reanalyses, *Dieng et al.* (2015) estimated that the global mean steric sea level is underestimated by approximately 0.25 mm yr^{-1} over the period January 2005 - December 2013. Even though we computed the value over a slightly shorter period, our estimate of 0.2 mm yr^{-1} is close to this value. They did however not discus the effect of the 300 km cut-off from the coast in GRACE global mass, which was based on the time series of *Johnson and Chambers* (2013). A 300 km cut-off effectively removes the whole TAS contribution from the global solution. We estimate that excluding the TAS in global mass estimates causes underestimation of 0.1 mm yr^{-1}. Combining both numbers gives a trend of 0.3 mm yr^{-1}, which is consistent with the 0.5±0.2 mm yr^{-1} computed by *Von Schuckmann et al.* (2014).

3.5 Conclusions

For the first time satellite altimetry, satellite gravimetry and reanalysis data are used to determine the steric and mass components of sea-level variations in the TAS. To study the sea-level variability in the TAS in more detail, time series of the sea-level components are computed for four regions. The uncertainties of the time series of total sea level from altimetry, mass from GRACE and steric sea level from reanalyses, are used to derive a statistically optimal separation between the steric and mass components. The statistically weighted time series are used to study the interannual variability and trends in the TAS, as well as their contribution to global mean sea level.

The largest variability in steric sea level is found in the deeper areas as the South China Sea and the Banda-Celebes seas. The small water column of the Thailand-Java and Timor-Arafura regions is not able to expand as far as the other two. In constrast, the largest mass signals are present in the shallower regions. We argue that this is a

Table 3.6: Contribution to GMSL over January 2005 - December 2010 in mm yr^{-1}. The first column contains the trends in the TAS. The second column contains the relative trends with respect to the global estimates. The last column shows the contribution to the global budget.

	TAS only	TAS-Global	Global contr.
Sum	12.4	10.7	0.3
Steric	8.2	8.1	0.2
mass	4.2	2.6	0.1

dynamical response to larger steric sea-level fluctuations in neighbouring areas.

Regression with the first two PCs of the equatorial Pacific wind stress and the DMI showed that the South China Sea largely is unaffected by ENSO and Indian Ocean dipole dynamics. The steric sea level in the Banda-Celebes and Timor-Arafura seas is strongly driven by PC1&2, which are used to represent wind forcing that is either in phase with ENSO (PC1), or peaked around the southward shift of anomalous winds (PC2). The DMI has a small effect on the temperatures in Thailand-Java and causes a substantial fraction of (thermo-)steric variability in Timor-Arafura. Mass signals in the shallow areas are almost 180 degrees out-of-phase with PC1. PC2 shows a strong contribution, especially in the Timor-Arafura region. We believe that the shallow region mass changes, which dominate the total mass change in the TAS, are due to a net transport from the neighboring WTPO to the shallow regions associated with variations in WTPO steric sea level, which are related to PC1&2.

Accounting for interannual variations associated with the PC1, PC2, and DMI indices impacts the estimation of linear trends. Regressing PC2 and the DMI through the time series for the whole TAS region, has a slight positive effect on the mass and steric trends, while regressing PC1 reduces the trends. This leads to a reduction in mass and steric trends. The mass trends are also affected by the nodal cycle, because it causes a mass change with a mimimum in 2006 and a maximum in 2015. Trends decrease with approximately 1.3 mm yr^{-1} when correcting for the nodal cycle.

The mass trend over the whole TAS is statistically consistent with the trend estimated from mass redistribution fingerprints. However, within the four regions there are differences: the deep regions have smaller mass trends than their fingerprint estimates, while in the Timor-Arafura region we find larger trends than its fingerprint. We argue that there is an internal redistribution of water within the TAS, where water flows from deep regions with a large steric response into the shallower regions.

Finally, we computed trends for the whole TAS and estimated the contribution to the global budgets. Omitting the TAS results in an underestimation of the mass and steric components with 0.1 and 0.2 mm yr^{-1}, respectively. These numbers are in line with previous studies.

Our approach for separating mass and steric contributions to sea-level changes can be applied to other basins where Argo float coverage is limited, such as the Caribbean Sea, the Gulf of Mexico and the Yellow Sea. To investigate the drivers of mass and steric sea-level variability, appropriate indices should be used.

Chapter 4

A comparison of data weighting methods to derive vertical land motion trends from GNSS and altimetry at tide gauge stations

4.1 Introduction

Tide Gauges (TGs) measure local relative sea level, which means that they observe sea level, but also Vertical Land Motion (VLM). Knowing VLM at TGs is essential to convert the observed sea level into a geocentric reference frame, in which among others satellite altimeters operate. The mean of VLM at TGs is not equal to that of the basin, and therefore local VLM estimates are required to get an accurate estimate of ocean volume change. The models for large scale far-field VLM processes, such as Glacial Isostatic Adjustment (GIA) and the elastic response of the Earth due to present-day mass redistribution, are becoming more accurate. TGs are often only corrected for the GIA signal, which typically reaches values of 10 mm yr^{-1} in Canada and Scandinavia (*Gutenberg et al.*, 1941). The elastic deformation due to present-day mass redistribution is often ignored. However, elastic deformation is becoming larger due to the increasing rate of Greenland's ice mass loss, and to a lesser extent due to other processes. Trends at TGs are also affected by a large number of other local signals, including water storage, postseismic deformation and anthropogenic activities (*Hamlington et al.*, 2016; *Wöppelmann and Marcos*, 2016). Since the local VLM processes cannot be captured by models, and the large-scale processes contain large uncertainties, measuring VLM at TGs is indispensable.

One method to estimate VLM at TGs uses geodetic Global Positioning System (GPS) antennas at fixed locations or Doppler Orbitography and Radiopositioning Integrated by Satellite (DORIS) observations. Since many other navigation satellites are currently providing range estimates as well, we will refer to the GPS stations as Global Navigation Satellite System (GNSS) stations. Most studies compute GNSS

Parts of this chapter have been been published as: Kleinherenbrink, M., Riva, R., & Frederikse, T. (2018). A comparison of data weighting methods to derive vertical land motion trends from GNSS and altimetry at tide gauge stations, Ocean Science, doi:10.5194/os-14-187-2018.

VLM at TG stations from one of the datasets by University of La Rochelle (ULR) (*Wöppelmann et al.*, 2007; *Pfeffer and Allemand*, 2016; *Wöppelmann et al.*, 2014; *Wöppelmann and Marcos*, 2016). Even though the ULR database contains several GNSS solution inland, its main focus is the coastal zone. Currently, 754 GNSS stations are processed in the ULR6 database. A more extensive database with approximately 14000 GNSS is processed by the Nevada Geodetic Laboratory (NGL). They use a different processing procedure to estimate trends from time series, which makes trends less vulnerable to jumps (*Blewitt et al.*, 2016). A statistical comparison between several GNSS solutions was recently made by *Santamaría-Gómez et al.* (2017). They concluded that the number of stations in the NGL database was larger, but that trend differences between neighboring stations were significantly larger than the Jet Propulsion Laboratory (JPL) and ULR6 trend estimates. They also discussed systematic errors due to differences in the origin of the reference frames, which were on the order of 0.2 mm yr^{-1} globally. Furthermore, they found that the error of VLM estimates increases with an increasing distance between the tide gauge and the GNSS station. Globally averaged, the error increased with 4×10^{-3} mm yr^{-1} km^{-1}. Most studies use the trends of either co-located GNSS stations or the closest GNSS station or the (weighted) mean of all GNSS stations within a radius of several tens of kilometers (*Santamaría-Gómez et al.*, 2014; *Pfeffer and Allemand*, 2016). Only *Hamlington et al.* (2016) involved a more complex GNSS post-processing procedure using NGL trends, based on a combination of spatial filtering, Delaunay triangulation and median weighting. One way to quantify the accuracy of GNSS-based VLM trends at TGs is to compute the spread of individual geocentric sea-level estimates or the spread of geocentric sea level between regions (*Wöppelmann and Marcos*, 2016). The spread of regional trends reduced from 0.9 mm yr^{-1} in the ULR1 solution (*Wöppelmann et al.*, 2007) to 0.5 mm yr^{-1} in the ULR5 solution (*Santamaría-Gómez et al.*, 2012; *Wöppelmann et al.*, 2014), which is approximately the expected residual climatic signal. Any further improvements in the GNSS trends require therefore another validation technique.

A second way to observe VLM at TGs, to overcome the limitations of the sparsely distributed GNSS stations, is differencing satellite altimetry and TG time series, which we will refer to as ALT-TG time series from here on. Initially, the ALT-TG time series were used to monitor the stability of satellite altimeters for the Global Mean Sea Level (GMSL) record, which is currently estimated to be 0.4 mm yr^{-1} (*Mitchum*, 1998, 2000). The first study to infer VLM trends from ALT-TG time series was *Cazenave et al.* (1999). Based on the method of *Mitchum* (1998) they compared ALT-TG to DORIS at six stations. Later, several studies were conducted on regional and global scale of which an overview is given by *Ostanciaux et al.* (2012). The first study to estimate more than 100 VLM trends (*Nerem and Mitchum*, 2002) presented uncertainties for 60 of 114 TGs smaller than 2 mm yr^{-1}, which is still larger than the 1 mm yr^{-1} uncertainty required for sensitive coastal assets (*Wöppelmann and Marcos*, 2016). However, they noted that the TGs should be visually inspected on a case-by-case basis to determine if the result was truly VLM. *Ostanciaux et al.* (2012) increased the number of ALT-TG VLM trend estimates sixfold to 641, but it included some outliers with trends above 20 mm yr^{-1}. They also made a comparison between their study

and several earlier studies. The best agreement was found over a small set of 28 tide gauges, where the results of *Ostanciaux et al.* (2012) differed from *Ray et al.* (2010) by an RMS of 1.2 mm yr^{-1}.

Recently, several studies have compared the GNSS trends to those of ALT-TG globally (*Santamaría-Gómez et al.*, 2014; *Wöppelmann and Marcos*, 2016; *Pfeffer and Allemand*, 2016). Several other studies did an equivalent comparison with DORIS and ALT-TG for a limited number of stations (*Cazenave et al.*, 1999; *Nerem and Mitchum*, 2002; *Ray et al.*, 2010). While the older studies primarily used along-track data from the Jason (TOPEX/POSEIDON (TP), Jason-1 (J1) and Jason-2 (J2)) series of satellite altimeters, the latest studies used preprocessed grids. *Wöppelmann and Marcos* (2016) made a comparison between several gridded products and one along-track dataset. All recent studies used ULR5 GNSS trends for comparison. The best results were obtained with an interpolated altimetry grid provided by AVISO (*Pujol et al.*, 2016), yielding a median of differences of 0.25 mm yr^{-1} with an RMS of 1.47 mm yr^{-1} based on a comparison at 107 locations (*Wöppelmann and Marcos*, 2016). It is important to note that the time series for all sites were visually inspected, primarily to remove those with non-linear behaviour. Additonally, the corresponding correlation between TG and nearby altimetry time series were found to be highest for AVISO. *Pfeffer and Allemand* (2016) did not apply visual inspection and obtained a comparable result for 113 stations (an RMS of 1.7 mm yr^{-1}), while only incorporating GNSS trends from stations within 10 km from the tide gauge.

This study aims to further reduce the discrepancies between GNSS and ALT-TG trends, while increasing the number of trend pairs. To do this, we will apply several steps to improve the VLM estimates at tide gauges. First of all, the number of reliable trend estimates is increased by using the GNSS trends from the larger NGL database. The NGL applies a trend estimation technique that is less sensitive to discontinuities to the time series (*Blewitt et al.*, 2016). Most TGs will neighbour multiple GNSS stations for which several combination methods are applied to determine the best procedure. Correlations between altimetry and TG time series are exploited to reduce residual ocean variability, which is often present in ALT-TG time series (*Vinogradov and Ponte*, 2011). The reduction in ocean variability should lead to more reliable ALT-TG VLM trends. Correlation thresholds additionally function as a filter, to remove time series that are uncorrelated due to differences in ocean signals, possible (undocumented) jumps in the TG time series, or interannual VLM signals that cannot be separated from the ocean signal (*Santamaría-Gómez et al.*, 2014). Additionally, we address the problem of contemporary mass redistribution on trends over different time spans using a fingerprinting method.

4.2 Data and Methods

In this section, we describe the processing procedures for deriving GNSS and ALT-TG VLM trends for comparison at TG locations. First, we will address the estimation of GNSS trends at the TG locations. The estimation of ALT-TG differenced trends is discussed in several steps. We briefly discuss the selection of the tide gauges.

After that we will discuss the altimetry processing procedures. We briefly review the Hector software (*Bos et al.*, 2013) for the estimation of trends from differenced ALT-TG time series. Eventually, trend corrections for contemporary mass redistribution using fingerprinting methods are described.

4.2.1 GNSS trends

The trend estimation at tide gauges primarily deals with two problems. First, a trend is estimated from a GNSS time series, which contains an autocorrelated noise signal, and often undocumented jumps. We use pre-computed trends, of which the procedure is briefly reviewed below. Second, many GNSS stations are not directly co-located to the TG station. Regular leveling campaigns, to monitor the relative VLM between the TG and the GNSS stations, are often absent. Therefore, the assumption is made that both locations are affected by the same VLM signal. When multiple GNSS receivers are present in the vicinity of the tide gauge, a method is required to estimate a single VLM trend from multiple GNSS stations. This is also discussed below.

GNSS trend estimation

To obtain VLM trends at TGs, often the products of the Université de La Rochelle (ULR) are used. ULR versions 5 and 6 make use of the Create and Analyze Time Series (CATS) software (*Williams*, 2008), which is able to estimate trends and errors from time series, taking into account temporally correlated noise. It has the advantage that it computes a more realistic trend uncertainty. The software is also able to estimate and detect discontinuities that occur due to earthquakes and equipment changes. Even though a large proportion of the trend estimates have formal accuracies better than 1 mm/yr, undetected discontinuities might bias the estimated trends (*Gazeaux et al.*, 2013).

In this study the results of NGL (*Blewitt et al.*, 2016) are used. *Blewitt et al.* (2016) proposed the Median Interannual Difference Adjusted for Skewness (MIDAS) approach, which is based on the Theil-Sen estimator. The procedure estimates trends from couples of daily data points separated by 365 days. It then removes all estimates outside two standard deviations, which are computed by scaling the Median of Absolute Devations (MAD) by 1.4826 (*Wilcox*, 2005), with respect to the median of the trend couples. Afterwards, a new median is computed, which serves as the trend estimate. *Blewitt et al.* (2016) demonstrated that MIDAS has a smaller equivalent step detection size than methods which included step detection. Besides the advantage of detecting smaller jumps, approximately 14000 GNSS time series are processed, which is almost 20 times more than ULR6. Unlike *Wöppelmann and Marcos* (2016), no manual screening is applied to the time series or trends.

Trend estimation at tide gauges

Despite several recommendations to co-locate GNSS receivers with TGs, currently only a few have a record that enables to estimate a trend with an uncertainty of 1 mm yr^{-1} or better. Therefore we take all stations into account that are within 50 km from a TG, provided that the standard deviation on the trend is lower than 1 mm yr^{-1} as estimated from the MIDAS algorithm. The threshold on the standard deviation ensures that most records containing large non-linear effects, due to for example water storage changes and co-seismic and post-seismic deformations, are removed from the analysis. Other studies used ranges from 10 km (*Pfeffer and Allemand*, 2016) up to 100 km (*Hamlington et al.*, 2016). At 100 km the uncertainty due to relative VLM trends increases substantially, on average with more than 0.5 mm yr^{-1} (*Santamaría-Gómez et al.*, 2017) for the NGL estimates, while taking a range of 10 km reduces the number of trends substantially. Therefore the range is set to 50 km, but comparable results are found for 30 and 70 km yielding a different number of trends.

Most studies simply average all neighbouring TG trends or take the trend from the closest station. However, many other techniques have been suggested in literature. We compare trends from several approaches in Sect. 4.3.1 and with the ALT-TG trends in Sect. 4.3.3. In total eight different approaches are considered. The first two involve all of the trends at neighbouring GNSS stations by computing their mean [1] and median [2]. Method [1] is among others applied by *Frederikse et al.* (2016) for regional sea-level reconstructions. One of the most frequently applied approach uses the trend at the closest station [3]. It is used in two recent studies by *Santamaría-Gómez et al.* (2012) and *Pfeffer and Allemand* (2016). We also investigate inverse distance weighting [4] in which the trend $\frac{dh_{TG}}{dt}$ is estimated as:

$$\frac{dh_{TG}}{dt} = \frac{\sum_i \frac{1}{d_i} \frac{dh_i}{dt}}{\sum_i \frac{1}{d_i}}, \tag{4.1}$$

where d_i and $\frac{dh_i}{dt}$ respresent the distance to the tide gauge and the trend at GNSS station i. We also use the GNSS trends based on the longest time series [5] and smallest error [6] from stations within the 50 km radius. The seventh approach involves weighting with the variances σ_i^2 of the trends [7], such that:

$$\frac{dh_{TG}}{dt} = \frac{\sum_i \frac{1}{\sigma_i^2} \frac{dh_i}{dt}}{\sum_i \frac{1}{\sigma_i^2}}. \tag{4.2}$$

And the last method [8] takes into account spatial dependency and trend uncertainty by combining methods [4] and [7], i.e. by weighting with the variance and with the distance, so that:

$$\frac{dh_{TG}}{dt} = \frac{\sum_i \frac{1}{\sigma_i^2 d_i} \frac{dh_i}{dt}}{\sum_i \frac{1}{\sigma_i^2 d_i}} \tag{4.3}$$

Method [8] is a variant of the method used in the altimeter calibration study of *Watson et al.* (2015). It penalizes the distance between the TG and the GNSS antenna and the uncertainty of the GNSS trends. Note that the uncertainties range mostly between 0.7-1 mm yr^{-1} and therefore method [8] is more sensitive to the distance from the TG than to the variance of the GNSS trends. The distance weights used in methods [4] and [8] quickly decrease with distance, effectively reducing the number of GNSS trends involved in the estimate. In several studies the method to estimate VLM trends at tide gauges from GNSS is not documented.

4.2.2 Tide-gauge time series

Monthly TG data are obtained from the PSMSL database (*Holgate et al.*, 2013). If any of the data points is flagged after 1993, the time series are removed from further analysis. Peak-to-peak variations in monthly time series are typically on the order of five decimeters. Monthly estimates outside of 1 meter from the mean are not likely to occur and are therefore removed from the data. This number is similar to our altimetry sea-level anomaly threshold and based on the criterion used by the National Oceanic and Atmospheric Administration (NOAA) for their global mean sea-level estimates (*Masters et al.*, 2012). To be consistent with the altimetry observations, we apply a Dynamic Atmosphere Correction (DAC) consisting of a low-frequency inverse barometer correction and short-term wind and pressure effects *Carrère and Lyard* (2003). Initially, we consider all TGs with at least 10 years of valid data.

4.2.3 Differenced ALT-TG time series

Wöppelmann and Marcos (2016) obtained the smallest standard deviation in the differenced time series by averaging grid cells within 1 degree from the TG using the AVISO interpolated product. The results obtained by taking the most correlated grid point from AVISO within 4 degrees around the TG increased the standard deviation. *Wöppelmann and Marcos* (2016) obtained lower correlations by averaging Goddard Space Flight Center (GSFC) along-track altimetry measurements within a radius of 1 degree from the TG. Note that the AVISO grid is constructed using correlation radii of 50-300 km (*Ducet et al.*, 2000) and it includes measurements from all altimetry satellites, not only the Jason series. The AVISO grid therefore effectively averages over a much larger radius around the TG and it includes data from more satellites. The larger uncorrelated noise using GSFC compared to AVISO, as shown by the combination of the increased RMS and the spectral index (*Wöppelmann and Marcos*, 2016), is therefore likely an effect of the limited number of GSFC altimetry measurements. However, using the large effective radius of AVISO, data far away from the TG are included, which might not correlate with the sea-level signal at the TG. This can result in a remaining ocean signal in ALT-TG time series, which contaminates the VLM trend estimates.

To overcome the limitations of gridded products, we work with along-track data and exploit the correlations between sea level at the satellite measurement location and at the TG on interannual and decadal scales by using a low-pass filter. We start by

Table 4.1: List of geophysical corrections and orbits applied in this study. Details on the geophysical corrections are given in Chapter 2.3.1.

Satellite	T/P	Jason-1&2
Orbits	CCI	GDR-E
Ionosphere	Smoothed dual-frequency	
Wet troposphere	Radiometer	
Dry troposphere	ECMWF	
Ocean tide	GOT4.10	
Loading tide	GOT4.10	
Solid Earth tide	Cartwright	
Sea state bias	CLS	
Mean sea surface	DTU15	
Dynamic atmosphere	MOG2D	

creating sea-level time series every 6.2 km along-track using the measurements from TP, J1 and J2 from the RADS database (*Scharroo et al.*, 2012) between 1993-2015. In the cross-track direction the measurements are within 2-3 km of each other, because the satellites are kept in a repeat-orbit. In order to get a consistent set of altimetry observations, the same geophysical correction models are used for all satellites, as are given in Table 4.1. All time series within 250 km from the TG are taken into account. This radius is larger than the open ocean correlation distances used by *Ducet et al.* (2000) and *Roemmich and Gilson* (2009), except for the equatorial region where the correlation scales become much larger. At distances larger than 250 km, one will still find some highly correlated signals, but the trends caused by large scale processes like GIA and present-day mass redistribution will differ from that at the TGs. It also ensures that at least one ground track of the altimeters is within the range of the tide gauge at the equator. Reducing the 250 km radius leads to a decreased number of available trends.

Additionally, intermission biases between TP-J1 and J1-J2 are removed. *Ablain et al.* (2015) revealed a large dependence of the intermission biases on the latitude. For the J1-J2 differences, a single polynomial is estimated through the differences between the sea-level observations of both instruments, such that the correction $\Delta h_{sla,ib}(\lambda)$ becomes:

$$\Delta h_{sla,ib}(\lambda) = c_0 + c_1 \cdot \lambda + c_2 \cdot \lambda^2 + c_3 \cdot \lambda^3 + c_4 \cdot \lambda^4, \tag{4.4}$$

with λ the latitude of the altimetry observations. For the TP-J1 differences, separate polynomials are estimated for four latitude regions and the ascending/descending tracks (*Ablain et al.*, 2015). The values for the parameters c_n are given in Table 6.1. More details on the computation procedure are provided in Appendix D.

The Jason satellite series samples sea level every ten days, hence we average monthly 3-4 measurements in order to make a first set of time series that is compatible with the monthly TG observations. Small discrepancies might still be present between the time series due to inaccurate corrections for or filtering of high-frequency signals, like tides or wind and pressure effects. As for the case of the TG monthly solutions, observations more than 1 m from the mean sea surface are removed and

the time series should have at least 10 years of valid observations. Additionally, a second set of time series at each along-track bin is created, by applying a yearly moving-average filter. This second set of altimetry time series is correlated with a yearly low-pass filtered version of the TG series, in order to test whether their signals match on interannual and longer time scales. The yearly moving-average filter allows to suppress the noise present in individual altimetry measurements. The full pole tide from RADS (which contains a solid Earth, loading and ocean tide as in *Desai et al.* (2015)) is subtracted from both time series before correlation, whereas for the TG time series we restore the solid Earth pole tide as computed in *Desai et al.* (2015). The loading tide is at its maximum only a few millimeters, which has no significant effect on the interannual correlation, and is therefore not restored. We also remove residual annual and semi-annual cycles and a linear trend before correlation, because the yearly moving-average filter has side-lobes causing these seasonal signals to be partly retained. Other longer filters are considered to reduce the side lobes, but they would introduce larger transient zones at the start and the end of the time series. An iterative procedure removes sea surface heights outside of 3 RMS up to a maximum of 10% of the observations. The outlier removal is primarily implemented to remove any spurious data present in the RADS database. It is unlikely that more than 10% of the observations contain processing problems or outliers due to extreme events. If more observations would be discarded, high correlations might not represent the corresponding ocean signal anymore. The result is a set of correlations that indicate which altimetry sea-level time series resemble the TG time series on interannual time scales and longer.

The monthly low-pass filtered altimetry time series are kept, if the corresponding correlation from yearly low-pass filtered time series are above a certain threshold. The level of the threshold is discussed in Sect. 4.3.2. We average the remaining monthly altimetry time series, to get a single altimetry time series per TG. Alternatively, we also use the correlations as weights, to get one correlation-weighted altimetry time series per tide gauge. In this case the monthly low-pass filtered time series are weighted by their corresponding correlation, then added together and accordingly normalized, so that the weights sum up to one. The resulting time series are subtracted from the TG time series if there are at least ten altimetry time series with a correlation above the threshold. The resulting differenced ALT-TG time series with less than 15 years of valid observations are further discarded. The length requirement is due to the fact that remaining ocean signals can still affect the estimated trends significantly. An example of the reduction of variability due to correlation thresholds and weighting is shown in Fig. 4.1. The white noise in the unfiltered time series is reduced in the red curve, however the opposite might happen if the number of altimetry time series decreases. Most important is to note that there is a strong reduction in the variance of temporally correlated residuals, represented here by the low-pass filtered time series. Correlated residual signal can strongly affect the estimated trend, especially in areas with large variability due to interannual events like ENSO. Note that for the ALT-TG trend computation only the solid Earth part of the pole tide is added to the TGs, but this time as is done in the IERS2010 conventions (*Petit and Luzum*, 2010), such that the trends are consistent with those of the GNSS

data. The main difference is that the altimetry pole tide correction of *Desai et al.* (2015) is computed with respect to a linearly drifting mean pole, while in the IERS conventions the mean pole location is modelled as a third order polynomial. If the pole tide is not taken into account consistently, it can introduce biases of 0.1 mm yr^{-1} (*Santamaría-Gómez et al.*, 2017). Since the mean polar motion is non-linear, this will introduce trend biases if the time spans between GNSS and altimetry do not match. The drift of the mean pole is caused by a redistribution of mass in the Earth system. This is corrected for using the mass-redistribution fingerprints discussed in Sect. 4.2.5, which are computed using a model that includes elastic responses and rotation changes. The drifting mean pole is primarily captured by the C_{21} and S_{21} spherical harmonic coefficients (*Wahr et al.*, 2015), which indicates a symmetrical pattern around a 45° inclinated line with respect to the Equator.

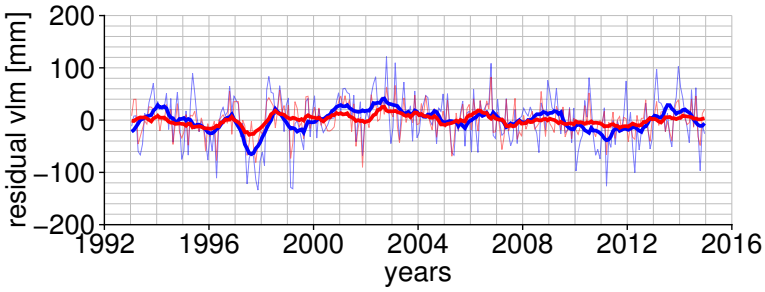

Figure 4.1: Time series of ALT-TG differenced VLM at Winter Harbour. After averaging or weighting with the correlation a moving-average filter is applied to visualize the remaining interannual variability. In blue: without a threshold on the correlation and without correlation weighting. In red: with a threshold of 0.7 for the correlation and with correlation weighting. In the background the time series without the moving-average filter applied.

4.2.4 Differenced ALT-TG trends

The ALT-TG time series have a monthly resolution, so they contain less observations, and they exhibit substantial interannual variability. These time series are therefore less suitable to be processed with the MIDAS algorithm used to compute GNSS trends. For the computation of the ALT-TG trends and the corresponding standard deviation, we fit a power-law in combination with a white noise model by using the Hector software (*Bos et al.*, 2013). The spectrum of power-law noise, $P(f)$, decays with frequency and is given by (*Bos et al.*, 2013):

$$P(f) = \frac{1}{f_s^2} \frac{\sigma^2}{(2\sin(\pi f / f_s))^{2d}}, \tag{4.5}$$

where f_s is the sampling frequency, σ the power-law noise scaling factor and d links to the spectral index κ in *Wöppelmann and Marcos* (2016) by $\kappa = -2d$. The value of d is related to the strength of the autocorrelation of the sequence (*Bos et al.*, 2013). This is required to capture the temporal correlation in the ALT-TG time series

as shown by Fig. 4.1 in which the low-pass filtered time series give an idea of the memory in the system. We use the function 'PowerlawApprox', which uses a Toeplitz approximation for power-law noise (*Bos et al.*, 2013).

4.2.5 Contemporary mass redistribution

The trends estimated from GNSS time series are computed over different time spans than the ALT-TG trends and will be affected by, e.g., non-linear VLM induced by elastic deformation due to present-day ice melt and changes in land hydrology storage (*Riva et al.*, 2017). To quantify those non-linear VLM signals, the response to mass redistribution is computed using a fingerprinting method at yearly resolution. We take into account the loads of Greenland, Antarctica and glacier mass loss, the effects of dam retention and hydrological loads. A detailed description of the input loads is given in *Frederikse et al.* (2016). To estimate the fingerprints of VLM, the sea-level equation is solved, including the rotational feedback (*Farrell and Clark*, 1976; *Milne and Mitrovica*, 1998). Since not all load information for the last years is available yet, we will limit the time series of ALT-TG up to 2015. Some GNSS trends are estimated from time series that span beyond 2015. Therefore we linearly extrapolate the fingerprint data, if necessary, to 2015 and 2016 based on the difference between years 2013 and 2014.

4.3 Results

This section first addresses the trends obtained from GNSS stations. The averaging methods are discussed and the NGL trends are compared to those of ULR5. Then the results of the correlation-weighted ALT-TG trends are discussed. These are compared to those from *Wöppelmann and Marcos* (2016). After that, the GNSS and ALT-TG trends are compared and best weighting methods are discussed. For the comparison we take into account that both trends are not computed from time series covering the same period by correcting for non-linear VLM trends estimated from fingerprints.

4.3.1 Direct GNSS trends

For 570 TGs at least one GNSS station is found within a 50 km radius with an uncertainty on the trend that is below 1 mm yr^{-1} (one standard deviation). The VLM for these TGs is shown in Fig. 4.2 using the median of the surrounding GNSS stations in case there are multiple GNSS stations available. The signature of GIA dominates the signal on large scales, and is primarily visible in Scandinavia and Canada. In Alaska there might be a significant contribution of present-day ice mass loss. If GIA is removed the VLM signals typically range between -3 and 3 mm yr^{-1} (*Wöppelmann and Marcos*, 2016), with a few exceptions.

Even though the large-scale GIA process appears to be captured properly, regional VLM have large effect on the GNSS trends. In Fig. 4.3 the differences between the lowest and highest VLM estimate from the eight methods discussed in Sect. 4.2.1 are

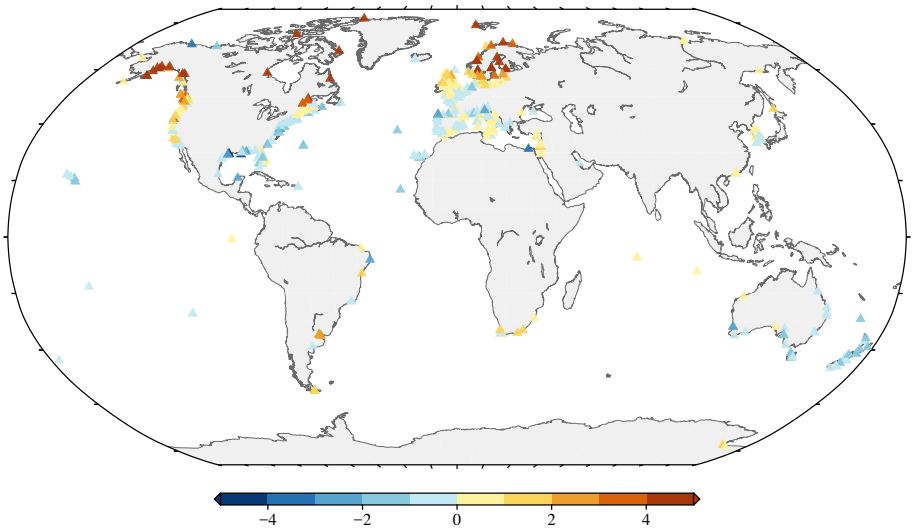

Figure 4.2: VLM (mm/yr) at TGs using the median of the neighbouring trends.

shown. The figure shows that the range is generally higher, where more GNSS trends are available. In particular the seismically active zones like the US West Coast show a larger range. In most cases the VLM trend furthest away from the mean of the eight methods is estimated with a methods involving only one station, i.e. methods 3, 5 and 6 (Fig. 4.4). The range of solutions, when considering all TGs with at least two GNSS trends, has a mean of 0.92 mm yr^{-1} with 25 and 75 percentiles of 0.38 and 1.20 mm yr^{-1}. In case at least three available GNSS trends are considered, the mean of the differences rises to 1.09 mm yr^{-1} and the 25 and 75 percentiles to 0.56 and 1.34 mm yr^{-1}. Since we only considered GNSS trends with a maximum standard deviation of 1 mm yr^{-1}, this implies that a significant contribution of kilometer-scale VLM variations is present along the West Coast of the US, where the difference between methods is often larger than 1 mm yr^{-1}. Note that the range of individual GNSS trends is on average even larger than the range between methods. *Santamaría-Gómez et al.* (2017) estimated the global numbers for the impact of spatial variations in VLM at 30 km and 100 km separation to be 0.2 mm yr^{-1} and 0.5 mm yr^{-1}. At coasts of Europe and North America, where most tide gauges are located, these numbers are substantially larger, i.e. even the range between methods is on average larger than 1 mm yr^{-1}. The differences between methods is often comparable in size as the VLM signal, especially after the GIA is removed.

Wöppelmann and Marcos (2016) show that a comparison between their ALT-TG trends and their GNSS trends yields an RMS of 1.47 mm yr^{-1}. They use visual inspection to remove tide gauges where clear non-linear effects or discontinuities were present. In Table 4.2 a comparison is made between the eight different approaches and the GNSS trends of *Wöppelmann and Marcos* (2016) that were used in the aforementioned comparison with ALT-TG trends at 70 locations. The values show that a substantial fraction of the RMS between GNSS and ALT-TG trends can already be

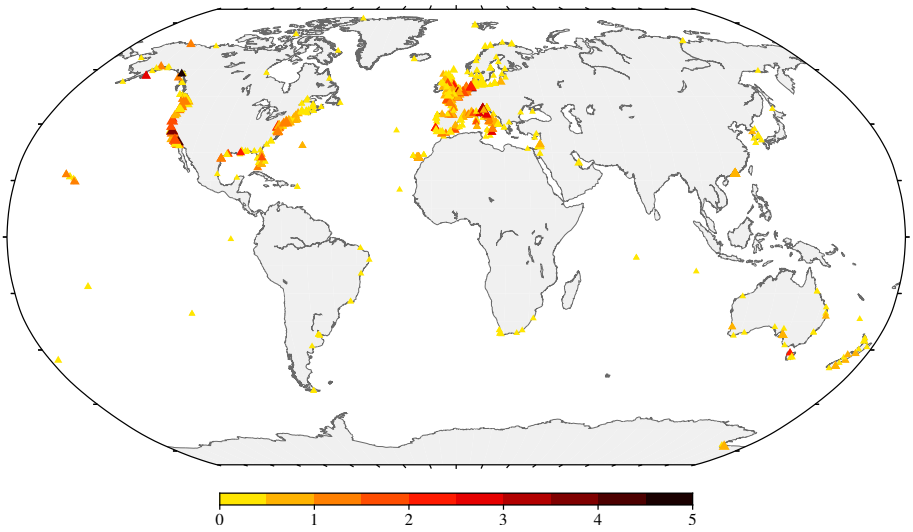

Figure 4.3: Range (mm/yr) of VLM estimates at TGs using eight different approaches. The size of the symbols indicates the number of GNSS trends available (with a maximum of ten). Red and black symbols indicate a difference between the approaches, which is larger than the formal uncertainties of the GNSS trends. This is an indication for significant relative VLM motion between the stations.

Table 4.2: Statistics of trend differences between NGL and ULR5 at 70 stations for the eight approaches.

		RMS	Mean	Median
Approach	Keyword	mm yr^{-1}	mm yr^{-1}	mm yr^{-1}
1	mean	1.11	0.07	0.05
2	median	1.05	0.12	0.03
3	closest	1.36	0.02	0.02
4	dist. weight.	1.21	0.00	0.03
5	longest	1.29	0.32	0.20
6	smallest error	1.15	0.24	0.17
7	error weight.	1.11	0.08	0.02
8	dist./error weight.	1.23	0.01	0.05

explained by different GNSS averaging and processing methods. Using the closest station (approach 3) an RMS of 1.36 mm yr^{-1}, which is comparable in magnitude to the RMS between GNSS and ALT-TG trends found by *Wöppelmann and Marcos* (2016). Note that we remove all NGL GNSS trends with an uncertainty larger than 1 mm yr^{-1} and therefore co-located stations are sometimes removed. The closest GNSS station in our selection is therefore not always the same as the one used by *Wöppelmann and Marcos* (2016). The best comparison is found with the median (approach 2), even though the RMS of differences is still above 1 mm yr^{-1}. Since the closest station method depends on a single station, there is a larger chance some outliers are present, which substantially increases the RMS of differences. For the closest station method three trend differences larger than 3 mm yr^{-1} are found, whereas only one is found for the median method.

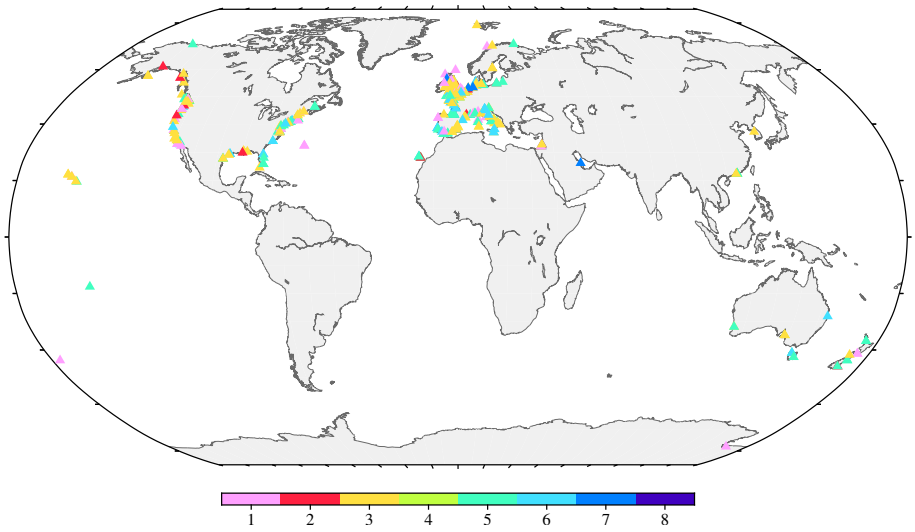

Figure 4.4: Plot indicating the method (1-8) that yields the largest deviation from the mean trend of the eight methods. Only locations shown where at least two GNSS stations are within 50 km of the tide gauge.

4.3.2 Differenced ALT-TG trends

Using correlation thresholds, we try to minimize the residual ocean signal in the ALT-TG time series. Additionally, it will filter problematic stations, where no correlation between TG and altimetry observations is found. A higher threshold reduces therefore the number of ALT-TG trends. Table 4.3 shows the reduction of the differenced VLM trends, when the correlation threshold increases. After a correlation threshold of 0.4, the number of observations drops substantially. At a threshold of 0.7, the number of TGs for which a trend is computed, is only half of that without a threshold. The remaining trends are generally more reliable, because of two reasons: VLM time series that exhibit relatively large residual ocean signals are removed; and secondly, TG time series that contain large jumps due to unidentified reasons (e.g. earthquakes or equipment changes) are removed.

Table 4.3: Number of TGs at which trends are estimated from differenced ALT-TG time series. The '-1.0' indicates no correlation threshold is set.

Threshold	Number of TGs
-1.0	663
0.0	660
0.1	658
0.2	655
0.3	638
0.4	602
0.5	549
0.6	470
0.7	344

In order to show that the method decreases the oceanic signal, we compare the standard deviation reduction by using correlation thresholds and weighting (Fig. 4.5). The plot in the top panel shows the comparison between the standard deviation of the differenced time series using no correlation threshold and the time series using a threshold of 0.7 together with a correlation weighting. The mean reduction in standard deviation is 3.9 mm, whereas the mean standard deviation is 37 mm. The change in standard deviations at several locations are coherent, which is expected because the sea-level fluctuations along continental slopes are coherent (*Hughes and Meridith*, 2006). Substantial reductions in standard deviation are apparent at both North American coasts, in Japan and in Northern Europe. *Vinogradov and Ponte* (2011) had already observed large discrepancies in interannual ocean signals between TGs and altimetry in North America and in Japan. It suggests that our method is capable to reduce these ocean signals. This is confirmed by the change in the median of the spectral indices, κ, as discussed in Sect. 4.2.4. The median of the spectral indices changes from -0.63 to -0.57, which indicates that the autocorrelation in the residuals decrease. The Winter Harbour (Canada) VLM time series (Fig. 4.1) shows a typical example in which especially the correlated noise is reduced. However, there are several locations where the standard deviation increases substantially. Most of them are sporadic, but in a few locations, like in the UK and France there is coherent increase.

Similar patterns of standard deviation decrease, albeit reduced in magnitude, are observed for the not-weighted against weighted VLM time series with a correlation threshold of 0.0 (bottom of Fig. 4.5), i.e. when only positively correlated altimetry time series are taken into account. Instead of 344 VLM trends, as for the comparison discussed above, 660 trends are compared. The mean reduction of the standard deviation is 1.4 mm, whereas the mean standard deviation is 38 mm. Remarkable is the strong reduction of the standard deviation at the southeast side of Australia. In the UK and France an increase in standard deviation is present again. In most cases an increase in white noise, likely due to the decreased effective number of altimetry measurements, is responsible for the higher standard deviation, as demonstrated in Fig. 4.6 for a VLM time series at Llandudno, UK. In most cases of an increasing standard deviation, the correlated ocean signals are still reduced or remain approximately equal.

Fig. 4.7 shows the VLM trends estimated from the ALT-TG time series using no correlation threshold and a threshold of 0.7. A comparison of Fig. 4.2 and Fig. 4.7 reveals that especially the Indian Ocean and the southern Pacific Ocean are sampled better using ALT-TG instead of GNSS trends. If the correlation threshold is set to 0.7, the number of trend estimates decreases, which has particularly an impact on the number of trend estimates at TGs in South America and Africa. Hence, for regional reconstructions, a careful choice should be made for the correlation threshold.

Compared with the GNSS trends, the neighbouring ALTG-TG trends show more variation, which is especially true for the UK and Japan. It is difficult to say whether this is a true VLM signal, but it is important to note that many GNSS stations are placed on bedrock, which exhibits more stable trends than the coastal locations of

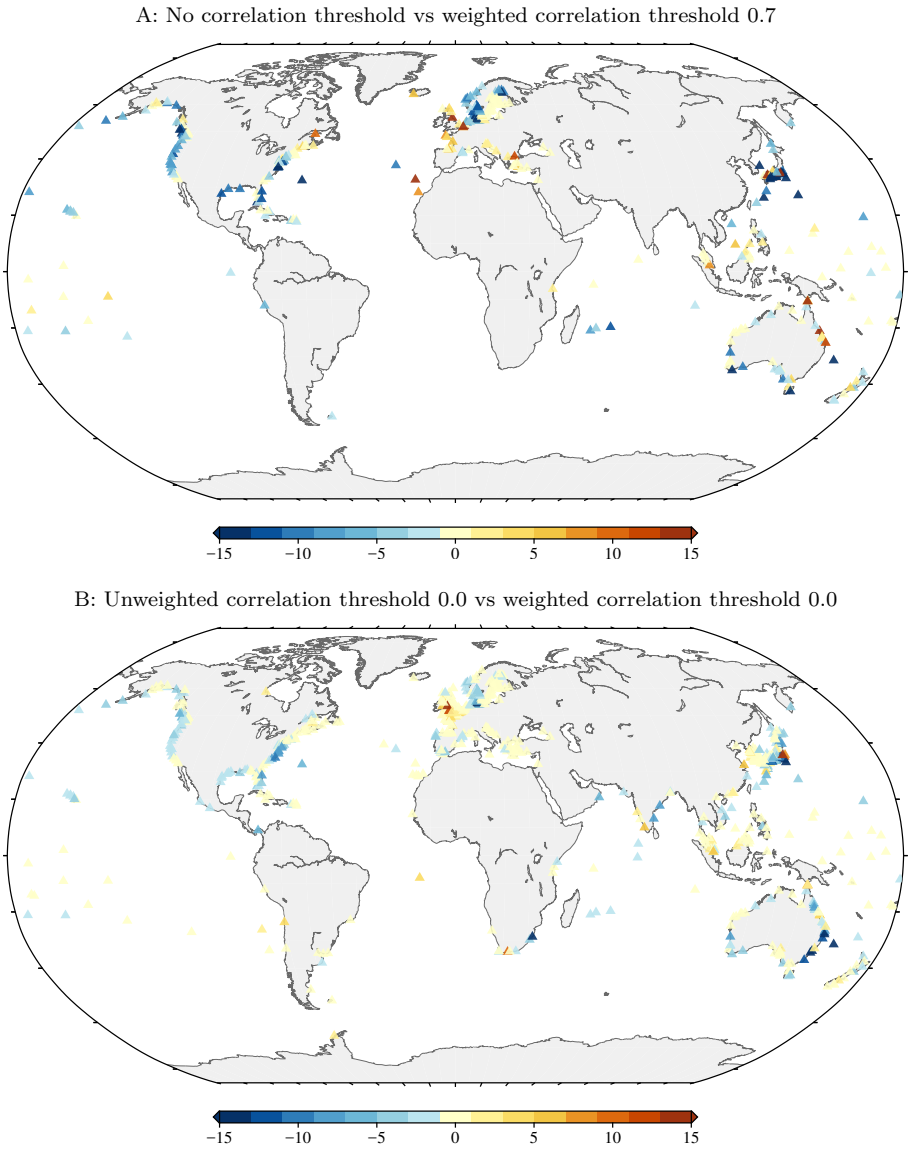

Figure 4.5: Change in standard deviation (mm) of the differenced time series using correlation thresholds and weighting. Note that a correlation threshold of 0.0 indicates positive correlations only.

tide gauges. Secondly, the GNSS trends with an uncertainty larger than 1 mm yr^{-1} are removed, which reduces the variability. Of the 663 ALT-TG trends, 293 (44 %) have a trend uncertainty smaller than 1 mm yr^{-1}. Therefore larger spatial trend variability can also be induced by remaining ocean signals in the VLM time series. In the Fig. 4.7B, showing the 0.7 threshold trends, the number of trends is reduced due to the correlation threshold. It removes most tide gauges in the highly variable regions mentioned before and the neighbouring differences are therefore less erratic.

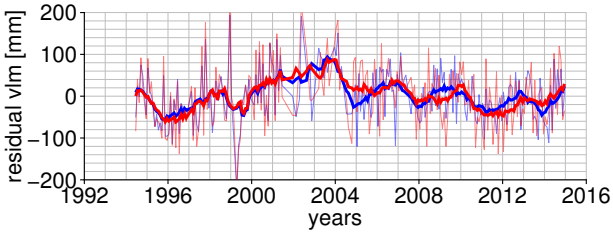

Figure 4.6: Time series of ALT-TG differenced VLM at the Llandudno (UK) TG. A moving-average filter is applied to visualize the interannual variability. In blue: with a threshold of 0.0 for the correlation, but without correlation weighting. In red: with a threshold of 0.0 for the correlation and with correlation weighting. In the background the time series without a moving-average filter applied.

284 out of 344 trends (83 %) have a trend uncertainty smaller than 1 mm yr^{-1} using the 0.7 correlation threshold.

The results of applying correlation weighting and thresholding are shown Fig. 4.7C. Two spots of coherent changes in the trends can be clearly identified: in Norway the trends increased by approximately 1 mm yr^{-1}, while in the East Coast of the United States the opposite happens. These spots exhibit longshore coherent sea-level signals that are not found in the open ocean (*Calafat et al.*, 2013; *Andres et al.*, 2013). Note that both locations also exhibit a strong reduction in standard devation (Fig. 4.5). Coherent changes are also present around Denmark. Other regions, where substantial reductions in the standard deviation are found, do not experience coherent changes in trends.

4.3.3 GNSS vs ALT-TG trends

In this section the VLM trends from GNSS using the eight approaches as described in Sect. 4.2.1 are compared with the differenced ALT-TG VLM trends using various correlation thresholds. Based on the intercomparison we determine the best solution for the GNSS approach and the correlation thresholds for altimetry. Additionally, a comparison is made with *Wöppelmann and Marcos* (2016). We also investigate the effect of present-day mass redistribution on the difference in trends due to varying time spans of the GNSS and the ALT-TG methods.

Fig. 4.8 shows the RMS of trends differences between various GNSS combination methods and correlation thresholds for ALT-TG. The RMS of trend differences is computed at 155 TG stations for which all solutions are available. The colors exhibit small differences horizontally and large differences vertically, indicating that the GNSS method is more important in reducing the RMS. The difference between the method with the lowest RMS of differences, which is obtained by taking the median of the GNSS trends (2), and the method with the highest RMS, which uses the closest GNSS station (3), is approximately 0.12 mm yr^{-1}. *Hamlington et al.* (2016) computed VLM trends at TG locations by using a complex filtering procedure that also implicitly takes into account the median of the GNSS trends. Next to taking the

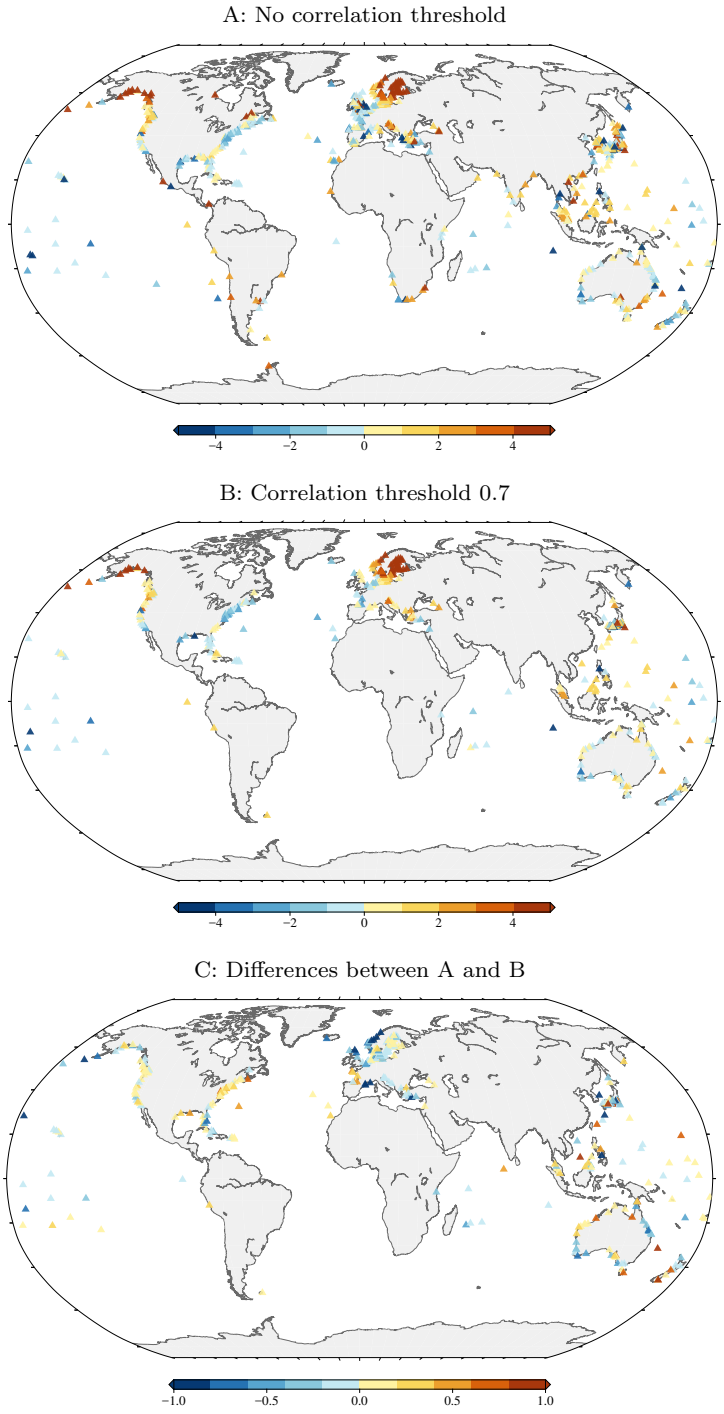

Figure 4.7: ALT-TG trends (mm yr^{-1}) estimated using no threshold (A), with a correlation threshold and correlation weighting (B) and the difference between them (C).

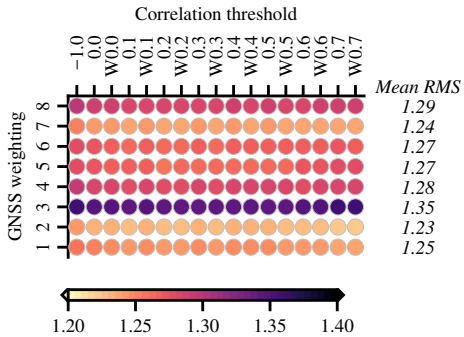

Figure 4.8: RMS (mm/yr) of differences between GNSS and ALT-TG VLM trends. The 'W' indicates weighting by correlation. The '-1.0' indicates no correlation threshold is set. The numbers of the y-axis refer to the approaches used to combine the GNSS trends as described in Sect. 4.2.1.

median of the GNSS trends, taking the mean (1) within the 50 km radius and using variance weighting (7) also yield substantially lower RMS differences than the other five methods. However, the median method performs slightly better. Besides, the median method is less sensitive to large values caused by GNSS trends with larger uncertainties (for which the mean method is sensitive) and also less to outliers caused by large local VLM differences (for which the variance weighting method is sensitive).

In Table 4.4 we analyze the results for different correlation thresholds in more detail by comparing them to the GNSS trends based on the median method. On the left side of the table the RMS, mean and median are shown for all VLM estimates available for each correlation threshold. Setting no correlation thresholds yields trend estimates at 294 TGs for comparison, while setting a threshold at 0.7 leaves only 155. While the number of trends decreases, the RMS decreases as well, indicating that the correlation thresholds can serve as a selection procedure, which filters out outliers. This is confirmed by Fig. 4.9, in which we see the decrease of the number of available trends, but also the removal of the outliers. If the threshold is set to 0.7 only three discrepancies in trends of larger than 3 mm yr^{-1} are found. Note that the reduction in RMS is not only caused by the removal of uncorrelated altimetry and TG time series. Large earthquakes for example might induces jumps or non-linear behaviour in both the TG and GNSS time series. Those tide gauges are not taken into account and therefore the problematic GNSS time series are left out as well. The larger range in Fig. 4.9 for no correlation threshold may therefore be partly attributed to problematic GNSS trends. In the last row the *Wöppelmann and Marcos* (2016) trends are compared with our GNSS trends. It has a similar RMS with the 0.4-0.5 correlation threshold trends, but it is computed with a substantially smaller number of trends.

On the right side of the table, we only included TGs for which all solutions are available, which reduces the number from 155 to 137, because W&M trends are also considered for comparison. The RMS of differences for 155 stations is only slightly larger as shown below in Table 4.5. Note that the RMS of the residuals using ALT-TG

Table 4.4: Statistics of the differences between the median of the GNSS trends (approach 2) and the ALT-TG trends for various correlation thresholds. The 'W' indicates that the altimetry time series are weighted by the correlation. The row 'W&M' shows the comparison with *Wöppelmann and Marcos* (2016) trends. The column 'NoT' indicates the number TGs for which trend estimates are computed. On the left side of the table all stations are taken into account, on the right side only stations are taken into account for which a solution exist for all correlations thresholds (and including those from W&M).

	All				Same			
Corr.	RMS	Mean	Median	NoT	RMS	Mean	Median	NoT
	mm yr^{-1}	mm yr^{-1}	mm yr^{-1}		mm yr^{-1}	mm yr^{-1}	mm yr^{-1}	
-1.0	2.141	-0.241	-0.107	294	1.234	-0.167	-0.099	137
0.0	2.108	-0.248	-0.101	294	1.226	-0.175	-0.068	137
0.0W	2.103	-0.250	-0.036	294	1.219	-0.172	-0.056	137
0.1	2.113	-0.258	-0.096	293	1.219	-0.174	-0.074	137
0.1W	2.108	-0.260	-0.043	292	1.218	-0.170	-0.045	137
0.2	2.082	-0.233	-0.073	292	1.217	-0.163	-0.074	137
0.2W	2.080	-0.234	-0.015	292	1.216	-0.168	-0.042	137
0.3	1.986	-0.152	0.047	283	1.221	-0.157	-0.066	137
0.3W	1.991	-0.157	0.056	283	1.217	-0.165	-0.044	137
0.4	1.695	-0.106	0.065	264	1.223	-0.152	-0.050	137
0.4W	1.696	-0.112	0.071	264	1.218	-0.158	-0.041	137
0.5	1.554	-0.086	0.044	239	1.220	-0.153	-0.058	137
0.5W	1.552	-0.087	0.056	239	1.217	-0.155	-0.067	137
0.6	1.417	-0.093	-0.065	204	1.209	-0.155	-0.087	137
0.6W	1.416	-0.093	-0.083	204	1.208	-0.156	-0.094	137
0.7	1.220	-0.142	-0.123	155	1.206	-0.140	-0.060	137
0.7W	1.220	-0.144	-0.124	155	1.206	-0.142	-0.074	137
W&M	1.658	-0.177	-0.050	211	1.328	-0.101	0.020	137

from W&M, is already 0.14 mm yr^{-1} lower than those in the study of *Wöppelmann and Marcos* (2016) and about 0.4 mm yr^{-1} lower than in *Pfeffer and Allemand* (2016), who incorporated only 109 and 113 stations, respectively. This is a consequence of the combined use of the median of the NGL trends and the selection based on correlation. Our altimetry solutions further decrease the RMS by another 0.1 mm yr^{-1} compared to W&M, even when no threshold on the correlation is set. In the study of *Wöppelmann and Marcos* (2016), the along-track altimetry ALT-TG trends performed worse than the AVISO results. The reason for this discrepancy could be the latitudinal intermission bias, or the small radius around the TG used in that study for including altimetry measurements.

Increasing the correlation threshold only slightly reduces the RMS between GNSS and ALT-TG trends and the additional weighting has a negligible effect on the RMS. As mentioned before, for higher thresholds and correlation weighting the standard deviation of the ALT-TG time series is generally reduced (Fig. 4.5) and Fig. 4.7 showed coherent changes in trend. Additionally, the NGL and ULR trends showed an RMS of differences more than a millimeter and the range of trend estimates between the eight approaches is often larger than a millimeter. We argue that the absence of a clear improvement or a change in RMS due to correlation thresholds is a result of the relatively large noise in the GNSS trends. The histogram in Fig. 4.9 shows that for 155 stations, only three discrepancies are larger than 3 mm yr^{-1}. For these TGs

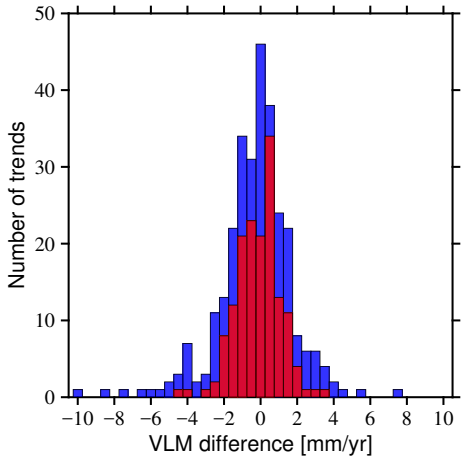

Figure 4.9: Histogram of GNSS and ALT-TG trend differences. In blue the results without any correlation threshold and in red with a correlation threshold of 0.7 and correlation weighting.

(located at Galveston (US), Eureka (US) and the Cocos Islands (Australia)) we find that the neighbouring GNSS stations are located at the other side of lagoons or on different islands. Therefore the likely cause for the largest discrepancies is not the ALT-TG trend, but local VLM differences between the GNSS stations and the TG.

The third column of Table 4.4 shows that the mean is in all cases negative, i.e. the GNSS trends are larger than those of ALT-TG. Trends obtained with correlations -1.0, 0.0, 0.1 and 0.2 are barely statistically different from zero based on a 95% confidence level, while the others are not. The 95% confidence level is approximated as two times the standard deviation of the mean of the residual trends ($\frac{\sigma_n}{\sqrt{N}}$, where N is the number of trends and σ_n the standard deviation of the residual trends). In the right 'mean' column for the 137 stations, the means are statistically insignificantly different from zero at the 95%-confidence level, wheras at a 90%-confidence level several are not. The medians in both columns are closer to zero and deviate up to 0.2 mm yr^{-1} from the mean, which indicates a slightly skewed distribution.

There is a non-linear VLM signal due to present-day mass loss in both GNSS and ALT-TG trends and since they cover different time spans this causes small systematic differences between trends. Due to the inhomogeneous distribution of the TGs and the spatial signal of non-linear VLM, this affects not only the mean, but also the skewness of the distribution. In Fig. 4.10 the trend differences between the GNSS and ALT-TG methods are visualized for all 294 stations. Most of the negative differences in trends are observed in Europe and parts of North-America, while positive differences in trends are observed in Australia. In Europe there is an uplift due to present-day mass loss, which increases over the last few years. Since the GNSS time series are generally shorter, they measure a larger uplift signal. By subtracting the present-day VLM that GNSS observes from altimetry observations, we obtain negative signals in Europe.

We applied a correction for the effect of present-day mass loss to the trends for

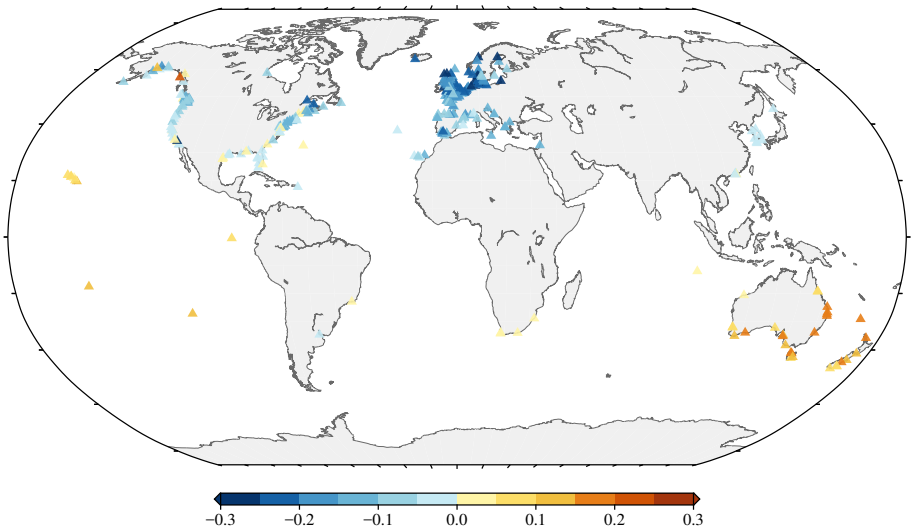

Figure 4.10: Trend differences (mm yr^{-1}) between the GNSS and ALT-TG time spans induced by non-linear VLM due to present-day mass redistribution.

the 155 stations for which a trend is found with all methods in Table 4.5. Similarly, this is done for the 137 stations, so that the results are comparable with Table 4.4. There is no significant reduction in RMS. The maximal deviation of the median from zero is 0.06 mm yr^{-1} for the 155 stations and maximally 0.07 mm yr^{-1} for the 137 stations, which is a reduction with respect to the values listed in Table 4.4. The mean is also reduced to approximately -0.1 mm yr^{-1}, which is not statistically different from zero. This result is at the level of the noise in the determination of the ITRF origin (*Santamaría-Gómez et al.*, 2017) and it is smaller than the 0.4 mm yr^{-1} to which global mean sea level trends from altimetry are gauranteed (*Mitchum*, 2000). Unless it is proven that the altimeters are more stable and the uncertainties in the ITRF origin are reduced, a mean of trend differences closer to zero cannot be expected.

4.4 Conclusions

We presented several ways to estimate VLM at TGs from GNSS and differenced ALT-TG time series. A comparison is made between eight different methods to obtain VLM at the TG from NGL GNSS trends. The range of the trends between the approaches is at the same level as the standard deviations of the GNSS trends, with a mean of 0.92 mm yr^{-1} and a median of 0.71 mm yr^{-1}. A comparison with the estimates of ULR5 (*Wöppelmann and Marcos*, 2016) at 70 stations yielded an RMS of at least 1.05 mm yr^{-1}. A comparison with ALT-TG showed that using the median of all neighbouring GNSS provided the best results.

For the ALT-TG trends we used along-track data from the Jason series of altimeters. At every 6 km along-track data were stacked, to create time series. The time series were low-pass filtered with a moving-average filter of one year and correlated

with low-pass filtered TG time series. An average or weighted monthly time series for altimetry was created taking into account only the time series corresponding to correlations above a threshold. The TG time series were subtracted from the average of monthly low-pass filtered altimetry time series to create a ALT-TG time series. Using the Hector software, between 344 and 663 trends were computed from the ALT-TG time series, depending on the correlation threshold set.

Table 4.5: Statistics of ALT-TG trend differences with the median GNSS approach for various correlation settings after applying a correction for non-linear VLM.

Correlation	NoT: 155 RMS mm yr^{-1}	Mean mm yr^{-1}	Median mm yr^{-1}	NoT: 137 RMS mm yr^{-1}	Mean mm yr^{-1}	Median mm yr^{-1}
-1.0	1.231	-0.102	-0.039	1.223	-0.100	0.030
0.0	1.225	-0.109	-0.027	1.215	-0.108	0.031
0.0	1.223	-0.106	0.016	1.209	-0.105	0.048
0.1	1.220	-0.107	-0.014	1.208	-0.107	0.034
0.1	1.222	-0.104	0.003	1.208	-0.104	0.072
0.2	1.220	-0.099	0.016	1.207	-0.096	0.027
0.2	1.221	-0.101	-0.001	1.206	-0.101	0.059
0.3	1.223	-0.091	0.011	1.211	-0.090	0.018
0.3	1.221	-0.098	-0.001	1.207	-0.098	0.036
0.4	1.226	-0.087	0.011	1.214	-0.085	0.021
0.4	1.223	-0.092	0.008	1.209	-0.091	0.037
0.5	1.225	-0.088	0.020	1.212	-0.086	0.042
0.5	1.222	-0.090	0.027	1.208	-0.088	0.045
0.6	1.222	-0.087	-0.007	1.202	-0.088	0.018
0.6	1.222	-0.087	-0.006	1.201	-0.089	0.028
0.7	1.220	-0.071	0.021	1.202	-0.073	0.037
0.7	1.219	-0.074	0.012	1.201	-0.075	0.036

The standard deviation of the differenced ALT-TG time series was reduced on average by approximately 10% when a correlation threshold of 0.7 was used instead of no correlation threshold. Spatially coherent differences in trends between various thresholds are observed at the east coast of the US and in Norway. We argue that residual interannual ocean variability in ALT-TG time series can locally induce VLM trend biases, especially when time series are short. For 155 globally distributed stations, increasing the correlation threshold does not significantly affect the RMS of differences between GNSS and ALT-TG trends. However, the correlation threshold also works as a selection procedure. When considering 294 VLM estimates from GNSS and ALT-TG at the same TGs for comparison, with no threshold the RMS of differences was 2.14 mm yr^{-1}, whereas an RMS of 1.22 mm yr^{-1} was reached using 155 stations and a threshold of 0.7. This is a substantial improvement with respect to the 1.47 mm yr^{-1} RMS of *Wöppelmann and Marcos* (2016) at 109 TGs, the best result so far. Note that increasing the threshold considerably reduces the number of time series in the southern hemisphere and therefore other thresholds might be better depending on the purpose.

The comparison with tide gauges also reveals that the trends from ALT-TG are biased low (similar to *Wöppelmann and Marcos* (2016)), even though this is barely significant. Using mass redistribution fingerprints, a correction is applied for trend differences caused by non-linear behaviour of present-day mass changes. The RMS

of differences is barely affected, but the mean of differences is changed from about -0.2 to -0.1 mm yr^{-1}, which is now statistically insignificant.

The trends for all solutions (median GNSS and ALT-TG for all correlations) are provided in the supplementary material of *Kleinherenbrink et al.* (2018). The ALT-TG trends are accompanied by error bars computed using the Hector software. The provided uncertainties for the GNSS use the MAD from the median of the trends within 50 km, scaled by 1.4826 (*Wilcox*, 2005). If only a single GNSS station is present, the MIDAS uncertainty is provided. If two GNSS stations are present and both trends are statistically equal, it takes the square-root of the mean of the GNSS variances to avoid very small error bars. When no correlation threshold is used 663 ALT-TG and 570 GNSS trends are available at 939 different TGs. By setting the correlation threshold to 0.7, the number of TGs, for which a trend is estimated, decreases to 759. Depending on the application, the value of the threshold can be varied to find an optimum between the reliability and the number of TG for which a trend is estimated. If both GNSS and ALT-TG trends are available, we recommend to use GNSS trends, because of correlated residual ocean signals between various ALT-TG time series. However, if a large discrepancy ($>$ 3 mm yr^{-1}) is found between the GNSS and ALT-TG trends, we recommend to use the ALT-TG trend, because the culprit is likely local VLM differences between the TG and the GNSS stations. The GNSS - ALT-TG histogram for no correlation threshold reveals large discrepancies between the two methods up to 10 mm yr^{-1}. While the problems with ALT-TG trends are mostly resolved by setting a higher threshold, the GNSS trends might still require some inspection before they are used in sea-level studies.

Chapter 5

Calibration of the TOPEX global mean sea level record using ERS1&2

5.1 Introduction

Since the publication of *Watson et al.* (2015) (from here on W15) there is renewed interest in the processing and interpretation of the first years of the Global Mean Sea-Level (GMSL) record based on satellite altimetry. The absence of a detectable acceleration in the 25-year altimeter record led to the suspicion that data collected during the first years of TOPEX were not properly calibrated (*Callahan et al.*, 2016; *Beckley et al.*, 2017) (from here on B17). Two studies (*Chen et al.*, 2017; *Dieng et al.*, 2017) reported that calibrations of the TOPEX altimeter with tide gauges, as done in W15, would lead to improved budget closure. However, the absence of an acceleration could also be partly attributed to the recovery of a dip in ocean heat content after the eruption of the Pinatubo in 1991 (*Fasullo et al.*, 2016; *Dieng et al.*, 2017). By compensating for the effects of the eruption on GMSL and removing a calibration correction (as done in B17), *Nerem et al.* (2018) came to the conclusion that there is an observable climate-driven acceleration in the altimeter record.

There is no significant acceleration present in the GMSL time series based on standard processing. W15 applied calibrated TOPEX, because of the presence of a U-shape drift in a comparison of the TOPEX side A (TOPEX-A) sea surface heights with tide-gauge records (*Mitchum*, 2000). The drift is related to a degradation of the Point Target Response (PTR) of TOPEX-A near the end of its operation (*Hancock et al.*, 1999). Since the PTR is directly related to the shape of the altimeter waveforms, parameters like Significant Wave Height (SWH) and radar range are directly affected by it. The effect on SWH is shown in B17 based on a method designed by *Ray and Beckley* (2012), which involves the comparison of TOPEX-derived SWH with bouys. This led to studies that produced corrections for the TOPEX SWH (*Queffeulou*, 2004), but not to the range. B17 indicated that the effect of the problematic PTR on the

Parts of this chapter will be published as: Kleinherenbrink, M., Riva, R., & Scharroo, R. (2018). Calibration of the TOPEX global mean sea level record using ERS1&2, Nature Geoscience, *In preparation*.

range was counteracted by an overly large Sea State Bias (SSB) correction, which is a consequence of overestimated SWHs. Therefore most studies involving TOPEX never applied any correction to the range.

However, in a globally-averaged tide-gauge comparison a millimeter-level variation is revealed during TOPEX-A. Even though the signal is small, it is large enough to significantly affect the acceleration. After the switch to TOPEX-B in January 1999 the drift disappeared. B17 showed that the drift is similar in shape as a calibration correction (cal-1), which is applied to deal with internal path delays of TOPEX (*Hayne et al.*, 1994). During the calibration phase for cal-1, the signal is routed back and not transmitted via the antenna, which yields a received signal that resembles a point target (B17). Since the PTR is changing over time it therefore also affects cal-1, which for the same reason provides incorrect range corrections for the degradation of the PTR.

Three solutions to compensate for the drift of TOPEX-A have been proposed. The tide-gauge calibration of W15, in which a drift for TOPEX-A, a drift for TOPEX-B and an intramission bias between them are removed. This however, makes the altimeter-derived GMSL dependent on tide-gauges. B17 proposed to unapply cal-1 to both TOPEX-A and TOPEX-B, which leads to a better overall agreement with the tide gauges and yields a small negative drift of -0.45 mm yr^{-1} of TOPEX-A with respect to tide gauges. B17 also used the retracked data of *Callahan et al.* (2016) based on an improved PTR for TOPEX-A, which reduced the difference in SWH between TOPEX-A and buoys. Furthermore, a better agreement was found with tide gauge, but the first two years of TOPEX-A had to be excluded because of anomalous sea surface heights. Note that W15 used a 4-parameter SSB correction model derived by *Chambers et al.* (2003), while B17 adopted a non-parametric model (*Tran et al.*, 2010). The intramission bias depends on the applied SSB correction.

The calibration and validation methods discussed above rely on the comparison with tide gauges. There are several issues with tide-gauge methods related to the intramission bias estimates and the drift estimates. *Ablain et al.* (2015) showed that the intermission biases between TOPEX-Jason-1 and Jason-1-Jason-2 are geographically varying. Due to the fact that the SSB corrections rely on the 'wrong' TOPEX-A SWH estimates, it is reasonable to assume that the intramission bias between TOPEX-A&B is also varying geographically. A tide-gauge comparison always overweights certain regions with respect to others, so the intramission bias might be affected. Secondly, the altimeter-tide gauge (ALT-TG) differences contain residual noise due to incomplete cancellation of ocean signal (*Mitchum*, 1998, 2000; *Beckley et al.*, 2017). ENSO-related signals propagate along the shores of North and South America (*Hughes and Meridith*, 2006). These signals have relatively small cross-shelf length scales, which can lead to significant differences between TGs and altimetry due to spatial separation. Altimetry measurements are generally taken several tens of kilometers from the coast where the signals are weaker. *Kleinherenbrink et al.* (2018) gave an example of ENSO signals affecting ALT-TG time series as far as the Winter Harbour tide gauge, located at the west coast of Canada. Since these signals are correlated between tide gauges, this could affect the short-term altimetry

drift detection as well as the intramission bias estimates. Thirdly, the Vertical Land Motion (VLM) trends estimated from GNSS or inferred from models based on loading input (e.g. GRACE) have been linearly extrapolated in W15 and B17. Studies showed there is a significant non-linear contribution of mass redistribution to VLM (*Riva et al.*, 2017). Therefore there might be a small bias in the estimated TOPEX drifts.

This study extends the work of W15 and B17 with respect to cal-1 and the SSB correction in several ways. Instead of a comparison with tide gauges, we use the crossovers of the satellite missions ERS1&2 to calibrate TOPEX. The main advantage of the crossover method over a comparison with tide gauges is the spatial coverage. Based on the crossovers analysis, we will argue whether cal-1 should be applied or not. Then we determine whether an TOPEX-A/B intramission bias should be estimated and whether TOPEX-A&B are drifting and how both are related to the applied SSB. A new calibration technique is proposed based on the crossovers with ERS1&2. A tide-gauge comparison using different averaging techniques to estimate the ALT-TG drifts and intramission biases is performed, to check the reliability of such a calibration or validation method. Eventually our crossovers results are benchmarked using the tide-gauge comparison. The effect of this calibration on GMSL is quantified and the question is answered whether there is a statistically significant acceleration in sea level from the altimetry record.

5.2 Methodology

This section discusses the processing steps for the validation and calibration of TOPEX time series using ERS-1&2 altimetry data and tide gauges. In Sect. 5.2.1, we describe the crossover approach using ERS-1&2. It requires the removal of an intermission bias between ERS-1&2, which might be latitude dependent. Then several SSB models for TOPEX are applied, for which we determine if the estimation of an intramission bias between TOPEX-A&B is required. In Sect. 5.2.2 we describe the comparison of TOPEX-A&B against tide gauges. This involves corrections for the non-linear part of VLM caused by present-day mass redistribution. Additionally, several averaging approaches are tested that combine the nonuniformly-spaced ALT-TG drifts and biases differently.

5.2.1 Crossovers

In order to perform the crossovers analysis in a consistent way, satellite altimetry data from the Radar Altimetry Database System (RADS) is used (*Scharroo et al.*, 2012). The geophysical corrections, listed in Table 5.1, are fixed except for the Sea State Bias (SSB), which is varied for TOPEX. For ERS-1&2 only one SSB correction is available, which is based on a 4-parameter model of (*Gaspar et al.*, 1994). To ensure a smooth transition between the ERS-1&2 sea surface heights, we remove a latitude-dependent intermission bias between both (*Ablain et al.*, 2015).

The crossover locations are determined with an algorithm which is implemented

in RADS. First it computes all crossover locations of the ERS and TOPEX ground tracks. Consecutively, it finds data close to the crossover location within a time window of half the repeat-period, which is 10 days for TOPEX and 35 days for ERS-1&2. The orbits of ERS-1 were changed several times during its life time and therefore the repeat periods differ from 35 days. The time window is adjusted accordingly, which implies that the number and the spatial distribution of the crossovers is different during several cycles. Sea surface height anomalies with an absolute value larger than 1 m are removed from the analysis. All crossovers are averaged monthly to created an equal temporal spacing in the global sea surface height difference time series. Spatial averaging is done by weighting the mean sea surface height difference per 1-degree latitude band with the sea surface area it represents, as in *Kleinherenbrink et al.* (2016).

Table 5.1: List of geophysical corrections used for ERS-1&2 and TOPEX. *Not applied in the comparison with tide gauges. **Only the solid Earth part of the pole tide is corrected for in the comparison with tide gauges, following the IERS2010 conventions. Details on the geophysical corrections are given in Chapter 2.3.1.

Correction	TOPEX	ERS-1&2
Orbital altitude	CCI	
Range	Ku-band	
Ionosphere	Smoothed dual-frequency	
Wet troposphere	Radiometer	
Dry troposphere	ERA	
Dynamic atmosphere	MOG2D*	
Ocean tide	GOT4.10*	
Loading tide	GOT4.10*	
Solid Earth tide	Cartwright*	
Pole tide	Desai2015**	
Sea state bias	bm4/CSR/CLS	bm4
Mean sea surface	DTU15	

Three models are fitted through the global sea surface height difference time series, to be able to determine whether TOPEX GMSL is drifting and/or an intra mission bias between TOPEX-A&B is present. The first model [1] only estimates a single trend through the TOPEX time series (1993.0-2002.5). The second model [2] includes an offset at the moment of the A-B altimeter switch (January 1999) and the third model [3] computes a bias with separate trends for the A and B periods. We use an F-test to determine whether there is a significant change in residuals if we use the second and third models (*Heij et al.*, 2004):

$$F = \frac{(e_1^T e_1 - e_i^T e_i)/g}{e_i^T e_i/(n-k)}, \tag{5.1}$$

where e_1 are the residuals of model 1 and e_i represent the residuals of the other two models [2,3], g is the number of additional parameters that is estimated and $n-k$ the degrees-of-freedom.

The above models are fitted to the TOPEX-ERS1&2 crossover time series with and without applying cal-1. It will be applied to time series generated with the three

SSB corrections available in RADS. The oldest parametric model, denoted as 'bm4' in Table 5.1, is computed from crossovers in TOPEX-A cycles 1-110 and consecutively applied to TOPEX-A&B (*Gaspar et al.*, 1994). The CSR SSB correction (*Chambers et al.*, 2003) uses separate parametric models for TOPEX-A&B, computed from crossovers in cycles 11-158 for TOPEX-A and from cycles 240-349 for TOPEX-B. A non-parametric SSB correction is computed by CLS (*Gasper et al.*, 2002; *Labroue and Tran*, 2004) from colinear differences in TOPEX-B cycles 240-350 and applied to the whole TOPEX time series.

5.2.2 Tide-gauge comparison

For the comparison with tide gauges, we use a procedure slightly modified with respect to W15. Instead of the fast delivery products (fast), the hourly research quality tide-gauge records (rqds) from UHSLC (*Caldwell et al.*, 2015) are used. This includes the tide gauges in and around Australia, which were separately added in W15. Initially, all records that span the period 1993.0-2002.5 are considered. The tide-gauge records within a radius of 1000 km from $\geq$7.5 moment-magnitude earthquake events during that period are removed.

The TOPEX altimetry data are extracted from RADS. Most geophysical corrections are similar to those used for the crossovers, but we do not apply the dynamic atmosphere, the ocean and load tide and the pole tide corrections. Only the solid Earth part of the pole tide is applied following the IERS2010 conventions, to be consistent with the GNSS VLM corrections. The discrepancy in VLM, attributed to the difference in time span between the altimeter and the GNSS time series, is corrected for by mass redistribution modelling, as discussed in Sect. 4.2.5. All altimetry time series within a radius of 220 km around a tide gauge are taken into account, with a minimum distance from the coast of 30 km to avoid land signals contaminating waveforms and radiometer wet troposphere delay estimates. The TOPEX data are colinearly stacked, so that we create altimetry time series at every 6 km along-track. Sea surface height anomalies larger than 1 meter are removed.

For every altimetry time series, cubicly interpolated UHSLC tide-gauge sea-level measurements are subtracted, creating an ALT-TG differenced time series at each altimeter location, refered to as Control Point (CP) in W15 and from here on. Similar to W15, we fit a model to the CP time series containing 12 ocean tides and we cope with a sloping sea surface, which can be caused by ocean dynamics, by including a latitudinal and longitudinal dependence. The trends and biases of the three models described in Sect. 5.2.1 are considered, so that we again estimate three different models. Spectrograms of the residuals of the models are computed and signals corresponding to peaks larger than $4\sigma^2$ are added to the model, after which it is recomputed. Outliers outside three times the RMS of the residuals are then iteratively removed. Ultimately, time series longer than 250 samples and their corresponding trends and biases are considered for further analyses.

Linear corrections for VLM are obtained by modelling or from GNSS trends. We take the median of all GNSS trends within 50 km from the tide gauge in the database

of the Nevada Geodetic Laboratory (NGL) (*Blewitt et al.*, 2016). Only GNSS trends with a formal uncertainty smaller than 1 mm yr^{-1} are included. To cope with VLM differences between the time spans of GNSS and TOPEX, due to non-linear present-day mass redistribution, we use the VLM estimates based on the models and loads used by *Frederikse et al.* (2016). The correction is implemented as in (*Kleinherenbrink et al.*, 2018) and implicitly also deals with the problem of polar wander, which is not captured by the IERS2010 pole tide used as background model for GNSS and altimetry. In case there are no GNSS stations nearby the tide gauge, the linear trends from the present-day mass redistribution VLM model and the ICE-6G_C VM5a GIA model (*Peltier et al.*, 2015) are used to estimate the total VLM trend at the tide gauge.

Thresholds are set to remove noisy CP time series, which require the propagation of uncertainties. To estimate uncertainties on the trends and biases, which are computed from the CP time series using ordinary least-squares, we fit an AR(1)-model through the residuals. With that we construct variance-covariance matrix Q_{yy}:

$$Q_{yy} = \begin{pmatrix} \sigma^2 & \phi_1\sigma^2 & \cdots & \phi_1^n\sigma^2 \\ \phi_1\sigma^2 & \sigma^2 & \cdots & \phi_1^{n-1}\sigma^2 \\ \vdots & \vdots & \ddots & \vdots \\ \phi_1^n\sigma^2 & \phi_1^{n-1}\sigma^2 & \cdots & \sigma^2 \end{pmatrix}, \tag{5.2}$$

where σ is the standard deviation of the residuals and ϕ_1 the first-lag autocorrelation. By propagation of errors, we estimate the variance-covariance matrix for the estimated parameters as:

$$Q_{xx} = (A^T Q_{yy}^{-1} A)^{-1}, \tag{5.3}$$

where A is the design matrix used in the ordinary least-squares estimate described above. The standard deviations for the drifts and biases are extracted from the matrix Q_{xx}. We remove the time series for which the standard deviation of the residuals is larger than 110 mm, with a TOPEX-A drift uncertainty larger than 10 mm yr^{-1} (both as in W15) or a TOPEX-A/B drift uncertainty larger than 8 mm yr^{-1}.

To inspect the stability of the ALT-TG comparison, the drifts and intramission biases are averaged using four methods. First we simply take the mean of all CP trends and biases (m1). The mean and uncertainties of the drifts and biases are computed from distributions estimated with a Monte-Carlo simulation, in which we randomly leave twenty tide gauges out of consideration. These uncertainties only reflect changes due to weighting and network geometry. The uncertainties are inflated by 0.3 mm yr^{-1} to account for reference frame stability issues (*Santamaría-Gómez et al.*, 2017) and differences between long-term ALT-TG and GNSS VLM trends (*Kleinherenbrink et al.*, 2018). This is done for all four methods. The second method is similar to W15 and weights the trends and biases with their variance (m2). A 1.5 mm yr^{-1} uncertainty for the GNSS trends is taken into account. Third, the means of trends and biases are computed for every tide gauge and consecutively all mean trends and biases are averaged (m3). Only tide gauges that are coupled with at least ten trends/biases are included, which makes the method less prone to outliers. And finally, a virtual station method (*Jevrejeva et al.*, 2006) is applied (m4). This takes an

average of the trends and biases between the nearest tide gauges and creates a virtual station at the midpoint. The virtual station is added and the two original stations are removed. This process loops until no stations are closer than 500 km from each other, which should be enough to remove most correlations between neighbouring stations and which creates a more homogeneously spaced network. The limit of 500 km is chosen to avoid generation of high weights for several remote stations, which would make the result sensitive to outliers. Secondly, in most regions ocean signals correlate at smaller radii. Similar to the third method, a minimum of ten trends and biases is required per tide gauge.

5.3 Results

Similar to the methodology section, the results section addresses the crossovers and the tide-gauge comparison separately. First, we discuss the results of the crossovers with ERS-1&2 using three SSB models and three model fits, as discussed in Sect. 5.2.1. After that, we discuss whether the complementary tide-gauge comparison confirms the findings with the crossovers and which issues remain. Eventually, the effect of the crossover calibration on the GMSL trend and acceleration is addressed.

5.3.1 Crossovers

Fig. 5.1 shows the original, cal-1 calibrated, global sea surface height differences between TOPEX and ERS1&2. Whatever SSB model is used, the U-shaped signal, supposedly caused by cal-1 is visible in the time series. This comparison supports the notion that cal-1 should be removed from the TOPEX-A time series.

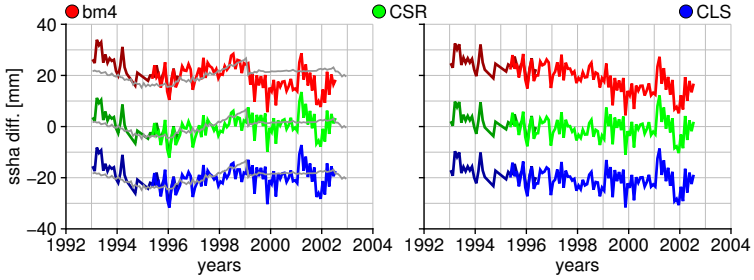

Figure 5.1: Global mean sea surface height differences from crossovers (TOPEX-ERS1&2) for three different SSB models. The darker shading indicates the ERS1 crossovers. Left: Cal-1 is applied and the cal-1 correction is plotted in grey. Right: Cal-1 is not applied.

Only the crossovers time series using the bm4 SSB correction clearly exhibit a discontinuity at the moment of the TOPEX-A/B transition. The cal-1 correction also exhibits a jump, however it appears to be slightly smaller that the one in the bm4 time series. The time series based on the CSR and CLS SSB correction have a relatively smooth transition between TOPEX-A/B. As a consequence, removing cal-1 from the TOPEX time series reduces the discontinuity when the bm4 correction is used, but

introduces a discontinuity when the CSR and CLS SSB correction are used. This latter is shown in the right panel of Fig. 5.1.

Comparison with W15

In Fig. 5.2, three models have been fit through the original data, which includes the cal-1 correction. The magnitude of the trends and biases are given in Table 5.2. Estimation of separate trends and an intramission bias is a similar approach to that of W15. The F-test indicates that also here an intramission bias is required for each of the SSB corrections. Computing separate drifts does not reduce the residuals significantly. In contrast to the positive drift estimates of W15, 1.5±0.5 mm yr^{-1} for TOPEX-A and 0.9±0.9 mm yr^{-1} for TOPEX-B, we find significantly different and even negative estimates for the TOPEX-A&B drifts no matter which SSB correction is used. Additionally, W15 observed a negative bias based on the CSR SSB model, while we find a positive one. The CSR and CLS SSB correction tested by W15 also yielded significantly different intramission biases, -2.9±2.5 and -7.6±2.5 mm yr^{-1}, while we find intramission biases similar in magnitude. Note that using model 2 and 3 gives similar results for the biases and the drifts between TOPEX-A&B do not differ more than 0.3 mm yr^{-1}.

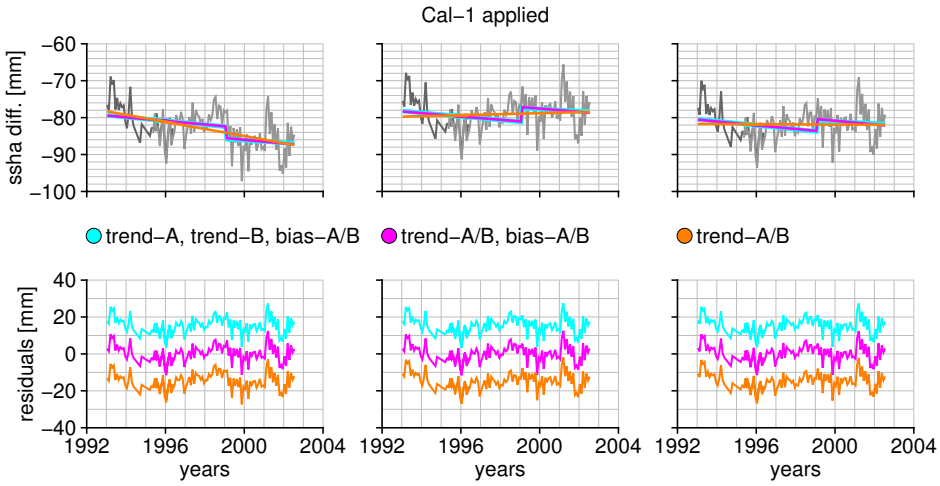

Figure 5.2: Top: time series of sea surface height differences (TOPEX-ERS1&2) for the bm4 (left), CSR (middle) and the CLS (right) SSB models for which cal-1 is applied, together with three models fitted to the data. Bottom: residuals after subtracting the models.

The observed differences with W15 could be due to several different causes. Firstly, the newer corrections together with the different orbits, could lead to different drifts and intramission biases. However, changing the TOPEX orbits (REAPER and GDR-CP) and the dry tropospheric corrections (ECMWF) did not lead to significantly different results. Most other corrections are not likely to have a dramatic effect on GMSL trends, because similar corrections are applied to TOPEX and ERS1&2. However, the SSB corrections in coastal waters (at most tide gauges) or at very high

SWHs (primarily in the circumpolar current) could influence estimates of the drift and biases due to the geometry of the tide-gauge network. Secondly, the sea surface heights estimated from the ERS1&2 missions are drifting and therefore an independent comparison with tide gauges is required. This cannot explain the difference in the intramission bias between our results and W15. And thirdly, the validation and calibration of TOPEX with tide gauges of W15 is biased. Remaining ocean signals in the ALT-TG time series could induce short-term trends and possibly misleading discontinuities in the models. GNSS receivers are often not colocated with the tide gauge and therefore several incorrect VLM trends might affect the drift. Over the whole altimetry period mean differences between VLM trends of ALT-TG and GNSS are in the order of 0.3 mm yr^{-1} (*Wöppelmann and Marcos*, 2016; *Kleinherenbrink et al.*, 2018). The geometry of and averaging techniques in the tide-gauge comparison could cause drift and bias changes, which is not unlikely because geographically varying intermission biases have already been detected between TOPEX and Jason-1 (*Ablain et al.*, 2015). Fourthly, W15 linearly extrapolated GNSS and GRACE trends back in time, while contemporary mass redistribution causes non-linear VLM trends (*Riva et al.*, 2017). This is further discussed in Sect. 5.3.2.

Table 5.2: Modeled drifts and biases from crossovers of TOPEX-ERS1&2 before and after removing cal-1. The models are described in Sect. 5.2.1. The F-scores are computed with respect to model 1, with high scores indicating a significant improvement. *For model 2 the 5% significance level is 3.9, while for model 3 it is 3.1.

SSB	Model	Drift A [mm yr^{-1}]	Drift B [mm yr^{-1}]	Bias A/B [mm]	F-score*
bm4	1	-0.96±0.16		0	-
CSR	1	0.14±0.16		0	-
CLS	1	-0.02±0.15		0	-
bm4	2	-0.48±0.28		-3.2±1.6	3.9
CSR	2	-0.45±0.28		3.9±1.6	5.9
CLS	2	-0.50±0.28		3.2±1.6	4.1
bm4	3	-0.51±0.31	-0.34±0.69	-3.4±1.8	**2.0**
CSR	3	-0.49±0.31	-0.27±0.69	3.7±1.8	**3.0**
CLS	3	-0.55±0.31	-0.27±0.68	3.0±1.7	**2.1**
bm4 no cal	1	-1.53±0.14		0	-
CSR no cal	1	-0.44±0.14		0	-
CLS no cal	1	-0.59±0.14		0	-
bm4 no cal	2	-1.13±0.25		-2.7±1.4	**3.6**
CSR no cal	2	-1.10±0.25		4.4±1.4	10.0
CLS no cal	2	-1.15±0.25		3.7±1.4	7.1
bm4 no cal	3	-1.22±0.27	-0.71±0.61	-3.2±1.5	**2.1**
CSR no cal	3	-1.19±0.27	-0.64±0.60	3.9±1.5	5.3
CLS no cal	3	-1.25±0.27	-0.64±0.60	3.1±1.5	4.0

Comparison with B17

Fig. 5.3 shows the time series and residuals after removal of cal-1. The drifts and biases for the accompanying models are given in the bottom of Table 5.2. Removal of cal-1, causes the drifts over the whole TOPEX period to decrease by at least 0.5 mm yr^{-1}, which corresponds closely to the results of B17 when applying the CSR and

CLS SSB corrections. The drift is reduced by incorporating a bias into the model, when we apply the bm4 SSB correction, but increases when the CSR or CLS SSB correction are applied. The F-test demonstrates that the use of an intramission bias no longer significantly reduces the residuals. For the other SSB corrections, the bias becomes larger and therefore regression of an intramission bias is required. Note that the drifts computed over the TOPEX-B period are for all SSB corrections about 0.5 mm yr^{-1} smaller than for the TOPEX-A period, if separate trends are estimated (model 3), but they are statistically equal. Separate estimation of TOPEX-A&B drifts is therefore not required.

B17 mentioned that the TOPEX-A/B intramission bias is sensitive to the number of cycles taken on either side of the transition. Based on the bias uncertainty, B17 noted that it added only 0.11 mm yr^{-1} uncertainty to the GMSL trend, however it can have a significant effect on the acceleration. Preferably, an intramission bias is not estimated at all, which therefore suggests that the 'old' bm4 SSB correction should be used. However, the estimated bias is close to the 2σ confidence interval and not estimating a bias yields a large drift between TOPEX and ERS1&2. Note that including a bias (model 2) leaves statistically consistent drifts no matter what SSB correction is used. It suggests that with a crossover analysis, it is possible to find accurate intramission biases if cal-1 is not applied. Model 2 could therefore serve as a calibration for TOPEX-A&B GMSL if the drift found from the crossovers can be confirmed with a tide-gauge comparison.

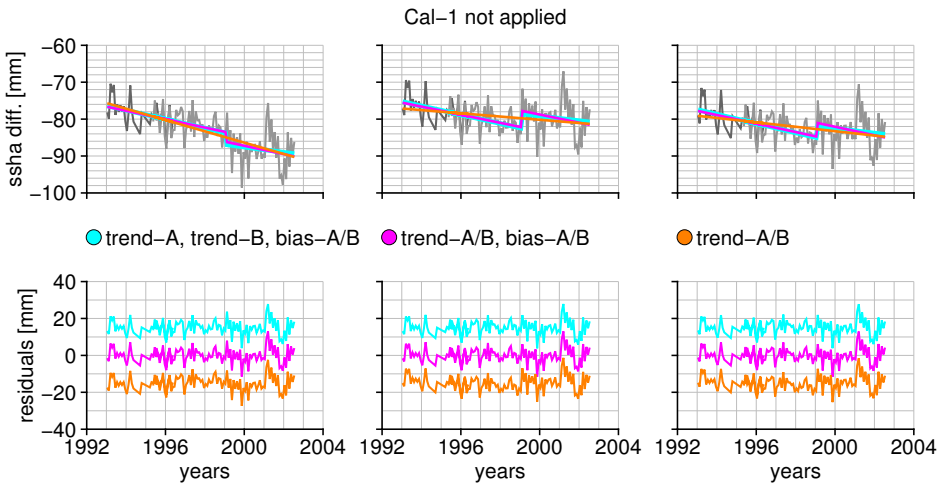

Figure 5.3: Top: time series of sea surface height differences (TOPEX-ERS1&2) for the bm4 (left), CSR (middle) and the CLS (right) SSB models for which Cal-1 is removed, together with three models fitted to the data. Bottom: residuals after subtracting the models.

It is however also possible to treat TOPEX-A&B as two separate systems (in contrast to B17), by only unapplying the cal-1 correction in TOPEX-A. As shown in Table 5.3, when using the bm4 correction and not estimating a bias, a drift is obtained, which is not statistically different from those for model 2 when cal-1 is not applied for the whole TOPEX time series. As for the results in the preceding paragraph, a sig-

Table 5.3: Modeled drifts and biases from crossovers of TOPEX-ERS1&2 after removing cal-1 only from TOPEX-A. The F-scores are computed with respect to model 1. *For model 2 the 5% significance level is 3.9, while for model 3 it is 3.1.

SSB	Model	Drift A [mm yr^{-1}]	Drift B [mm yr^{-1}]	Bias A/B [mm]	F-score*
bm4 no cal-A	1	-1.25±0.13		0	-
bm4 no cal-A	2	-1.07±0.24		-1.20±1.37	**0.7**
bm4 no cal-A	3	-1.22±0.27	-0.34±0.60	-2.06±1.51	**1.3**

nificant negative drift between TOPEX and ERS remains, which implies that GMSL from ERS exhibits a larger secular trend.

Regional differences

The drifts and especially intramission biases are geographically different. To demonstrate this, the crossover differences are averaged over the southern and northern hemisphere, respectively. The resulting time series are shown in Fig. 5.4 with their corresponding fitted models. For all SSB corrections, both TOPEX-A&B crossovers exhibit a negative drift in the southern hemisphere, while TOPEX-B exhibits a positive drift with respect to ERS2 in the northern hemisphere. The intramission bias is negative for bm4 in the southern hemisphere and neglectable for the other two SSB corrections. In the northern hemisphere, the bm4 intramission bias is neglectable, but for CSR and CLS they become substantially larger. For the northern hemisphere, there is also a substantial difference between the intramission biases, depending on the model used (model 2 or 3). On smaller scales, i.e. latitudinal bands, the differences become even larger, but the signals also substantially noisier, partly due to differences in the amplitudes of seasonal cycles observed by the two altimetry systems, TOPEX and ERS.

Also note that the SSB corrections in undeep coastal zones, where tide gauges are often located, might not be appropriate due to the changing wave climate. *Andersen and Scharroo* (2011) showed that the magnitude of the SSB is correlated with water depth and/or distance to the coast. Averaging crossovers only in the coastal zones ($<$ 200 km) yields intramission bias differences up to a millimeter. The largest bias differences between the coastal zones and the open ocean are obtained with the CLS SSB correction. The differences are not significant, but note that these values are with respect to the ERS1&2 sea surface heights, which in themselves are also likely to be affected by coastal effects.

The geographical depence of the SSBs and the intramission bias have two implications. First, if a globally averaged intramission bias is estimated, it is only applicaple to GMSL studies. For regional studies, a separate intramission bias should be estimated, but the size of the region has a lower bound depending on the altimeter noise in the considered area, because the estimates become noisier and therefore eventually lead to uncertainties in regional sea-level trends. It is therefore also not recommendable to use TOPEX-A in sea-level trend studies on sub-basin scales or in marginal seas. Second, it sets strong requirements for the geometry of the tide-gauge

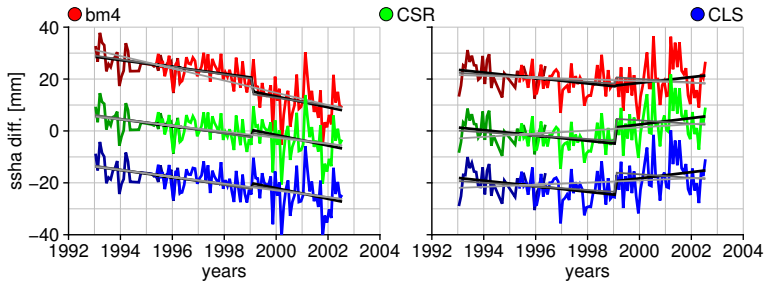

Figure 5.4: Right: Averaged crossover sea-level differences between TOPEX and ERS1&2 over the southern hemisphere. Left: Averaged sea-level differences over the northern hemisphere. Cal-1 is in all cases unapplied.

network for validation and calibration of altimeters. Overweighting certain regions might over- or underestimate the intramission biases and drifts of TOPEX. Likely, the uncertainties of 2-2.5 mm yr^{-1} of the intramission bias estimates of B17 and W15 are underestimated.

5.3.2 Tide-gauge comparison

First, the depence of the results on the averaging methods is discussed. It is determined under which circumstances a stable and reliable result is obtained. Then our methods are compared to those of crossover results and previous studies.

Models and averaging methods

The number of CPs varies strongly per tide gauge (Fig. 5.5). In combination with the variance of the residuals of the CP time series this leads to varying weights per tide gauge (Fig.5.6). Method m1 heavily weights the Pacific and the high-latitude regions, especially Europe, for which more CPs are available. In method m2, the high-latitude regions are still strongly represented, but the contribution of the Pacific is reduced. All tide gauges in method m3 are weighted equally and in the virtual station method (m4) a better geographical distribution is achieved. However, methods m3 and m4 are more sensitive to outliers due to remaining ocean signals, because tide gauges containing only a few CPs are weighted equally or possibly even heavier than tide gauges surrounded by many CPs. Methods m1, m2 and m4 all suffer from sensitivity to outliers in VLM estimates, due to the strongly enhanced weighting of a few stations. In all methods, large parts of the Pacific and Atlantic Oceans are underrepresented.

As a reference, the three models are computed through the time series with the cal-1 correction unapplied. The histograms of the drifts and biases estimated with models 1 (Fig. 5.7), model 2 (Fig. 5.8) and model 3 (Fig. 5.9) demonstrate the effects of the weighting methods. With model 1, a slightly larger drift is found for the bm3 SSB time series than for the other two. Despite the differences in the weighting methods, all model 1 results are statistically equivalent on a 95% confidence level

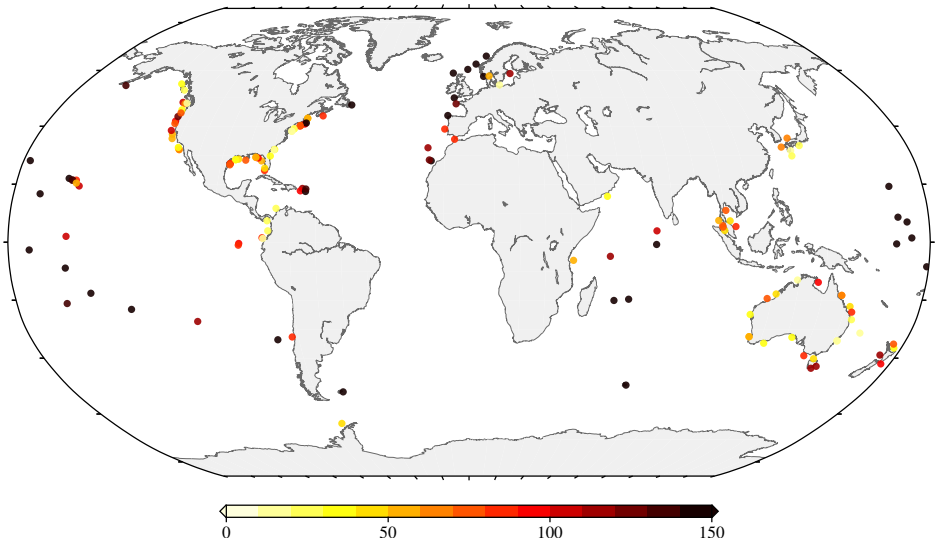

Figure 5.5: Number of CPs per tide gauge. Only stations with more than ten CPs are shown.

to the crossovers (Table 5.2). As shown by the crossover analysis, for the bm4 time series modelling a single drift should be sufficient. This suggests there is a drift in TOPEX and not in the ERS1&2 sea surface heights.

However, when additionally a bias (model 2) is estimated in the ALT-TG time series, different intermission biases are obtained than for the crossovers (Fig. 5.8). Indepent of the averaging method and the SSB correction the intramission biases become 4-6 mm lower than those found when using the crossovers. This leads to an TOPEX-A/B drift that is statistically indistinguishable from zero. As demonstrated in Sect. 5.3.1, the intramission bias is geographically varying. This, in combination with the over- and underweighting of certain regions in the tide-gauge validations could affect the estimated intramission bias. We argue that the intramission bias obtained from the crossovers is therefore more accurate. Besides geographical varying TOPEX-A/B bias, the problem of residual ocean signals in ALT-TG time series, which can be correlated between tide gauges, could also bias the results. ALT-TG bias estimates from CPs located in the tropical Pacific and along the American shore are especially prone to remaining signals from the consecutive 97-98 El Niño and 99-00 La Niña events, because they occurr around the time of the TOPEX-A/B transition.

The statistics of model 3 (Fig. 5.9) show that the averaging methods find large differences in the drift of TOPEX-B. The estimated biases are closer to zero with respect to model 2 and appear to be negatively correlated with the drifts in TOPEX-B. The drifts in TOPEX-A are negative for methods m1, m2 and m3 and slightly higher for m4, but all of them close to zero and statistically consistent between the methods. Large deviations between the methods suggest that geographically varying signals affect the global estimate. Additionally, for estimating an accurate drift through TOPEX-B, the time series appear to be too short.

A stability check is carried out to inspect the sensitivity of the methods to the

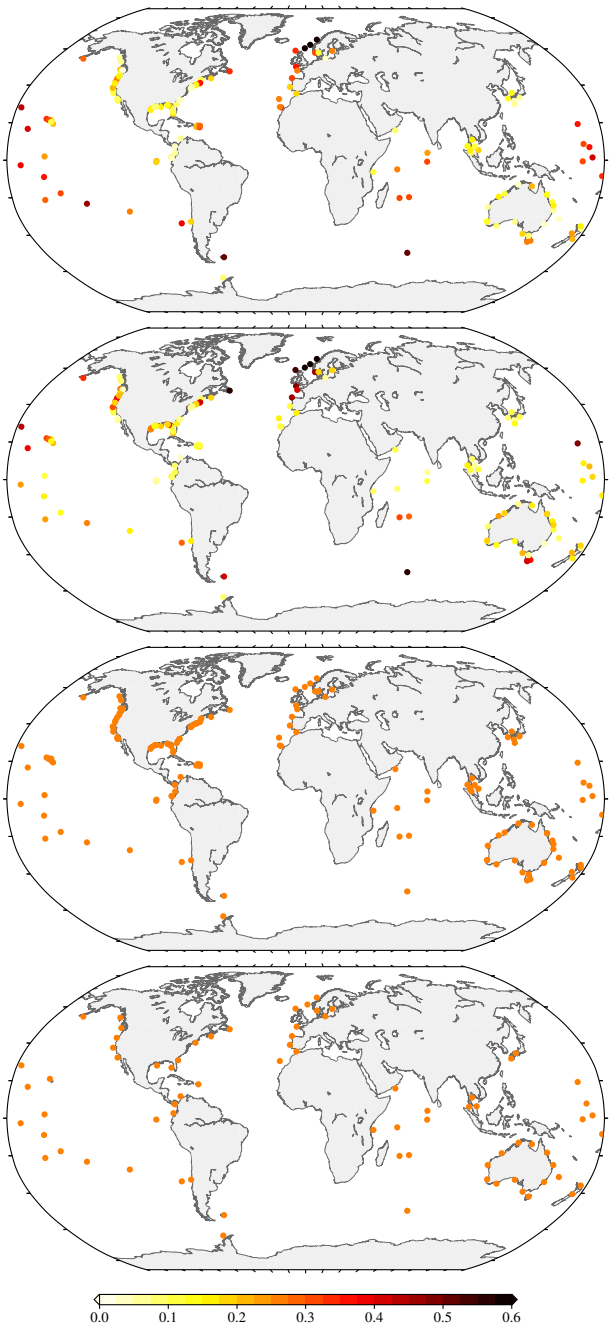

thresholds set by W15 for the standard deviation of the residuals and the TOPEX-A drift uncertainty and by us for the TOPEX-A/B drift uncertainty. In Fig. 5.10, the threshold on the standard deviation of the residuals is varied while we set the trend uncertainty thresholds to 100 mm yr^{-1}. In Fig. 5.11, the threshold on the trend uncertainty is varied, while the threshold on the standard deviation of the residuals

Figure 5.6: (Caption previous page.) Relative weight per tide gauge or virtual station. Top-left: m1 (mean). Top-right: m2 (variance weighting). Bottom-left: m3 (mean per station). Bottom-right: m4 (virtual stations).

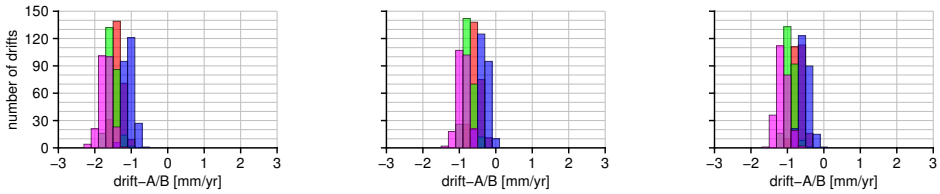

Figure 5.7: Histograms of the TOPEX A/B drift for the four averaging methods based on model 1 without cal-1 applied to TOPEX-A&B. On the left, at the middle and on the right the histograms for the bm4, CSR and CLS SSB corrections. In red, green, blue and purple the methods m1, m2, m3 and m4, respectively.

is set to 200 mm. Note that the nominal thresholds were 110 mm for the standard deviation and 10 mm yr^{-1} and 8 mm yr^{-1} for the trend uncertainties of TOPEX-A (model 1) and TOPEX-A/B (models 2 and 3), respectively. As already suggested by the histograms, it is difficult to constrain a drift for TOPEX-B. The TOPEX-B drifts between methods differ more than 1 mm yr^{-1} and the estimated drift strongly depends on the threshold for the standard deviation of residuals. This also appears to negatively correlate with the estimated intramission bias and slightly with the estimated TOPEX-A drift. Therefore, we do not recommend to apply model-1 for validation purposes, and certainly not for calibration. More stable results are obtained for models 2 and 3. The virtual station method (m4) yields a larger intramission bias at higher thresholds than the other methods. This could be related to the overall geometry of the network, but the method is also more prone to outliers as shown by the wider distributions in the histograms. The estimated TOPEX-A/B drift in both models 2 and 3 for all methods is statistically equivalent. Overall, the results of the variance weighting method (m2) yields the most stable result, i.e. it does not vary much when the thresholds are changed. However, this does not mean it is the best method, because the results are biased towards several stations at high latitudes (Fig. 5.6). In conclusion, we should only rely on tide-gauge comparisons when all methods give the statistically equivalent results, which is only the case for model 1.

Comparison with crossovers and previous studies

The crossover analysis (Tables 5.2 and 5.3) indicated that TOPEX GMSL is drifting with respect to ERS1&2 GMSL. The TOPEX-tide-gauge comparison is required to determine whether TOPEX or ERS1&2 GMSL is drifting. Since it is not possible to accurately constrain an intramission bias with a tide-gauge comparison, we will focus on the application of model 1. All statistics for the drifts and intramission biases discussed here are shown in Table 5.4. The histograms in Fig. 5.12 show that from four methods drifts are obtained between -0.8±0.3 and -1.4±0.3 mm yr^{-1} for the

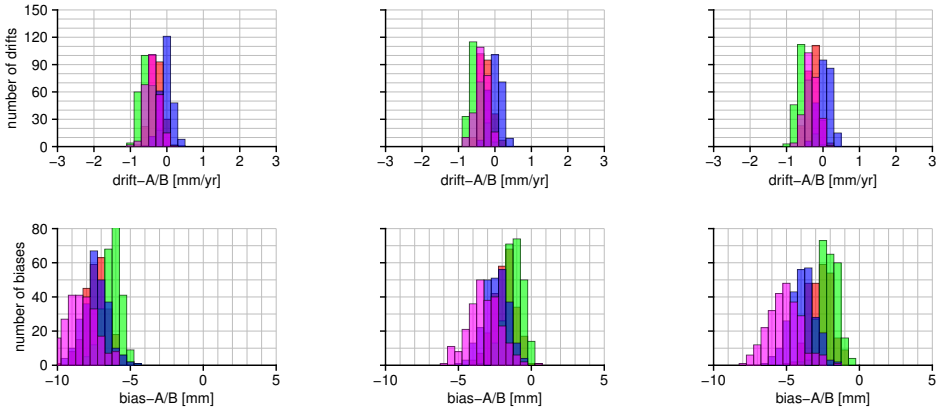

Figure 5.8: Histograms of the TOPEX A/B drift and intramission bias for the four averaging methods based on model 2 without cal-1 applied to TOPEX-A&B. On the left, at the middle and on the right the histograms for the bm4, CSR and CLS SSB corrections. In red, green, blue and purple the methods m1, m2, m3 and m4, respectively.

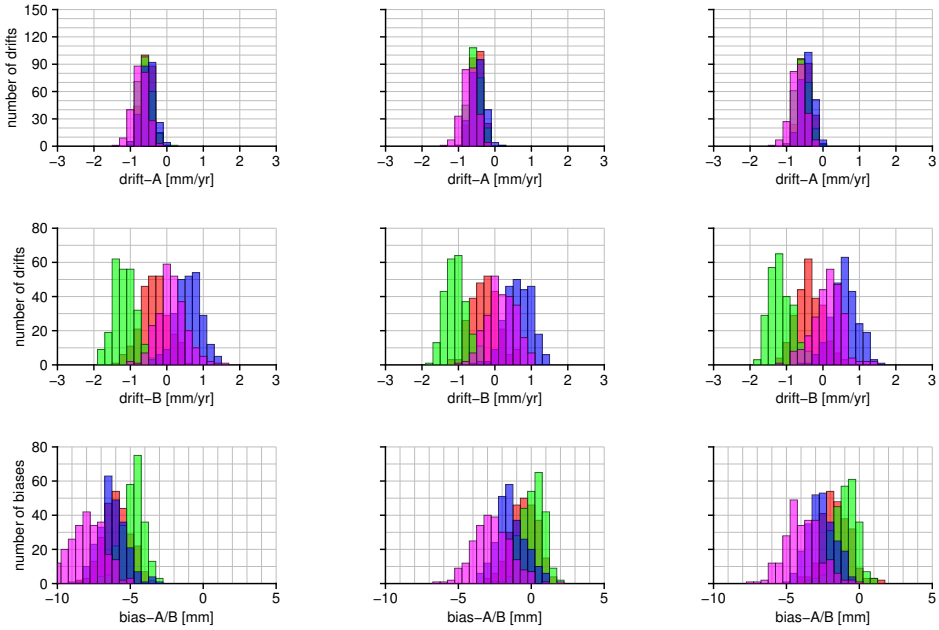

Figure 5.9: Histograms of the TOPEX A&B drifts and intramission bias for the four averaging methods based on model 3 without cal-1 applied to TOPEX-A&B. On the left, at the middle and on the right the histograms for the bm4, CSR and CLS SSB corrections. In red, green, blue and purple the methods m1, m2, m3 and m4, respectively.

case that the bm4 SSB correction is applied and cal-1 is only applied to TOPEX-B (as in Table 5.3). This is statistically equivalent to the crossover drift. Additionally, we computed model 1 for the TOPEX-tide-gauge comparison for the case that the CSR SSB correction is applied and cal-1 is unapplied to TOPEX-A&B. This allows for

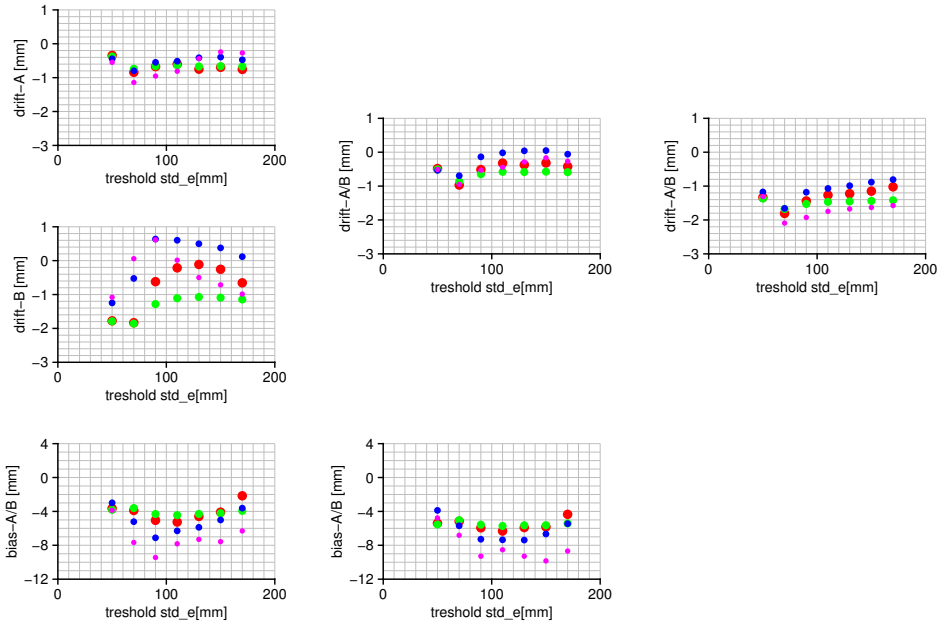

Figure 5.10: Sensitivity of the four averaging methods m1 (red), m2 (green), m3 (blue) and m4 (pink) to the threshold for the standard deviation of the residuals. On the left separate drifts are estimated for TOPEX-A&B and an intramission bias (model 3), in the center one drift for TOPEX is estimated and an intramission bias (model 2) and on the right only one drift is estimated (model 1).

another comparison with the crossovers and with B17. All four methods are equal on a 95% confidence level to both B17 and the crossovers. Note that the crossovers for the CSR SSB indicate a positively biased TOPEX-B GMSL with respect to TOPEX-A. Removal of the intramission bias as determined with the crossovers would lead to a stronger drift than found by B17. Both results confirm that the crossover drift is caused by TOPEX and not by ERS1&2 and therefore we recommend to calibrate TOPEX GMSL using the crossovers.

Even though no stable results are obtained from the tide-gauge comparison in combination with model 3, the results are given in Table 5.4 for an intercomparison with W15 and B17. W15 and B17 both computed two separate drifts and an intramission bias for TOPEX with cal-1 applied. The drifts for TOPEX-A in both studies are significantly higher than our tide-gauge- and crossover-derived drifts. The drifts obtained for TOPEX-B are difficult to constrain and therefore there is a huge spread, but all results are captured in two standard deviations of W15 results. Our tide-gauge-based intramission biases are just or just not statistically equivalent to the positive bias obtained by the crossovers. W15 finds a negative bias, which is statistically consistent with our tide-gauge results. B17 finds a much larger bias, which is probably related to their processing scheme. It remains unclear why W15s TOPEX-A drift is so much larger than our results, but it is probably a combination of several factors, like the weighting procedure, tide-gauge selection and VLM correction.

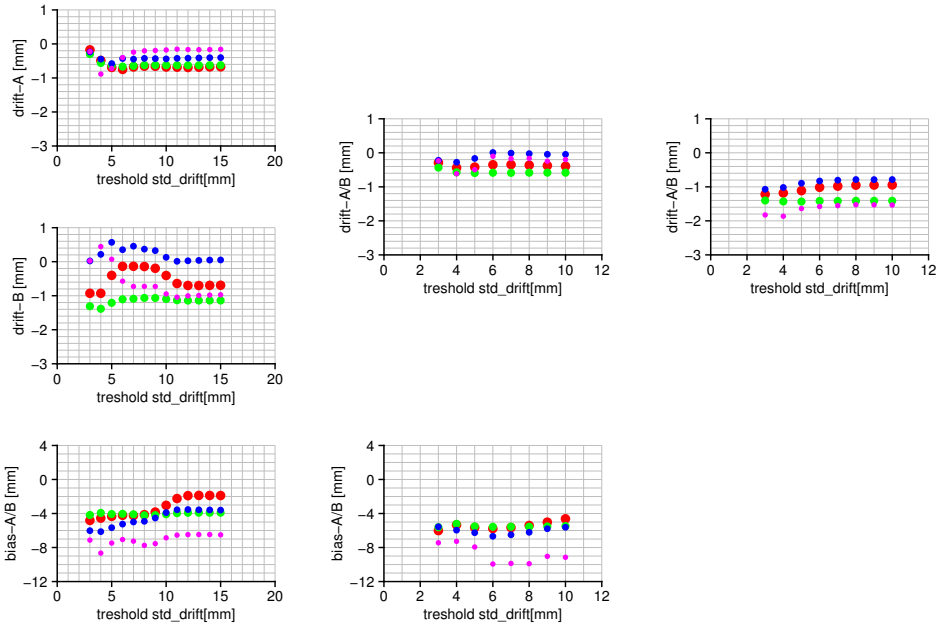

Figure 5.11: Sensitivity of the four averaging methods m1 (red), m2 (green), m3 (blue) and m4 (pink) to the threshold for the trend uncertainties. On the left separate drifts are estimated for TOPEX-A&B and an intramission bias (model 3), in the center one drift for TOPEX is estimated and an intramission bias (model 2) and on the right only one drift is estimated (model 1).

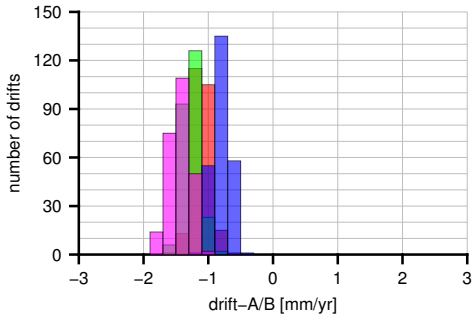

Figure 5.12: Histogram of the TOPEX-A/B drift for the four averaging methods based on the bm4 SSB and model 1. Cal-1 is only applied to TOPEX-B. In red, green, blue and purple the methods m1, m2, m3 and m4, respectively.

Model 3 is also computed after unapplying cal-1. The drift of TOPEX-A found by B17 is just outside the 95% confidence interval of our tide-gauge results. The TOPEX-B drift is similar to three averaging methods and the crossovers. For only two averaging methods the intramission bias is statistically similar to B17, while the crossovers yield an intramission bias of opposite sign. Since our results and those of B17 for model 1 are similar, but not model 3, it supports the notion that estimating two separate drifts and an intramission bias for TOPEX-A/B leads to unreliable

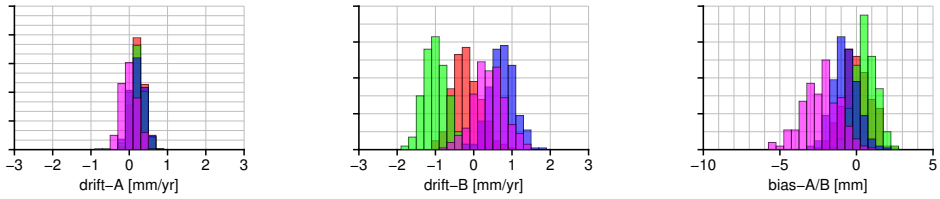

Figure 5.13: Histograms of the TOPEX-A&B drifts and intramission bias for the four averaging methods based on model 3 with the CSR SSB correction applied. Cal-1 is applied to TOPEX-A&B.

Table 5.4: Drift and biases for the W15 and B17 comparison with model 3 (Fig. 5.12) and for the crossover and B17 comparison with model 1 (Fig. 5.13).

	SSB	Method	Drift A [mm yr^{-1}]	Drift B [mm yr^{-1}]	Bias A/B [mm]
Model 1	bm4 No cal-1 TP-A	m1	-1.10±0.33		0
	bm4 No cal-1 TP-A	m2	-1.26±0.33		0
	bm4 No cal-1 TP-A	m3	-0.80±0.33		0
	bm4 No cal-1 TP-A	m4	-1.44±0.34		0
	bm4 No cal-1 TP-A	X-overs	-1.25±0.13		0
Model 1	CSR No cal-1	m1	-0.55±0.33		0
	CSR No cal-1	m2	-0.75±0.33		0
	CSR No cal-1	m3	-0.33±0.33		0
	CSR No cal-1	m4	-0.90±0.33		0
	CSR No cal-1	X-overs	-0.44±0.14		0
	B17		-0.45		0
Model 3	CSR	m1	0.24±0.34	-0.19±0.47	0.0±0.9
	CSR	m2	0.21±0.35	-0.99±0.43	0.6±0.7
	CSR	m3	0.21±0.35	0.75±0.45	-0.7±0.8
	CSR	m4	-0.01±0.36	0.39±0.50	-2.3±1.2
	CSR	X-overs	-0.49±0.31	-0.27±0.69	3.7±1.8
	W15		1.49±0.49	0.92±0.93	-2.9±2.5
	B17		1.02	0.53	-8±2
Model 3	CSR No cal-1	m1	-0.50±0.34	-0.27±0.47	-0.5±0.9
	CSR No cal-1	m2	-0.54±0.35	-1.07±0.42	0.1±0.7
	CSR No cal-1	m3	-0.48±0.35	0.64±0.47	-1.4±1.0
	CSR No cal-1	m4	-0.71±0.36	0.18±0.49	-2.7±1.3
	CSR No cal-1	X-overs	-1.19±0.27	-0.64±0.60	3.9±1.5
	B17		0.25	0.23	-5±2

results.

5.3.3 Global mean sea level

A time series of GMSL is computed using the TOPEX, Jason-1 and Jason-2 data from the RADS database with the correction applied as in Table 5.1. For the Jason-1&2 the Geophysical Data Record version E (GDR-E) orbits are taken and the SSB correction from *Tran et al.* (2012) is used. Fig. 5.14 shows the effects of the removal of cal-1 and the calibration with ERS1&2 on the GMSL record. Table 5.5 lists the corresponding trends and accelerations. In the original setting, a trend is obtained of 2.8±0.4 mm yr^{-1}, which exludes a GIA correction of approximately 0.3 mm yr^{-1}. There is no significant acceleration detected in GMSL based on a 95% confidence

level. By not applying cal-1 the trend decreases by 0.16 mm yr^{-1} and a significant acceleration of 0.052±0.013 mm yr^{-2} is detected, which corresponds closely to the value of 0.051±0.020 mm yr^{-1} of B17.

As observed by the ERS1&2 crossovers and confirmed by the tide-gauge comparison, a significant drift and a TOPEX-A/B intramission bias are present after the removal of cal-1. The intramission biases from model 2 (Table 5.2) are subtracted from the TOPEX-B GMSL time series and accordingly a drift correction is applied to the whole TOPEX time series. For all of the SSB corrections this lead to comparable GMSL trends and accelerations and all of the acceleration become statistically insignificant on a 95% confidence interval. If the cal-1 is only not applied to TOPEX-A, while using the bm4 SSB correction, the removal of only one trend through TOPEX-A&B and no intramission bias would suffice. This leads to a statistically equivalent trend and acceleration with respect to the other three calibrated solutions. Based on the results of *Nerem et al.* (2018), the acceleration increases when the effects of the Mount Pinatubo eruption in 1991 are taken into account, which cause our acceleration estimates to become just significant. However, a consecutive correction for ENSO leads to a decrease in the accelerations, which makes them likely insignificant again.

Table 5.5: GMSL trends and accelerations before and after cal-1 and drift corrections based on the crossovers with ERS1&2.

	SSB	Trend [mm yr^{-1}]	Acceleration [mm yr^{-2}]
Original	CSR	2.8±0.4	0.017±0.013
No cal-1	CSR	2.7±0.4	0.052±0.013
No cal-1 + model 2	CSR	2.8±0.4	0.017±0.013
No cal-1 + model 2	CLS	2.8±0.4	0.018±0.013
No cal-1 + model 2	bm4	2.8±0.4	0.019±0.013
No cal-1 TP-A + model 1	bm4	2.9±0.4	0.015±0.014

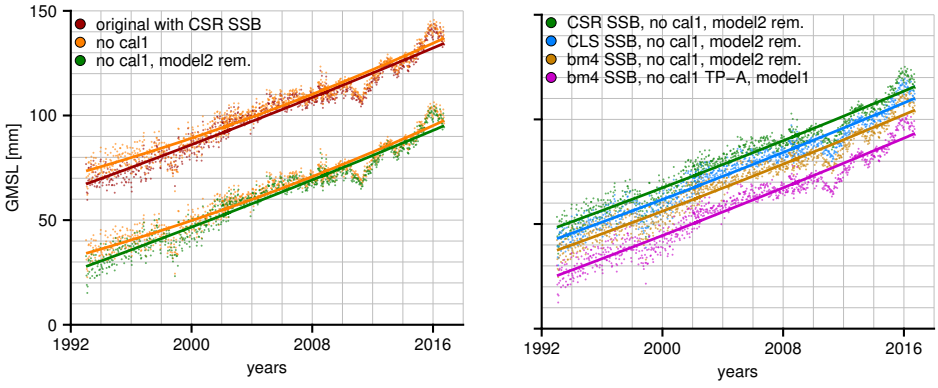

Figure 5.14: Residuals time series after removing the seasonal cycles for crossover time series based on various SSB, cal-1 and model corrections.

5.4 Conclusions

This study proposes a calibration method for TOPEX GMSL time series. The calibration method is based on a crossover analysis with the ERS1&2 satellites. We focussed on the effects of the sea state bias corrections, the estimation of a TOPEX-A/B intramission bias an possible drifts in the TOPEX altimeter. Then a tide-gauge comparison using four averaging methods is applied to investigate whether it is possible to calibrate or validate TOPEX GMSL using tide gauges. The results of the tide-gauge comparison are compared with the crossover analysis. Both the results of the crossover analysis and the tide-gauge comparison have been compared to the studies of W15 and B17.

The TOPEX-ERS1&2 crossovers indicate that there is clear U-shape drift in the TOPEX-A time series and that not applying cal-1 as done in B17 is justified. The remaining drift in the crossovers is similar to the one found by the tide-gauge comparison of B17. However, models indicate that next to a drift, the estimation of an TOPEX-A/B intramission bias is required to obtain a consistent drift of about -1.1 mm yr^{-1}, independently of the SSB correction applied. A similar drift is also obtained without estimating a bias, by using the bm4 SSB correction while only removing the cal-1 correction of TOPEX-A. These approaches are only applicable to GMSL, because regional differences in the intramission bias are observed. Regional intramission biases can be estimated, but we recommend caution, because the uncertainty increases substantially over sub-basin-scale regions.

These regional differences have a profound effect on the estimation of the intramission bias using tide gauges. The geometry of the network in combination with the averaging method applied tends to overweight certain regions. Besides these issues, remaining ocean signals in ALT-TG time series that correlate between tide gauges or control points could bias the overall solution. Note that two ENSO events, an El Niño (1997-1998) and a La Niña (1999-2000), occurred around the time of the TOPEX-A/B transition, which could affect the estimation of the TOPEX-A/B intramission bias. The estimated TOPEX-B drift varies strongly between the four ALT-TG averaging methods applied and is therefore difficult to constrain. Separately estimating TOPEX-A&B drifts and intramission biases from tide gauges, as done by W15, is therefore not recommended. Even though the TOPEX-A drift is stable among four averaging methods, the drift is significantly smaller than those obtained by W15. The discrepancies may be related to the VLM correction for the tide gauge, but the cause is unresolved. By only estimating a single drift through TOPEX-A&B, similar results are obtained as with the crossovers and B17.

We therefore calibrate TOPEX with the ERS1&2 crossovers. Either cal-1 is removed from both TOPEX-A&B and accordingly a drift over the whole TOPEX period is removed together with an intramission bias, where the magnitude depends on the SSB correction. Or the bm4 SSB model is applied and cal-1 is only removed over the TOPEX-A period. Then a drift of 1.25±0.13 mm yr^{-1} is removed. Both solutions lead to statistically consistent GMSL trends and accelerations. This has implications for the trend and acceleration estimated from GMSL records. The removal of cal-

1 decreases the estimated trend by 0.1-0.2 mm yr^{-1}, but this is restored again by the crossover calibration. The removal of cal-1 also yields a significant acceleration, but the ERS1&2 calibration reduces the acceleration so that it becomes statistically insignificant again.

Chapter 6

Conclusions and recommendations

This chapter consists of two parts. Sect. 6.1 lists and answers the research questions posed in the first chapter. Sect. 6.2 provides recommendations for future work and possible improvements to the research.

6.1 Conclusions

Can the sea-level budget be closed on a regional scale in the North Atlantic Ocean using satellite altimetry, satellite gravimetry and Argo float observations? To investigate this research question the North Atlantic Ocean has been split into ten regions, such that the uncertainties on the trends do not exceed 1 mm yr^{-1}. For all three observation systems, state-of-the-art or novel post-processing techniques have been applied to obtain adequate solutions for the sum of the GRACE mass and Argo steric components and the Jason total sea level. Budget closure is assumed if the sum of the component equals the total, or absolute, sea level over the region on a 95% confidence level, based on the uncertainties of all three observation systems. The uncertainties for mean steric and mean total sea level are approximated using well-known correlation functions.

The primary focus for budget closure lies, however, on the mass component derived from GRACE. Filtering of the GRACE solutions is required to suppress noise due to stripes in the gravity fields. An anisotropic Wiener filter is used to reduce the loss of resolution, which is large if a Gaussian filter would be applied. Four different solutions are compared: the standard degree-96 Center for Space Research DDK5 filtered gravity field (CSR-DDK) as a reference and furthermore the Wiener-filtered degree-60 CSR (CSR60-W), degree-96 CSR (CSR96-W) and degree-90 Institute of Theoretical geodesy and Satellite Geodesy (ITSG90-W) solutions. We determine that the summation of Argo steric sea level with ITSG90-W mass closed best the sea level budget with Jason-1&2 altimeters. Using ITSG90-W in nine-out-of-ten sub-basins the sea level trend budget is closed when an uncertainty of 20% on the Glacial Isostatic Adjustment (GIA) correction is assumed. In seven-out-of-ten regions the annual amplitudes are statistically comparable. After subtracting linear trends and annual cycles, the sum of ITSG90-W mass and Argo steric sea level explains 24-53% of the

residuals in Jason-1&2 mean sea levels.

The trend budget in the region next to the Gibraltar strait is not closed. We suggest that this is due to density changes at depths below the considered 1000 m, because of saline water influx from the Mediterranean. Temperature and salinity measurements below 1000 m are not considered, because not enough Argo floats descended deep enough in the first years of the considered period. In the northernmost regions the annual amplitudes of Argo and GRACE do not equal those of altimetry. It is not clear why the amplitude budget does not close, but possible culprits are GRACE filters that destroy part of the signal, yearly deep convections events and Argo interpolation issues. On interannual scales, Argo+GRACE and altimetry are both capable to detect centimeter-level signals in sea level, such as north-south shifts of the Gulf Stream. However, close to the Amazon basin altimetry detects some additional variability, which is likely not captured due to a sampling issue of Argo.

To summarize, in most of the North Atlantic Ocean sea level budgets can be closed at sub-basin scales. However, steric estimates over a larger depth are required to find the definitive cause for the non-closures. Even smaller scales (< 1/10th North Atlantic) and meridionally-oriented averaging regions are not considered, because the trend uncertainties become larger than 1 mm yr^{-1}. We expect however that in those cases stronger filters are required to suppress the striping noise in GRACE, which likely destroys part of the signal. From the Argo perspective improvements are expected, because the number of floats is still increasing after 2014 and the larger depths are better sampled.

How can we consistently separate the mass and the steric component of sea level on continental shelves and in coastal regions?

This question is answered by using the Tropical Asian Seas (TAS) as a case study, because it is sufficiently large to contruct sea level budgets. The TAS is furthermore an interesting study area for its ocean dynamics and large sea level trends. The region is split into four areas, of which two are shallow (<200 m) and two are deep (>1000 m).

Similar to the budgets over the open ocean, absolute sea level and the mass component are derived from Jason altimetry and GRACE. Since correlation scales in complex regions like the TAS differ from those over the open ocean, variograms are used to estimate covariance parameters between Jason altimetry measurements. For GRACE the uncertainties are propagated from the formal variance-covariance matrices. Additionally, a bottom deformation correction is applied to GRACE, because of the large mass variability in the region. Temperature and salinity estimates from eight ocean reanalyses are used to estimate steric sea level and their variances.

The time series match quite well, but the seasonal signals and the trends statistically differ from each other. Therefore the variances of the three time series are used in a least-squares inversion to estimate consistently the mass and steric components of sea level. This leads to a statistically-weighted mass time series that still strongly resembles the GRACE time series, but a statistically-weighted steric time series that differs from the ocean reanalysis time series.

We investigate interannual dynamics in the steric and mass components by regressing two principal components of the Pacific equatorial wind stress and the Dipole Mode Index (DMI). In the South China Sea, we cannot explain the interannual variability with these components and sea level is apparently driven by other processes. In the deep Banda and Celebes Seas, there is large steric variability which is related to the DMI and the Pacific equatorial wind stress. The shallow regions exhibit a large mass signal, which is primarily related to the first principal component and coupled to the El Niño Southern Oscillation (ENSO).

The mass and steric trends are reduced by 0-3 mm yr^{-1} by including the two principal components of wind stress and the DMI into the regression. Additionally, a small mass signal is caused by the nodal cycle which affects the trends by another 1 mm yr^{-1}. The residual mass trends are close to the trends estimated by mass-redistribution models. Omission of the TAS in global sea level budgets leads to a bias of 0.3 mm yr^{-1}.

In conclusion, statistically weighting the time series of sea level components from two observing systems (GRACE and Jason altimetry) and from ocean reanalyses allows to get a consistent separation between mass and steric sea level. This is primarily required to find consistent trends and annual signals, while most of the interannual variability in the statistically-weighted time series can be explained with well-known oceanic indices. The estimated mass trend can be accounted for by models and regression of the same indices.

Can we improve the ALT-TG-derived and GNSS-derived VLM estimates at tide gauges?

Using a cross-validation, the consistency of altimetry-tide gauge (ALT-TG) and Global Navigation Satellite System (GNSS) methods has been investigated. A number of improvements for both methods have been suggested. The Nevada Geodetic Laboratory (NGL) database has been used for the GNSS trends and they are compared to the commonly used University of La Rochelle trends. Besides the larger number of GNSS trends, the processing procedure of NGL makes the trend estimates less sensitive to discontinuities caused by earthquakes or equipment changes. Eight methods have been compared to combine nearby GNSS trends into a single VLM trend estimate at the tide gauge. It is found that taking the median of the GNSS trend provides the best agreement with the ALT-TG trends.

In ALT-TG time series interannual signals related ocean dynamics are present, which might bias VLM trend estimates. In order to reduce this, thresholds are set on the correlation between along-track altimetry and tide-gauge time series, so that surrounding altimetry time series are only considered if their oceanic signals are similar to those at the tide gauge. Per tide gauge the remaining altimetry time series are averaged and subtracted from the tide-gauge record. Note that in case of a discontinuity in the tide-gauge record, the chosen thresholds automatically remove the tide gauge as well. We are indeed able to reduce the oceanic signals in ALT-TG time series and find spatially coherent changes in the trend, but the agreement with GNSS trends is not significantly improved in a statistical sense. However, the correlation

threshold also acts as a filter to remove problematic ALT-TG trends. This reduces the number of tide gauges for which trends are computed, but enhances the reliability of the estimated trends.

In conclusion, the consistency between the ALT-TG and GNSS VLM trends is improved by reducing the RMS of the differences from 1.47 mm yr^{-1} (*Wöppelmann and Marcos*, 2016) to 1.22 mm yr^{-1} for a larger number of stations. The cross-validation shows that a large part of the improvement can be attributed to using the median of the surrounding GNSS stations instead of the nearest station. Applying correlation thresholds and weights do not further reduce the RMS of the differences. Correcting for non-linear VLM due to present-day mass redistribution reduces the mean of ALT-TG and GNSS trend differences.

How to process and calibrate GMSL derived from the TOPEX altimeter using crossovers, tide gauges and VLM estimates?

Due to issues with the point target response of the TOPEX side-A altimeter, drifts of non-geophysical origin contaminate the GMSL record. There is also a discontinuity present between TOPEX-A&B, which requires the removal of an intramission bias. Two methods to cope with these problems are investigated: 1) the calibration of separate TOPEX-A&B drifts and an intramission bias estimate based on a comparison with tide gauges and 2) the removal of an internal calibration (cal-1) from the whole TOPEX time series. We analyse the two strategies by means of a crossover analyis with ERS1&2 sea surface heights.

Since the intramission bias is spatially varying and the tide-gauge calibration tends to overweight certain geographical regions, the accurate estimation of an intramission bias is challenging. Additionally, when relying on tide gauges for calibration, the intramission bias and two short-term drifts for TOPEX-A&B are likely affected by remaining oceanic signals in the difference ALT-TG time series. Therefore, we show that solution 1 is not suitable to calibrate TOPEX GMSL.

The crossover analysis with ERS1&2 sea surface heights shows that not applying cal-1 over the TOPEX period is justified as in solution 2, so it is removed. However, the analysis also reveals that the intramission bias depends on the Sea State Bias (SSB) correction and that there is a negative drift of TOPEX with respect to ERS. By estimating a single drift over the TOPEX period and an intramission bias, a drift of more than 1 mm yr^{-1} is found that is independent of the SSB correction. A similar drift is obtained without estimating an intramission bias if the bm4 SSB correction (*Gaspar et al.*, 1994) is used and cal-1 is only applied to TOPEX-B. The latter is confirmed by the presence of a drift estimated from a comparison with tide gauges.

Our results have strong implications for the acceleration detected in the GMSL record. If cal-1 is unapplied to the whole TOPEX time series, an acceleration in sea level is detectable in case the commonly used CSR and CLS SSB corrections are applied. However, after calibration with the intramission biases and the drifts found by the crossover analysis, the acceleration becomes statistically insignificant.

In summary, findings from TOPEX-ERS crossovers and a comparison with tide gauges suggest that there is a drift in the TOPEX GMSL record if cal-1 is not applied.

If any of the available SSB corrections is used and cal-1 is not applied, a single drift over TOPEX-A&B and an intramission bias should be corrected for. Similar results are obtained by only removing a TOPEX-A&B drift when the bm4 SSB correction is used and cal-1 is applied to TOPEX-B alone. Tide gauges should not be used to estimate two separate drifts for TOPEX-A&B and an intramission bias, but only used for validating a single drift over the whole TOPEX record. After calibration with the crossover results, there is no significant acceleration detectable in the GMSL record.

6.2 Recommendations

In the North Atlantic sea level budget study it is assumed that the contribution of sea floor deformation to absolute sea level is only caused by GIA. The sea floor deformation due to present-day ice mass loss is neglected. The time series of GRACE are currently 3 years longer and even though those solutions are of poorer quality, the uncertainties on the trends and the amplitudes of the annual cycle likely decrease. Besides that, the ice mass loss of Greenland has been accelerating (*Svendsen et al.*, 2013). Both could cause sea floor deformation to have a significant effect on several of the considered sub-basins. Therefore we recommend to apply either a correction to GRACE or altimetry for sea floor deformation due to loading, which can be computed using models (*Riva et al.*, 2017; *Frederikse et al.*, 2017) or inferred directly from GRACE (*Fenoglio-Marc et al.*, 2012). Note that the GRACE-derived correction does correct for ocean floor deformation caused by rotation changes.

In this thesis, the steric and mass components of the budgets have been associated with ocean dynamics (ENSO, Gulf stream variability) and possibly salinity variations (from the Gibraltar Strait). We recommend to expand both budget studies to other parts of the ocean to further understand sea level behaviour at regional spatial scales and various temporal scales. The approach here applied to the TAS can be applied on continental regions and marginal seas where no data-driven budget studies have been performed yet like the Yellow-Bohai seas, the Gulf of Mexico and the North Sea. The approach we applied to the North Atlantic Ocean could be applied to open-ocean regions where interannual variations are expected to occur such as the Kuroshio and the Algulhas currents. Furthermore, as demonstrated for the Gibraltar outflow region, budget studies can give insight and help to contrain deep-steric expansion.

Having multiple GNSS stations around a tide gauge provides only limited insight in local VLM variability. For single GNSS stations, in the absence of regular levelling campaigns, it cannot be assumed that the relative VLM between GNSS station and tide gauge is zero. Since the launch of Sentinel-1 in 2014, Synthetic Aperture Radar (SAR) data is available worldwide at a sampling rate of 6 (two satellites) to 12 (one satellite) days. By using interferograms derived from SAR data, we expect that the relative VLM between GNSS and tide-gauge stations can be estimated over the last few years. This is propably not long enough yet to estimate an accurate (< 1 mm yr^{-1}) relative trend, therefore we suggest two solutions. Over several tide gauge sites, SAR data are available from other satellites like ERS1&2, Envisat, Radarsat

and TerraSAR-X, so time series could be long enough to estimate accurate trends. Secondly, the short Sentinel-1 time series can possibly be used to estimate VLM correlation scales, which help to enhance the uncertainty propagation.

The correlation thresholds, which were set to reduce the remaining oceanic signal in ALT-TG time series, did not significantly reduce the RMS of differences between VLM estimated from ALT-TG and GNSS time series. However, coherent differences in ALT-TG VLM trends at several coastal regions are observed e.g., Norway and the US east coast. This suggests that for several regions an improvement is possible and therefore regional statistics should be computed. Furthermore, it appears that the GNSS-derived VLM trends at tide gauges are too noisy to properly validate if there is any improvement caused by setting correlation thresholds. A manual selection of the best GNSS records is suggested to evaluate the improvements due to ALT-TG thresholding and weighting.

Boundary waves propagate over the continential shelves such that their signals are largest at many tide-gauge locations. The first accurate altimetry measurements are made several 10s of kilometers from the coast and therefore differencing them with tide gauge leaves an oceanic signal in the time series, which affects the estimated ALT-TG VLM trends. Sentinel-3 measurements enable the use of a delay/Doppler or even fully-focussed SAR processing to enhance the along-track resolution. Reliable sea surface height measurements can therefore be made closer to the coast. Using Sentinel-3 data, it should be possible to inspect the shape and size of boundary waves as function of distance from the coast. This could help to correct or identify problematic ALT-TG time series. Furthermore, once the Sentinel time series are long enough, VLM trends can be estimated with substantially smaller correlated noise. As an alternative solution, ALT-TG VLM trends can be estimated from regressions that include relevant oceanic indices like ENSO 3.4.

Appendices

Appendix A

The Wiener filter is in principle a joint inversion of the spherical harmonic coefficients of the background field $\hat{x}_b$ and those of the time-varying gravity field $\hat{x}$. Suppose that C_x is the error variance-covariance matrix of $\hat{x}$ and D_x the signal variance-covariance matrix, then the filtered coefficients $\hat{x}_f$ are expressed as:

$$\hat{x}_f = (C_x^{-1} + D_x^{-1})^{-1} C_x^{-1} \hat{x} + (C_x^{-1} + D_x^{-1})^{-1} D_x^{-1} \hat{x}_b. \tag{6.1}$$

Assuming the spherical harmonic coefficients of the background field are zero, this equation reduces to Eq. 2.27. The associated variance-covariance matrix $C_{x,f}$ is computed using:

$$\begin{aligned} C_{x,f} = {} & (C_x^{-1} + D_x^{-1})^{-1} C_x^{-1} C_x ((C_x^{-1} + D_x^{-1})^{-1} C_x^{-1})^T \\ & + (C_x^{-1} + D_x^{-1})^{-1} D_x^{-1} D_x ((C_x^{-1} + D_x^{-1})^{-1} D_x^{-1})^T \ . \end{aligned} \tag{6.2}$$

Since the matrices $(C_x^{-1} + D_x^{-1})^{-1}$ and C_x^{-1} are symmetric, we obtain:

$$\begin{aligned} C_{x,f} = {} & (C_x^{-1} + D_x^{-1})^{-1} C_x^{-1} C_x C_x^{-1} (C_x^{-1} + D_x^{-1})^{-1} \\ & + (C_x^{-1} + D_x^{-1})^{-1} D_x^{-1} D_x D_x^{-1} (C_x^{-1} + D_x^{-1})^{-1} \ , \end{aligned} \tag{6.3}$$

which is further simplified by using the identity $C_x^{-1} C_x = I$ to:

$$\begin{aligned} C_{x,f} = {} & (C_x^{-1} + D_x^{-1})^{-1} C_x^{-1} (C_x^{-1} + D_x^{-1})^{-1} \\ & + (C_x^{-1} + D_x^{-1})^{-1} D_x^{-1} (C_x^{-1} + D_x^{-1})^{-1} \ . \end{aligned} \tag{6.4}$$

Finally, this equation is rewritten, such that:

$$C_{x,f} = (C_x^{-1} + D_x^{-1})^{-1} (C_x^{-1} + D_x^{-1}) (C_x^{-1} + D_x^{-1})^{-1}, \tag{6.5}$$

which is identical to Eq. 2.28.

Appendix B

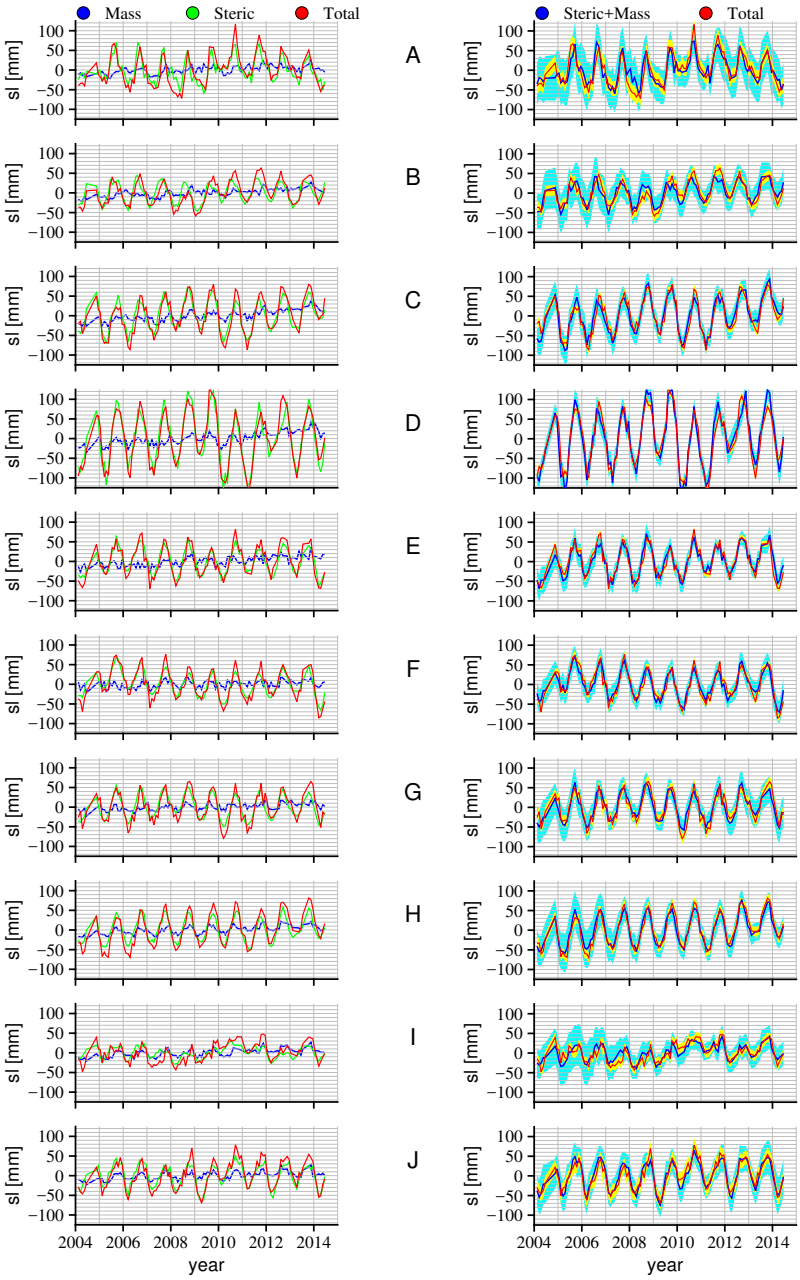

Figure B1: Time series of sea level budgets of the sub-basins. In both columns the red line indicates the MSL from altimetry. In the left column the green line indicates the steric sea level from Argo and the blue line respectively the MC from ITSG90-W. In the right column the blue line represents the sum of the steric and the mass components. The corresponding 95% confidence intervals are given in yellow and light blue.

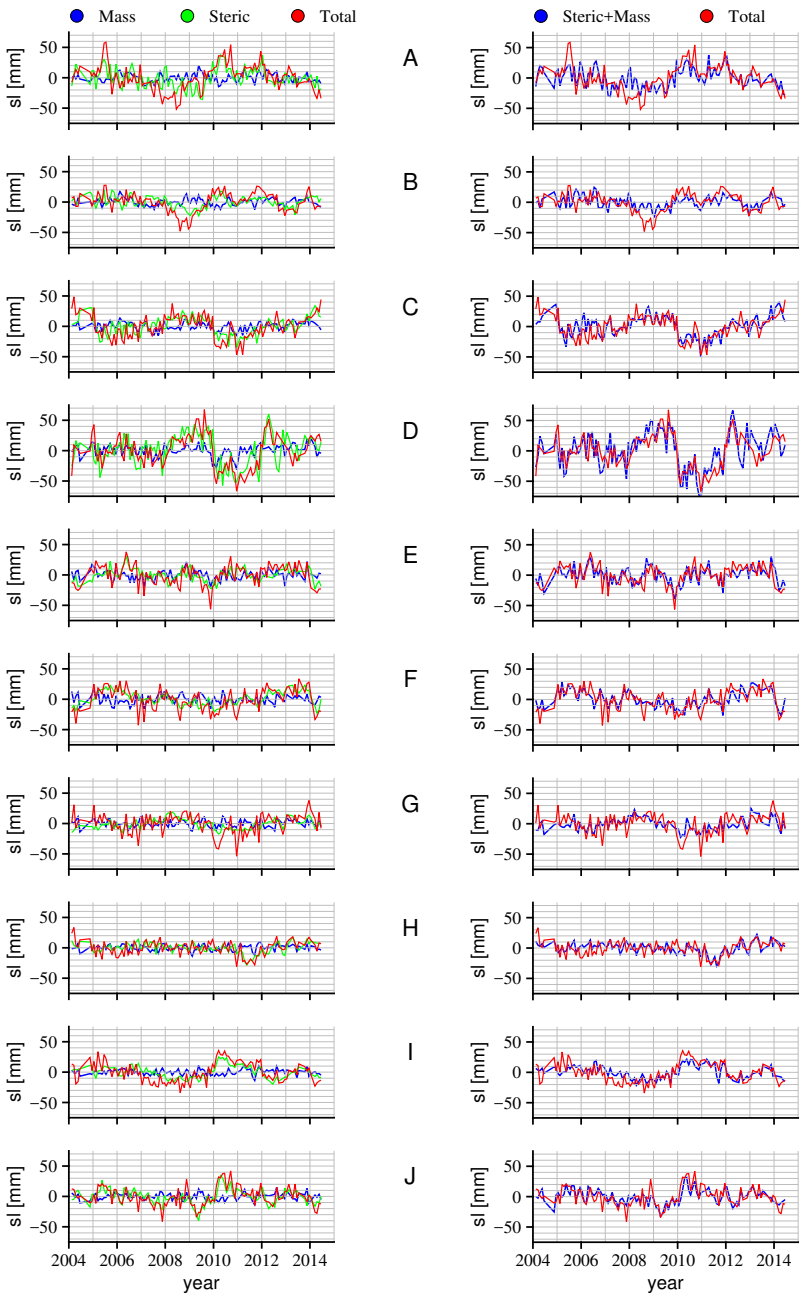

Figure B2: Time series of residual sea level budgets of the sub-basins. In both columns the red line indicates the MSL from altimetry. In the left column the green line indicates the steric sea level from Argo and the blue line respectively the MC from ITSG90-W. In the right column the blue line represents the sum of the steric and the mass components.

Appendix C

This appendix contains figures related to Chapter 3.

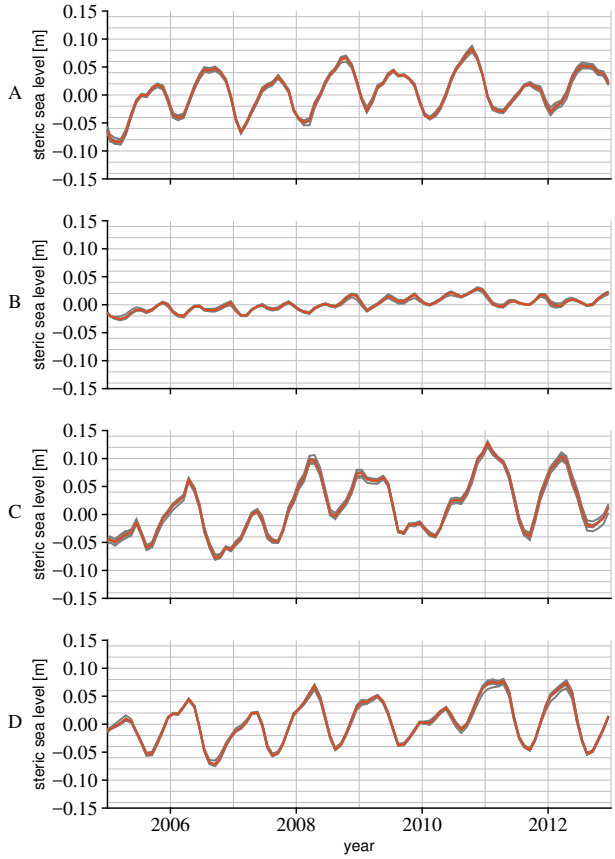

Figure C1: In gray: Eight steric sea level time series computed from the combination of seven-of-eight reanalysis products. For each time series another reanalysis is left out. In red: the time series averaged over all eight products used in this study. The South China Sea, Thailand-Java, Banda-Celebes and Timor-Arafura regions are respectively indicated with A, B, C and D.

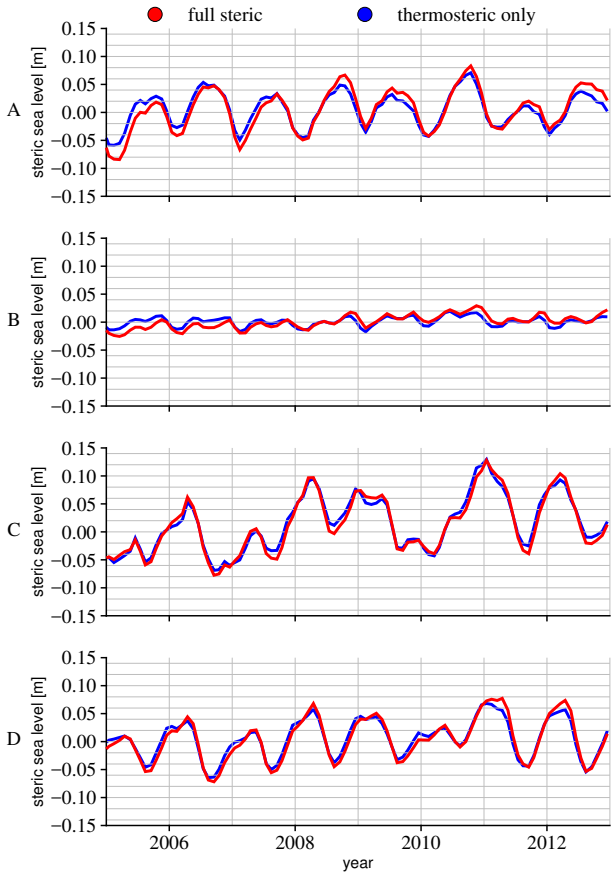

Figure C2: Comparison of time series of steric sea level and thermosteric sea level for all four regions. The South China Sea, Thailand-Java, Banda-Celebes and Timor-Arafura regions are respectively indicated with A, B, C and D.

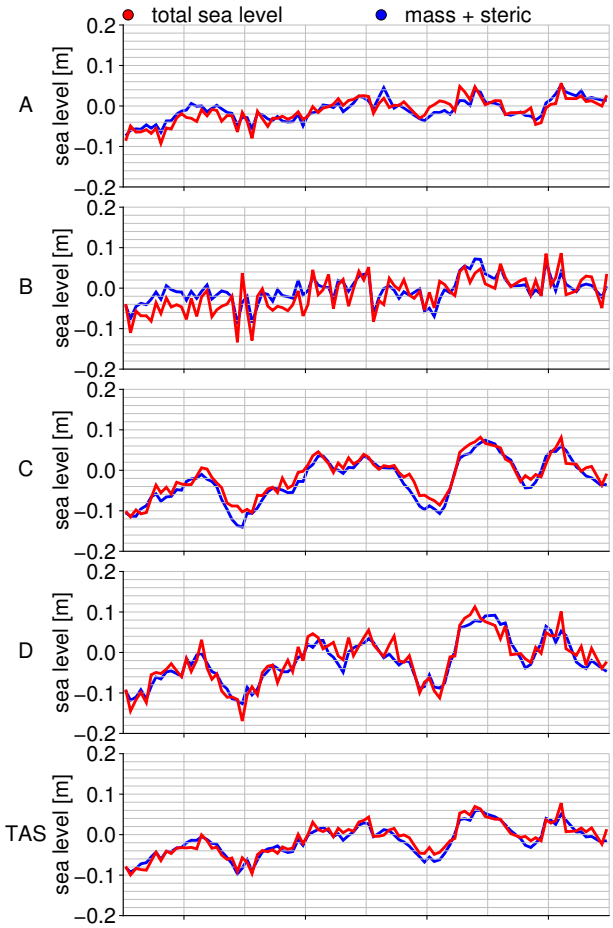

Figure C3: Sea level time series for the subregions and the total TAS after subtracting the annual and semi-annual cycles. The South China Sea, Thailand-Java, Banda-Celebes and Timor-Arafura regions are respectively indicated with A, B, C and D. In blue GRACE mass + steric sea level from the reanalyses. In red altimetry-derived total sea level.

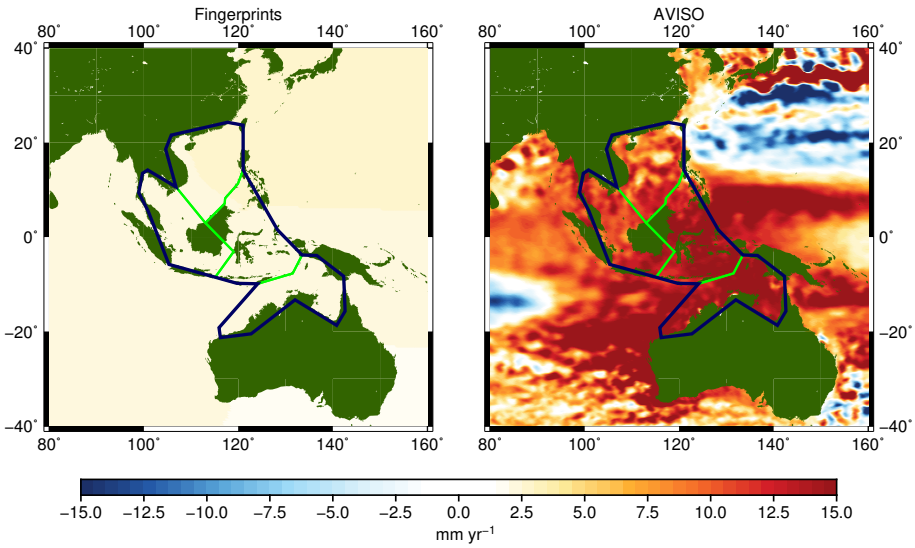

Figure C4: Trends obtained from the sum of the mass redistribution fingerprints on the left. Total sea level trend obtained from monthly gridded SSALTO/DUACS multimission altimetry products on the right (obtained from: `https://www.aviso.altimetry.fr/en/data/product-information/information-about-mono-and-multi-mission-processing/ssaltoduacs-multimission-altimeter-products.html`).

Appendix D

The latitude-dependent intermission biases are computed from 1/8 degree latitudinally averaged sea surface height differences between TOPEX and Jason-1 (TP-J1) and Jason-1 and Jason-2 (J1-J2). For the TP-J1 bias four separate functions are fitted for ascending tracks and four for the descending tracks, while for J1-J2 a single function is estimated. Depending on the geophysical corrections and the processing of the altimetry data, not all parameters are statistically different from zero based on variances of the residuals. However, to be consistent with the study of *Ablain et al.* (2015), we maintain the functions as such.

Table D1: Values for the parameters of the latitudinal intermission bias correction. These numbers are added to the sea surface height anomalies of the respective satellites. TP asc. and TP desc. indicates the function variables that should be added to the ascending and descending tracks of TOPEX/POSEIDON using Eq. (4.4), respectively. J2 indicates the function variables to be used for Jason-2.

	TP asc.		TP desc.		Jason-2	
Parameter	Lat(deg)	Value	Lat(deg)	Value	Lat(deg)	Value
c_0 (mm)	(-66.2,-1.5)	80.3	(-66.2,-1.5)	77.3	(-66.2,66.2)	98.1
c_1 (mm deg^{-1})		$-2.3\cdot10^{-1}$		$-1.7\cdot10^{-1}$		$-9.3\cdot10^{-2}$
c_2 (mm deg^{-2})		$-1.1\cdot10^{-2}$		$1.2\cdot10^{-3}$		$3.8\cdot10^{-3}$
c_3 (mm deg^{-3})		$-3.0\cdot10^{-4}$		$2.9\cdot10^{-4}$		$8.4\cdot10^{-7}$
c_4 (mm deg^{-4})		$-2.4\cdot10^{-6}$		$3.8\cdot10^{-6}$		$-7.6\cdot10^{-7}$
c_0 (mm)	(-1.5,0.2)	83.8	(-1.5,1.3)	79.9		
c_1 (mm deg^{-1})		1.3		2.4		
c_2 (mm deg^{-2})		-1.3		$5.2\cdot10^{-1}$		
c_3 (mm deg^{-3})		$-5.3\cdot10^{-1}$				
c_4 (mm deg^{-4})						
c_0 (mm)	(0.2,4)	84.9	(1.3,4)	73.3		
c_1 (mm deg^{-1})		$-8.0\cdot10^{-1}$		13.7		
c_2 (mm deg^{-2})		$-8.6\cdot10^{-1}$		-5.1		
c_3 (mm deg^{-3})		$1.5\cdot10^{-1}$		$4.9\cdot10^{-1}$		
c_4 (mm deg^{-4})						
c_0 (mm)	(4,66.2)	72.9	(4,66.2)	75.8		
c_1 (mm deg^{-1})		$8.1\cdot10^{-1}$		$7.9\cdot10^{-1}$		
c_2 (mm deg^{-2})		$-2.8\cdot10^{-2}$		$-3.3\cdot10^{-2}$		
c_3 (mm deg^{-3})		$3.4\cdot10^{-4}$		$6.4\cdot10^{-4}$		
c_4 (mm deg^{-4})		$-1.1\cdot10^{-6}$		$3.9\cdot10^{-6}$		

References

Ablain, M., Cazenave, A., Larnicol, G., Balmaseda, M., Cipollini, P., Faugère, Y., Fernandes, M.J., Henry, O., Johannessen, J.A., Knudsen, P., Andersen, O., Legeais, J., Meyssignac, B., Picot, N., Roca, M., Rudenko, S., Scharffenberg, M.G., Stammer, D., Timms, G., & Benveniste, J. (2015). Improved sea level record over the satellite altimetry era (1993-2010) from the Climate Change Initiative Project. Ocean Science, 11, 67-82.

Andersen, O.B., & Scharroo, R. (2011). Range and Geophysical Corrections in Coastal Regions: And Implications for Mean Sea Surface Determination. In: Vignudelli S., Kostianoy A., Cipollini P., Benveniste J. (eds) Coastal Altimetry. Springer, Berlin, Heidelberg, doi:10.1007/978-3-642-12796-0_5.

Andersen, O. B., Knudsen, P., & Stenseng, L. (2015). The DTU13 MSS (Mean Sea Surface) and MDT (Mean Dynamic Topography) from 20 Years of Satellite Altimetry. In International Association of Geodesy Symposia. 1-10. Springer. (International Association of Geodesy Symposia). DOI: 10.1007/1345_2015_182

Andres, M., Gawarkiewicz, G. G., & Toole, J. M. (2013). Interannual sea level variability in the western North Atlantic: Regional forcing and remote response. Geophysical Research Letters, 40(22), 5915-5919.

Balmaseda, M. A., Mogensen, K., & Weaver, A. T. (2013). Evaluation of the ECMWF ocean reanalysis system ORAS4. Quarterly Journal of the Royal Meteorological Society, 139(674), 1132-1161.

Bamber, J., & Riva, R. (2010). The sea level fingerprint of recent ice mass fluxes. The Cryosphere 4, 621-627.

Beckley, B. D., Callahan, P. S., Hancock, D. W., Mitchum, G. T., & Ray, R. D. (2017). On the 'cal-mode' correction to TOPEX satellite altimetry and its effect on the global mean sea level time series. Journal of Geophysical Research: Oceans, 122, 8371-8384, doi:10.1002/2017JC013090.

Behringer, D. W., & Xue, Y. (2004). Evaluation of the global ocean data assimilation system at NCEP: The Pacific Ocean. In Proc. Eighth Symp. on Integrated Observing and Assimilation Systems for Atmosphere, Oceans, and Land Surface.

Bingham, R. J., & C. W. Hughes (2012). Local diagnostics to estimate density-induced sea level variations over topography and along coastlines, Journal Geophysical Research, 117, C01013, doi:10.1029/2011JC007276.

Blewitt, G., Kreemer, C., Hammond, W. C., & Gazeaux, J. (2016). MIDAS robust trend estimator for accurate GPS station velocities without step detection, Journal of Geophysical Research: Solid Earth, 121, 2054-2068, doi:10.1002/2015JB012552.

Boening, C., J. K. Willis, F. W. Landerer, R. S. Nerem, & J. Fasullo (2012), The 2011 La Niña: So strong, the oceans fell, Geophysical Research Letters, 39, L19602, doi:10.1029/2012GL053055.

Bos, M. S., Fernandes, R. M. S., Williams, S. D. P., & Bastos, L. (2013). Fast error analysis of continuous GNSS observations with missing data. Journal of Geodesy, 87(4), 351-360.

Bos, M. S., Williams, S. D. P., AraÃžjo, I. B., & Bastos, L. (2013). The effect of temporal correlated noise on the sea level rate and acceleration uncertainty. Geophysical Journal International, 196(3), 1423-1430.

Broerse, T., R. Riva, W. Simons, R. Govers, & B. Vermeersen (2015), Post-seismic GRACE and GPS observations indicate a rheology contrast above and below the Sumatra slab, J. Geophys. Res. Solid Earth, 120, 5343âĂŞ5361, doi:10.1002/2015JB011951.

Bouin, M. N., & Wöppelmann, G. (2010). Land motion estimates from GPS at tide gauges: a geophysical evaluation. Geophysical Journal International, 180(1), 193-209.

Bretherton, F. P., Davis, R. E., & Fandry, C. B. (1976). A technique for objective analysis and design of oceanographic experiments applied to MODE-73. Deep-Sea Research, 23, 559-582, doi:10.1016/0011-7471(76)90001-2.

Calafat, F. M., Marcos, M., and Gomis, D. (2010). Mass contribution to Mediterranean Sea level variability for the period 1948-2000. Global and Planetary Change, 73(3-4), 193-201, doi:10.1016/j.gloplacha.2010.06.002.

Calafat, F. M., Chambers, D. P., & Tsimplis, M. N. (2013). Inter-annual to decadal sea-level variability in the coastal zones of the Norwegian and Siberian Seas: The role of atmospheric forcing. Journal of Geophysical Research: Oceans, 118(3), 1287-1301.

Cabanes, C., Grouazel, A., Schuckmann, K. V., Hamon, M., Turpin, V., Coatanoan, C., ... & Boyer Montégut, C. D. (2013). The CORA dataset: validation and diagnostics of in-situ ocean temperature and salinity measurements. Ocean Science, 9(1), 1-18.

Caldwell, P. C., Merrifield, M. A., & Thompson, P. R. (2015). Sea level measured by tide gauges from global oceans - the Joint Archive for Sea Level holdings (NCEI Accession 0019568). Version 5.5, NOAA National Centers for Environmental Information, Dataset, doi:10.7289/V5V40S7W.

Callahan, P. S., McMichael, J., & Williams, B. A. (2016). Progress in retracking TOPEX data for the climate data record. Paper presented at Ocean Surface Topography Science Team meeting, La Rochelle, France.

Carrère, L., & Lyard, F. (2003). Modelling the barotropic response of the global ocean to atmospheric wind and pressure forcing - comparisons with observations, Geophysical Research Letters, 30(6), 1275, 2003.

Carton, J. A., & Giese, B. S. (2008). A reanalysis of ocean climate using Simple Ocean Data Assimilation (SODA). Monthly Weather Review, 136(8), 2999-3017.

Cartwright, D. E., & Tayler, R. J. (1971). New Computations of the Tide-generating Potential, Geophysical Journal of the Royal Astronomical Society, 23: 45-73. doi:10.1111/j.1365-246X.1971.tb01803.x.

Cartwright, D. E., & Edden, A. C. (1973). Corrected Tables of Tidal Harmonics, Geophysical Journal of the Royal Astronomical Society, 33: 253-264. doi:10.1111/j.1365-246X.1973.tb03420.x.

Cazenave, A., Dominh, K., Ponchaut, F., Soudarin, L., Cretaux, J. F., & Le Provost, C. (1999). Sea level changes from Topex-Poseidon altimetry and tide gauges, and vertical crustal motions from DORIS. Geophysical Research Letters, 26(14), 2077-2080.

Cazenave, A., Dominh, K., Guinehut, S., Berthier, E., Llovel, W., Ramillien, G., Ablain, M., & Larnicol, G. (2008). Sea level budget over 2003-2008: A reevaluation from GRACE space gravimetry, satellite altimetry and Argo, Global and Planetary Change, 65, 83-88, doi:10.1016/j.gloplacha.2008.10.004.

Cazenave, A., & Le Cozannet, G. (2013). Sea level rise and its coastal impacts. Earth's Future, 2, 15-34.

Chambers, D. P., Hayes, S. A., Ries, J. C., & Urban, T. J. (2003). New TOPEX sea state bias models and their effect on global mean sea level. J. Geophys. Res., 108, 3305, doi:10.1029/2003JC001839.

Chambers, D.P., & Willis, J.K. (2010). A global evaluation of ocean bottom pressure from GRACE, OMCT, and steric-corrected altimetry, Journal of Atmospheric and Oceanic Technology, 27(8), 1395-1402, doi:10.1175/2010JTECHO738.1.

Chambers, D.P., Cazenave, A., Champollion, N., Dieng, H., Llovel, W., Forsberg, R., Von Schuckmann, K., & Wada, Y. (2017). Evaluation of the Global Mean Sea Level Budget between 1993 and 2014. Surveying in Geophysics, 309, doi:10.1007/s10712-016-9381-3.

Chaussard, E., Amelung, F., Abidin, H., & Hong, S. H. (2013). Sinking cities in Indonesia: ALOS PALSAR detects rapid subsidence due to groundwater and gas extraction. Remote Sensing of Environment, 128, 150-161.

Chelton, D. B., Schlax M. G., Samelson, R. M., & De Szoeke, R. A. (2007). Global observations of large oceanic eddies. Geophysical Research Letters, 34, L15606, doi:10.1029/2007GL030812.

Chen, X., Zhang, X., Church, J.A., Watson, C.S., King, M.A., Moselesan, D., Legresy, B., & Harig, C. (2017). The increasing rate of global mean sea-level rise during 1993-2014. Nature Climate Change, 7, 492-495, doi:10.1038/nclimate3325.

Cheng, M.K., Tapley, B.D., & Ries, C. (2013). Deceleration in the Earth's oblateness. Journal of Geophysical Research: Solid Earth, 118, 740-747, doi:10.1002/jgrb.50058.

Church, J.A., & White, N.J. (2011). Sea-Level Rise from the Late 19th to the Early 21st Century. Surveying in Geophysics, 32, 585-602, doi:10.1007/s10712-011-9119-1.

Dangendorf, S., Marcos, M., WÃűppelmann, G., Conrad, C. P., Frederikse, T., & Riva, R. (2017). Reassessment of 20th century global mean sea level rise. Proceedings of the National Academy of Sciences, 201616007, doi:10.1073/pnas.1616007114.

DeConto, R.M., & Pollard, D. (2016). Contribution of Antarctica to past and future sea-level rise. Nature, 531, 591-597, doi:10.1038/nature17145.

Desai, S., Wahr, J., & Beckley, B. (2015). Revisiting the pole tide for and from satellite altimetry. Journal of Geodesy, 89(12), 1233-1243.

Dieng, H. B., Cazenave, A., von Schuckmann, K., Ablain, M., & Meyssignac, B. (2015). Sea level budget over 2005-2013: missing contributions and data errors. Ocean Science, 11(5), 789.

Dieng, H.B., Cazenave, A., Meyssignac, B., & Ablain, M. (2017). New estimate of the current rate of sea level rise from a sea level budget approach. Geophys. Res. Lett., 44, 3744-3751, doi:10.1002/2017GL073308.

Dobslaw, H., Flechtner, F., Bergmann-Wolf, I., Dahle, C., Dill, R., Esselborn, S., & Thomas, M. (2013). Simulating high-frequency atmosphere-ocean mass variability for dealiasing of satellite gravity observations: AOD1B RL05. Journal of Geophysical Research: Oceans, 118, 3704-3711, doi:10.1002/jgrc.20271.

Ducet, N., Le Traon, P. Y., & Reverdin, G. (2000). Global high-resolution mapping of ocean circulation from TOPEX/Poseidon and ERS-1 and -2. Journal of Geophysical Research: Oceans, 105(C8), 19477-19498.

Dutton, A., Carlson, A. E., Long, A. J., Milne, G. A., Clark, P. U., DeConto, R., Horton, B. P., Rahmstorf, S. & Raymo, M. E. (2015). Sea-level rise due to polar ice-sheet mass loss during past warm periods. Science, 349(6244), aaa4019, doi:10.1126/science.aaa4019.

Einarsson, I., Hoechner, A., Wang, R., & Kusche, J. (2010). Gravity changes due to the Sumatra-Andaman and Nias earthquakes as detected by the GRACE satellites: a reexamination. Geophysical Journal International, 183(2), 733-747.

England, M. H., McGregor, S., Spence, P., Meehl, G. A., Timmermann, A., Cai, W., Sen Gupta, A., McPhaden, M.J., Purich, A., & Santoso, A. (2014). Recent intensification of wind-driven circulation in the Pacific and the ongoing warming hiatus. Nature Climate Change, 4(3), 222-227, doi:10.1038/nclimate2106.

Farrell, W. E., & Clark, J. A. (1976). On postglacial sea level. Geophysical Journal International, 46(3), 647-667, doi:10.1111/j.1365-246X.1976.tb01252.x.

Feng, M., Y. Li, & G. Meyers (2004). Multidecadal variations of Fremantle sea level: Footprint of climate variability in the tropical Pacific, Geophysical Research Letters, 31, L16302, doi:10.1029/2004GL019947.

Feng, M., M. J. McPhaden, & T. Lee (2010). Decadal variability of the Pacific subtropical cells and their influence on the southeast Indian Ocean, Geophysical Research Letters, 37, L09606, doi:10.1029/2010GL042796.

Feng, W., Zhong, M., & Xu, H. (2012). Sea level variations in the South China Sea inferred from satellite gravity, altimetry, and oceanographic data. Science China Earth Sciences, 55(10), 1696-1701.

Feng, W., Lemoine, J. M., Zhong, M., & Hsu, H. T. (2014). Mass-induced sea level variations in the Red Sea from GRACE, steric-corrected altimetry, in situ bottom pressure records, and hydrographic observations, Journal of Geodynamics, 78, 1-7, doi:10.1016/j.jog.2014.04.008.

FenoglioâĂŘMarc, L., Kusche, J., and Becker, M. (2006). Mass variation in the Mediterranean Sea from GRACE and its validation by altimetry, steric and hydrologic fields. Geophysical Research Letters, 33(19), doi:10.1029/2006GL026851.

Fenoglio-Marc, L., Rietbroek, R., Grayek, S., Becker, M., Kusche, J., & Stanev, E. (2012). Water mass variation in the Mediterranean and Black Seas. Journal of Geodynamics, 59, 168-182.

Ferry, N., Parent, L., Garric, G., Barnier, B., & Jourdain, N. C. (2010). Mercator global Eddy permitting ocean reanalysis GLORYS1V1: Description and results, Mercator-Ocean Quarterly Newsletter, 36, 15-27.

Forget, G. A. E. L., Campin, J. M., Heimbach, P., Hill, C. N., Ponte, R. M., & Wunsch, C. (2015). ECCO version 4: an integrated framework for non-linear inverse modeling and global ocean state estimation. Geoscience Model Development, 8(10), 3071-3104.

Fasullo, J. T., Nerem, R. S., & Hamlington, B. (2016). Is the detection of accelerated sea level rise imminent? Nature Scientific reports, 6, 31245, doi:10.1038/srep31245.

Frederikse, T., Riva, R., Kleinherenbrink, M., Wada, Y., Broeke, M., & Marzeion, B. (2016). Closing the sea level budget on a regional scale: Trends and variability on the Northwestern European continental shelf. Geophysical Research Letters, 43(20).

Frederikse, T., Riva, R. E., & King, M. A. (2017). Ocean Bottom Deformation Due To Present-Day Mass Redistribution and Its Impact on Sea Level Observations. Geophysical Research Letters, 44(24), doi:10.1002/2017GL075419.

Frederikse, T., Jevrejeva, S., Riva, R. E. M., & Dangendorf, S. (2018). A consistent sea-level reconstruction and its budget on basin and global scales over 1958-2014. Journal of Climate, 31(3), 1267-1280, doi:10.1175/JCLI-D-17-0502.1.

Gaillard, F., Autret, E., Thierry, V., Galaup, P., Coatanoan, C., & Loubrieu, T. (2009). Quality control of large Argo datasets, Journal of Atmospheric and Oceanic Technology, 26, 337-351, doi:10.1175/2008JTECHO552.1.

García, D., Chao, B. F., Del Río, J., Vigo, I., & García-Lafuente, J. (2006). On the steric and mass-induced contributions to the annual sea level variations in the Mediterranean Sea, Journal of Geophysical Research: Oceans, 111, C09030, doi:10.1029/2005JC002956.

Gaspar, P., Ogor, F., Le Traon, P. Y., & Zanife, O. Z. (1994). Estimating the sea state bias of the TOPEX and POSEIDON altimeters from crossover differences. Journal of Geophysical Research: Oceans, 99(C12), 24981-24994, doi:10.1029/94JC01430.

Gaspar, P., Labroue, S., Ogor, F., Lafitte, G., Marchal, L., & Rafanel, M. (2002). Improving nonparametric estimates of the sea state bias in radar altimeter measurements of sea level. Journal of atmospheric and oceanic technology, 19(10), 1690-1707, doi:10.1175/1520-0426(2002)019<1690:INEOTS>2.0.CO;2.

Gazeaux, J., Williams, S., King, M., Bos, M., Dach, R., Deo, M., Moore, A. W., Ostini, L., Petrie E., Roggero, M., Teferle, F. N., Olivares, G., & Webb, F.H. (2013). Detecting offsets in GPS time series: First results from the detection of offsets in GPS experiment. Journal of Geophysical Research: Solid Earth, 118(5), 2397-2407.

Gregory, J. M., White, N. J., Church, J. A., Bierkens, M. F. P., Box, J. E., Van den Broeke, M. R., Cogley, J. G., Fettweis, X., Hanna, E., Huybrechts, P., Konikow, L. F., Leclercq, P. W., Marzeion, B., Oerlemans, J., Tamisiea, M. E., Wada, Y., Wake, L. M., & Van de Wal, R. S. W. (2013). Twentieth-century global-mean sea level rise: Is the whole greater than the sum of the parts?. Journal of Climate, 26(13), 4476-4499, doi:10.1175/JCLI-D-12-00319.1.

Griffies, S. M. (2004). Fundamentals of Ocean Climate Models. Princeton, New Jersey: Princeton University Press, 518 + xxxiv.

Grosso, P., Le Menn, M., De La, J. L. D. B., Wu, Z. Y., & Malardé, D. (2010). Practical versus absolute salinity measurements: New advances in high performance seawater salinity sensors. Deep Sea Research Part I: Oceanographic Research Papers, 57(1), 151-156.

Gutenberg, B. (1941). Changes in sea level, postglacial uplift, and mobility of the EarthâĂŹs interior, Bull. Geol. Soc. Am., 52, 721-772.

Haigh, I. D., Wahl, T., Rohling, E. J., Price, R. M., Pattiaratchi, C. B., Calafat, F. M., & Dangendorf, S. (2014). Timescales for detecting a significant acceleration in sea level rise. Nature Communications, 5, 3635, doi:10.1038/ncomms4635.

Hamlington, B. D., Thompson, P., Hammond, W. C., Blewitt, G., & Ray, R. D. (2016). Assessing the impact of vertical land motion on twentieth century global mean sea level estimates. Journal of Geophysical Research: Oceans, 121(7), 4980-4993.

Hancock, D. W., Hayne, G. S., Brooks, R. L., Lee, J. E., & Lockwood, D. W. (1999). TOPEX radar altimeter engineering assessment report update: From launch to turn-off of Side-A on February 10, 1999. NASA TM-2003-212236, 12, Greenbelt, MD: NASA, Goddard Space Flight Center. Retrieved from www.sti.nasa.gov.

Hayne, G. S., Hancock, D. W., & Purdy, C. L. (1994). TOPEX altimeter range stability estimates from calibration mode data. TOPEX/POSEIDON Res. News, 3, 18-22.

Heij, C., De Boer, P., Franses, P. H., Kloek, T., & Van Dijk, H. K. (2004). Econometric methods with applications in business and economics. OUP Oxford.

Henry, O., Ablain, M., Meyssignac, B., Cazenave, A., Masters, D., Nerem, S., & Garric, G. (2014). Effect of the processing methodology on satellite altimetry-based global mean sea level rise over the Jason-1 operating period. Journal of Geodesy, 88(4), 351-361.

Hetland, E. A., & Hager, B. H. (2006). The effects of rheological layering on post-seismic deformation. Geophysical Journal International, 166(1), 277-292.

Hulbe, C. (2017). Is ice sheet collapse in West Antarctica unstoppable? Science, 356(6341), 910-911, doi:10.1126/science.aam9728.

Hughes, C.W., & Meredith, M.P. (2006). Coherent sea-level fluctuations along the global continental slope. Phil. Trans. R. Soc., 364, 885-901.

Holgate, S. J., Matthews, A., Woodworth, P. L., Rickards, L. J., Tamisiea, M. E., Bradshaw, E., Foden, P. R., Gordon, K. M., Jevrejeva, S., & Pugh, J. (2013). New data systems and products at the permanent service for mean sea level. Journal of Coastal Research, 29(3), 493-504.

IOC, SCOR (2010). IAPSO: The international thermodynamic equation of seawater-2010: Calculation and use of thermodynamic properties, Intergovernmental Oceanographic Commission, Manuals and Guides No. 56. UNESCO, 3212(30), 7.

Ishii, M., Kimoto, M., Sakamoto, K., & Iwasaki, S.I. (2006). Steric sea level changes estimated from historical ocean subsurface temperature and salinity analyses, Journal of Oceanography, 62, 115-170, 2006, doi:10.1007/s10872-006-0041-y.

Ivanovic, R. F., Valdes, P. J., Gregoire, L., Flecker, R., & Gutjahr, M. (2014). Sensitivity of modern climate to the presence, strength and salinity of Mediterranean-Atlantic exchange in a global general circulation model, Climate dynamics, 42, 859-877, doi:10.1007/s00382-013-1680-5.

Jevrejeva, S., Grinsted, A., Moore, J. C., & Holgate, S. (2006). Nonlinear trends and multiyear cycles in sea level records. J. Geophys. Res., 111, C09012, doi:10.1029/2005JC003229.

Jevrejeva, S., Moore, J.C., Grinsted, A., Matthews, A.P., & Spada, G. (2014). Trends and acceleration in global and regional sea levels since 1807. Global and Planetary Change, 113, 11-22, doi:10.1016/j.gloplacha.2013.12.004.

Johnson, G. C., & D. P. Chambers (2013), Ocean bottom pressure seasonal cycles and decadal trends from GRACE Release-05: Ocean circulation implications, Journal of Geophysical Research: Oceans, 118, 4228-4240, doi:10.1002/jgrc.20307.

Klees, R., Revtova, E. A., Gunter, B. C., Ditmar, P., Oudman, E., Winsemius, H. C., & Savenije, H. H. G. (2008). The design of an optimal filter for monthly GRACE gravity models. Geophysical Journal International, 175(2), 417-432.

Kleinherenbrink, M., Riva, R., & Sun, Y. (2016). Sub-basin-scale sea level budgets from satellite altimetry, Argo floats and satellite gravimetry: a case study in the North Atlantic Ocean. Ocean Science, 12(6), 1179-1203, doi:10.5194/os-12-1179-2016.

Kleinherenbrink, M., Riva, R., & Frederikse, T. (2018). A comparison of methods to estimate vertical land motion trends from GNSS and altimetry at tide gauge stations. Ocean Science, 14(2), 187-204, doi:10.5194/os-14-187-2018.

Klinger, B., Mayer-Gürr, T., Behzadpour, S., Ellmer, M., Kvas, A., Zehentner, N. (2016). The new ITSG-Grace2016 release. EGU General Assembly 2016, Vienna.

Knudsen, P., Andersen, O. B., & Knudsen, T. (1996). ATSR sea surface temperature data in a global analysis with TOPEX/POSEIDON altimetry. Geophysical research letters, 23(8), 821-824.

Köhl, A. (2015). Evaluation of the GECCO2 ocean synthesis: transports of volume, heat and freshwater in the Atlantic. Quarterly Journal of the Royal Meteorological Society, 141(686), 166-181.

Kopp, R. E., Kemp, A. C., Bittermann, K., Horton, B. P., Donnelly, J. P., Gehrels, W. R., Hay, C.C., Mitrovica, J.X., & Rahmstorf, S. (2016). Temperature-driven global sea-level variability in the Common Era. Proceedings of the National Academy of Sciences, 113(11), E1434-E1441, doi:10.1073/pnas.1517056113.

Kusche, J. (2007). Approximate decorrelation and non-isotropic smoothing of time-variable GRACE-type gravity field models, Journal of Geodesy, 81, 733-749, doi:10.1007/s00190-007-0143-3.

Kusche, J., Schmidt, R., Petrovic, S., & Rietbroek, R. (2009). Decorrelated GRACE time-variable gravity solutions by GFZ, and their validation using a hydrological model, Journal of geodesy, 83, 903-913, doi:10.1007/s00190-009-0308-3.

Labroue, S., Gaspar, P., Dorandeu, J., Zanife, O. Z., Mertz, F., Vincent, P., & Choquet, D. (2004). Non-parametric estimates of the sea state bias for Jason-1 radar altimeter. Mar. Geod., 27, 453-481,

Landerer, F. W., J. H. Jungclaus, & J. Marotzke (2007). Ocean bottom pressure changes lead to a decreasing length-of-day in a warming climate, Geophysical Research Letters, 34, L06307, doi:10.1029/2006GL029106.

Lee, T., & M. J. McPhaden (2008). Decadal phase change in large-scale sea level and winds in the Indo-Pacific region at the end of the 20th century, Geophysical Research Letters, 35, L01605, doi:10.1029/2007GL032419.

Levermann, A., Clark, P.U., Marzeion, B., Milne, G.A., Pollard, D., Radic, V., & Robinson, A. (2013). The multimillennial sea-level commitment of global warming. Proceedings of the National Academy of Sciences, 110(34), 13745-13750, doi:10.1073/pnas.1219414110.

Li, J., Zuo, J., Chen, M., Tan, W., & Yang, Y. (2013). Assessing the global averaged sea-level budget from 2003 to 2010, Acta Oceanologica Sinica, 32, 16-23, doi:10.1007/s13131-013-0361-x.

Le Traon, P.Y., Nadal, F., & Ducet, N. (1998). An improved mapping method of multisatellite altimeter data. Journal of atmospheric and oceanic technology, 15(2), 522-534.

Le Traon, P. Y., Dibarboure, G., & Ducet, N. (2001). Use of a high-resolution model to analyze the mapping capabilities of multiple-altimeter missions. Journal of Atmospheric and Oceanic Technology, 18(7), 1277-1288.

Leuliette, E. W., & Miller, L. (2009). Closing the sea level rise budget with altimetry, Argo, and GRACE, Geophysical Research Letters, 36, L04608, doi:10.1029/2008GL036010.

Leuliette, E. W., & Scharroo, R. (2010). Integrating Jason-2 into a multiple-altimeter climate data record, Marine Geodesy, 33, 504-517, doi:10.1080/01490419.2010.487795.

Leuliette, E. W., & Willis, J. K. (2011). Balancing the sea level budget. Oceanography, 24(2), 122-129, doi:10.5670/oceanog.2011.32.

Llovel, W., Willis, J. K., Landerer, F. W., & Fukumori, I. (2014). Deep-ocean contribution to sea level and energy budget not detectable over the past decade. Nature Climate Change, 4(11), 1031-1035.

Llovel, W., & Lee, T. (2015). Importance and origin of halosteric contribution to sea level change in the southeast Indian Ocean during 2005-2013. Geophysical Research Letters, 42(4), 1148-1157, doi:10.1002/2014GL062611.

Mantua, N.J., & Hare, S.R. (2002). The Pacific Decadal Oscillation. Journal of Oceanography, 58, 35-44, doi:10.1023/A:1015820616384.

Marcos, M., Calafat, F. M., Llovel, W., Gomis, D., & Meyssignac, B. (2011). Regional distribution of steric and mass contributions to sea level changes, Global and Planetary Change, 76, 206-218, 2011, doi:10.1016/j.gloplacha.2011.01.007.

Masters, D., Nerem, R. S., Choe, C., Leuliette, E., Beckley, B., White, N., & Ablain, M. (2012). Comparison of global mean sea level time series from TOPEX/Poseidon, Jason-1, and Jason-2. Marine Geodesy, 35(sup1), 20-41.

Mayer-Gürr, T., Zehentner, N., Klinger, B., & Kvas, A. (2014). ITSG-Grace2014: a new GRACE gravity field release computed in Graz. Procedings of GRACE Science Team Meet, Potsdam.

McGregor, S., Gupta, A. S., & England, M. H. (2012). Constraining wind stress products with sea surface height observations and implications for Pacific Ocean sea level trend attribution. Journal of Climate, 25(23), 8164-8176.

McGregor, S., Timmermann, A., Schneider, N., Stuecker, M. F., & England, M. H. (2012). The Effect of the South Pacific Convergence Zone on the Termination of El Niño Events and the Meridional Asymmetry of ENSO*. Journal of Climate, 25(16), 5566-5586.

Menemenlis, D., Fukumori, I., & Lee, T. (2005). Using Green's functions to calibrate an ocean general circulation model. Monthly weather review, 133(5), 1224-1240, doi:10.1175/MWR2912.1.

Mercer, J.H. (1978). West Antarctica ice sheet and CO_2 greenhouse effect: a threat of disaster. Nature, 271, 321-325, doi:10.1038/271321a0.

Merrifield, M. A. (2011). A shift in western tropical Pacific sea level trends during the 1990s. Journal of Climate, 24(15), 4126-4138.

Merrifield, M. A., & M. E. Maltrud (2011). Regional sea level trends due to a Pacific trade wind intensification, Geophysical Research Letters, 38, L21605, doi:10.1029/2011GL049576.

Merrifield, M. A., P. R. Thompson, & M. Lander (2012). Multidecadal sea level anomalies and trends in the western tropical Pacific, Geophysical Research Letters, 39, L13602, doi:10.1029/2012GL052032.

Meyers, G., McIntosh, P., Pigot, L., & Pook, M. (2007). The years of El NiÃśo, La NiÃśa, and interactions with the tropical Indian Ocean. Journal of Climate, 20(13), 2872-2880.

Milne, G. A., & Mitrovica, J. X. (1996). Postglacial sea-level change on a rotating Earth: first results from a gravitationally self-consistent sea-level equation. Geophysical Journal International, 126(3), F13-F20.

Milne, G. A., & Mitrovica, J. X. (1998). Postglacial sea-level change on a rotating Earth. Geophysical Journal International, 133(1), 1-19.

Mitchum, G. T. (1998). Monitoring the stability of satellite altimeters with tide gauges. Journal of Atmospheric and Oceanic Technology, 15(3), 721-730.

Mitchum, G. T. (2000). An improved calibration of satellite altimetric heights using tide gauge sea levels with adjustment for land motion. Marine Geodesy, 23(3), 145-166.

Nerem, R. S. (1995). Measuring global mean sea level variations using TOPEX/POSEIDON altimeter data. Journal of Geophysical Research: Oceans, 100(C12), 25135-25151, doi:10.1029/95JC02303.

Nerem, R. S., & Mitchum, G. T. (2002). Estimates of vertical crustal motion derived from differences of TOPEX/POSEIDON and tide gauge sea level measurements. Geophysical Research Letters, 29(19).

Nerem, R. S., Chambers, D. P., Choe, C., & Mitchum, G. T. (2010). Estimating mean sea level change from the TOPEX and Jason altimeter missions, Marine Geodesy, 33, 435-446, doi:10.1080/01490419.2010.491031.

Nerem, R. S., Beckley, B. D., Fasullo, J. T., Hamlington, B. D., Masters, D., & Mitchum, G. T. (2018). Climate-changeâĂŞdriven accelerated sea-level rise detected in the altimeter era. Proceedings of the National Academy of Sciences, doi:10.1073/pnas.1717312115.

Ostanciaux, É., Husson, L., Choblet, G., Robin, C., & Pedoja, K. (2012). Present-day trends of vertical ground motion along the coast lines. Earth-Science Reviews, 110(1), 74-92.

Passaro, M., Cipollini, P., Vignudelli, S., Quartly, G. D., & Snaith, H. M. (2014). ALES: A multi-mission adaptive subwaveform retracker for coastal and open ocean altimetry. Remote Sensing of Environment, 145, 173-189, doi:10.1016/j.rse.2014.02.008.

Pawlocwicz, P., McDougall, T. J., Feistel, R., & Tailleux, R. (2012). An historical perspective on the development of the Thermodynamic Equation of Seawater-2010. Ocean Science, 8, 161-174.

Peltier, W.R., Argus, D.F., & Drummond, R. (2015). Space geodesy constrains ice-age terminal deglaciation: The global ICE-6G_C model. J. Geophys. Res. Solid Earth, 120, 450-487, doi:10.1002/2014JB011176.

Pérez-Hernández, M. D., & Joyce, T. M. (2014). Two modes of Gulf Stream variability revealed in the last two decades of satellite altimeter data, Journal of Physical Oceanography, 44, 149-163, doi:10.1175/JPO-D-13-0136.1.

Petit, G., & Luzum, B. (2010). IERS conventions (2010) (No. IERS-TN-36). BUREAU INTERNATIONAL DES POIDS ET MESURES SEVRES (FRANCE).

Pfeffer, J., & Allemand, P. (2016). The key role of vertical land motions in coastal sea level variations: a global synthesis of multisatellite altimetry, tide gauge data and GPS measurements. Earth and Planetary Science Letters, 439, 39-47.

Pfeffer, J., Spada, G., Ménin, A., Boy, J-.P. & Allemand, P. (2017). Decoding the origins of vertical land motions observed today at coasts, Geophysical Journal International, 210, 148-165, doi:10.1093/gji/ggx142.

Phien-Wej, N., Giao, P. H., & Nutalaya, P. (2006). Land subsidence in Bangkok, Thailand. Engineering Geology, 82(4), 187-201.

Philander, S.G.H. (1983). El Niño Southern Oscillation phenomena. Nature, 302, 295-301, doi:10.1038/302295a0.

Piecuch, C.G., & Quinn, K.J., (2016). El Niño, La Niña, and the global sea level budget. Ocean Science, 12, 1165-1177, doi:10.5194/os-12-1165-2016.

Proudman, J. (1960). The condition that a long-period tide shall follow the equilibrium-law. Geophysical Journal International, 3(2), 244-249.

Pugh, D., & Woodworth, P. (2014). Sea-level science: understanding tides, surges, tsunamis and mean sea-level changes. Cambridge University Press.

Pujol, M. I., Faugére, Y., Taburet, G., Dupuy, S., Pelloquin, C., Ablain, M., & Picot, N. (2016). DUACS DT2014: the new multi-mission altimeter data set reprocessed over 20 years. Ocean Science, 12(5).

Purkey, S. G., Johnson, G. C., & Chambers, D. P. (2014). Relative contributions of ocean mass and deep steric changes to sea level rise between 1993 and 2013, Journal of Geophysical Research: Oceans, 119(11), 7509-7522, doi:10.1002/2014JC010180.

Queffeulou, P. (2010). Long-Term Validation of Wave Height Measurements from Altimeters, Marine Geodesy, 27:3-4, 495-510, doi:10.1080/01490410490883478.

Raucoules, D., Le Cozannet, G., Wöppelmann, G., De Michele, M., Gravelle, M., Daag, A., & Marcos, M. (2013). High nonlinear urban ground motion in Manila (Philippines) from 1993 to 2010 observed by DInSAR: implications for sea-level measurement. Remote Sensing of Environment, 139, 386-397.

Ray, R. D., Beckley, B. D., & Lemoine, F. G. (2010). Vertical crustal motion derived from satellite altimetry and tide gauges, and comparisons with DORIS measurements. Advances in Space Research, 45(12), 1510-1522.

Ray, R. D., & Beckley, B. D. (2012). Calibration of Ocean Wave Measurements by the TOPEX, Jason-1, and Jason-2 Satellites. Marine Geodesy, 35:sup1, 238-257, doi:10.1080/01490419.2012.718611.

Ray, R. D. (2013). Precise comparisons of bottom-pressure and altimetric ocean tides, Journal of Geophysical Research: Oceans, 118, 4570-4584, doi:10.1002/jgrc.20336.

Rietbroek, R., Brunnabend, S. E., Kusche, J., Schröter, J., & Dahle, C. (2016). Revisiting the contemporary sea-level budget on global and regional scales. Proceedings of the National Academy of Sciences, 113(6), 1504-1509.

Riva, R. E., Frederikse, T., King, M. A., Marzeion, B., & van den Broeke, M. R. (2017). Brief communication: The global signature of post-1900 land ice wastage on vertical land motion. The Cryosphere, 11(3), 1327.

Rodolfo, K. S., & Siringan, F. P. (2006). Global sea-level rise is recognised, but flooding from anthropogenic land subsidence is ignored around northern Manila Bay, Philippines. Disasters, 30(1), 118-139.

Roemmich, D., & Gilson, J. (2009). The 2004-2008 mean and annual cycle of temperature, salinity, and steric height in the global ocean from the Argo Program. Progress in Oceanography, 82(2), 81-100.

Sallenger Jr, A. H., Doran, K. S., & Howd, P. A. (2012). Hotspot of accelerated sea-level rise on the Atlantic coast of North America, Nature Climate Change, 2, 884-888, doi:10.1038/nclimate1597.

Santamaría-Gómez, A., Gravelle, M., Collilieux, X., Guichard, M., Míguez, B. M., Tiphaneau, P., & Wöppelmann, G. (2012). Mitigating the effects of vertical land motion in tide gauge records using a state-of-the-art GPS velocity field. Global and Planetary Change, 98, 6-17.

Santamaría-Gómez, A., Gravelle, M., & Wöppelmann, G. (2014). Long-term vertical land motion from double-differenced tide gauge and satellite altimetry data. Journal of Geodesy, 88(3), 207-222.

Santamaría-Gómez, A., Gravelle, M., Dangendorf, S., Marcos, M., Spada, G., & Wöppelmann, G. (2017). Uncertainty of the 20th century sea-level rise due to vertical land motion errors. Earth and Planetary Science Letters, 473, 24-32.

Scharroo, R. (2006). Presentation to the Ocean Surface Topography Science Team, Venice, 16-18 March 2006.

Scharroo, R., Leuliette, E. W., Lillibridge, J. L., Byrne, D., Naeije, M. C., & Mitchum, G. T. (2012). RADS: Consistent multi-mission products. In Proceedings of Symposium on 20 Years of Progress in Radar Altimetry (Vol. 20).

Siemes, C., Ditmar, P., Riva, R. E. M., Slobbe, D. C., Liu, X. L., & Farahani, H. H. (2013). Estimation of mass change trends in the Earth's system on the basis of GRACE satellite data, with application to Greenland, Journal of Geodesy, 87, 69-87, doi:10.1007/s00190-012-0580-5.

Storto, A., Masina, S., Balmaseda, M., Guinehut, S., Xue, Y., Szekely, T., Fukumori, I., Forget, G., Chang, Y. -S., Good, S. A., Köhl, A., Vernieres, G., Ferry, N., Peterson, A. K., Behringer, D., Ishii, M., Masuda, S., Fujii, Y., Toyoda, T., Yin, Y., Valdivieso, M., Barnier, B., Boyer, T., Lee, T., Gourrion, J., Wang, O., Heimback, P., Rosati, A., Kovach, R., Hernandez, F., Martin, M. J., Kamachi, M., Kuragano, T., Mogensen, K., Alves, O., Haines, K., & Wang, X. (2017). Steric sea level variability (1993-2010) in an ensemble of ocean reanalyses and objective analyses, Climate Dynamics, 49(3), 709-729, doi:10.1007/s00382-015-2554-9.

Strassburg, M. W., Hamlington, B. D., Leben, R. R., Manurung, P., Lumban Gaol, J., Nababan, B., Vignudelli, S., & Kim, K. Y. (2015). Sea level trends in Southeast Asian seas. Climate of the Past, 11(5), 743-750.

Svendsen, P.L., Andersen, O.B., & Nielsen, A.A. (2013). Acceleration of the Greenland ice sheet mass loss as observed by GRACE: confidence and sensitivity. Earth and Planetary Science Letters, 364, 24-29, doi:10.1016/j.epsl.2012.12.010.

Swenson, S., & Wahr, J. (2002). Methods for inferring regional surface-mass anomalies from Gravity Recovery and Climate Experiment (GRACE) measurements of time-variable gravity. Journal of Geophysical Research: Solid Earth, 107(B9), 2193, doi:10.1029/2001JB000576.

Swenson, S., Chambers, D., & Wahr, J. (2008). Estimating geocenter variations from a combination of GRACE and ocean model output. Journal of Geophysical Research: Solid Earth, 113, B08410, doi:10.1029/2007JB005338.

Tai, C. K., & Wagner, C. (2011). Sampling errors of the global mean sea level derived from TOPEX/Poseidon altimetry. Acta Oceanologica Sinica, 30, 12-18, doi:10.1007/s13131-011-0156-x.

Tapley, B. D., Bettadpur, S., Watkins, M., & Reigber, C. (2004). The gravity recovery and climate experiment: Mission overview and early results. Geophysical Research Letters, 31, L09607, doi:10.1029/2004GL019920.

Tamisiea, M. E., Hill, E. M., Ponte, R. M., Davis, J. L., Velicogna, I., & Vinogradova, N. T. (2010). Impact of self-attraction and loading on the annual cycle in sea level. Journal of Geophysical Research: Oceans, 115, C07004, doi:10.1029/2009JC005687.

Tamisiea, M. E. (2011). Ongoing glacial isostatic contributions to observations of sea level change. Geophysical Journal International, 186, 1036-1044, doi:10.1111/j.1365-246X.2011.05116.x.

Tangdamrongsub, N., Ditmar, P. G., Steele-Dunne, S. C., Gunter, B. C., & Sutanudjaja, E. H. (2016). Assessing total water storage and identifying flood events over Tonlé Sap basin in Cambodia using GRACE and MODIS satellite observations combined with hydrological models. Remote Sensing of Environment, 181, 162-173.

Tran, N., Labroue, S., Philipps, S., Bronner, E., & Picot, N. (2010). Overview and update of the sea state bias corrections for the Jason-2, Jason-1 and TOPEX missions. Marine Geodesy, 33(S1), 348-362, doi:10.1080/01490419.2010.487788.

Tran, N., Philipps, S., Poisson, J. C., Urien, S., Bronner, E., & Picot, N. (2012). Impact of GDR-D standards on SSB correction, Ocean Science Topography Science Team Meeting, Venice, Italy, 27-29 September 2012.

Våge, K., Pickart, R. S., Thierry, V., Reverdin, G., Lee, C. M., Petrie, B., Agnew, T.A., Wong, A., & Ribergaard, M. H. (2009). Surprising return of deep convection to the

subpolar North Atlantic Ocean in winter 2007-2008, Nature Geoscience, 2, 67-72, doi:10.1038/ngeo382.

Vinogradov, S. V., Ponte, R. M., Heimbach, P., & Wunsch, C. (2008), The mean seasonal cycle in sea level estimated from a data-constrained general circulation model, Journal of Geophysical Research, 113, C03032, doi:10.1029/2007JC004496.

Vinogradov, S. V., & Ponte, R. M. (2011). Low-frequency variability in coastal sea level from tide gauges and altimetry. Journal of Geophysical Research: Oceans, 116(C7).

Von Schuckmann, K., Sallée, J. B., Chambers, D., Le Traon, P. Y., Cabanes, C., Gaillard, F., ... & Hamon, M. (2014). Consistency of the current global ocean observing systems from an Argo perspective. Ocean Science, 10(3), 923-949.

Wada, Y., Van Beek, L. P. H., & Bierkens, M. F. (2011). Modelling global water stress of the recent past: on the relative importance of trends in water demand and climate variability. Hydrology and Earth System Sciences, 15(12), 3785-3808.

Wagner, C., McAdoo, D., Klokočník, J., & Kostelecký, J. (2006). Degradation of geopotential recovery from short repeat-cycle orbits: application to GRACE monthly fields, Journal of Geodesy, 80, 94-103, doi:10.1007/s00190-006-0036-x.

Wahr, J. M. (1985). Deformation of the Earth induced by polar motion. Journal of Geophysical Research, 90, 9363-9368, doi:10.1029/JB090iB11p09363.

Wahr, J., Molenaar, M., & Bryan, F. (1998). Time variability of the Earth's gravity field: Hydrological and oceanic effects and their possible detection using GRACE. Journal of Geophysical Research: Solid Earth, 103(B12), 30205-30229.

Wahr, J., Smeed, D. A., Leuliette, E., & Swenson, S. (2014). Seasonal variability of the Red Sea, from satellite gravity, radar altimetry, and in situ observations. Journal of Geophysical Research: Oceans, 119, 5091-5104, doi:10.1002/2014JC010161.

Wahr, J., Nerem, R. S., & Bettadpur, S. V. (2015). The pole tide and its effect on GRACE time-variable gravity measurements: Implications for estimates of surface mass variations. Journal of Geophysical Research: Solid Earth, 120(6), 4597-4615.

Wang, G., Cheng, L., Boyer, T., & Li, C. (2017). Halosteric sea level changes during the Argo era. Water, 9(7), 484, doi:10.3390/w9070484.

Wang, Y. M., & Rapp, R. H. (1994). Estimation of sea surface dynamic topography, ocean tides, and secular changes from Topex altimeter data, Rep. 430, Department of Geodetic Science and Surveying, The Ohio State University, Columbus, 89.

Watkins, MM, DN Wiese, D-N Yuan, C Boening, & FW Landerer (2015), Improved methods for observing Earth's time variable mass distribution with GRACE using spherical cap mascons. Journal of Geophysical Research Solid Earth, 120, 2648-2671. doi: 10.1002/2014JB011547.

Watson, C. S., White, N. J., Church, J. A., King, M. A., Burgette, R. J., & Legresy, B. (2015). Unabated global mean sea-level rise over the satellite altimeter era. Nature Climate Change, 5(6), 565-568.

Wei, F., & Zhong, M. (2015). Global sea level variations from altimetry, GRACE and Argo data over 2005-2014. Geodesy and Geodynamics, 6(4), 274-279, doi:10.1016/j.geog.2015.07.001.

Widlansky, M. J., Timmermann, A., McGregor, S., Stuecker, M. F., & Cai, W. (2014). An interhemispheric tropical sea level seesaw due to El Niño Taimasa. Journal of Climate, 27(3), 1070-1081.

Wijffels, S., & Meyers, G. (2004). An intersection of oceanic waveguides: Variability in the Indonesian Throughflow region. Journal of Physical Oceanography, 34(5), 1232-1253.

Wilcox, R. R. (2005), Introduction to Robust Estimation and Hypothesis Testing, Elsevier Academic Press, Burlington, Mass.

Williams, S. D. P. (2008). CATS: GPS coordinate time series analysis software. GPS Solutions, 12(2), 147-153, doi:10.1007/s10291-007-0086-4.

Willis, J. K., Chambers, D. P., & Nerem, R. S. (2008). Assessing the globally averaged sea level budget on seasonal to interannual timescales. Journal of Geophysical Research: Oceans, 113, C06015, doi:10.1029/2007JC004517.

Woodworth, P. L. (2011). A note on the nodal tide in sea level records. Journal of Coastal Research, 28(2), 316-323.

Wöppelmann, G., Miguez, B. M., Bouin, M. N., & Altamimi, Z. (2007). Geocentric sea-level trend estimates from GPS analyses at relevant tide gauges world-wide. Global and Planetary Change, 57(3), 396-406.

Wp̈pelmann, G., Letetrel, C., Santamaria, A., Bouin, M.-N., Collilieux, X., Altamimi, Z., Williams, S. D. P., & Martin Miguez, B. (2009). Rates of seaâĂŘlevel change over the past century in a geocentric reference frame. Geophysical Research Letters, 36, L12607, doi:10.1029/2009GL038720.

Wöppelmann, G., Marcos, M., Santamaría-Gómez, A., Martín-Míguez, B., Bouin, M. N., & Gravelle, M. (2014). Evidence for a differential sea level rise between hemispheres over the twentieth century. Geophysical Research Letters, 41(5), 1639-1643.

Wöppelmann, G., & Marcos, M. (2016). Vertical land motion as a key to understanding sea level change and variability. Reviews of Geophysics, 54(1), 64-92.

Zhang, X., & J. A. Church (2012). Sea level trends, interannual and decadal variability in the Pacific Ocean, Geophysical Research Letters, 39, L21701, doi:10.1029/2012GL053240.

Zhang, S., Harrison, M. J., Rosati, A., & Wittenberg, A. (2007). System design and evaluation of coupled ensemble data assimilation for global oceanic climate studies. Monthly Weather Review, 135(10), 3541-3564.

Zhang, Z. Z., Chao, B. F., Lu, Y., & Hsu, H. T., (2009). An effective filtering for GRACE time-variable gravity: Fan filter, Geophysical Research Letters, 36, L17311, doi:10.1029/2009GL039459.

Zheng, F., Feng, L., & Zhu, J. (2015). An incursion of off-equatorial subsurface cold water and its role in triggering the "double dip" La Niña event of 2011. Advances in Atmospheric Sciences, 32(6), 731-742.

Zuo, H., Balmaseda, M. A., & Mogensen, K. (2015). The new eddy-permitting ORAP5 ocean reanalysis: description, evaluation and uncertainties in climate signals. Climate Dynamics, 1-21.

Acknowledgements

This section contains the sources for the most important datasets that have been used in this thesis.

Argo float data
Argo float data and metadata from Global Data Assembly Centre.
Carval, T., Keeley, R., Takatsuki, Y., Yoshida, T., Loch, S., Schmid, C., Goldsmith, R., Wong, A., McCreadie, R., Thresher, A., & Tran, A.
Describing literature: doi:10.13155/29825.
Link to data: doi:10.17882/42182.

CSR gravity field solutions
Bettadpur, S. & the CSR Level-2 Team.
Describing literature: `http://www2.csr.utexas.edu/grace/Bettadpur_RL05.pdf`.
Link to data: `ftp://podaac.jpl.nasa.gov/allData/grace/L2/CSR/`.

Generic Mapping Tools
Wessel, P., Smith, W.H.F., Scharroo, R., Luis, J., & Wobbe, F.
Describing literature: doi:10.1002/2013EO450001. Link to software: `http://gmt.soest.hawaii.edu/projects/gmt/wiki/Download`.

ICE-6G(VM5a) GIA stokes coefficients
Peltier, W.R., Argus, D.F., & Drummond, R.
Describing literature: doi:10.1002/2014JB011176. Link to data: `http://www.atmosp.physics.utoronto.ca/~peltier/data.php`.

ITSG-GRACE2016 gravity field solutions
Mayer-Gürr, T., Behzadpour, S., Ellmer, M., Kvas, A., Klinger, B., & Zehentner, N.
Describing literature: doi:10.5880/icgem.2016.007.
Link to data: `https://www.tugraz.at/institute/ifg/downloads/gravity-field-models/itsg-grace2016`.

Mercator Ocean Glorys 2V3 reanalyses
Ferry, N., Parent, L., Garric, G., Barnier, B., Jourdain, N.C., & the Mercator Ocean team.
Describing literature: `http://www.earth-prints.org/bitstream/2122/`

9666/1/2010_01_Mercator_Quarterly_Newsletter_36.pdf#page=15.
Link to data: http://marine.copernicus.eu/services-portfolio/access-to-products/.

Nevada Geodetic Laboratory (NGL) MIDAS GPS trends
Blewitt, G., Kreemer, C., Hammond, W., & Gazeaux, J.
Describing literature: doi:10.1002/2015JB012552.
Link to data: http://geodesy.unr.edu/.

Permanent Service for Mean Sea Level (PSMSL)
Holgate, S., Matthews, A., Woodworth, P., Rickards, L., Tamisiea, M., Bradshaw, E., Foden, P., Gordon, K., Jevrejeva, S., & Pugh, J.
Describing literature: doi:10.2112/JCOASTRES-D-12-00175.1.
Link to data: http://www.psmsl.org/data/.

Radar Altimetry Database System (RADS)
Naeije, M., Schrama, E., & Scharroo, R.
Describing literature: doi:10.1109/IGARSS.2000.861605.
Link to data: Contacted Remko Scharroo by email.

Selection of University of La Rochelle (ULR) GPS and ALT-TG trends
Wöppelmann G., & Marcos, M.
Describing literature: doi:10.1002/2015RG000502.
Link to data: Contacted Marta Marcos by email.

Scripps Argo-based temperature and salinity grids
Roemmich, D., & Gilson, J.
Describing literature: doi:10.1016/j.pocean.2009.03.004.
Link to data: http://www.argo.ucsd.edu/Gridded_fields.html.

TOPEX calibration mode 1 (cal-1) correction
Hayne, G.S., Hancock, D.W., & Purdy, C.L.
Describing literature: https://topex.wff.nasa.gov/wp-content/uploads/RangeStabEst.pdf
Link to data: ftp://podaac.jpl.nasa.gov/allData/woce/retired/L3/v1/topex/docs/html/rangbias.htm.

USGS earthquake database
National Earthquake Hazards Reduction Program.
Link to data: https://earthquake.usgs.gov/earthquakes/search/.

List of Publications

Kleinherenbrink, M., Ditmar, P., & Lindenbergh, R. (2014). Retracking Cryosat data in the SARIn mode and robust lake level extraction. Remote sensing of environment. 152, 38-50, doi:10.1016/j.rse.2014.05.014.

Levinsen, J., Khvorostovsky, K., Ticconi, F., Shepherd, A., Forsberg, R., Sorensen, L., Muir, A., Pie, N., Felikson, D., Flament, T., Hurkmans, R., Moholdt, G., Gunter, B., Lindenbergh, R., & Kleinherenbrink, M. (2015). ESA ice sheet CCI: derivation of the optimal method for surface elevation change detection of the Greenland ice sheet-round robin results. International Journal of Remote Sensing, 36(2), 551-573, doi:10.1080/01431161.2014.999385.

Kleinherenbrink, M., Lindenbergh, R., & Ditmar, P. (2015). Monitoring of lake level changes on the Tibetan Plateau and Tian Shan by retracking Cryosat SARIn waveforms. Journal of Hydrology, 521, 119-131, doi:10.1016/j.jhydrol.2014.11.063.

Kleinherenbrink, M., Riva, R., & Sun, Y. (2016). Sub-basin-scale sea level budgets from satellite altimetry, Argo floats and satellite gravimetry: a case study in the North Atlantic Ocean. Ocean Science, 12(6), 1179-1203, doi:10.5194/os-12-1179-2016.

Frederikse, T., Riva, R., Kleinherenbrink, M., Wada, Y., Broeke, M. & Marzeion, B. (2016). Closing the sea level budget on a regional scale: Trends and variability on the Northwestern European continental shelf. Geophysical Research Letters, 43(20), doi:10.1002/2016GL070750.

Lei, Y., Yao, T., Yang, K., Sheng, Y., Kleinherenbrink, M., Yi, S., Bird, B., Zhu, L., & Zhang, G. (2017). Lake seasonality across the Tibetan Plateau and their varying relationship with regional mass changes and local hydrology. Geophysical Research Letters, 44(2), 892-900, doi:10.1002/2016GL072062.

Simon, K., Riva, R., Kleinherenbrink, M., & Tangdamrongsub, N. (2017). A data-driven model for constraint of present-day glacial isostatic adjustment in North America. Earth and Planetary Science Letters, 474, 322-333, doi:10.1016/j.epsl.2017.06.046.

Kleinherenbrink, M., Riva, R., Frederikse, T., Merrifield, M., & Wada, Y. (2017). Trends and interannual variability of mass and steric sea level in the Tropical Asian Seas. Journal of Geophysical Research: Oceans, 122(8), 6254-6276, doi:10.1002/2017JC012792.

Kleinherenbrink, M., Riva, R., & Frederikse, T. (2018). A comparison of data weighting methods to derive vertical land motion trends from GNSS and altimetry at tide gauge stations. Ocean Science, 14, 187-204, doi:10.5194/os-14-187-2018.

Simon, K., Riva, R., Kleinherenbrink, M., & Frederikse, T. (2018). The glacial isostatic adjustment signal at present-day in northern Europe and the British Isles estimated from geodetic observations and geophysical models, Solid Earth, 9(3), 777-795, doi:10.5194/se-9-777-2018.

Vermeersen, B. L., Slangen, A. B., Gerkema, T., Baart, F., Cohen, K. M., Dangendorf, S., Duran-Mature, M., Frederikse, T. F., Grinsted, A., Hijma, M. P., Jevrejeva, S., Kiden, P., Kleinherenbrink, M., Meijles, E. W., Palmer, M. D., Rietbroek, R., Riva, R. E. M., Schulz, E., Slobbe, D. C., Simpson, M. J. R., Sterlini, P., Stocchi, P., Van de Wal, R. S. W., & Van der Wegen, M. (2018). Sea-level change in the Dutch Wadden Sea. Netherlands Journal of Geosciences, 97(3), 79-127, doi:10.1017/njg.2018.7.

Kleinherenbrink, M., Scharroo, R., & Riva, R. (2018). Calibration of the TOPEX global mean sea level record using ERS1&2. Nature Geoscience, *In preparation*.

Curriculum Vitae

October 29, 1987	Born in Zwolle, The Netherlands
1992-2000	De Regenboog
2000-2006	Carmel College Salland
2006-2012	Bachelor of Science in Aerospace Engineering Delft University of Technology
2010-2013	Master of Science in Aerospace Engineering Delft University of Technology
	Master thesis "Implementation and application of a numerical Cryosat retracker to retrieve lake level estimates on the Tibetan plateau"
	Internship at Institute for Tibetan Plateau Research Chinese Academy of Sciences
2013-2018	PhD candidate at Geoscience and Remote Sensing Delft University of Technology
2018-present	Postdoc at Astrodynamics and Space Missions Delft University of Technology